# 3D ductile damage to fracture transition based on phase field and mesh adaptation : application to metal forming processes

Hazem Eldahshan

PSL UNIVERSITÉ PARIS

THÈSE DE DOCTORAT
DE L'UNIVERSITÉ PSL

Préparée à MINES ParisTech

# Transition endommagement-rupture en 3D basé sur le champ de phase et l'adaptation du maillage: application aux procédés de mise en forme

# 3D ductile damage to fracture transition based on phase field and mesh adaptation: application to metal forming processes


Soutenue par

**Hazem Eldahshan**

le 11 Janvier 2022


Ecole doctorale n° 364

Sciences fondamentales et appliquées

Spécialité

Mécanique Numérique et Matériaux

Composition du jury :

| | | |
|---|---|---|
| Yann Monerie | Professeur, Université de Montpellier | Président |
| Laura De Lorenzis | Professeur, ETH Zurich | Rapporteur |
| Carl Labergère | Professeur, Université de Technologie de Troyes | Rapporteur |
| Jacques Besson | Directeur de recherche CNRS, Mines Paristech | Examinateur |
| Dr. José Alves | Développeur scientifique, Transvalor S.A | Examinateur |
| Pierre-Olivier Bouchard | Professeur, Mines Paristech | Directeur de thèse |
| Daniel Pino Munoz | Chargé de recherche, Mines Paristech | Co-Directeur de thèse |
| Etienne Perchat | Directeur du développement, Transvalor S.A. | Invité |

MINES ParisTech | PSL

# ACKNOWLEDGEMENT

First of all, I would like to express my gratitude to Mme Elisabeth de Givenchy, director of the Doctoral School of Fundamental and Applied Sciences, for validating my engineering degree as an equivalent to a master's degree in order to start my PhD. I also want to thank Mr Patrick Coels, former Administrative and Financial Director at CEMEF, for his outstanding efforts in facilitating the administrative procedures of my admission. Special thanks to Marie-Françoise Guenegan for her dedication to work and her valuable assistance during my PhD.

I would like to express my appreciation to the members of the thesis committee who accepted to review my work: Prof. Jacques Besson, Prof. Laura De Lorenzis, Prof. Carl Labergère and Prof. Yann Monerie. I am sure that their evaluation will enhance the quality of my thesis and will open up new horizons to future extensions of my work.

I would also like to thank my academic supervisors: Pierre-Olivier Bouchard and Daniel Pino Munoz for their patience, guidance and encouragement during the three years of my PhD. Special thanks to Pierre-Olivier for his exceptional guidance in the fields of damage and fracture mechanics and also for his continuous efforts in improving the quality of my work. I gratefully acknowledge the contributions of Daniel for his ambition in scientific research that helped me to acquire new skills during the PhD.

My Special thanks also to my industrial supervisors at Transvalor: José Alves and Etienne Perchat who placed trust in me by funding the work of my PhD. I sincerely appreciate the broad experience of José in different scientific and engineering aspects. José helped me a lot in understanding the industrial challenges related to my work which helped me to achieve my goals effectively. I would also like to thank Etienne for his professionalism and outstanding expertise in the scientific development of industrial softwares. The work done in the PhD would not have been possible without the collaboration of the different team members in which I represent one of them.

Special thanks to Prof. Mostafa Abdalla at Zewail city of Science and Technology who helped me to acquire a deep understanding of different concepts in science and engineering. His outstanding way of teaching helped me to enhance my technical background before starting the PhD. I cannot also forget to thank my colleagues at CEMEF: Saoussen Ouhiba, Mohamed Mahmoud and Ichrak Rahmoun for their continuous support during the past three years. Finally, I would like to express my gratefulness to my parents and my two sisters who gave me all the needed support during the difficult times of the last period.

# Nomenclature

| | |
|---|---|
| $W_e$ | Elastic strain energy density |
| $W_p$ | Plastic strain energy density |
| $\bar{\theta}$ | Normalized Lode angle |
| $\boldsymbol{L}$ | Lode parameter |
| $\eta$ | Stress triaxiality |
| $X$,$x$ | Position vectors in the reference and current configurations |
| $u$ | Displacement vector |
| $v$,$p$ | Velocity vector and pressure field |
| $\bar{\boldsymbol{\varepsilon}}$ | Equivalent plastic strain |
| $\lambda_p$ | Plastic multiplier |
| $f_p^{trial}$, $f_p$ | Trial yield function and yield function |
| $\boldsymbol{\varepsilon}$ | Total strain tensor |
| $\boldsymbol{\varepsilon}^e$ | Elastic strain tensor |
| $\boldsymbol{\varepsilon}^p$ | Plastic strain tensor |
| $\bar{\boldsymbol{\sigma}}$ | von Mises stress |
| $\boldsymbol{\sigma}_y$ | Yield stress |
| $\boldsymbol{\sigma}_1$, $\boldsymbol{\sigma}_2$, $\boldsymbol{\sigma}_3$ | Principal stresses |
| $l_c$ | Characteristic length scale |
| $\lambda, \mu$ | Lamé coefficients |
| $\kappa$ | Bulk modulus |
| $E$ | Young's modulus |

| | |
|---|---|
| $\nu$ | Poisson's ratio |
| $G_c$ | Fracture toughness |
| $W_0$ | Plastic energy Threshold |
| $D$ | Local damage variable |
| $\bar{D}$ | Non-local damage variable |
| $\beta_1, \beta_2$ | Elastic and plastic energies control parameters |
| $d$ | Phase field variable |
| $D_{thresh}$ | Damage threshold for the coupled phase field - damage model |
| $\eta_c$ | Fracture parameter for the coupled phase field - damage model |

# TABLE OF CONTENTS

# LIST OF FIGURES

# Introduction

This work addresses the modeling of damage and fracture within the framework of metal forming processes. Damage affects the quality of the final component and most of the time, predicting fracture based on a damage threshold is accurate enough since the part is not good anymore. However, damage to fracture transition and fracture modeling become essential in specific cases: $(i)$. multi-stage operations where the product of each single stage affects the quality of the final product; $(ii)$. predicting properties of components obtained after cutting or blanking operations.

The industrial importance toward lightweight components requires the development of robust computational tools capable of accurately simulating the fracture process. Ductile damage can be described as a degradation of material properties that are often handled at the macro-scale but which is due to the change of micro-structural composition of the material. Although the damage itself can be seen as a material property rather than a defect [1], its excessive accumulation leads to the initiation and propagation of cracks at the macro-scale. In the field of metal forming, the formation of cracks can be either a requirement as part of the manufacturing process in order to produce a given component such as the metal cutting processes, or an undesired defect that should be avoided such as the apparition of chevron-shaped cracks in extrusion processes.

Numerical treatment of damage to fracture transition can be seen from two different perspectives: $(i)$. physical description of the damage micro-mechanics that establishes the appropriate relationship between the evolution of void area/volume fraction and the degradation of macroscopic material properties such as effective Young's modulus, density and plastic yield surface; $(i)$. numerical treatment of the topological changes due to the initiation and propagation of cracks at the macro-scale. The accuracy of modeling the ductile damage to fracture transition relies on the ability to establish physically-relevant damage models and computationally efficient tools.

## Industrial context

The main objective of the industrial partner (**TRANSVALOR S.A.**) is to improve the computational capability of simulating the transition from ductile damage to fracture within the finite element software **FORGE ®** that is specialized in metal forming processes. Historically, the element deletion method (or known as kill element) is used to simulate the topological discontinuity introduced by the formation of a crack in the material. Elements are continuously deleted from the mesh upon reaching a critical damage threshold that can be identified experimentally. This technique is extremely robust and simple to implement making it a good choice for 3D

numerical simulations with large number of degrees of freedom. However, a main drawback of this approach is the dependency of the fracture surfaces on the mesh size as can be observed in Fig. 1. The crack path becomes also dependent on the mesh size since the crack front is not uniquely defined. The quality of the surfaces deteriorates with coarse meshes which requires the use of extremely fine meshes in order to obtain accurate results which in turn increases the computation time significantly. In addition, a non-physical volume loss is introduced in the simulation that has significant effects on the results especially in multi-stage processes.

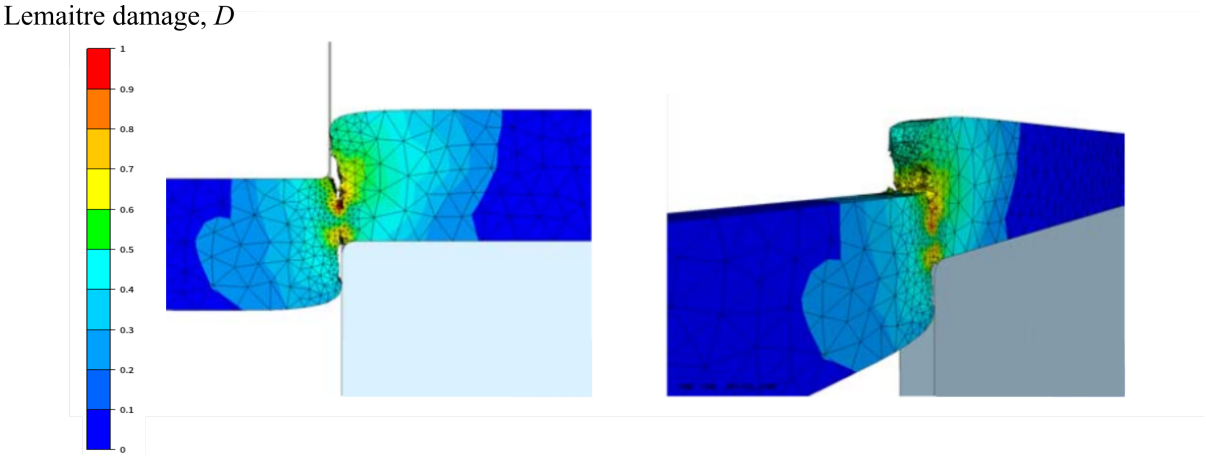


**Fig. 1** The element deletion method is used to predict the initiation and propagation of cracks during the trimming operation. This image is adopted from [2].

## Industrial objectives

The main industrial objective of the present work is to improve the ability of the software to simulate the ductile damage to fracture transition by replacing the kill element technique by a real crack insertion algorithm to simulate the initiation and propagation of cracks in continuum media. The ultimate goal is to accurately simulate the ductile fracture process with relatively coarse meshes and therefore reasonable computation time. All the previously mentioned drawbacks of the kill element technique are expected to be resolved while the following features should be maintained:

1. Robustness: the algorithm must be able to deal with complex scenarios of crack initiation, propagation, merging and branching of multiple cracks that might appear in metal forming processes with 3D finite element meshes.
2. Efficiency: all computations should be carried out in parallel while minimizing the communication cost and optimizing the load balance between computational units (CPUs for instance).
3. Modularity: the algorithm should be structurally designed as a separate unit that can be easily integrated with all the other components of the program such as the mechanical solver and the contact algorithm.

In order to illustrate the ability of the algorithm to tackle all the mentioned drawbacks, standard benchmark cases are initially tested in order to establish a good understanding of the functionality of the algorithm. Then, the algorithm is tested on metal forming processes with complex loading conditions. Comparisons are carried out with the kill element technique in order to clearly observe the main improvements introduced by the algorithm. A detailed description of the role of numerical and physical parameters in the problem will also presented. One of the objectives is to facilitate, to a maximum extent, the use of the new algorithm by the metal forming community. Thus, special attention will be paid to the relationship between the proposed models and the classical damage approaches used in the metal forming community.

## Scientific challenges and strategy

The study of damage to fracture transition in the field of metal forming is very challenging from the scientific point of view due to many reasons:

- Even if discontinuities appear at finer scales, ductile damage is usually modeled at the macro-scale through continuum mechanics approaches. The modeling at the macro-scale poses many difficulties in the determination of the moment at which a crack initiates and in the definition of the crack propagation direction and distance.
- In many metal forming applications that include crack propagation, the crack is intentionally induced in the material in order to obtain new parts with prescribed shapes. Thus, it is required to explicitly represent the crack surfaces in the domain. In this case, a continuous-discontinuous modeling of the damage to fracture process is the only possible solution. In consequence, an accurate modeling strategy should take into account the transition between the two modeling paradigms.
- Since computational domains are very large in many problems, adaptive remeshing techniques are required to reduce the computation time. In this context, the mesh is only refined in the regions where cracks are expected to propagate and coarsened in the rest of the domain. In addition, large plastic strains may lead to a degradation in the finite element mesh quality. Thus, continuous remeshing is also essential in order to keep a good mesh quality throughout the simulation. The developed methodology should therefore be compatible with remeshing techniques.
- A proper detection of complex crack paths is highly questionable since some information at the lower modeling scale (usually the micro-scale) might be lost at the higher modeling scale (the macro-scale). The difficulty is explained by the accurate determination of a discontinuous crack path from a continuous damage field. In addition, the identification of multiple cracks that might merge together or a single crack that can branch to multiple cracks becomes challenging. The problem becomes more difficult in 3D since the crack path is a two dimensional surface that propagates through the domain. Most importantly,

the continuous/discontinuous transition in 3D must be properly handled with a relatively low computational cost.

- Handling the kinematics of crack propagation is also an essential aspect in the numerical strategy. The fracture energy release rate is dependent on the crack propagation velocity. Thus, it is important to have a good control of fracture energy release during the simulation.
- In 3D metal forming simulations, parallel computing is essential to reduce the total computation time. The main idea here is to use multiple processing units with a minimal level of communication in order to get a significant improvement in the results. The main challenge in the crack propagation is the ability to minimize the cost of communication while handling multiple cracks that can cross the interfaces between different processors.

## Outline of the thesis

The thesis is organised as follows:

Chapter 1 presents a comprehensive literature review about the physical phenomena and modeling tools in damage to fracture transition. This chapter starts by discussing the importance of the study of damage to fracture transition in ductile materials. This initial discussion establishes the need for accurate and robust computational methodologies along with the experimental investigations in order to optimize the production process. In this context, a detailed description of the ductile damage mechanisms at the micro-scale is presented with the aim of highlighting the complexity of the process. The last section presents the computational models that have been proposed in the literature to tackle the problem. The objective of this last part is to show the advantages, limitations and challenges of each modeling strategy.

In chapter 2, a general introduction of the main concepts of continuum mechanics including both kinematic and kinetic descriptions is presented. Then, a numerical validation of the developed phase field model with the literature is carried out. Following that, a comparison between the phase field and classical non-local damage models is also presented. The objective of this comparison is to reveal the main features of both modeling approach from both mathematical and numerical points of view. The comparison starts with a one-dimensional simplified case followed by a numerical simulation in order to illustrate the main differences between the two approaches.

In chapter 3, an adaptive remeshing strategy combined with the phase field model at large strains is described in details. Different remeshing criteria are tested where the advantages and disadvantages of each one are discussed. It is well known that a numerical diffusion is always associated with each field transfer operation. In order to minimize this numerical diffusion, a new strategy based on defining a volume quality metric is introduced. The aim is to refine the mesh only in the regions where the crack is expected to propagate while minimizing the number of remeshing operations. The section ends with numerical simulations of benchmark

problems while comparisons are carried out with pre-refined fixed meshes in order to show the main advantages of the algorithm.

Chapter 4 introduces a crack initiation and propagation algorithm based on the phase field model. First, a general overview about the main algorithmic operations is presented. Then, a discussion about the ability to control the crack increment length is shown. The main bricks that constitute the crack propagation are then described in details. The first step is the identification of a discrete crack path in a 3D mesh based on a continuum field that regularizes the sharp crack interface. Then, a local mesh partitioning algorithm is developed in order to fit arbitrary crack topologies inside the mesh using local remeshing operations. The next step is to introduce a geometric discontinuity in the mesh by duplicating all the nodes that lie on the crack surface except those on the crack front. The final part is dedicated to the description of the parallel framework that is designed to reduce the computation time of the crack propagation process. Standard test cases from the literature are used to validate the developed framework and prove the numerical efficiency of the calculations.

In the first part of chapter 5, a new coupling between the phase field model and a general damage criterion is proposed in such a way that the advantages of each one are combined together. The main features of the new proposed model are discussed in details starting with a simplified 1D homogeneous solution followed by 3D numerical examples. The new proposed model is mainly developed for the treatment of complex stress states that exist in metal forming processes. In the next part of the chapter, ductile fracture simulations are carried out on different metal forming cases. A first example of bar extrusion is presented where the formation of chevron-shaped cracks is possible. A second case of metal cutting processes such as bar shearing and blanking simulations is also illustrated. The main challenge is to demonstrate the ability of the algorithm to capture the main features of the sheared surfaces while keeping the computation time as minimum as possible. Finally, a multi-stages process is presented where a comparison between the new numerical strategy and the element deletion method is shown. The main goal of this example is to test the ability of the new algorithm to predict the mechanical behaviour at each stage and its effect on the following stages and in particular on crack initiation.

A summary of the main contributions of the thesis is provided at the end. Following that, discussions are presented about the importance of the outcomes and their potential benefits to the scientific and industrial communities. Last but not least, a list of suggestions is shown and the possible research directions in the future are also presented with the aim of maximizing the benefit of the present work.

## Scientific dissemination

This work has given rise to **three** scientific articles in **peer-reviewed international journals**:

- H. Eldahshan, P.-O. Bouchard, J. Alves, E. Perchat, D.P. Munoz, ”Phase field modeling

of ductile fracture at large plastic strains using adaptive isotropic remeshing", Computational Mechanics 67 (2021), 763–783.

- H. Eldahshan, J. Alves, P.-O. Bouchard, E. Perchat, D. P. Munoz, "CIPFAR: A 3D unified numerical framework for the modeling of ductile fracture based on the phase field model and adaptive remeshing", Computer Methods in Applied Mechanics and Engineering 387 (2021), 114171.
- H. Eldahshan, D. P. Munoz., J. Alves, E. Perchat and P.-O. Bouchard, "3D crack initiation and propagation applied to metal forming processes", (Under review in International Journal of Material Forming), (2021).

**and to three oral communications**:

- H. Eldahshan, "Phase Field Modeling of Ductile Fracture at Large Plastic Strains using an Adaptive Isotropic Remeshing", 14th Virtual Congress WCCM and ECCOMAS, (2020).
- J. Alves and H. Eldahshan, "Modeling of Ductile Damage Transition to Fracture, Transvalor International Simulation Days (TISD)", (2021).
- P.-O Bouchard,"Numerical Modeling of Ductile Damage during Metal Forming: State of the Art and Future Challenges", 13th International Conference on the Technology of Plasticity (Plenary Lecture), (2021).

# Literature review

## Contents

## 1.1 Damage and fracture in metal forming applications

The prediction of damage and fracture is essential in metal forming applications with two main scenarios: (i). inducing the fracture; (ii). avoiding the possible initiation of cracks. In the first scenario, the fracture is induced by creating new crack surfaces under controlled conditions in which fracture is part of the process: blanking, punching and machining. Blanking is defined as a forming process of metal sheets to a given shape with the help of upper and lower dies. In blanking, the part that is removed from the original sheet is considered as the workpiece. On the other hand, when the final product is the remaining sheet, the process is known as punching. In the second scenario, the initiation of cracks during the metal forming processes should be avoided. In both cases the need for an accurate damage model is essential to predict the instant and location of the possible crack initiation. While the accuracy of crack modeling is not important for the latter scenario, it is essential for the first one for which crack surfaces need to be accordingly predicted. Detailed descriptions of both modeling scenarios are presented in the following sections.

### 1.1.1 Metal forming processes based on fracture

Laser technology has been widely used in trimming, blanking and punching processes as it generates sheared surfaces with high quality [3]. However, some problems arise with the use of laser technology: $(i)$. long process time due to the locality of laser beam exposure which is not acceptable for the mass production especially for large structural components; $(ii)$. high energy consumption which significantly increases the product cost. On the other hand, mechanical trimming resolves the two issues raised by the laser cutting process as it provides an optimum solution for mass production with a minimum energy consumption. The main challenge of mechanical trimming is that the quality of sheared surfaces is deteriorated and hence special configurations are needed to optimize the surface quality. Fig. 1.1 illustrates different products from blanking and punching operations where a precise quality of sheared surfaces is essential. Fig. 1.2 illustrates the main characteristic surface features of a sheared surface.

Two main factors affect the production process with mechanical trimming: $(i)$. the appearance of surface defects such as the burrs (burr is an extension of the edge of the sheared edge that deteriorates the surface quality as shown in Fig. 1.3) and slivers (slivers are hair like parts that are separated from the aluminum sheared edges as shown in Fig. 1.4); $(ii)$. the choice of best industrial configurations and parameters that minimize the energy consumption needed in the process.

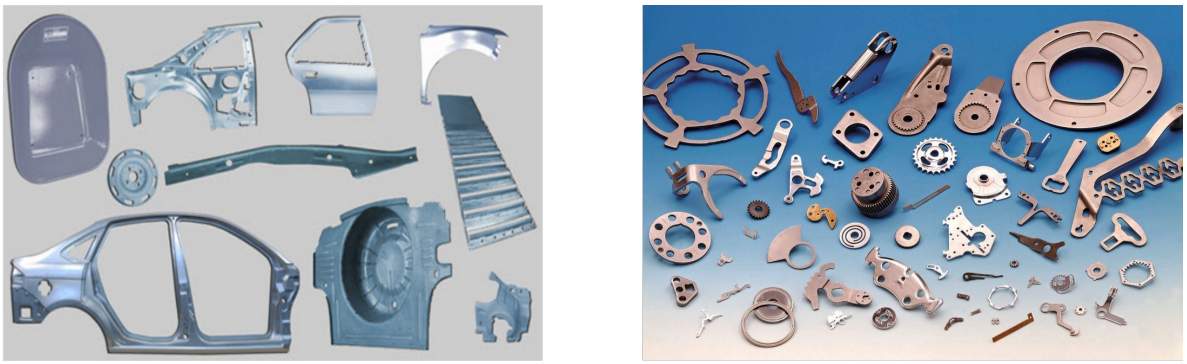

(a) (b)

**Fig. 1.1** Products of punching process in automotive industry (a) (https://www.totalmateria.com). A wide range of fine blanking products in different industries such as: aerospace, automotive, electrical, medical and watch industries (b) (https://www.etmm-online.com).

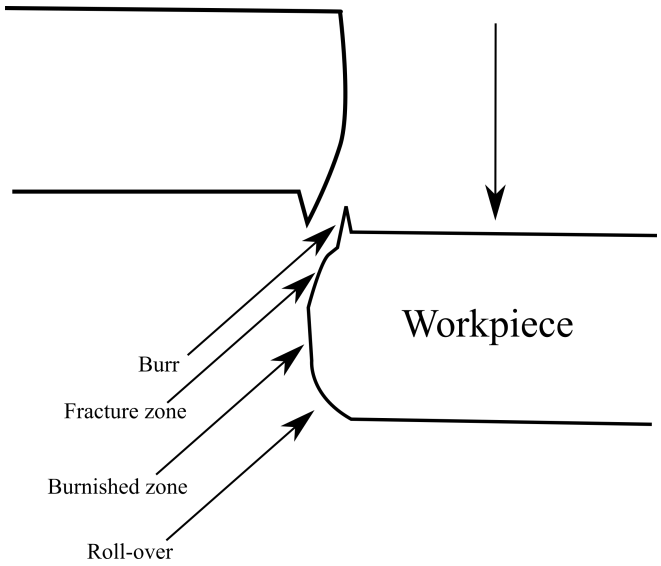


**Fig. 1.2** Characteristic surface features of a sheared surface.

Fig. 1.5 shows the relationship between the clearance (clearance is defined as the distance between the punch and the die normalized with respect to the sheet thickness). It can be observed that the burr height increases with the increase in the clearance as observed in Fig. 1.5a. It is important to accurately predict the burr height in order to control it. Another observation is shown in Fig. 1.5b in which the punch load at fracture decreases with the increase in punch wear $R_{usp}$ according to the experimental results. The objective in this case is to choose the best design parameters that minimize the energy consumption during the process.

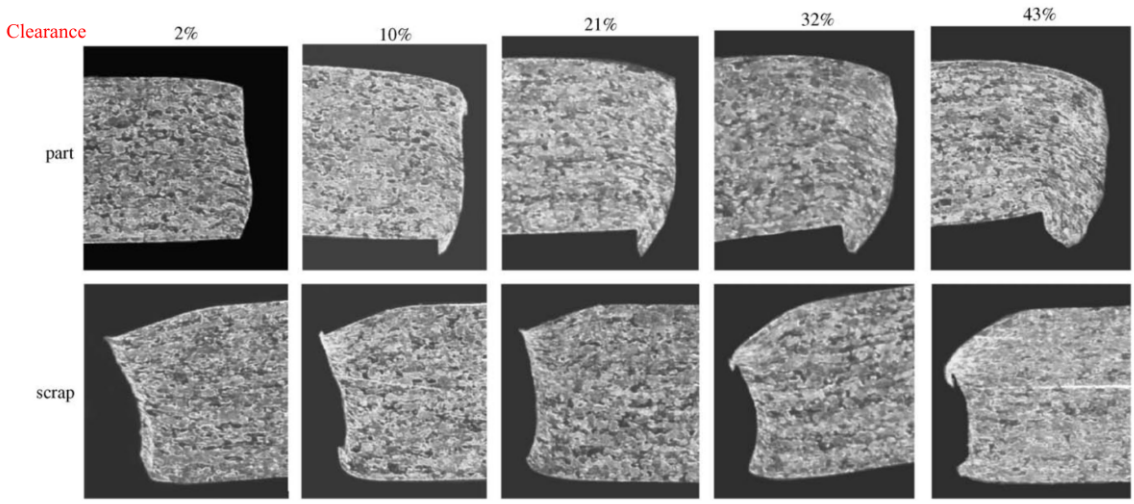


**Fig. 1.3** The apparition of non favorable burrs during the aluminum cutting operations at different clearance values [4].

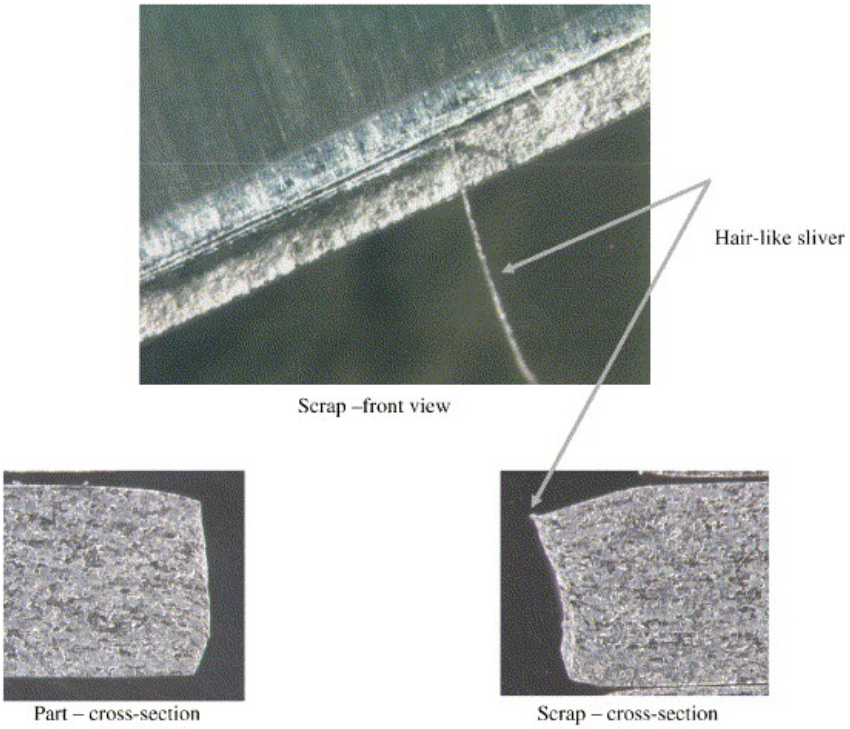


**Fig. 1.4** The apparition of non favorable slivers during the aluminum cutting operations [4].

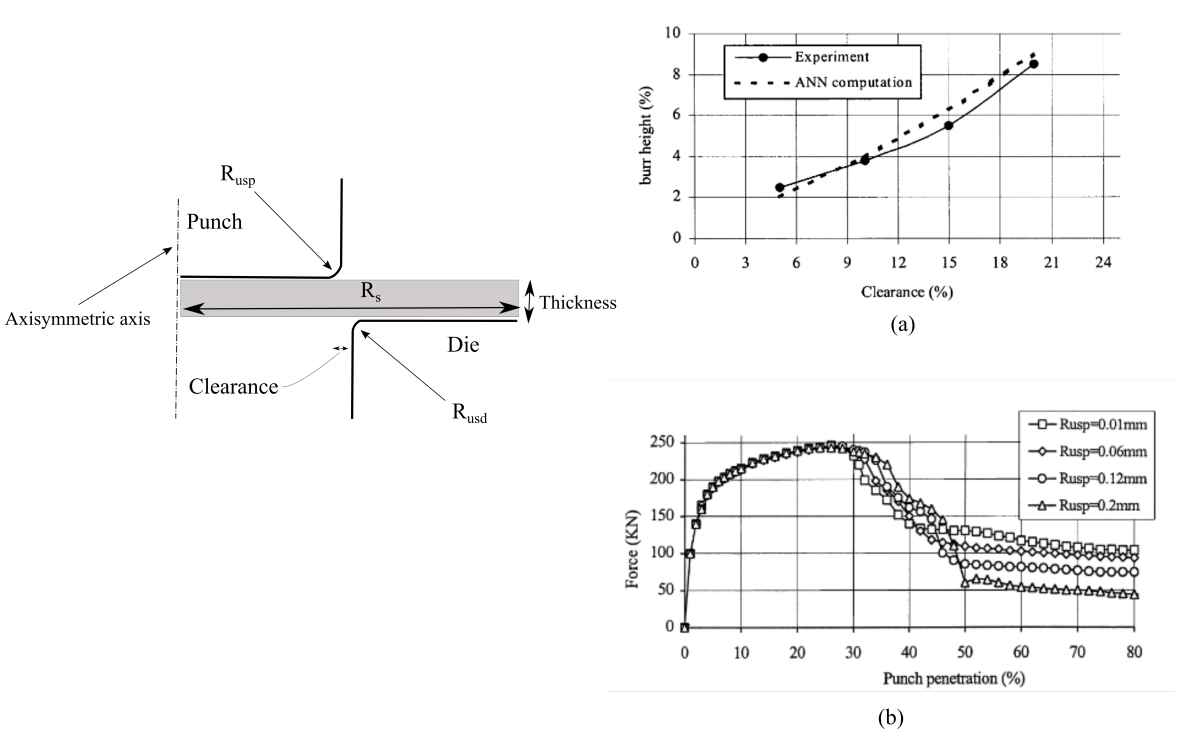


**Fig. 1.5** The relationship between clearance and burr height for a blanking operation [5] is shown in (a). The relationship between the punch penetration and the punch force [6] is shown in (b). The punch penetration is defined as the ratio between punch displacement and workpiece thickness.

Authors in [7] have proposed an energy efficient configuration for the mechanical trimming as shown in Fig. 1.6. In the first step, a half-trimming operation is carried out up to a given penetration depth $D_h$ at the same time of hot stamping as shown in Fig. 1.6a. Next, a full trimming operation is used to separate the additional surface extensions as shown in Fig. 1.6b. The following conclusions have been drawn: (i). a decrease of about 50 $\%$ of the maximum punch force can be observed between the conventional and new blanking approaches as shown in Fig. 1.7. This decrease in force can be explained by the fact that deformation is highly localized in the contact edges between the punch and the die as a result of the hot half-trimming operation. In addition, the reduced thickness requires a small punch penetration until the final crack propagation. As a result, the needed amount of energy is considerably reduced; (ii). the burnish and fracture depths increase with the increase in hot half-trimming depth while the burr and roll-over zones are relatively insensitive to the half trimming depth variation as show in Fig. 1.8. It has been concluded the proposed mechanism gives a better surface quality contrary to cold blanking mechanism. Another contribution was presented in [8] in which warm blanking was studied as a potential choice for the trimming process since the ductility of the material increases with the increase in temperature.

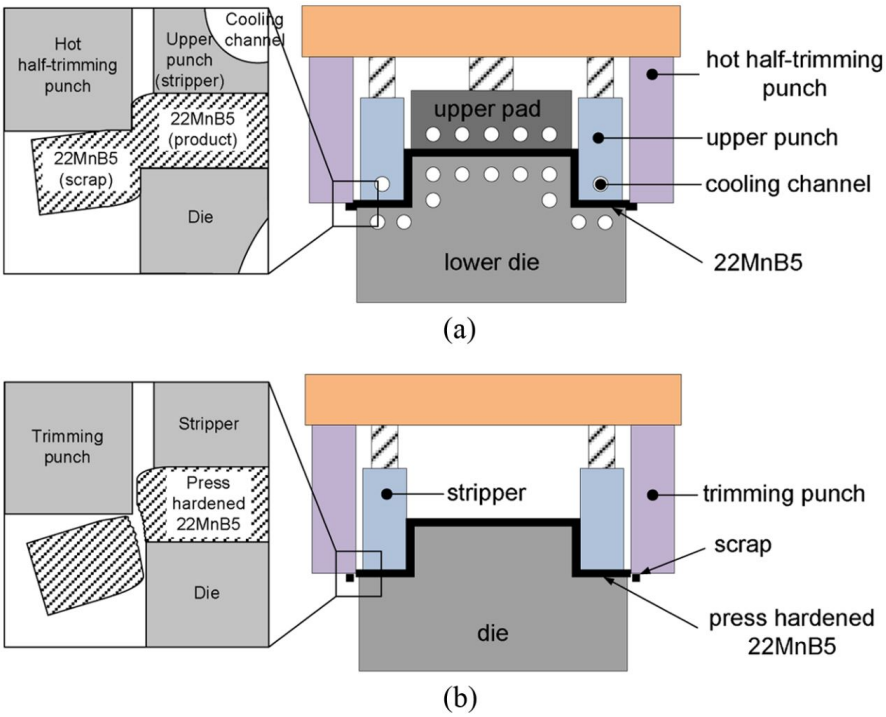


**Fig. 1.6** An energy efficient mechanism for mechanical blanking using hot half-trimming [7].

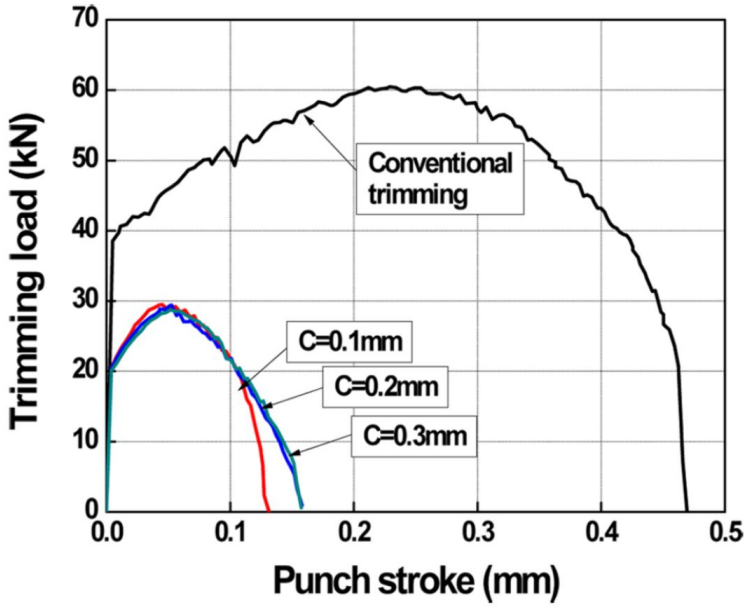


**Fig. 1.7** The force vs. displacement curves between conventional blanking vs. an energy-efficient approach proposed in [7]. Results are shown for different clearance $c$ values.

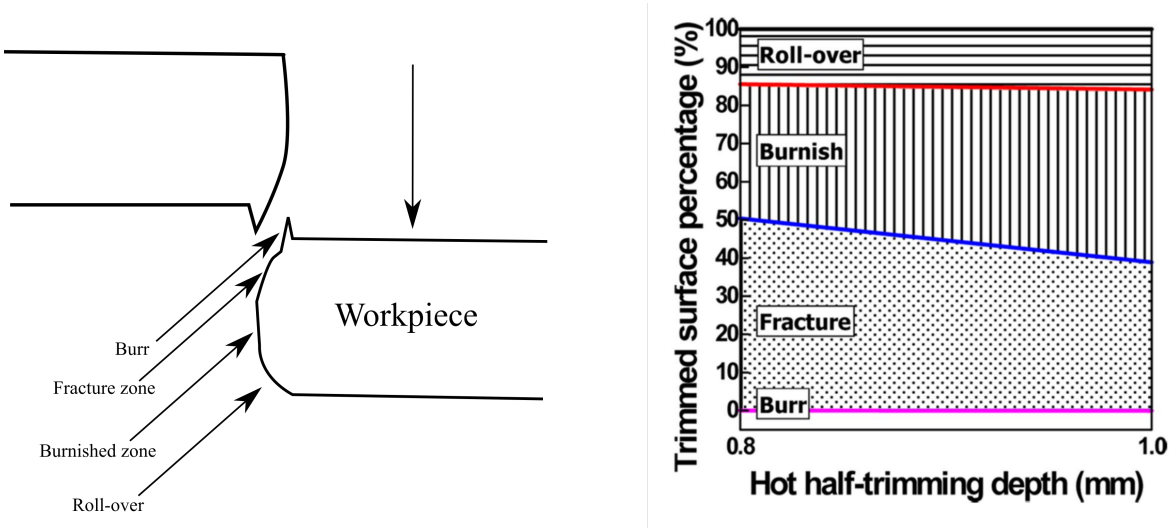


**Fig. 1.8** The sensitivity of sheared surface characteristic features with the half-trimming penetration depth [7].

The presented challenges confirm the necessity to develop numerical and physical models that are capable of describing the complex fracture mechanisms. Indeed, high fidelity computational models need to be implemented in this context. The main advantage of numerical simulations is the ability to choose the optimal design configurations and process parameters without running a large number of experiments.

### 1.1.2 Avoiding fracture in conventional metal forming processes

A second challenge in ductile fracture problems is the prediction of possible crack initiations. The goal being to optimize the forming process parameters in order to avoid such initiation in the formed component. Different fracture modes appear in Fig. 1.9 that can occur during metal forming processes such as the apparition of internal chevron cracks that are difficult to inspect visually and requires the use of ultrasonic techniques. These cracks are formed due to a complex interaction between the stress state and plastic deformation. In order to simulate this complex fracture mechanism, authors in [9] used the Latham-Cockcroft damage model to predict the crack initiation where the element deletion method is used for fracture modeling. Results are shown in Fig. 1.10 for different mesh sizes. Two main observations can be made: (i). The number of internal cracks varies with the mesh refinement where the maximum damage value increases; (ii). the shape and dimensions of chevron cracks vary with the mesh refinement. The reported problems are typical while applying a local damage criterion with the element deletion method. Indeed, it is clear that a better modeling strategy should be found.

In the second example shown in Fig. 1.9, a diagonal crack is formed during the compression of aluminum cylinders. The objective in this example is to determine the loading, contact and

geometric conditions that might lead to such failure mode. As explained in [10], the effect of hydrostatic pressure and Lode angle should be included in the damage model in order to precisely capture the fracture process. T.-S. Cao applied the enhanced Xue damage model [11] to predict the damage evolution prior to the crack propagation. The element deletion method has been used to initiate the crack in the material as shown in Fig. 1.11. It can be shown that the adopted numerical strategy is able to predict the slant fracture pattern. However, an extremely fine mesh should be used in such case in order to track the crack propagation properly. This last constraint increases the computation time significantly especially in 3D calculations. In such compressive cases, handling contact between the two fracture surfaces is also an an important challenge.


**Fig. 1.9** Initiation of internal cracks during the forward extrusion process [12]; diagonal crack is formed within the billet during the compression of an aluminium cylinder [10].

Again, the illustrated examples confirm the importance of having a robust numerical framework that is able to predict the different fracture modes while respecting the physical aspects of the problem such as the volume and energy loss. In addition, the ability to solve complex fracture problems with relatively coarse meshes while keeping a good level of accuracy represents one of the challenges in the current study.

The plan of the upcoming discussions is divided into two parts: (i). describing the physical mechanisms that are responsible for the ductile damage and fracture from both material and mechanical points of view; (ii). presenting the different numerical modeling strategies that are used in the literature to tackle the problem.

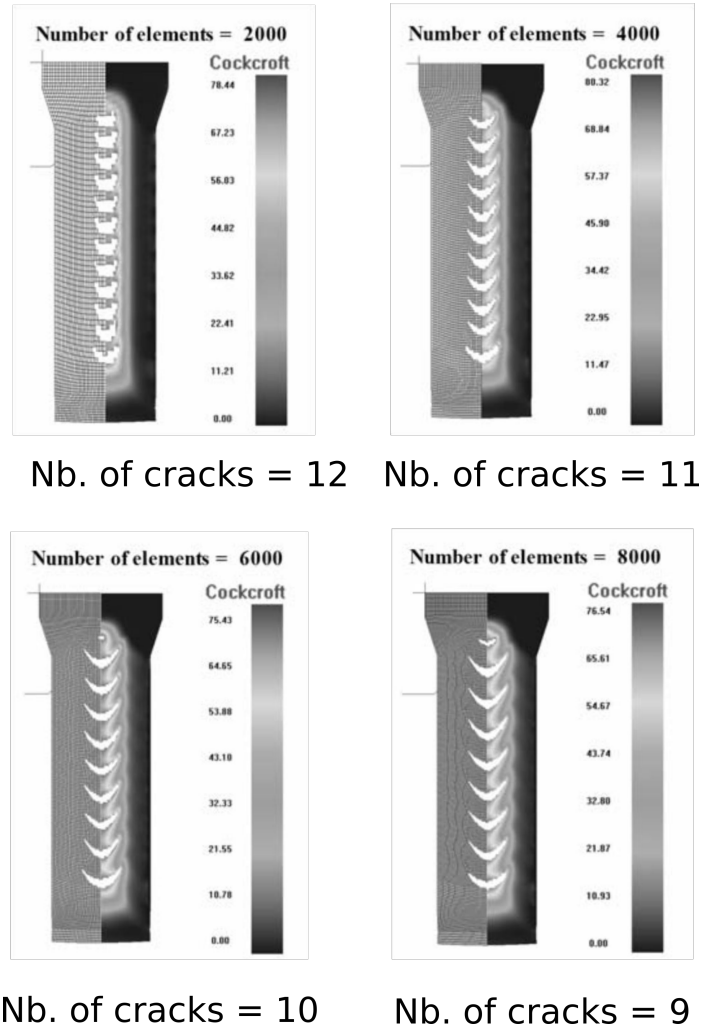


**Fig. 1.10** The effect of mesh size on the shape and number of chevron cracks. A Latham-Cockcroft damage criterion is used where the element deletion method is adopted for the modeling of fracture [9].

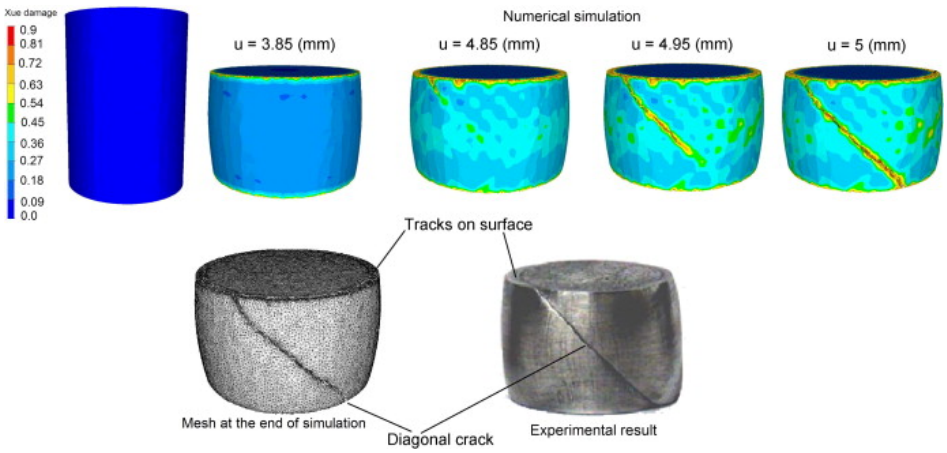


**Fig. 1.11** A comparison between experimental and numerical results for the prediction of slant cracks during the compression of an aluminum cylinder [13]. The enhanced Xue damage model [11] is used in the simulation results.

## 1.2 Ductile damage and fracture mechanisms

Ductile damage and fracture are two interconnected mechanisms that describe the material softening followed by the creation of discontinuous surfaces. Damage occurs due to void nucleation, growth and coalescence (material point of view) that leads to the reduction in load carrying capacity (mechanical point of view).

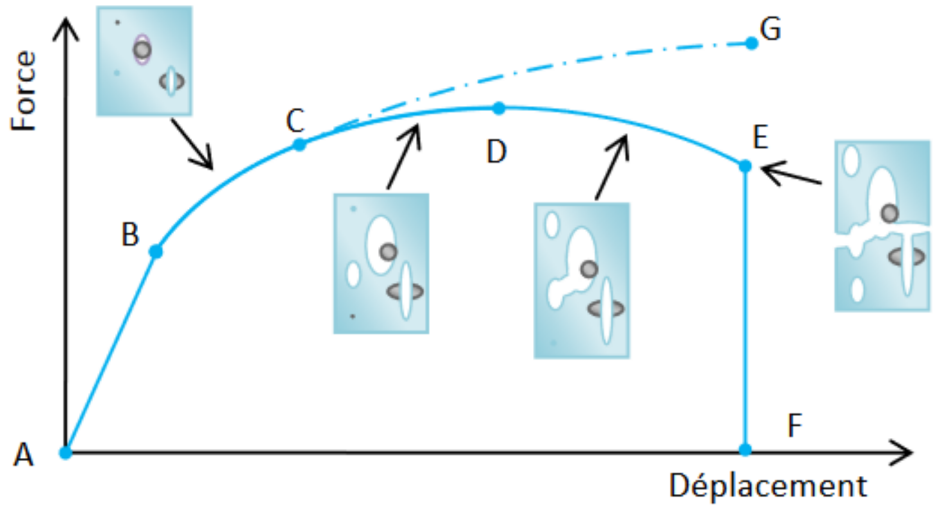


**Fig. 1.12** A schematic representation of the Force vs. Displacement curve for a tensile test [14].

It should be mentioned that other mechanisms such as phase transformations due to thermal effects [15] and hydrogen uptake [16] can lead to a similar behaviour which makes it difficult to accurately define the damage. However, the damage in current study is linked to the void evolution mechanisms. The word ”ductile” is used to indicate that the damage mechanism is mainly associated with plastic flow. Ductile damage mechanisms can be described at different modeling scales that range from the atomic to the macroscopic scales. At the atomic scale, the breaking of atomic bonds is responsible for the fracture process. However, two main challenges arise with the use of atomic approaches: (i). high resolution equipment are needed; (ii). the determination of damage initiation is challenging since the bonds are also broken due to plastic dislocations. On the other hand, modeling of damage at the micro-scale leads to a more convenient description of the main mechanisms that lead to loss of the load-carrying capacity of the material. This can be explained by the better availability of experimental tools with high resolution at the micro-scale. The micro-mechanical mechanisms that are responsible for the evolution of damage in materials are (i). void nucleation; (ii). void growth; (iii). void coalescence.

In fact, earlier evidences of the ductile damage mechanisms were illustrated in [17] where the void expansion under triaxial stresses were found to be the main cause of final ductile failure. In addition, it was concluded that the grain size has a great effect on the ductile frac-

ture mechanism. For example, the formation of cup-cone fracture pattern under plane strain condition was favored in fine-grained materials during the stage of strain hardening. On the other hand, shear cracks are observed in the necking zone in coarse-grained materials. Another evidence of the role of void growth in ductile fracture was shown in [18] where microscopic images (fractographs) of fracture surfaces were taken at the center of a broken sharp notched specimen as shown in Fig. 1.13. It can be observed that traces of fracture surface dimples appear in which they are originated from the void coalescence process. Damage mechanisms are described in more details in the following sections.

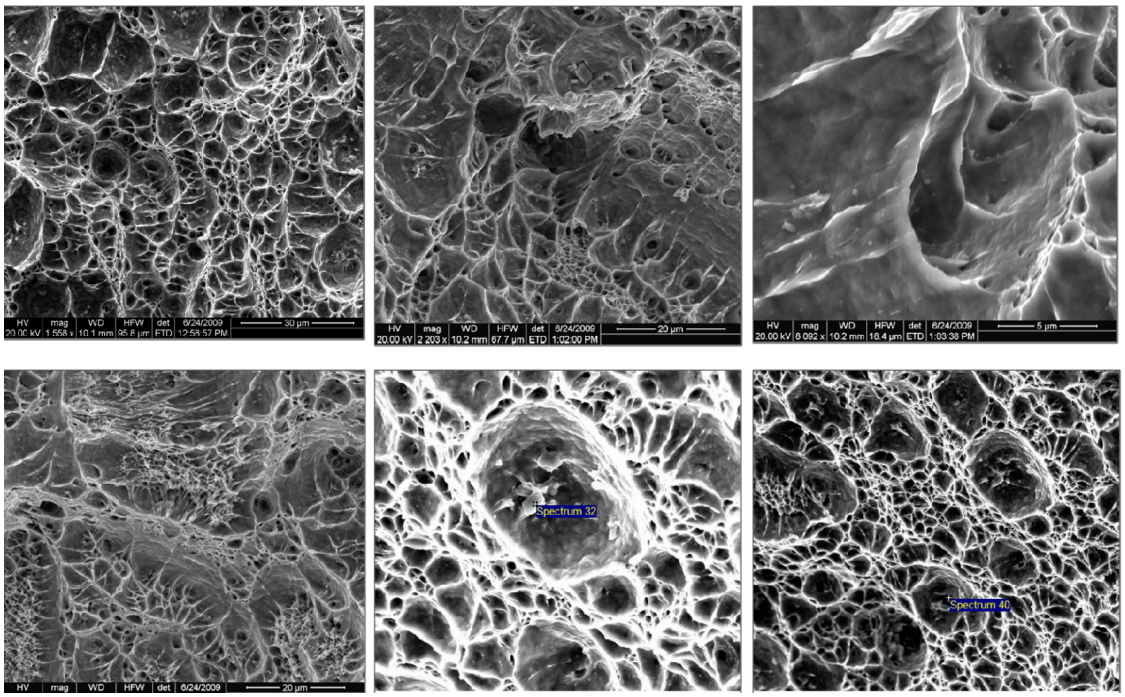


**Fig. 1.13** Fracture surface images taken from the center of a broken sharp notched specimen [18].

## 1.2.1 Void nucleation

Voids nucleate at the grain/phase boundaries, at matrix-particle interfaces or due to particle fragmentation. The strain incompatibility at these interfaces lead to stress concentrations due to the abrupt change in the stiffness of the different phases. Illustrations of the different nucleation mechanisms can be found as follows: (i). Fig 1.14a shows the void nucleation by a particle debonding mechanism; (ii). Fig 1.14b shows the void nucleation at the interface between two metallurgical phases. In addition to the different nucleation mechanisms, voids do not nucleate at the same time at all interfaces due to different factors such as: particles shape, size and orientation, particle stiffness, matrix/particle decohesion and stress state. The effect of each factor on the nucleation process can be found in [19].

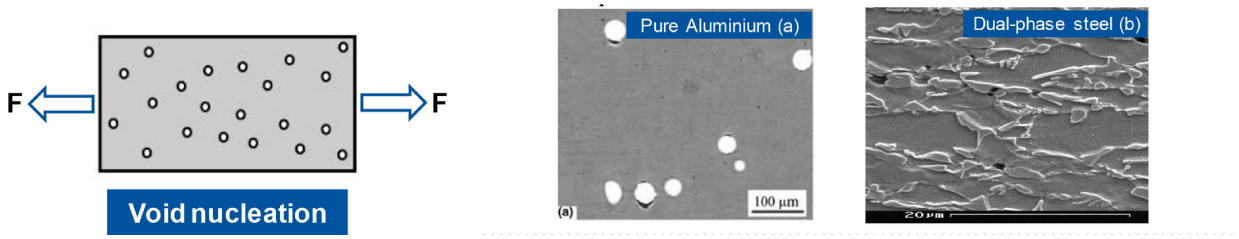


**Fig. 1.14** Two void nucleation mechanisms are shown in the image. (a). Void nucleation by the particle/matrix debonding mechanism in pure aluminium [20]. (b). Void nucleation by the decohesion at the ferrite-martensite interface [21]. The image is adopted from [1].

An illustration of the particle/matrix decohesion process under tensile loading can be seen in Fig. 1.15. In this case, a continuous creation of micro voids leads to an ellipsoidal void formation along the loading path. At the final stage, the particle is fully separated from the matrix at the right and left sides. Nucleation under shear loading can be shown in Fig. 1.16. Microscopic images were taken at points located at Line 1 (high shear stress) and Line 2 (low shear stress) as shown in Fig. 1.16a . In addition, a third point located between the two lines with a moderate level of shear stress was also traced. The debonding of a particle-matrix interface of the sample located at line 1 can be shown in Fig. 1.16b. The sample with a moderate shear stress shows a mixed debonding/fragmentation void nucleation mode as seen in Fig. 1.16c. The particle fragmentation mechanism can also be observed at line 2 with a lower shear stress level. These results confirm that the stress state could change the void nucleation mechanism even with the same micro-structural composition.

It can be shown in Fig. 1.12 that the void nucleation phase (segment B-C) does not lead to any softening in the material behaviour. However, the effect of void nucleation in some cases cannot be neglected where it might have a significant contribution in the softening behaviour. For example, T.-S Cao found that the void nucleation mechanism is dominant over the coalescence mechanism in which the latter happens in a very short strain interval [22]. This can be explained by the fact that the strain at which the nucleation phase is triggered is very small.

### 1.2.2 Void growth

Void growth is mainly driven by extrinsic factors such as the plastic deformation and stress state [23]. Fig. 1.17a shows void growth in aluminum and Fig. 1.17b shows void growth in a dual-phase steel. It can be observed that the particle shape and size can change simultaneously during the deformation process. Two modeling approaches of void growth can be found in the literature that are based on either: (i). crystal plasticity models; (ii). micro-mechanical models. In the former description, simple analytical formulas were derived in order to describe the effect of dislocation movement on the enlargement of voids size as proposed by Ashby in [24] and by McLean in [25]. However, these models have limitations due to the complexity of precisely describing the effect of dislocation movement on the void growth. Authors in [26] performed a 3D numerical simulation using the crystal plasticity theory to show the effect of

crystallographic orientation on the void growth mechanisms. They showed that the crystallographic orientation has a significant effect on both the shape and size of voids. In addition, they concluded that voids in soft orientation have more tendency to grow in single crystal.

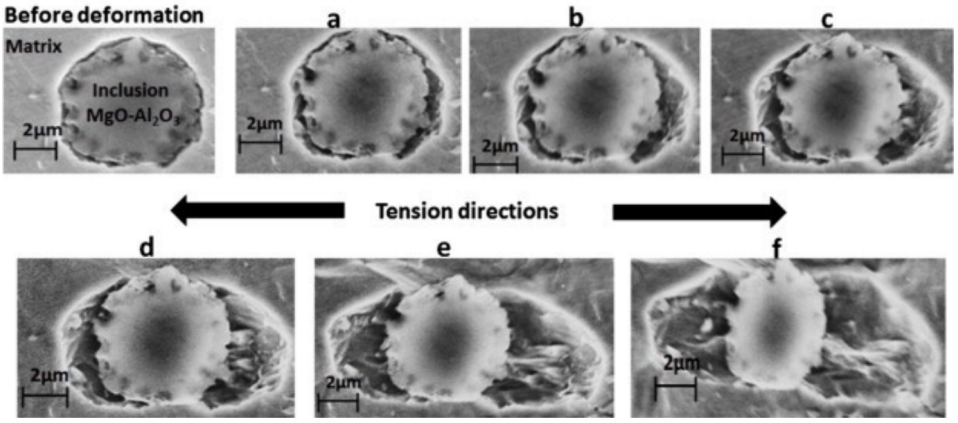


**Fig. 1.15** Illustration of particle/matrix decohesion mechanism under a tensile loading condition. The figure is adopted from [27].

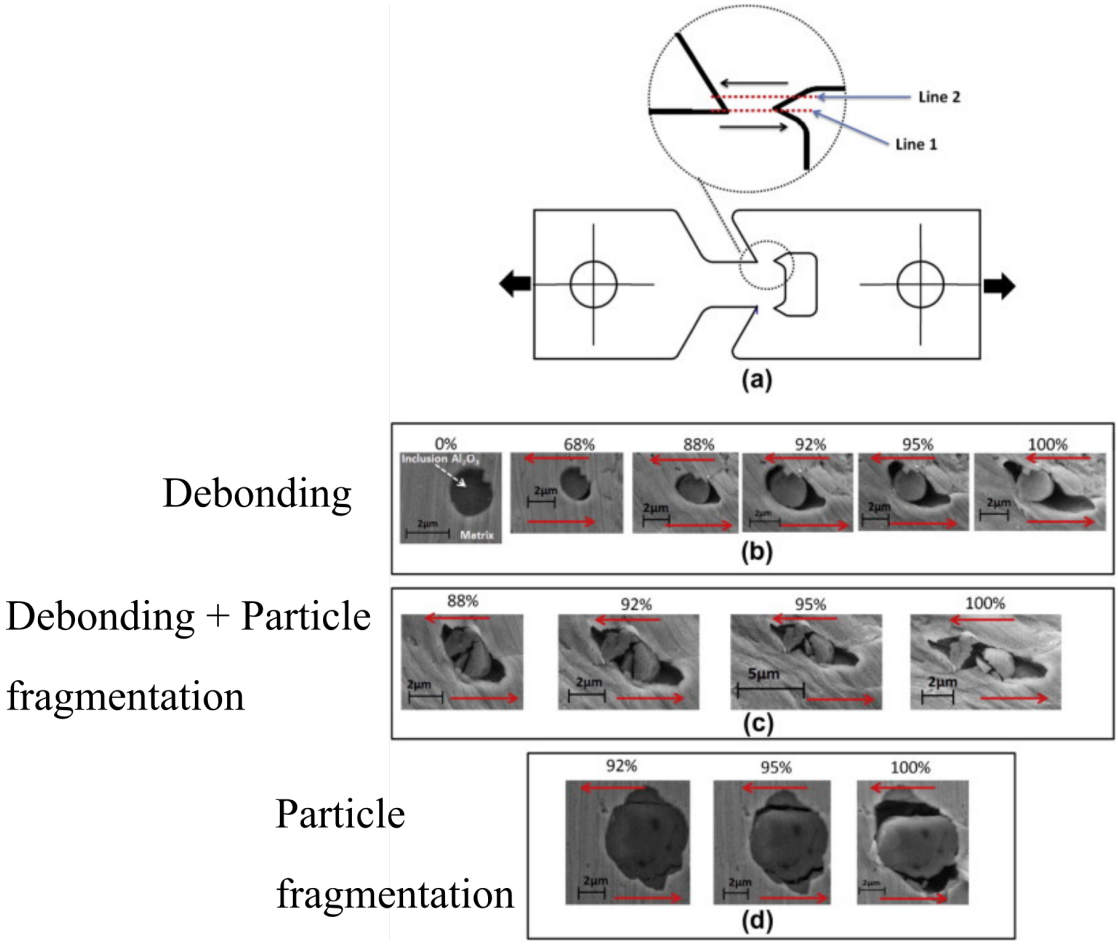


**Fig. 1.16** Illustration of particle/matrix decohesion mechanism under shear loading conditions. The figure is adopted from [27].

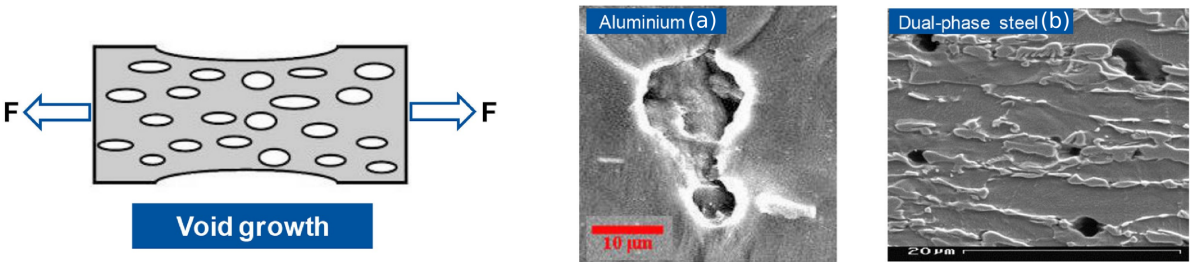


**Fig. 1.17** Void growth at the particle-matrix interface in an aluminium alloy [28] is shown in (a). Void growth at the ferrite-martensite interface is shown in (b) [21]. The image is adopted from [1].

On the other hand, micro-mechanical models assume a given shape of a void that is immersed in either a non-hardening or hardening plastic matrix. The aim is to describe the plastic deformation in the matrix around the void that leads to the void growth. McClintock first proposed a model in which a cylindrical hole is subjected to axisymmetric loading in both hardened and non-hardened materials [29]. The main observations in the results obtained by McClintock can be listed as follows: (i). the role of high stress triaxiality is essential in increasing the void growth rate; (ii). the void growth rate is decelerated when the work hardening coefficient is increased at a constant stress state which has been confirmed experimentally in [30]; (iii). the rate of void growth increases with the increase in the amount of strain at a fixed stress level.

Similarly, Rice and Tracey proposed a continuum mechanics based model of a spherical void in a perfectly plastic medium [31]. The final expression of the void growth equation reads as

$$D_L = \frac{\dot{R}}{\dot{\bar{\varepsilon}} R} = \alpha \, exp(\frac{\sqrt{3}}{2}\eta) \tag{1.1}$$

where $D_L$ is called the dilatation amplification factor, $R$ is the average radius of the spherical void, $\eta$ is the stress triaxiality and $\dot{\bar{\varepsilon}}$ is the equivalent plastic strain rate. It is assumed that voids can only grow witha positive stress triaxiality values. The parameter $\alpha$ was chosen as 0.283 in [31] in order to have a good matching with experimental observations. Equation 1.1 ensures that the void growth rate is directly dependent on the stress triaxiality ratio through an exponential relationship. The former result also gives a convenient estimate of the load carrying capacity based on the stress triaxiality input. It should be noted that the presented work by McClintock and also by Rice and Tracey did not assume any interaction between the various voids' growth. This assumption can be only valid in the case where the distances between voids is large enough so that the interaction of stress field can be neglected. In order to account for the interaction between the voids, a finite body analysis is essential with an accurate calculation of the stress field around each void.

The effect of void growth on the force vs. displacement curve is seen in the C-D segment in Fig. 1.12. It can be shown that the void growth leads to a softening behaviour in the material.

### 1.2.3 Void coalescence

Void coalescence can be described as a merging of smaller voids in order to form larger voids. It could be in the form of void necking, void shearing or void-sheet formation. Fig. 1.18a shows a microscopic image of the internal necking mechanism. Internal necking occurs when the loading direction is perpendicular to the line that connects the two voids. Smaller voids start to develop along the inter-void ligament. Finally, the two voids are completely merged leading to a larger void. In order to describe the inter-void failure process, Thomason developed a critical condition in which necking starts between two voids upon reaching the plastic limit loading [32]. In this case, Rice and Tracey model of void growth was adopted in order to describe the lateral expansion along the ligament between the voids. One clear disadvantage of this model is that it overestimates the limit loading as it neglects the effect of damage evolution along the ligament. In addition, the model does not account for the strain hardening effect as it assumes a perfect plasticity condition.

Void shearing and void-sheet formation are characterized by the formation of a highly localized shear band. Void shearing is characterized by the formation of a few number of voids along the shear band that grow and finally coalesce together [33]. On the other hand, the void-sheet is formed by a large number of nucleated voids with a small size that will be coalesced together just after the nucleation as shown in Fig. 1.18b. Cox et al. showed in [34] a microscopic image of void-sheet mechanism in a 4340 steel alloy which can be seen in Fig. 1.19. It was shown that the secondary voids are nucleated at the precipitated carbides leading to the formation of void-sheet.

The D-E segment in the force vs. displacement curve seen in Fig. 1.12 indicates that the material softening is accelerated in the coalescence phase. The void coalescence is followed by the initiation of cracks at the macro-scale due to the continuous coalescence of voids at the micro scale. The crack initiation and propagation at the macro-scale leads to a very fast loss of the load carrying capacity that can be observed in the E-F phase leading to the final fracture of the material. The transition between damage (in the sense of void nucleation, growth and coalescence at the micro-scale) to fracture (in the sense of the initiation and propagation of cracks at the macro-scale) represents a major scientific challenge.

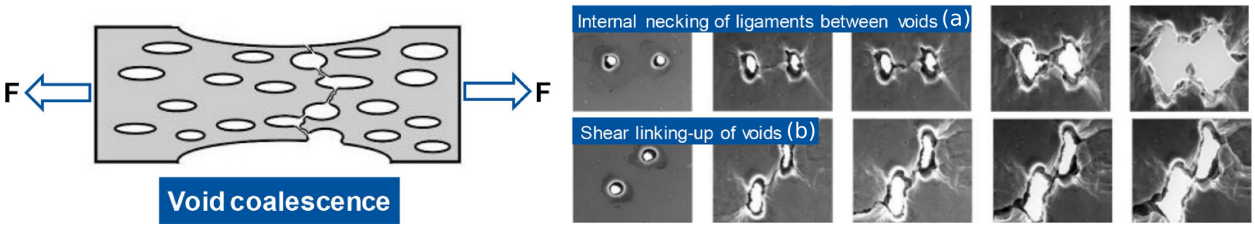


**Fig. 1.18** Two different void coalescence mechanisms: (i). internal necking mechanism in (a) and void shearing mechanism in (b) [35]. The image is adopted from [1].

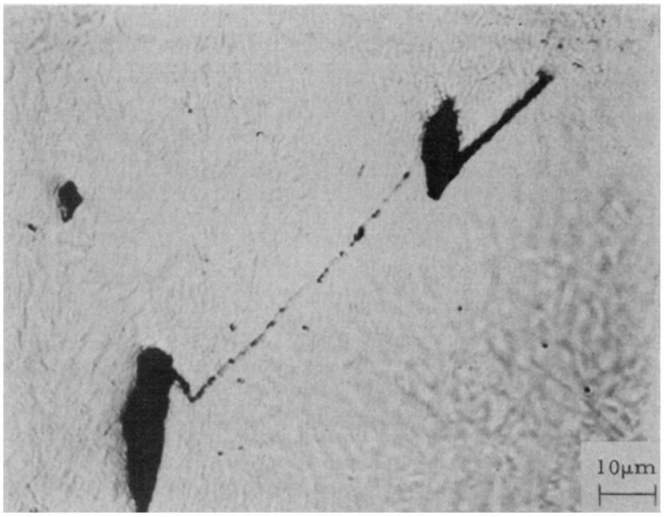


**Fig. 1.19** Coalescence of two voids by the void-sheet formation [34].

This is because of the complex nature of the different phenomena that lead to the final failure of the material that usually requires a proper combination of micro and macro scales modeling approaches. In the next sections, an overview about the damage modeling techniques is first presented. Then, the existing models that deal with the damage to fracture transition will be also detailed and discussed.

## 1.3 Modeling of damage to fracture transition

The damage to fracture transition can be handled using different modeling strategies. According to the classification of fracture approaches proposed by J. Mediavilla in Fig. 1.20, three modeling categories exist: (i). continuous models: no material separation is modeled, i.e., the displacement field is always continuous and the failure is modeled by defining an auxiliary variable/field that can be either uncoupled or coupled to the material behaviour. This field is used to indicate the crack initiation and propagation zones; (ii). discontinuous models: an explicit discontinuity is embedded in the domain based on an identified crack path. However, these techniques usually require predefined crack initiation sites unless they are coupled with a crack initiation model; (iii). continuous-discontinuous models: a continuous field is computed to identify the fracture zones followed by explicit crack insertion in order to model the decohesion of the material. In order to accurately model the discontinuous transition to fracture, the damage field should not diffuse in the regions far from the crack path for two main reasons: (i). to reproduce the accurate material behaviour; (ii). to prevent the numerical instabilities that rise from the diffusion of the damaged zone.

For the study of ductile fracture, either continuous or continuous-discontinuous models are used to handle the damage to fracture transition since a plastic strain localization zone near the crack front is responsible for the crack propagation. In consequence, a continuous model is needed to describe the void nucleation, growth and coalescence with a possibility to insert

a real crack increment to represent the material separation at the macro scale. In multi-stages processes in the field of metal forming it is necessary to explicitly represent the real crack topology in the material in order to use the output components of each stage in the following ones. Thus, a continuous-discontinuous modeling strategy is necessary in this case. Fig. 1.21 explains the main idea of damage to fracture transition algorithms. First, a continuous damage field is computed in the whole domain. When the damage field reaches a critical value, a crack identification algorithm detects the crack path (a line in 2D and a surface in 3D). Finally, a crack increment is inserted in the domain by a proper numerical technique.

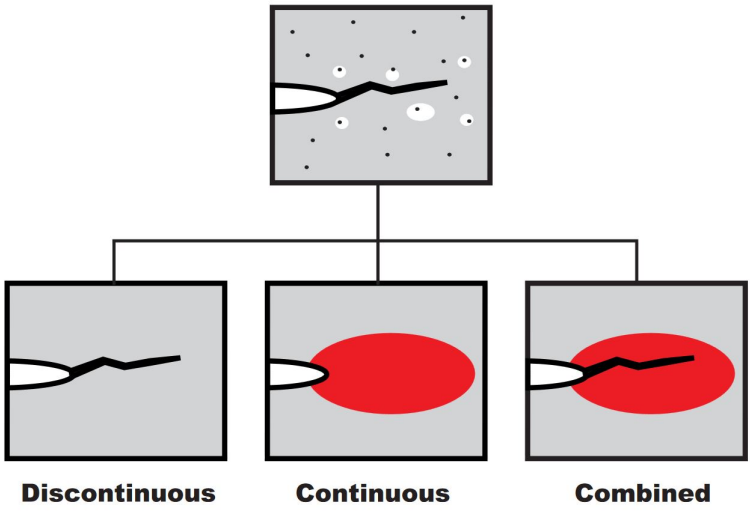


**Fig. 1.20** Classification of modeling strategies of damage to fracture transition according to J. Mediavilla [36].

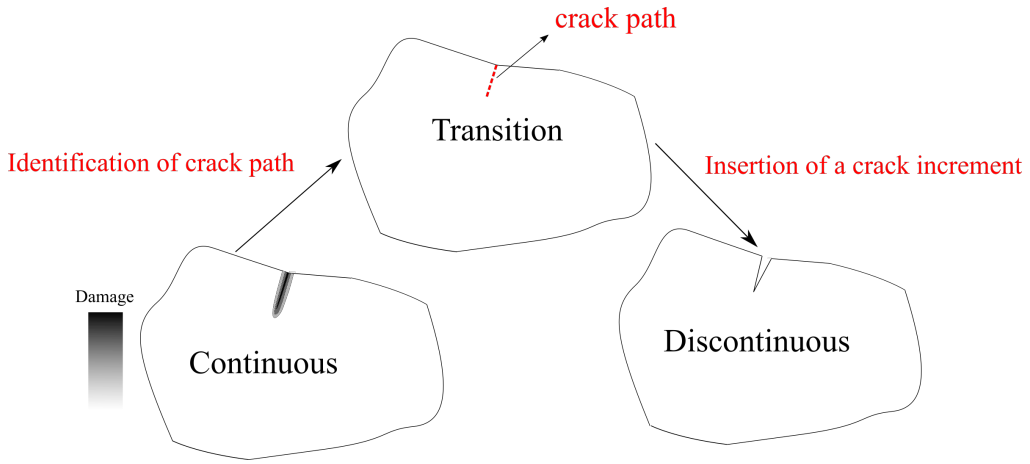


**Fig. 1.21** Illustration of the continuous damage-discontinuous fracture transition.

The choice of the best modeling strategy depends on different factors: (i). the type of application: for example, it is essential in many metal forming processes to fully separate the crack bodies in order to reuse the output components in other production processes (multi-stages

processes). In addition, the crack initiation sites are generally unknown due to the complexity of geometry and loading path. These constraints require the use of a combined continuous-discontinuous modeling technique in order to handle the fracture problem; (ii). the level of accuracy and the final objective of the analysis. If the requirement is to predict the moment of failure, the continuous models in this case serve as an optimum choice without any additional computational cost to handle the explicit crack propagation which is therefore not necessary. However, in some applications the objective is to define the effect of production parameters on the shape of fracture surfaces. In this case, the explicit tracking of crack surfaces propagation is essential in order to accurately detect all the surface features in the end of the simulation.

### 1.3.1 Continuous models

As mentioned in the introduction, ductile damage models can be either uncoupled or coupled to the material behaviour. Additionally, the coupling can affect the Young's modulus and/or the yield surface. Coupled damage models can be based on either phenomenological or micro-mechanical approaches. Fig. 1.22 presents the main features of most of the modeling techniques of damage in the literature.

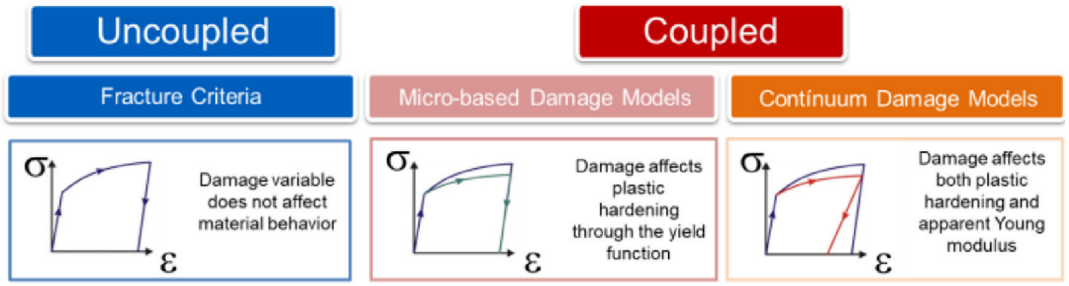


**Fig. 1.22** Comparison between the different modeling techniques of damage [1].

Uncoupled damage models (also called fracture criteria) are widely used in the industrial domains in the preliminary design phases. They are used to get a good estimation about fracture resistance of the product without a precise prediction of the softening in the material due to the damage evolution.

In order to characterize the damage state in the material, the stress state is defined with respect to a given set of non-dimensional quantities known as: stress triaxiality $\eta$ that controls the voids size and Lode angle $\theta$ $(0 \leq \theta \leq \frac{\pi}{3})$ that controls the voids shape can be visualized in the stress space as shown in Fig. 1.23. Before defining the stress state parameters, it is worth defining the invariants of a deviatoric stress tensor as follows

$$J_1 = tr(\boldsymbol{s}) = 0 \tag{1.2}$$

$$J_2 = \frac{1}{2}\boldsymbol{s} : \boldsymbol{s} \tag{1.3}$$

$$J_3 = det(\boldsymbol{s}). \tag{1.4}$$

The stress triaxiality ratio and the normalized Lode angle $\bar{\theta}$ ($-1 \leq \bar{\theta} \leq 1$) can be defined as follows

$$\eta = \frac{\sqrt{2}}{3\tan\varphi} \tag{1.5}$$

$$\bar{\theta} = 1 - \frac{\sqrt{2}}{3}\arccos\left(\frac{r}{\bar{\boldsymbol{\sigma}}}\right)^3 \tag{1.6}$$

where $r$ and $q$ are defined with respect to the deviatoric stress invariants as follows

$$r = \left(\frac{27}{2}J_3\right)^{\frac{1}{3}} = \left(\frac{27}{2}det(s)\right)^{\frac{1}{3}} \tag{1.7}$$

$$\bar{\boldsymbol{\sigma}} = \sqrt{3J_2} = \sqrt{\frac{3}{2}\boldsymbol{s} : \boldsymbol{s}}, \tag{1.8}$$

another parameter known as the deviatoric state parameter $\zeta_L$ can also be defined as

$$\zeta_L = \left(\frac{r}{\bar{\boldsymbol{\sigma}}}\right)^3. \tag{1.9}$$

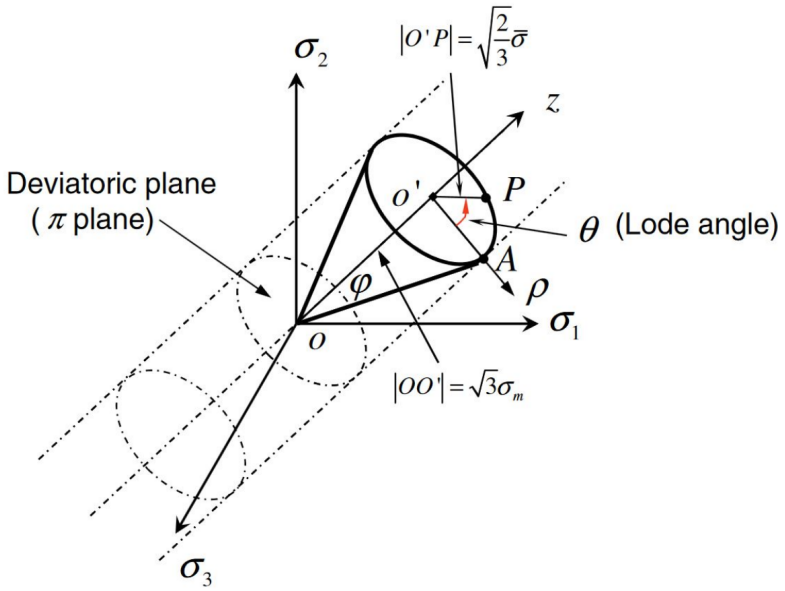


**Fig. 1.23** Illustration of stress states definition in stress space. The image is adopted from [10].

It should be also noted that similar definitions of the parameter exist in the literature such as the Lode parameter $\boldsymbol{L}$ defined in as follows [37]

$$\boldsymbol{L} = \frac{2\boldsymbol{\sigma}_2 - \boldsymbol{\sigma}_1 - \boldsymbol{\sigma}_3}{\boldsymbol{\sigma}_1 - \boldsymbol{\sigma}_3} \tag{1.10}$$

where $\boldsymbol{\sigma}_1$, $\boldsymbol{\sigma}_2$ and $\boldsymbol{\sigma}_3$ are the principal stress components. The Lode parameter can be interpreted as a measure of how far is the intermediate principal stress from the normal stress which has a direct effect on the void shape.

An uncoupled damage variable is usually defined in terms of the stress triaxiality $\eta$, the normalized Lode angle $\bar{\theta}$ (or equivalently the Lode parameter $\boldsymbol{L}$), the maximum principal stress $\boldsymbol{\sigma}_1$ and the maximum shear stress $\frac{\boldsymbol{\sigma}_1-\boldsymbol{\sigma}_3}{2}$ as follows

$$\boxed{D = \int_0^{\bar{\varepsilon}_f} f(\eta, \bar{\theta}, \boldsymbol{\sigma}_1, \boldsymbol{\sigma}_3)\, d\bar{\boldsymbol{\varepsilon}}} \tag{1.11}$$

where $\bar{\varepsilon}_f$ is the critical strain at fracture. The dependency of a local damage model on stress triaxiality is straightforward as it is a major factor in void growth and coalescence as shown in details in section 1.2. The importance of incorporating the third invariant of deviatoric stress in damage evolution in metals was studied in [10, 38].

The different types of ductile damage models offer a good description of the complex damaging mechanisms driven by the plastic strains, stress triaxiality [12] and Lode parameter [39]. Some uncoupled damage models are purely phenomenological such as Latham-Cockcroft [40] and Johnson-Cook [41] and others are based on micro-mechanical mechanisms such as the Rice-Tracey model [31]. A comprehensive review about the available uncoupled damage models can be found in [1, 42]. Table 1.1 gives some examples of different uncoupled damage criteria along with their driving factors.

**Table 1.1** Different uncoupled damage models adopted for complex loading conditions

| Model | Driving factor | Formula |
|---|---|---|
| Latham-Cockcroft [40] | $\boldsymbol{\sigma}_1$ | $\int_0^{\bar{\varepsilon}_f} \langle \boldsymbol{\sigma}_1 \rangle \, d\bar{\boldsymbol{\varepsilon}}$ |
| Rice and Tracey [31] | $\eta$ | $\int_0^{\bar{\varepsilon}_f} A\, exp(\frac{3}{2}\langle \eta \rangle)\, d\bar{\boldsymbol{\varepsilon}}$ |
| Johnson-Cook [41] | $\eta$ | $\int_0^{\bar{\varepsilon}_f} \Big(B_1 + B_2\, exp(B_3\, \langle \eta \rangle)\Big)\, d\bar{\boldsymbol{\varepsilon}}$ |
| Lou and Huh [43] | $\eta$, $\bar{\theta}$ | $\int_0^{\bar{\varepsilon}_f} D_1 \left(\frac{2}{\sqrt{3}cos(\bar{\theta}\frac{\pi}{6})}\right)^{-D_2} \left(\frac{\langle 1+3\eta \rangle}{2}\right)^{-D_3} d\bar{\boldsymbol{\varepsilon}}$ |
| Clement Defaisse [44] | $\eta$, $\boldsymbol{L}$ | $\int_0^{\bar{\varepsilon}_f} \Big(E_1\, exp(E_2\, \langle \eta \rangle) + E_3(1 - \lvert \boldsymbol{L} \rvert^{E_4})\Big)\, d\bar{\boldsymbol{\varepsilon}}$ |
| Bariani el al. [45] | $\eta$, $\zeta_L$ | $\int_0^{\bar{\varepsilon}_f} \left(F_1\, exp(-F_2\, \langle \eta \rangle) \left[\frac{sin(\frac{\pi}{3})}{sin(\frac{2\pi - arccos(\zeta_L)}{3})}\right]^{\frac{1}{n}}\right)^{-1} d\bar{\boldsymbol{\varepsilon}}$ |

The angle bracket operator is defined as follows:

$$< x >= \begin{cases} x & x \geq 0 \\ 0 & x < 0 \end{cases}$$

where all the constants are considered as material parameters that should be calibrated experimentally.

In coupled damage models, the damage mechanisms at the micro-structural level are taken into account in the form of a progressive degradation of mechanical properties such as the Young's modulus and the yield surface. A damage variable can be found in different ways in the literature as shown in Fig. 1.24. The two most common definitions in are: (i). area fraction damage which is defined as the ratio between void area to the total area of a cross section of a representative volume element (RVE); (ii). the volume fraction damage which is defined as the ratio between voids volume to the total volume of a RVE. Fig. 1.25 illustrates representative volume elements showing both area and volume fraction damage definitions.

Although it seems logical that the different definitions of damage correlate to a unified definition, however, the experimental measurements based on each definition show a significant divergence between the results as shown in Fig. 1.26. This can be partially explained by the anistropic nature of the damage evolution which is not taken into account in neither the experimental calibration nor in the physical models due to its complexity. In addition, the accuracy of each calibration technique may also have an effect of the results.

Coupled damage models can be based on either phenomenological or micro-mechanical definitions. The first ones are macro-scale models based on a continuum mechanics description of the damage process. In this context, continuum mechanics variables such as the plastic deformation and stress state are used in order to describe the loss of load carrying capacity of a material point through a damage variable. On the other hand, micro-mechanical models handle the damage process by describing the mechanisms of void nucleation, growth and coalescence at the micro-scale.

It should be noted that coupled damage models induce mesh dependency due to the loss of ellipticity/hyperbolicity of the differential equations in the static and dynamic cases, respectively. This leads to a non-physical localization of damage within one element in the context of FE analysis. This last conclusion leads to a vanishing dissipated fracture energy as the mesh is refined [46]. Different techniques have been proposed in the literature in order to regularize the solution (integral formulation, implicit gradient formulation, micromorphic approaches) as can be found in [47, 48, 49]. These non-local techniques use a length scale parameter to define the regularized zone. More details about the non-local damage models can be found in section 1.3.1.4.

Recently, the phase field approach was first proposed by Francfort and Marigo [50] for brittle fracture problems where a minimization of the total energy of the system leads to a full

description of the initiation and propagation of cracks. Due to the numerical complexity to deal with the original formulation, Ambrosio and Tortorelli [51] proposed a regularized form in which the discrete crack topology is approximated by a finite damage parameter with a continuum field that varies between 0 (intact) and 1 (totally damaged) zone where the width of this zone is controlled by a characteristic length scale. An important feature of the formulation is the $\Gamma$-convergence in which the regularized solution converges to the original solution when the characteristic length scale goes to zero [52]. Miehe et al. proposed a new thermodynamically-consistent phase field model [53] with the introduction of the crack surface density in a purely geometric approach. The crack surface density replaces the description of the sharp crack topology by a continuous phase field where the evolution of this field is governed by a local history functional. According to this definition, cracks are initiated due to the equilibrium between the crack driving force and the geometric resistance of the material. Many extensions to ductile fracture have been proposed in the literature where the main purpose was to add the effect of other driving factors such as the plastic strain and stress triaxiality to the crack driving force that contribute in the ductile fracture [54, 55, 56, 57].

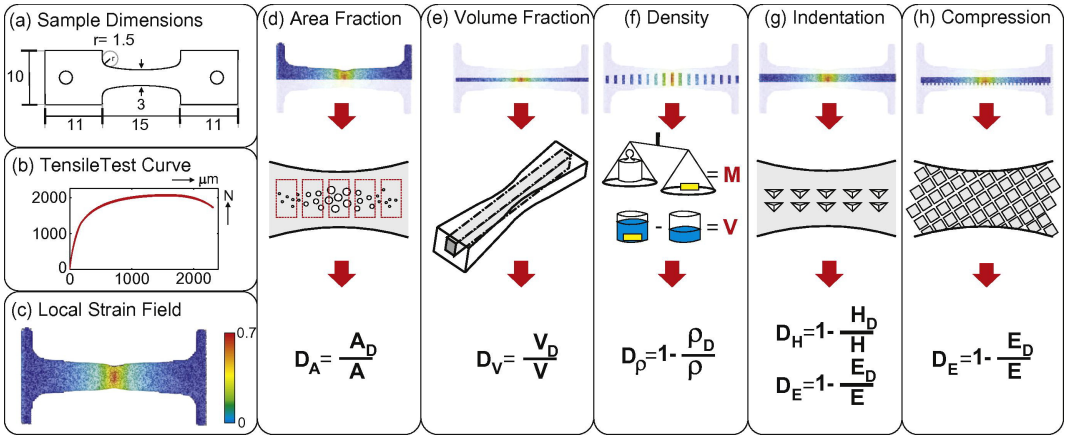


**Fig. 1.24** Different measures of a damage variable [58].

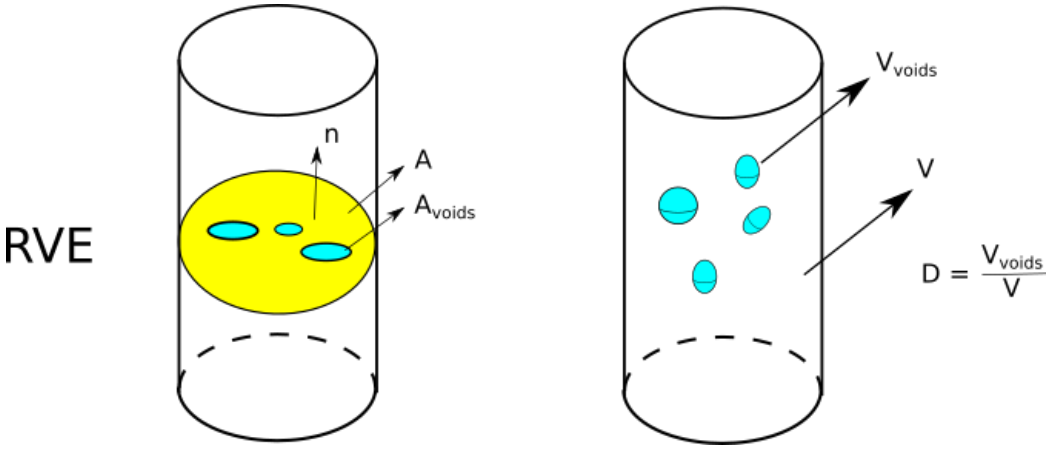


**Fig. 1.25** Different ways to represent the damage in a representative volume element (RVE).

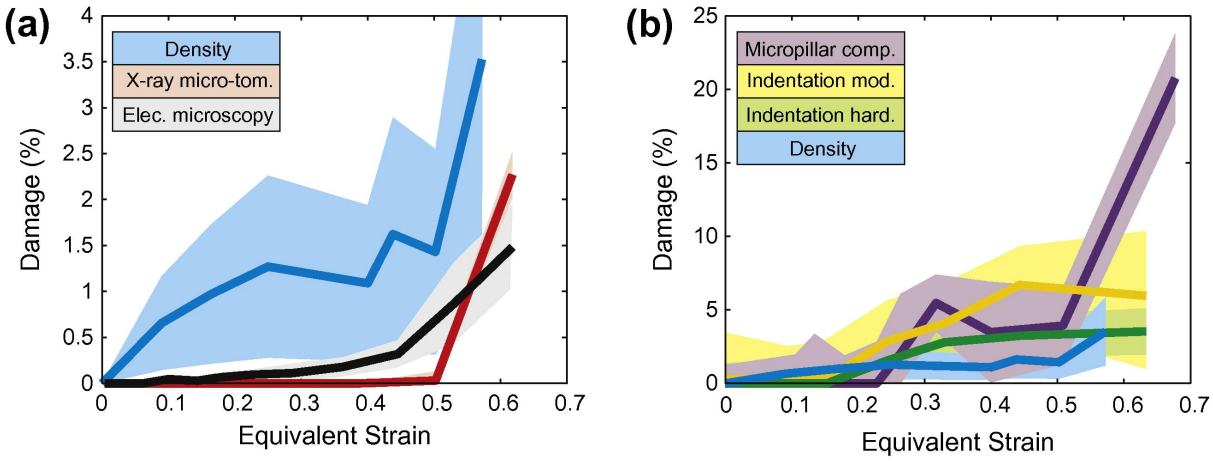


**Fig. 1.26** Different experimental measurements describing the damage parameter evolution vs. equivalent plastic strain [58]. Direct calibration methods are shown in (a) and indirect calibration methods are shown in (b).

In the following sections, a brief introduction about the different categories of coupled damage models is presented.

#### 1.3.1.1 Phenomonological damage models

Kachanov first proposed in [59] the concept of effective stress through a damage variable. This definition follows a continuum damage mechanics description. In this context, a homogenization of the micro defects within a representative volume element leads to the definition of a damage variable. This damage variable is derived from a thermomechanically consistent formulation that describes the loss of load carrying capacity in the material due to the damage evolution [60]. Chaboche introduced in [61] an anistropic damage model based on a continuum damage mechanics description. One of the most popular continuum damage mechanics (CDM) models is the Lemaitre model. In the initially proposed Lemaitre model [62], the damage variable $D$ is assumed to be isotropic in the sense that it is independent on the loading direction. The Lemaitre damage variable is defined in the rate form as follows

$$\boxed{\dot{D} = -\frac{\partial F_D}{\partial Y}} \tag{1.12}$$

where $F_D$ is the damage dissipation potential and $Y$ is the strain energy release rate. The damage variable $D$ is defined as follows

$$D = \frac{A_{voids}}{A} \tag{1.13}$$

where $A_{voids}$ is the total area of the voids and $A$ is the total area of the cross section. The effective stress $\boldsymbol{\sigma}_{eff}$ can be then defined as

$$\boldsymbol{\sigma}_{eff} = \frac{\boldsymbol{\sigma}}{1-D} \tag{1.14}$$

where $\boldsymbol{\sigma}$ is the damaged stress tensor. The damage dissipation potential proposed by Lemaitre reads as

$$F_D = \frac{S_0}{(s_0+1)}\left(\frac{-Y}{S_0}\right)^{s_0+1}, \tag{1.15}$$

and the strain energy release rate reads as

$$-Y = \frac{\bar{\boldsymbol{\sigma}}^2}{2E(1-D)^2}\left[\frac{2}{3}(1+\nu) + 3(1-2\nu)\eta^2\right] \tag{1.16}$$

where

$$\bar{\boldsymbol{\sigma}} = \sqrt{\frac{3}{2}\boldsymbol{s} : \boldsymbol{s}}. \tag{1.17}$$

The final damage evolution rate becomes

$$\dot{D} = \left(\frac{-Y}{S_0}\right)^{s_0} \dot{\bar{\boldsymbol{\varepsilon}}} \tag{1.18}$$

where $S_0$ and $s_0$ are two material parameters. In addition, a damage threshold $D_c$ with the range $0 \leq D_c \leq 1$ is introduced in order to indicate the critical damage value at which the material fails. The parameter $s_0$ is usually of the order of unity as explained in [62]. It should be noted that other forms of the $F_D$ functional can be found in [12] since the choice is phenomenological. Equation 1.18 shows that the damage evolution is quadratically dependent on the stress triaxiality (when $s_0$ = 1). Fig. 1.27 shows the relationships between strain at fracture and stress triaxiality for both Lemaitre model and McClintock/Rice-Tracey models. The domain covered by solid curves represents the Lemaitre model results between extreme limits of plastic strain at which damage is initiated while the domain covered by the dashed curves represent the results of McClintock and Rice-Tracey models. It can be observed that except for low stress triaxialities, the Lemaitre model has a good correlation with the other two models. This concludes that the quadratic dependency on stress triaxiality is a valid assumption for many engineering applications. A linear interpolation is proposed between the non damaged material and fully damaged material by degrading the Young's modulus as follows

$$\boxed{\tilde{E} = (1-D)E_0} \tag{1.19}$$

where $\tilde{E}$ is the degraded Young's modulus and $E_0$ is the initial Young's modulus.

It is important to mention that the linear relationship between the stiffness degradation and the damage variable is not always valid experimentally as shown in [1]. The difference in

magnitude between a small increment in the damage value and the resulting degradation of stiffness degradation can be of the order of $10^3$. This indicates that a non-linear relationship can be adopted between the damage, in the sense of micro-voids evolution, and stiffness degradation.

It should also be noted at this point of discussion that the damage evolution is generally an anisotropic process. Authors in [63] have shown the effect of inclusions orientation on the ductility of the material. It is well known that the void nucleation and growth mechanisms are highly dependent on the inclusions shape and orientation. The isotropy assumption is important from the industrial point of view as it simplifies the calibration process of the damage model. However, this assumption might lead to physically inconsistent results so a better modeling strategy should be found. For example, T. Pardoen and J. W. Hutchinson found that the void spacing anisotropy can lead to an non-negligible effect on the fracture toughness in the material [64] as it highly affects the void coalescence mechanism. In order to get physically reliable results while keeping the assumption of isotropy, authors in [12] suggested that the critical damage parameter $D_c$ can be dependent on the grain flow orientation while keeping the isotropic nature of the damage variable and its kinetics. However, this model can not accurately deal with the complex nature of damage anisotropy in the general case as the damage evolution itself should be dependent on the direction.

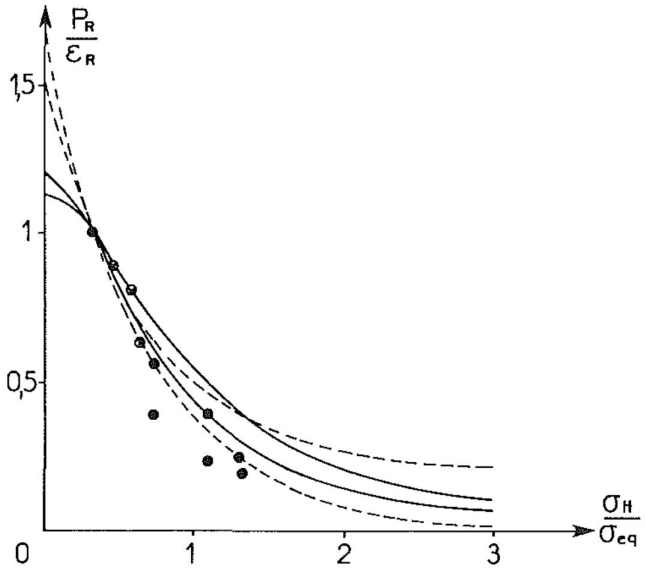


**Fig. 1.27** The relationship between strain at fracture and stress triaxiality [62]. The domain covered by solid curves represents the Lemaitre model results while the domain covered by the dashed curves represents the results of McClintock [29] and Rice-tracey model [31]. $\frac{P_R}{\varepsilon_R}$ is the ratio between the total equivalent plastic strain to the plastic strain in 1D.

#### 1.3.1.2 Micro-mechanical damage models

Gurson [65] introduced an approach to describe the evolution of voids in ductile media that is based on mean field analysis. An enhanced model known as GTN was proposed in [66] that

is able to predict the nucleation, growth and coalescence of micro-voids in the material. The main contribution of the GTN model was to reflect the effect of porosity on the yield stress in the material. The void evolution is represented by a void volume fraction $f$ that is defined as the ratio between the voids volume to the total volume of the domain. The evolution rate of the void volume fraction can be split into two parts that describe the nucleation and growth of voids in the material as follows

$$\dot{f} = \dot{f}_{nucleation} + \dot{f}_{growth} \tag{1.20}$$

$\dot{f}_{nucleation}$ is usually defined according to an empirical formula as follows

$$\dot{f}_{nucleation} = K\dot{\bar{\boldsymbol{\varepsilon}}} \tag{1.21}$$

where $K$ is a parameter that is the ratio between the volume fraction of particles that contribute in the void nucleation divided by a unit plastic strain. $K$ can be defined as follows [67]

$$K = \frac{\psi}{s_N\sqrt{2\pi}} exp\Big(-\frac{1}{2}\big(\frac{\bar{\boldsymbol{\varepsilon}} - \bar{\varepsilon}_N}{s_N}\big)^2\Big) \tag{1.22}$$

where $\psi$ is calibrated such that nucleated void volume fraction is consistent with the particles volume fraction, $\bar{\varepsilon}_N$ and $s_N$ are the mean plastic strain at which nucleation is triggered and $s_N$ is the corresponding standard deviation. $\dot{f}_{growth}$ is defined according to the principle of mass conservation as follows

$$\dot{f}_{growth} = \frac{d}{dt}\big(\frac{V_t - V_m}{V_t}\big) = \cancelto{0}{\frac{-\dot{V}_m}{V_t}} - (1-f)\frac{\dot{V}_t}{V_t} \approx (1-f)tr(\dot{\boldsymbol{\varepsilon}}^p) \tag{1.23}$$

where $tr(\dot{\boldsymbol{\varepsilon}}^p)$ is the trace of the plastic strain rate tensor, $V_t$ and $V_m$ are the total and matrix volumes, respectively. Here it is assumed that the material is incompressible in the elastic regime.

The modified yield surface $f_M$ reads as

$$f_M = \big(\frac{\bar{\boldsymbol{\sigma}}}{\boldsymbol{\sigma}_y}\big)^2 - 2q_1\, f^*\, cosh\big(\frac{3}{2}q_2\frac{p}{\boldsymbol{\sigma}_y}\big) - 1 - \big(q_1 f^*\big)^2 \tag{1.24}$$

where $f^*$ is introduced in order to reflect the effect of void coalescence on the shape of the yield surface which is defined as follows [66]

$$f^* = \begin{cases} f & f < f_c \\ f_c + \frac{f_u^* - f_c}{f_f - f_c}(f - f_c) & f \geq f_c \end{cases} \tag{1.25}$$

where $f_c$ is the critical void volume fraction at coalescence, $f_f$ is the void volume fraction at complete failure and $f_u^*$ is the value of the effective void fraction function $f^*$ at failure. $\bar{\boldsymbol{\sigma}}$ is the

effective stress, $\boldsymbol{\sigma}_y$ is the yield stress, $p$ is the pressure and $q_1$, $q_2$ are two material parameters. It should also be noted that the modified yield surface reduces to von Mises yield criterion when $f = 0$.

GTN model has been adopted in many simulations of ductile fracture. The cup cone fracture pattern has been accurately predicted in [66] using the GTN damage model. Authors in [68] proposed a coupling between GTN damage model and the phase field formulation for ductile fracture. It has been shown that the model is able to predict all stages of the ductile fracture process.

R. Hambli has carried out a comparison between the phenomenological Lemaitre model and GTN model in a blanking simulation [69]. It was demonstrated that the GTN model does not accurately predict the damage evolution process due to the dominant shear stress state. Fig. 1.28 shows the predicted crack path using both damage model with the element deletion method. It can be observed that the predicted crack path with the GTN method is far from the sheared zone. This conclusion can be explained by the fact that in the case of zero hydrostatic pressure, the growth rate of the void volume fraction in the material becomes zero.

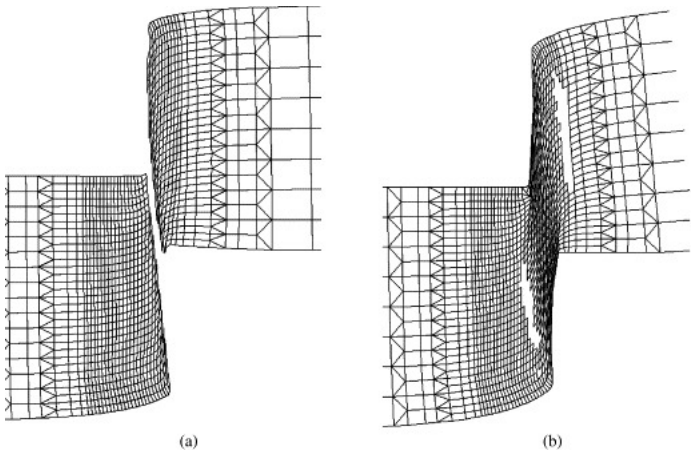


**Fig. 1.28** A comparison between the predicted crack path using the element deletion method for two different damage models [69]. Lemaitre damage model (left) and GTN damage model (right).

In order to account for the shear effect, Nahshon and Hutchinson proposed in [70] a modification in the void volume fraction rate in order to take the shear effects into account. Equation 1.23 is modified as follows

$$\dot{f}_{growth} = (1-f)\, tr(\dot{\boldsymbol{\varepsilon}}^p) + k_\omega f \omega(\boldsymbol{\sigma}) \Big(\frac{\boldsymbol{s}_{ij} : \dot{\boldsymbol{\varepsilon}}^p}{\bar{\boldsymbol{\sigma}}}\Big) \tag{1.26}$$

with $0 \leq \omega(\boldsymbol{\sigma}) \leq 1$ and defined as follows

$$\omega(\boldsymbol{\sigma}) = 1 - \Big(\frac{27 J_3}{2\bar{\boldsymbol{\sigma}}}\Big)^2 \tag{1.27}$$

where $\omega(\boldsymbol{\sigma}) = 1$ for the pure shear stress state plus a hydrostatic contribution. $k_w$ is a parameter

that controls the rate of void volume fraction evolution due to shear stress and $J_3$ is the third invariant of deviatoric stress tensor. The results of this modification on the numerical results have been shown in [68]. A detailed review about the GTN model can be found in [71].

#### 1.3.1.3 Experimental calibration of a damage model parameters

In order to identify the material parameters from experimental analysis, curve fitting techniques based on the minimization of the sum of square errors are usually used. The cost function $\boldsymbol{g}$ can be then expressed in the vector form as follows

$$\boldsymbol{g}(\beta_{opt}) = [\hat{\boldsymbol{y}}(\beta_{opt}) - \boldsymbol{y}]^t \boldsymbol{W} [\hat{\boldsymbol{y}}(\beta_{opt}) - \boldsymbol{y}] \tag{1.28}$$

where $\hat{\boldsymbol{y}}$ is the curve fit function, $\boldsymbol{y}$ is the measured data vector, $\boldsymbol{W}$ is a weighting matrix and $\beta_{opt}$ is the vector of design variables. The choice of the measured data depends on the type of the calibrated parameters. For example, Defaisse et al. have proposed in [44] to compute the maximum damage value using their uncoupled damage model so that the resulting cost function can be expressed as

$$\boldsymbol{g}(\beta_{opt}) = [D^{max}(\beta_{opt}) - 1]^t [D^{max}(\beta_{opt}) - 1] \tag{1.29}$$

where $D^{max}$ is the vector of maximum damage value predicted by the model. In this case, the maximum damage value at failure is set to one and the weighting matrix is set to an identity matrix. In addition, the Levenberg–Marquardt algorithm [72] was adopted in order to identify the set of material parameters. In the Levenberg–Marquardt algorithm, the update of the design variables at each iteration is done by adding $\delta\beta_{opt}$ to the previously identified set. The update of design variables can be obtained by solving the following system of linear equations

$$(\boldsymbol{J}^t \boldsymbol{J} + \lambda_{visc}\, \boldsymbol{I}) \delta\beta_{opt} = \boldsymbol{J}^t (\boldsymbol{y} - \hat{\boldsymbol{y}}) \tag{1.30}$$

where $\boldsymbol{J} = \frac{\partial \hat{\boldsymbol{y}}}{\partial \beta_{opt}}$ is the Jacobian and $\lambda_{visc}$ is a damping parameter that can be adapted during the computations in order to obtain a good convergence behaviour.

Another approach is the so-called EGO (Efficient Global Optimization) that was proposed in [73] in order to have a fast identification method. The idea is to use the so-called Gaussian process regression in order approximately compute the cost function based on the neighborhood of the design variables. E. Roux developed in [74] a parallel computational toolbox called MOOPI that is based on the EGO algorithm in order to obtain a best fit for the mechanical models. Bouchard et al. used the MOOPI library [75] in order to calibrate the Lemaitre damage model. The cost function has been built as follows

$$\boldsymbol{g}(\beta_{opt}) = [F(\beta_{opt}) - F^{exp}]^t [F(\beta_{opt}) - F^{exp}] \tag{1.31}$$

where $F(\beta_{opt})$ is the vector of forces calculated in the simulation at different increments and $F^{exp}$ is the experimental force. In order to make sure that the force is defined in the same range in both the experiments and the simulation, constant force data points are added at the end of the initial curve obtained from the simulation. It was shown that the uniqueness of the solution might be lost if the size of the measured data is not sufficient (the inverse problem becomes ill-posed). In other words, more than one local minimum can be found with different values for the same parameter. In order to solve this problem, two solutions were proposed: (i). additional force vs. displacement curves should be obtained by performing more experiments; (ii). use full field measurement (local displacement field for example) in order to enhance the curve fitting process. It was found that an accurate determination of the model parameters was possible when full field measurements were used. The MOOPI library has been also used in [76] in order to find the best fit of parameters for different phenomenological damage models.

It should be noted that the identification of the GTN model parameters can be also done by measuring the void volume fraction at different deformation stages. Authors in [77] measured the void volume fraction during the in situ tensile test using a scanning electron microscope (SEM). They determined the void volume fraction at three phases: nucleation, growth and coalescence in order to calibrate the parameters $\psi$ and $\bar{\varepsilon}_N$ that appear in equation 1.22 in addition to $f_c$ and $f_f$ that appear in equation 1.25. On the other hand, the material parameters $q_1$ and $q_2$ that appear in equation 1.24 have been taken from [66] as 1.5 and 1, respectively. The identified parameters were quite successful in matching the model results with the experimental measurements. However, the model was not able to continuously measure the evolution of the void volume fraction which limits its precise description of void evolution mechanisms.

In the same context, T.-S Cao identified the parameters of the GTN model by analyzing the in situ X-ray tomography measurements of a high carbon steel grade [22]. The main advantage in that case was the ability to measure the continuous evolution of the void volume fraction at different strain states. This advantage led to an important conclusion: the void nucleation phase is dominant over the coalescence phase. In other word, void coalescence occurs in a very short strain interval which does not have a significant effect of the measured results. Finally, the identified parameters were verified by performing tensile mechanical tests at the macro-scale.

#### 1.3.1.4 Non-local damage models

Non-local damage models are introduced in order to regularize the local damage field by adding a non-local effect to the material through a material length scale $l_c$. The basic idea is to take into account the damage (or strain) state in the neighborhood of each point as shown in [47]. The resulting formulation results in a well-posed solution that solves the problem of mesh dependency that appear with the local formulation. A weighing function $g(\kappa)$ is used to homogenize

the local damage field by adopting the following convolution rule

$$\bar{D} = \frac{1}{V}\int_{\Omega} g(\kappa) D(x+\kappa)\, d\Omega \tag{1.32}$$

where

$$\frac{1}{V}\int_{\Omega} g(\kappa)\, d\Omega = 1, \tag{1.33}$$

and $V$ is the volume of integration domain. Due to the relatively high computational cost needed to compute the convolution, gradient approaches are preferred over the integral approaches. The non-local damage variable can be obtained by expanding the local damage variable using the Taylor's series as follows

$$D(x+\kappa) = D(x) + \nabla D(x)\,\kappa + \frac{1}{2}\nabla^2 D(x)\,\kappa^2 + H.O.T, \tag{1.34}$$

by substituting 1.34 in 1.32, the non-local gradient damage equation after neglecting the higher order terms H.O.T can be described as

$$\boxed{\bar{D} - a\nabla^2 \bar{D} = D} \tag{1.35}$$

where $D$ is the local damage variable and $\bar{D}$ is the non-local damage variable. The coefficient $a$ is calculated based on the choice of the weighing function $g(\kappa)$. Assuming that $g(\kappa)$ is a Gaussian function, the parameter $a$ can be linked to a length scale $l_c$ as follows

$$a = \frac{1}{V}\int_{\Omega} \frac{g(\kappa)}{2}\,\kappa^2\, d\Omega = l_c^2. \tag{1.36}$$

The resulting PDE is usually solved using the finite element method in order to find the distribution of the non-local damage variable in the material. Geers et al. introduced a non-local formulation with a variable length scale [78]. The proposed methodology leads to a proper localization of the damage field near the crack path without affecting the regions far from the crack surface.

The use of GTN model also leads to a mesh dependency problem. Zhang et al. presented in [79] a non-local gradient-based version of the GTN model where the hardening variable is regularized. Numerical results have confirmed that the model results are mesh independent.

#### 1.3.1.5 Phase field model

Francfort and Marigo introduced an energetic formulation for brittle fracture problems [50]. A free energy functional $\mathcal{E}$ which is a Mumford–Shah type [80] is defined as follows

$$\mathcal{E} = \int_{\Omega} W_e(\boldsymbol{\varepsilon}^e)\, d\Omega + \int_{\Gamma} G_c\, d\partial\Omega \tag{1.37}$$

where $\boldsymbol{\varepsilon}^e$ is the elastic strain tensor, $W_e$ is the elastic energy density, $G_c$ is the fracture toughness, $\Gamma$ is the crack surface in the reference configuration and $\Omega$ is the occupying volume in the reference configuration (Fig. 1.29a). Later on, a regularized approximation presented in [51] was used instead of the original formulation for the purpose of numerical computations, since the original formulation was numerically intractable. The regularized total energy functional $\mathcal{E}_l$ can be described as follows

$$\mathcal{E}_l = \int_\Omega g_e(d)\, W_e(\boldsymbol{\varepsilon}^e)\, d\Omega + \int_\Omega \frac{G_c}{2l_c}(d^2 + l_c^2 \nabla d^2)\, d\Omega \tag{1.38}$$

where an elastic degradation function $g_e$ is used to couple the effect of crack propagation on the bulk material which is defined as follows

$$g_e(d) = (1-d)^2 + \zeta. \tag{1.39}$$

The choice of the degradation function satisfies the following conditions: $g_e(0) = 1$, $g_e(1) = 0$, $g_e'(1) = 0$. $\zeta$ is a numerical parameter usually chosen as $10^{-6}$ in order to prevent numerical singularities. A phase field $d$ was introduced in order to interpolate between the intact $(d = 0)$ and totally damaged $(d = 1)$ material points as shown in Fig. 1.29b. The minimization of the regularized energy functional with respect to the phase field parameter gives

$$\begin{cases} \dfrac{G_c}{l_c}(d - l_c^2 \nabla^2 d) = -g_e'(d)\mathcal{H}(x,t) \text{ (Evolution of the phase field)} & \text{(1.40a)} \\ \mathcal{H} = \max\limits_{n} W_e(\boldsymbol{\varepsilon}^e(x, d_n)) \text{ (Local history functional)} & \text{(1.40b)} \\ \nabla d \cdot \mathbf{n} = 0 \text{ (Neumann boundary condition on } \partial\Omega) & \text{(1.40c)} \end{cases}$$

where $\boldsymbol{n}$ is a unit vector normal to the body boundary. A detailed derivation of the strong form of the phase field evolution equation can be found in Appendix A.1. The minimization of the energy functional with respect to the displacement field gives an expression for the principle of linear momentum conservation as follows

$$\operatorname{div} \boldsymbol{\sigma} = 0 \tag{1.41}$$

where $\boldsymbol{\sigma}$ is the degraded stress tensor that can be expressed as

$$\boxed{\boldsymbol{\sigma} = g_e(d)\, \frac{\partial W_e}{\partial \boldsymbol{\varepsilon}^e}} \tag{1.42}$$

In parallel, another formulation was presented by C. Miehe [53] with a general description of the problem through the geometric regularization of the sharp crack topology. The phase field parameter can be obtained as follows

$$d = \arg\{\inf_d(\Gamma_l)\} \tag{1.43a}$$

$$\Gamma_l = \int_\Omega \frac{1}{2l_c}(d^2 + l_c^2 \nabla d^2)\, d\Omega \tag{1.43b}$$

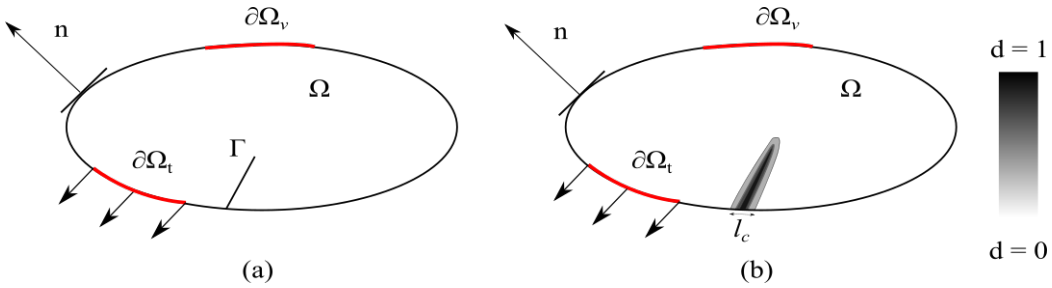


**Fig. 1.29** Geometry and boundary conditions of a domain with discontinuity $\Gamma$ in (a). Phase field regularization of the crack topology in (b).

where $\Gamma_l$ is a second-order regularized crack surface that converges to the discrete crack surface as $l_c \to 0$. The Euler equation of the above problem gives the following

$$d - l_c^2 \nabla^2 d = 0. \tag{1.44}$$

Assuming homogeneous boundary conditions, the phase field profile is described as

$$d = e^{\frac{-|x|}{l_c}} \tag{1.45}$$

and illustrated in Fig. 1.30.

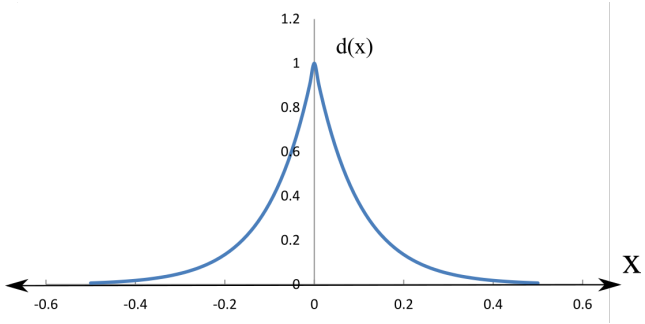


**Fig. 1.30** Phase field profile in 1D.

The solution of the above differential equation gives a diffused crack topology that converges to the actual discrete crack topology when the length scale $l_c$ goes to zero as can be clearly seen in Fig. 1.31.

In order to track the crack evolution in brittle materials, an energetic criterion for the crack surfaces propagation is proposed as follows

$$\underbrace{G_c\,\delta\Gamma_l\,\dot{d}}_{\text{Rate of fracture energy gain}} = \underbrace{\int_\Omega -\delta_d(g(d)\,W_e)\,\dot{d}\,d\Omega}_{\text{Rate of loss of elastic energy}}. \tag{1.46}$$

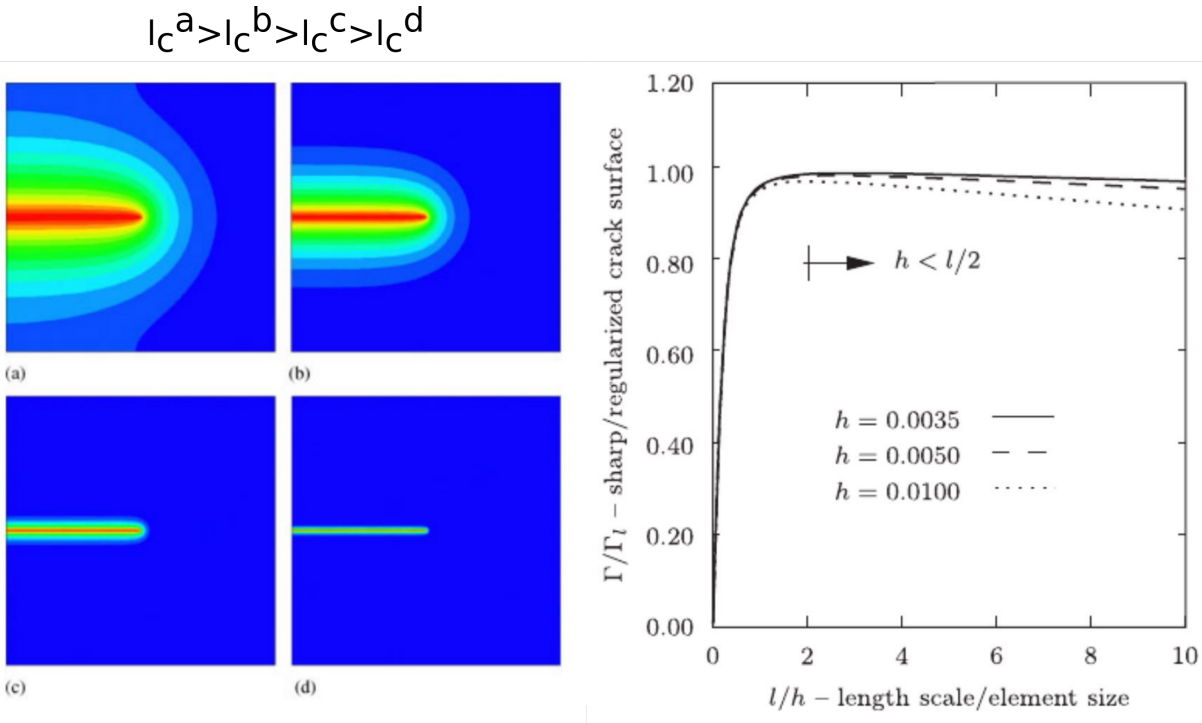


**Fig. 1.31** Numerical convergence of the regularized crack surface to a discrete crack surface when the length scale $l_c$ is diminished [53].

As suggested by C. Miehe [81], the crack propagation is then linked to a monotonically increasing local history functional $\mathcal{H}$ that drives the crack initiation and propagation in order to impose the irreversibly condition. The governing equation of the crack propagation is shown as follows

$$\underbrace{d - l_c^2\nabla^2 d}_{\text{Geometric resistance}} = \underbrace{2(1-d)\,\mathcal{H}(x,t)}_{\text{Crack driving force}}$$

$$\mathcal{H} = \frac{l_c}{G_c}\max_n W_e(\boldsymbol{\varepsilon}^e(x,d_n)). \tag{1.47}$$

Numerical simulations using the phase field method in brittle fracture have shown unrealistic interpenetration of crack as shown in [82] when the total elastic strain energy is used in the driving force. In addition, phase field also evolves in highly compressed regions as opposed to experimental results that show that the creation of cracks surfaces is expected in tension dominated zones. Decomposing the elastic strain energy into positive and negative parts while degrading solely the positive part is one of the solutions to this problem. This type of formulations is known as the ”anisotropic” formulation. Different anisotropic formulations can be found in Appendix A.2.

A fourth-order theory of the crack surface regularization that gives a better representation of the discrete surface approximation was also proposed by Borden et al. [83]. The higher order theory was shown to give a better accuracy of the stress calculation around the crack tip and a faster convergence rate of the fracture energy. Fig. 1.32 shows the ability of the phase field model to predict complex crack initiation and propagation mechanisms for both the second and fourth order theories. It can be observed that the fourth order theory gives more accurate description of the branching mechanism, which is related to the better accuracy in the calculation of the stress concentration around the crack tip.

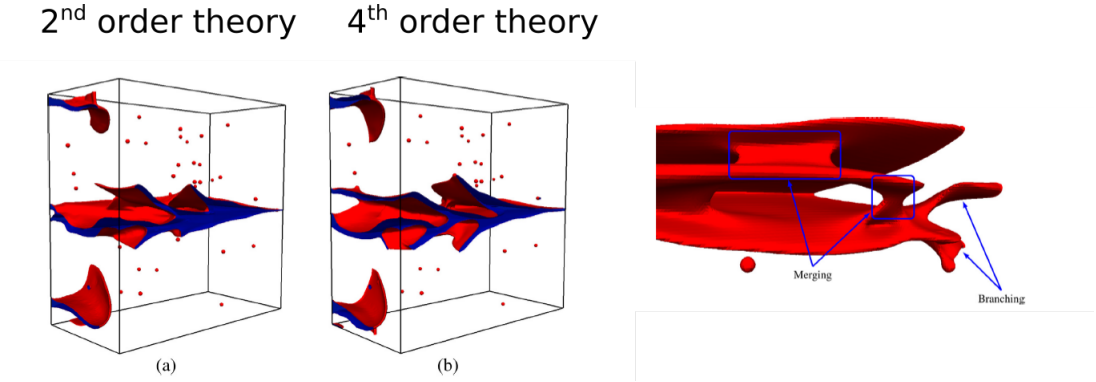


**Fig. 1.32** The initiation, propagation, merging and branching of complex crack patterns in a test case of randomly distributed voids that serve as crack initiation sites [83]. Results are shown for the second-order theory in (a) and fourth-order theory in (b).

The formulation presented by C. Miehe gives the possibility to generalize the phase field model to the case of ductile fracture by adding the effect of plastic deformation, stress triaxiality ratio and Lode angle in the local history functional $\mathcal{H}$. Different forms of the local energy functional can be found in the literature (see [84]). Table 1.2 gives some examples of the local history functional.

**Table 1.2** Different forms of the local history functional $\mathcal{H}$

| Model | $\mathcal{H}$ |
|---|---|
| Borden et al. [56] | $\frac{l_c}{G_c}\left(\beta_1 \max_n W_e + \beta_2 < W_p^{eff}(\bar{\boldsymbol{\varepsilon}}) - W_0 > \right)$ |
| Miehe et al. [84] | $< \frac{W_e}{W_c} + \frac{W_p}{W_c} - 1 >$ |
| Aldakheel et al. [68] | $\zeta < \frac{f}{f_{cr}} - 1 >$ |

In the first model, $\beta_1$ and $\beta_2$ are two weighing parameters for the elastic and effective plastic energy densities $W_e$ and $W_p^{eff}$, respectively. $W_0$ is an energy threshold that is used to delay the contribution of the plastic energy in the phase field formulation. The effective plastic energy can be computed as follows

$$W_p^{eff} = \int_0^T \frac{\dot{W}_p}{\phi(\eta)}\, dt \tag{1.48}$$

where $W_p$ is the plastic energy density and $\phi$ is a stress triaxiality function. In the second model, $W_c$ is the specific fracture energy per unit volume (the amount of absorbed energy before the crack initiation). In the third model, $f$ is the void volume fraction calculated by the GTN model, $f_{cr}$ is a critical void fraction and $\zeta$ is a material parameter used to control the speed of the phase field evolution. The main advantage of the third model is the ability to draw a connection between the damage evolution in the sense of micro-voids and crack propagation at the macro-scale through the phase field model.

In addition to the previous extension to plasticity, Ambati et al. proposed in [54] to couple the plastic deformation with the stress degradation function $g_e$ instead of the local energy functional. The proposed form of the stress degradation function can be expressed as

$$g_e(d, \boldsymbol{\varepsilon}) = (1-d)^{2\left(\frac{\bar{\boldsymbol{\varepsilon}}}{\bar{\boldsymbol{\varepsilon}}_{crit}}\right)^m}, \tag{1.49}$$

$\bar{\boldsymbol{\varepsilon}}_{crit}$ is a plastic deformation threshold and $m$ is a parameter that is used to control the speed of the phase field evolution. Using the perturbation analysis, it was shown that the plastic strain has a similar effect as the elastic strain energy on the phase field evolution. Another idea proposed by Dittmann et al. [85] based on degrading the fracture toughness due to the evolution of the equivalent plastic strain. An exponential degradation function was proposed as follows

$$G_c(\bar{\boldsymbol{\varepsilon}}) = G_{c\infty} + (G_{c0} - G_{c\infty})\, exp(-\omega_f\, \bar{\boldsymbol{\varepsilon}}) \tag{1.50}$$

where $G_{c0}$ and $G_{c\infty}$ are the initial and final values of the fracture toughness and $\omega_f$ is a parameter that controls the rate at which the fracture toughness is degraded.

The great advantage of the phase field model is the ability to describe the processes of initiation, propagation, merging and branching of cracks without an ad-hoc criteria. More importantly, the model offers the ability to control the width of the damaged zone around the crack through the length scale. However, the condition of $\Gamma$-convergence cannot be proven in the case of ductile materials. In other words, there is no variational formulation such as the one proposed for brittle fracture. Thus, no unique formulation can be accepted for all the ductile fracture problems. The objective in this case is to find a rich form for the crack driving force that can be used to predict the ductile fracture process.

It can be observed in the previous reviews that although the non-local gradient damage and phase field models have different origins, their mathematical structures are very similar. The following section aims at highlighting the main similarities and differences between the phase field and non-local gradient damage models.

#### 1.3.1.6 Similarities and differences between the phase field and non-local gradient damage models

A comparison between the mathematical formulation of both modeling techniques can be shown in Fig. 1.33

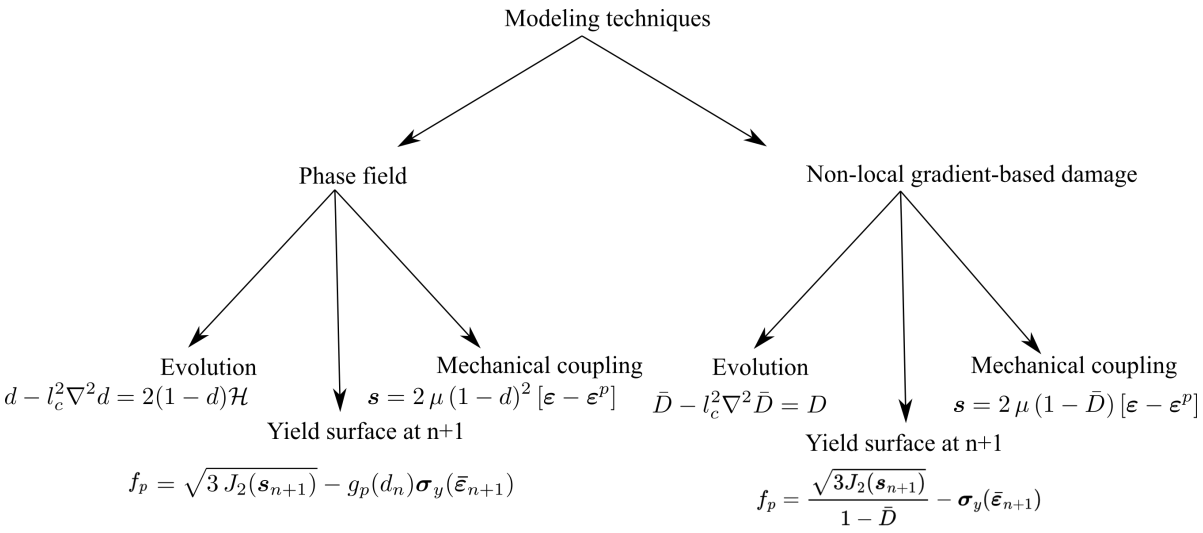


**Fig. 1.33** Comparison between the phase field and non-local gradient damage mathematical formulations.

The mathematical formulations of the two models seem to be similar although the origins of both are different. As indicated in [86], the phase field model can be conceptually considered as a special category of non-local gradient damage models. The main differences between the classical form of phase field and non-local damage models can be explained as follows:

First, the interpretation of the length scale $l_c$ in the phase field model is that it controls the size of the damaged zone, on the other hand, the characteristic length scale in the non-local damage models is introduced to prevent the ill-posedness of the solution. It stands for the physical localization zone where damage leads to fracture at the micro-scale. This length scale parameter should be of the order of the mean distance between particles in a metallic material. This would require a particularly fine mesh since the mesh size should be lower than the length scale. In practice, this parameter is often chosen bigger to reduce the computation time.

Second, the right hand side of the phase field equation contains a degradation term $(1-d)$ which has been shown in [87] to limit the damage broadening when the phase field reaches a value of one, i.e., when the crack is initiated. On the other hand, the right hand side of the non-local damage evolution equation includes only the effect of the local damage variable. This last characteristic leads to a continuous broadening of the damage field even after reaching a critical value of 1 which usually indicates the location of the crack initiation. The broadening effect has been shown to lead to some numerical instabilities in addition to nonphysical behaviour in the mechanical response at large strains for some types of damage laws as shown in [78].

## 1.3.2 Continuous-discontinuous models

Continuous-discontinuous approaches regroup two main challenges: (i). handling the transition from a continuous damage approach to a discontinuous modeling of fracture; (ii). modeling the initiation and propagation of cracks in a 3D finite element mesh.

### 1.3.2.1 Transition from damage to fracture

Mediavilla et al. [88] developed a crack initiation and propagation strategy in 2D based on the calculation of the maximum value of the damage field. First, the damage field is calculated at different points that lie at different distances $d_i$ in front of the previous crack front. Then, a crack increment is inserted at an angle $\theta$ that passes through all the fully damaged points.

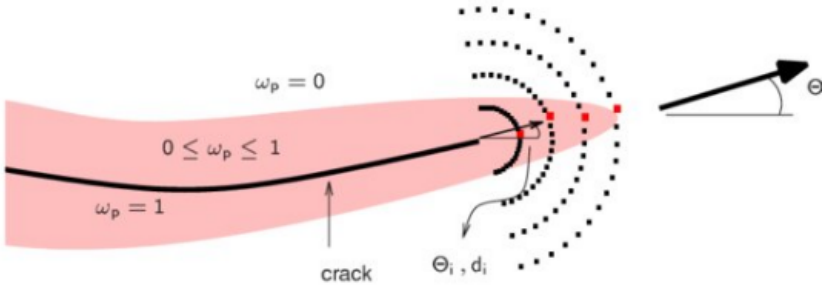


**Fig. 1.34** Crack identification path using the maximum damage value. $w_p$ denotes the damage field, $\theta_i$ and $d_i$ are the crack propagation angle and the distance between the crack front and a test point, respectively. The image is taken from [88].

Authors in [89] presented a crack initiation and propagation strategy using XFEM applied to ductile materials. The Lemaitre damage model was used to impose the material softening and predict the zones at which the crack is expected to initiate. Next, a crack path direction is identified by determining the point with the highest damage value selected from a ring of points ahead of the crack tip as shown in Fig. 1.35. Finally, a crack increment is inserted by enforcing a discontinuity in the elements crossed by the crack.

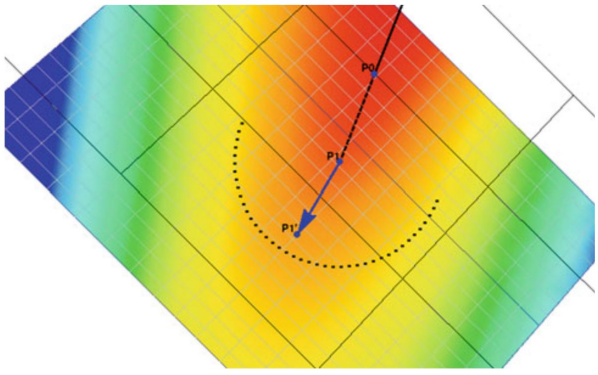

**Fig. 1.35** Identification of the crack propagation path using the Lemaitre damage model [89].

Hussein et al. [90] proposed a crack path identification strategy formulated as a minimization problem. The problem is to find the crack path that minimizes the sum of squared projected distances (denoted by $s$ in Fig. 1.36) of all points that exceed a phase field threshold of 0.9. The optimization problem is formulated as follows

$$X_{2,tip} = \arg\{\min_{X_{2,tip}} \Big( \sum_i s_i^2 \Big) \} \tag{1.51}$$

where $s$ is the distance between each point and the vector $\boldsymbol{b}$ that connects $\boldsymbol{X}_{start}$ with $\boldsymbol{X}_{2,tip}$ as shown in Fig. 1.36. The main advantage of the proposed algorithm is its ability to insert arbitrary cracks in the mesh without having the problem of hanging nodes that is common with the finite element method. It can be seen in Fig. 1.37 that the model is able to handle the discrete crack propagation for the mode II of fracture in 2D. The crack in this case follows the phase field evolution at each loading step until the final failure is reached.

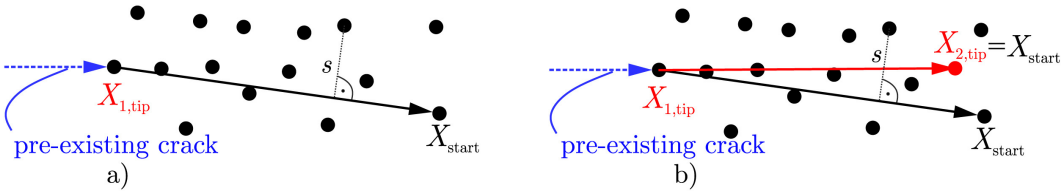


**Fig. 1.36** Identification of the discrete crack path from the continuous phase field solution. The image is taken from [90].

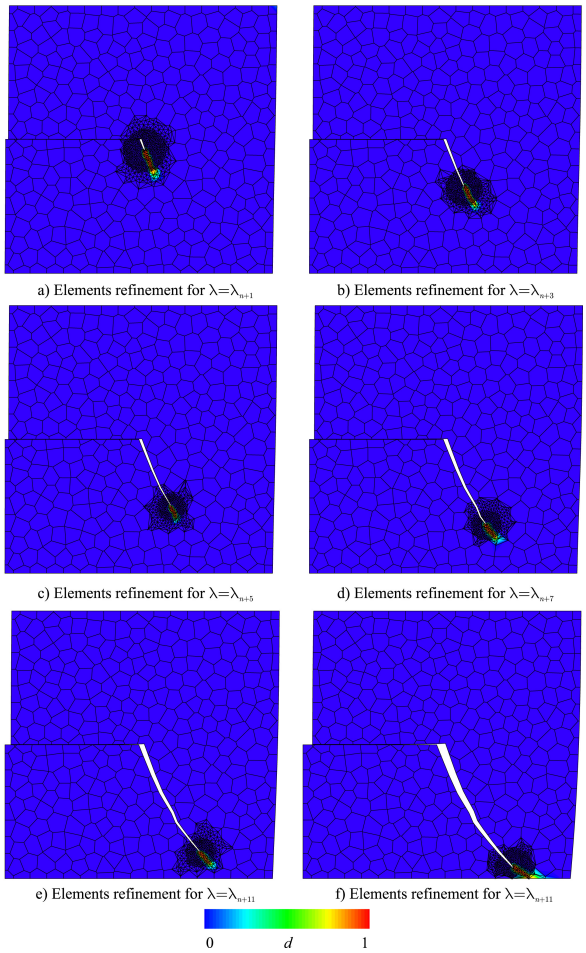


**Fig. 1.37** Propagation of discrete crack surface in a 2D mesh using a discrete crack propagation combined with the phase field model. The image is taken from [90].

Feld-Payet et al. [88] have introduced a crack path tracking algorithm known as the "Marching ridges" that can be used to identify the discrete crack path by detecting the ridges of a given continuous non-local damage field in 2D polar coordinate system as shown in Fig. 1.38. A point that lies at the circumference of a circle of radius $R$ is identified as a ridge if it satisfies the following conditions

$$\underline{\boldsymbol{e}}_\theta(\theta - \frac{\Delta\theta}{2}) \cdot \nabla f\Big(\underline{\mathrm{x}}_0 + R\,\underline{\boldsymbol{e}}_r\big(\theta - \frac{\Delta\theta}{2}\big)\Big) > 0 \tag{1.52a}$$

$$\underline{\boldsymbol{e}}_\theta(\theta + \frac{\Delta\theta}{2}) \cdot \nabla f\Big(\underline{\mathrm{x}}_0 + R\,\underline{\boldsymbol{e}}_r\big(\theta + \frac{\Delta\theta}{2}\big)\Big) < 0 \tag{1.52b}$$

where $\underline{\boldsymbol{e}}_\theta$ is the tangential unit vector to the circle, $\underline{\boldsymbol{e}}_r$ is the radial unit vector to the circle, $\Delta\theta$ is the angular distance between the tested points along the circumference and $f$ is a damage field. A scanning of the whole circumference is essential to find a ridge where a finite number of points separated by $\Delta\theta$ are tested. Fig. 1.39 shows the extension of the algorithm in 3D. First, a crack front is constructed by applying the marching ridges algorithm in three orthogonal planes starting from a point that lies on the crack surface. Once the front is constructed, a search

process is carried out in the planes perpendicular to each crack front segment. Finally, a crack surface increment is constructed by extending the crack front in the identified direction by the search process.

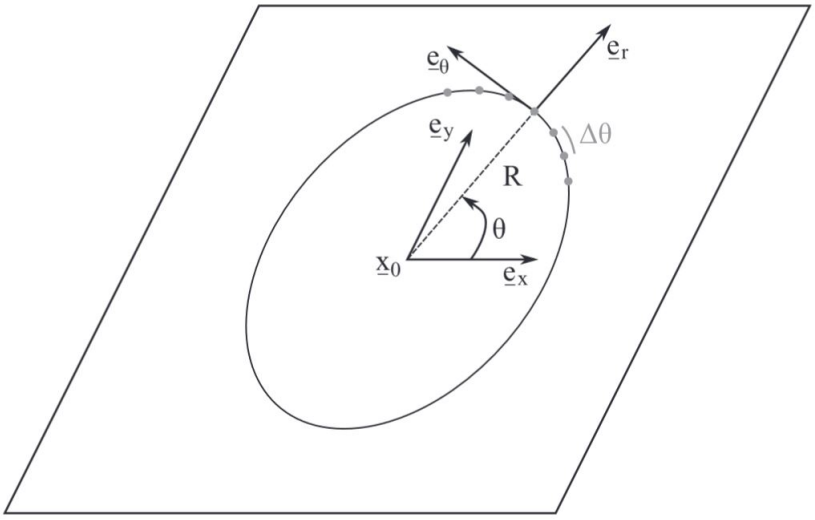


**Fig. 1.38** A 2D Polar plane used to identify a ridge along the circle with radius $R$ [91].

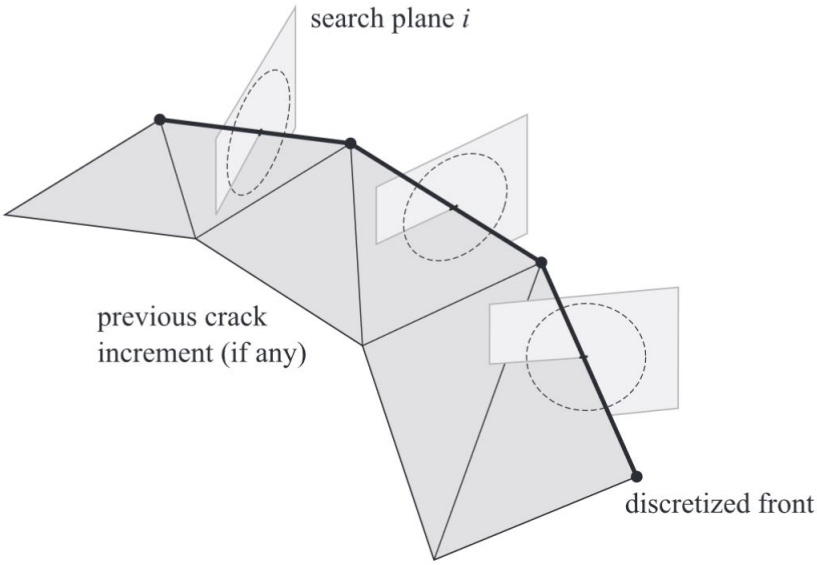


**Fig. 1.39** The construction of the crack front followed by the propagation of the crack surface. The image is taken from [91].

It can be concluded that the techniques used for damage to fracture transition can be divided into two categories: (i). detecting a crack path by calculating the maximum values of a given damage/phase field; (ii). finding the positions at which the directional derivative a given damage field vanishes along a direction perpendicular to the crack. It should be noted that the detected positions in the second approach should have a damage value close to one to ensure that the material points are fully degraded. It has been shown in the previous analysis that

both approaches give reasonable results in 2D. It can be expected that the extension of the first approach to 3D is challenging especially in the cases of merging and branching of multiple cracks. The problem in this case is that several points can have a maximum damage value at the same time so that the uniqueness of the crack path identification is lost. However, the second approach is the only one that has been extended to 3D and has been tested with complex crack paths. In this work, the second approach is used for the modeling of damage to fracture transition in 3D. In this context, another crack identification strategy is proposed that satisfies two main requirements: (i). robustness in handling complex crack propagation in 3D; (ii). can be easily integrated within a parallel computing framework.

#### 1.3.2.2 Modeling a discontinuity in the material

The simplest technique in the discontinuous modeling of ductile fracture is the element deletion method which is used frequently in industrial finite element codes. The main advantages of this technique are the simplicity and robustness as shown in [13, 92, 93]. Once a given damage threshold is reached, elements are removed from the mesh in order to simulate the fracture process. The element deletion method can be used in two types of applications: (i). to predict the initiation of unwanted cracks during the bulk forming processes such as the formation of internal chevron cracks during the extrusion processes; (ii). to predict the surface features of sheared edges during the metal cutting processes where a crack is introduced in the material intentionally.

The element deletion technique presents major deficiencies such as (i). non-physical volume loss; (ii). the crack path and the quality of crack surfaces are dependent on the mesh size. R. El khaoulani and P.-O Bouchard used an anistropic mesh adaptation strategy with the element deletion method in order to improve the quality of the crack surfaces and reduce the amount of volume loss [93]. Fig. 1.40 shows the initiation and propagation of a crack leading to the well-known cup cone fracture using the anistropic mesh adaptation strategy. Although the method is able to roughly predict the initiation and propagation of the crack, it leads to a volume and energy loss with no convergence in the solution with mesh refinement. In fact, the crack path is strongly dependent on the chosen mesh size since the crack front is not uniquely defined. In consequence, such method cannot be used for an accurate prediction of the characteristic features of the sheared edges. Another example of damage to fracture transition of a tooth of seat recliner is shown in Fig. 1.41 using two different mesh sizes. It can be observed that the crack path is very dependent on the mesh size. It is worthy to note that the results are expected to improve when the mesh is refined in the damaged zone. However, this leads to a considerable increase in the computation time especially for 3D cases.

In the domain of metal forming, the element deletion method can be very efficient when the prediction of the onset of fracture is important without the need to accurately predict the crack path. However, it is important to predict the fracture path in some specific metal forming

applications such as the multi-stages operations. For example, in the blanking processes, the output workpiece is used in other manufacturing stages. The objective in this case is not only to predict the onset of fracture, but also to accurately describe the fracture zones [5] in order to optimize the production processes.

The extended finite element method XFEM was introduced in [94] as a numerical technique that handles the existence of cracks in brittle fracture by incorporating discontinuous functions to the classical finite element formulation. The main advantage is that the crack can be propagated within the mesh without any remeshing which reduces significantly the computation time. It also avoids any mechanical field transfer, which is necessary when using remeshing. However, the need of remeshing in metal forming applications is essential especially because of large deformations. The application of XFEM in the modeling of ductile fracture is very limited due to the following reasons: (i) complexity of the transfer of fields after remeshing; (ii) applying the incompressibility constraints [95]; (iii) the necessity of representing the real crack topology in the multi-stages processes which requires the modification of mesh topology and nodal duplication.

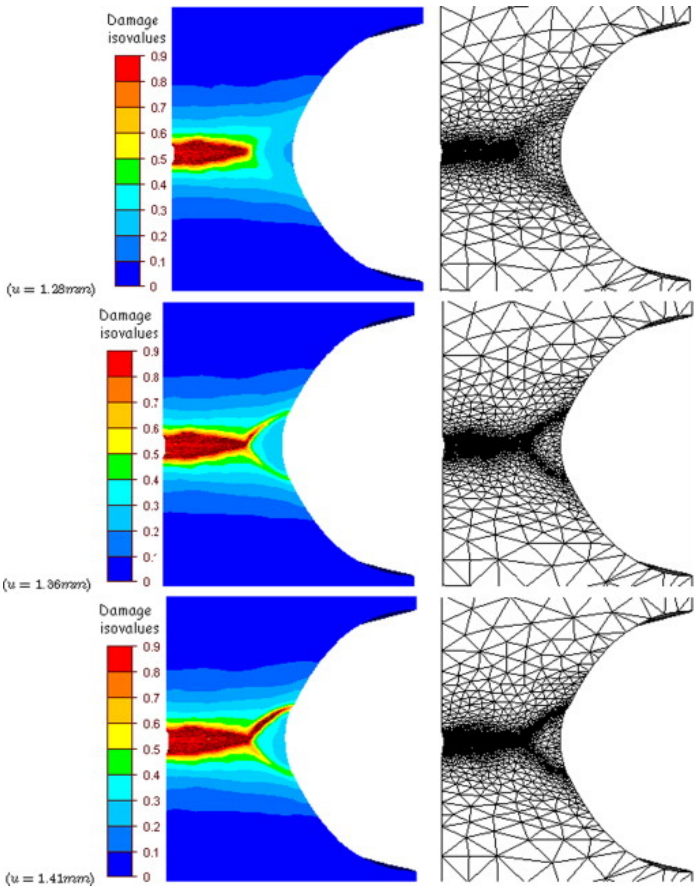


**Fig. 1.40** Initiation and propagation of cracks leading to cup-cone failure using the element deletion (kill element) technique. Images are taken from [93].

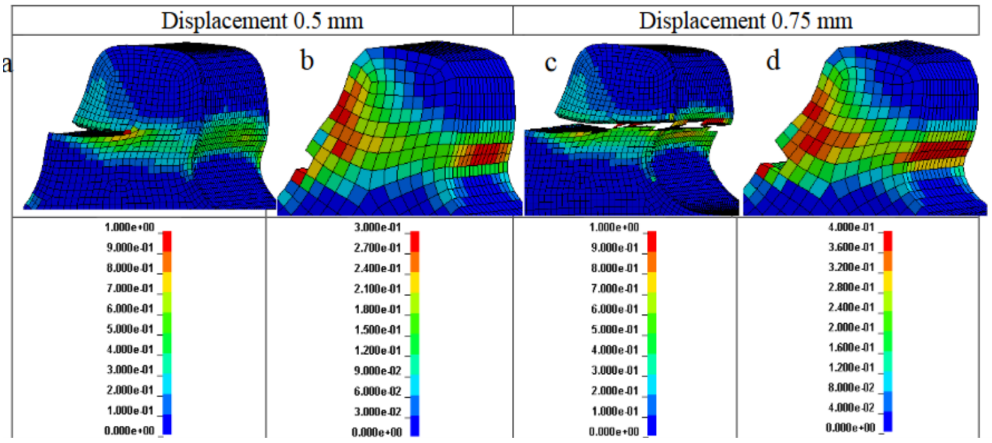


**Fig. 1.41** Ductile fracture of a tooth of seat recliner during a crash test [96]. Figures a and c show the crack propagation at two displacements for a fine mesh. Figures b and d show the crack propagation at two displacements for a coarse mesh. A phenomenological damage model based on the stress triaxiality and normalized Lode angle is used in this simulation. The values reported for each bar correspond to the values of the damage field.

Hussein et al. proposed an adaptive crack simulation framework using the phase field method and the Virtual element method (VEM) in brittle materials. [90]. The VEM is as a generalization of the classical finite elements method that can be used to form any shape of elements with an arbitrary number of nodes [97, 98]. The mesh is refined around the crack tip when the maximum value of the phase field reaches a given threshold which is followed by an equilibrium step using the staggered algorithm. A cutting algorithm is used to split the virtual elements and open the crack faces as shown in Fig. 1.42. New nodes are inserted at the locations crossed by the crack path. The main advantage of using the VEM framework in this case is the ability to construct the new elements with arbitrary number of nodes. The new inserted nodes are duplicated in order to simulate the crack propagation step. Finally, consecutive mesh coarsening/refining operations are used to minimize the computation time during the crack propagation. The remaining challenges are the ability to handle crack branching in addition to extending the algorithm to 3D.

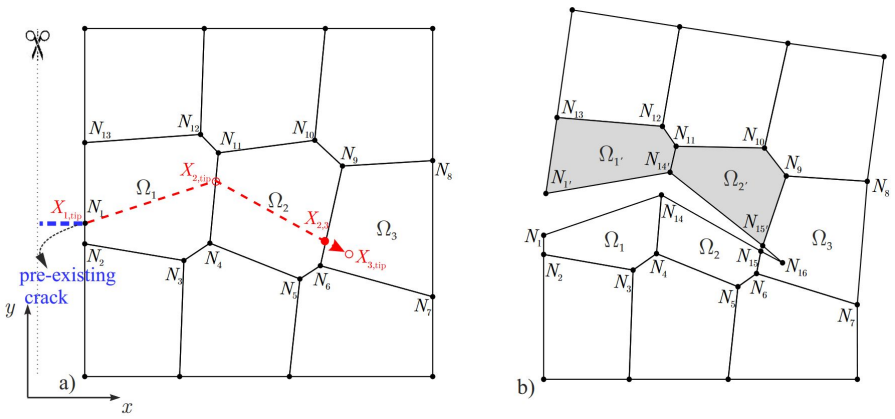


**Fig. 1.42** Inserting a crack increment within a mesh that is constructed with the VEM [90].

Chiaruttini et al. developed in [99] a mesh cutting strategy based on remeshing techniques in order to simulate complex crack propagation. As observed in Fig. 1.43, the idea is to construct a surface mesh at the intersection between the initial volume mesh and the crack surface. A search process is carried out over all the elements that are intersected by the crack in order to modify their mesh topology accordingly. It is assumed that a flat crack segment cuts the element in order to increase the robustness of the algorithm and reduce the numerical errors. The algorithm has been used by S. Feld-Payet in [100] in order to simulate the initiation and propagation of cracks in ductile media. A crack surface is constructed by the extension of a crack front in the directions predicted by the "Marching ridges" algorithm. Finally, the crack surface is inserted in the volume mesh followed by a nodal duplication step as shown in Fig. 1.44. The developed strategy is very promising in the study of ductile damage to fracture transition. However, the extension of the algorithm to more complex cracking scenarios was not investigated, such as the internal crack initiation in bulk materials, crack branching and merging of crack branches. The algorithmic implementation within a parallel framework was not presented either.

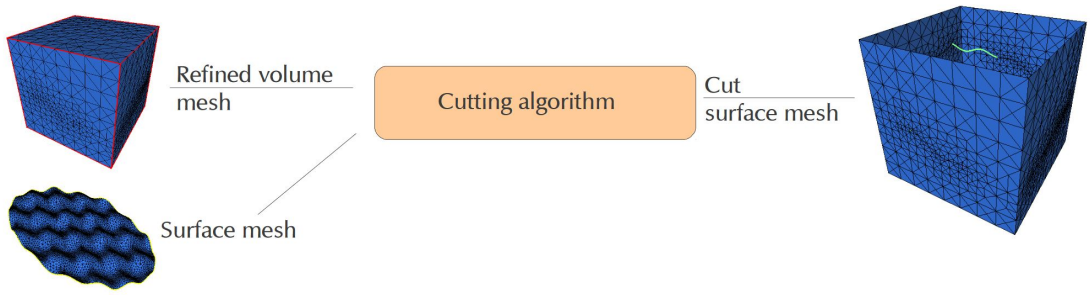


**Fig. 1.43** A mesh cutting strategy using the remeshing techniques [99].

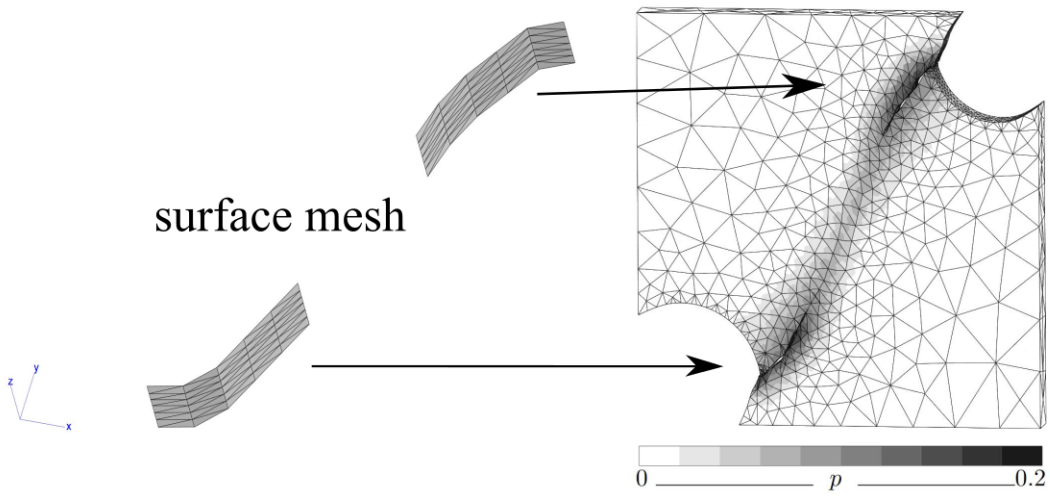


**Fig. 1.44** Propagation of a two crack branches in an asymmetric double notched specimen [100].

Another crack insertion strategy using remeshing techniques was developed in 2D by J. Mediavilla [36, 88]. The algorithm has shown the ability to deal with complex loading conditions in particular in fine blanking operations. A main limitation of the proposed numerical strategy is the extension to 3D cases. The main challenge comes from the necessity to define and propagate two dimensional crack surfaces within a 3D finite element mesh.

Crack propagation in 2D based on remeshing techniques was also presented within the context of cohesive element modeling [101]. The algorithm begins by detecting the crack propagation angle, then a remeshing operation is carried out to insert nodes on the detected crack path. Finally, cohesive elements are added on the ply between the crack faces in order to control the strain energy release rate. Fig. 1.45 shows all the algorithmic operations.

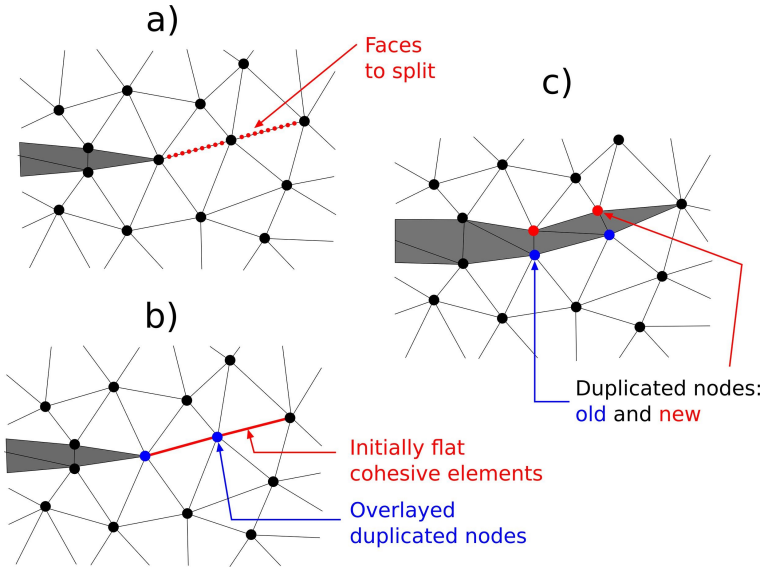


**Fig. 1.45** Different steps of simulating a crack propagation using cohesive element modeling [101]: (i). a crack path is identified in a); (ii). nodal duplication to split the cracked elements in b); (iii). insertion of cohesive elements in c).

As presented above, there is a large variety of numerical techniques in the literature, however, there is not yet a robust strategy that can be applied to complex cases in 3D for large plastic strain configurations. The element deletion technique is very simple but it leads to major problems such as the volume loss and dependency of the final crack path on the mesh size. The need for simulating real crack propagation in multi-stages processes also favors the use of remeshing techniques over the XFEM method. In addition, large plastic strains in many metal forming applications require the use of remeshing in order to keep a good quality of the finite element mesh. Thus, the use of remeshing techniques with a proper crack identification strategy is preferred in this work.

## 1.4 Summary of chapter 1

This chapter starts with an overview about the different metal forming applications in which the ductile fracture plays a pivotal role in the quality of the final products. Then, a comprehensive discussion about the physical mechanisms at the micro-scale that lead to the final failure was also presented. It has been shown that the complexity of the problem comes from the combination of extrinsic and intrinsic factors that affect the void nucleation, growth and coalescence.

Ductile fracture can be modeled using either continuous or continuous-discontinuous approaches. Continuous models can be either uncoupled or coupled to the material behaviour. Continuous models are usually adopted if the goal is to predict if the material will fail or not during the forming processes. Among the reviewed continuous models, the phase field approach for ductile fracture seems a convenient choice as it provides a general framework in which all the damage driving factors can be easily included in the formulation. In addition, the phase field provides a proper regularization of the cracked zone with a length scale that controls the width of the damaged zone. In consequence, it accurately captures the damage localization prior to the crack initiation and propagation. On the other hand, it is necessary in many applications to introduce discrete crack surfaces in the domain in order to use the final products in multi-stages operations. In this case, continuous-discontinuous modeling is essential which is the purpose of the current work. In this context, introducing a discontinuity in the domain using remeshing techniques is a proper choice as it resolves the problems that appear with element deletion method such as the volume loss and mesh dependency.

In this thesis, a crack initiation and propagation algorithm is developed based on the phase field model and adaptive remeshing techniques. A 3D modeling framework is presented within the context of the FE method. The numerical framework is based on the development of four main strategies: (i). an adaptive remeshing strategy for the phase field calculations in order to refine the mesh a priori only in the regions where the crack is expected to propagate; (ii). a damage to fracture transition methodology based on the detection of the local maxima of the phase field profile; (iii). a local mesh partitioning algorithm that can be used to fit the identified crack topology within the finite element mesh within a parallel framework; (iv). introducing a proper phase field formulation for the metal forming applications with complex loading conditions. Numerical examples for benchmark cases will be used for the model validation so that real metal forming applications can be tested. In the next chapter, the main mathematical models that will be used in the current work will be shown followed by a numerical validation with the literature.

## 1.5 Résumé en français

Ce chapitre commence par un résumé des différentes applications de mise en forme dans lesquelles la rupture ductile joue un rôle central dans la qualité des produits finaux. Ensuite,

une discussion complète sur les mécanismes physiques à une échelle micromécanique qui conduisent à la rupture a également été présentée. Il a été démontré que la complexité du problème provient de la combinaison de facteurs extrinsèques et intrinsèques qui affectent la germination, la croissance et la coalescence des porosités.

La rupture ductile peut être modélisée à l'aide d'approches continues ou continues-discontinues. Les modèles continus peuvent être soit découplés, soit couplés au comportement du matériau. Des modèles continus sont généralement adoptés si l'objectif est de prédire si le matériau va se fissurer ou non pendant les processus de formage. Parmi les modèles continus examinés, l'approche du champ de phase pour la rupture ductile semble être un choix pratique car elle fournit un cadre général dans lequel tous les facteurs d'endommagement peuvent être facilement inclus dans la formulation. De plus, le champ de phase permet une régularisation correcte de la zone fissurée avec une échelle de longueur qui contrôle la largeur de la zone endommagée. En conséquence, il capture avec précision la localisation de l'endommagement avant l'amorçage et la propagation de la fissure. D'autre part, il est nécessaire dans de nombreuses applications d'introduire des surfaces de fissures discrètes dans le domaine afin d'utiliser les produits finaux dans des opérations multi-étapes. Dans ce cas, la modélisation continue-discontinue est essentielle, ce qui est l'objet du présent travail. Dans ce contexte, l'introduction d'une discontinuité dans le domaine à l'aide de techniques de remaillage est un bon choix car elle résout les problèmes qui apparaissent avec la méthode de suppression d'éléments tels que la perte de volume et la dépendance au maillage.

Dans cette thèse, un algorithme d'amorçage et de propagation des fissures est développé sur la base du modèle de champ de phase et des techniques de remaillage adaptatif. Un cadre de modélisation 3D est présenté dans le cadre de la méthode EF. Le cadre numérique est basé sur le développement de quatre stratégies principales : (i). une stratégie de remaillage adaptatif pour les calculs de champ de phase afin d'affiner le maillage a priori uniquement dans les régions où la fissure est prévue de se propager ; (ii). une méthodologie de transition endommagement-rupture basée sur la détection des maxima locaux du profil de champ de phase ; (iii). un algorithme de partitionnement de maillage local qui peut être utilisé pour ajuster la topologie de fissure identifiée dans le maillage d'éléments finis dans un cadre parallèle; (iv). l'introduction d'une nouvelle formulation de champ de phase appropriée pour les applications de mise en forme des métaux avec des conditions de chargement complexes. Des exemples numériques de cas de référence seront utilisés pour la validation du modèle afin que de véritables applications de mise en forme des métaux puissent être testées. Dans le chapitre suivant, les principaux modèles mathématiques qui seront utilisés dans le travail actuel seront présentés suivis d'une validation numérique avec la littérature.

# Mathematical formulations and numerical validations

## Contents

## 2.1 Introduction

The first objective of this chapter is to review the mathematical models that are adopted in the literature for the modeling of damage to fracture transition. Then, a numerical validation of the phase field model for ductile fracture combined with the velocity/pressure Finite element formulation with the literature is presented. Finally, a comparison between the phase field model for fracture and the non-local gradient damage model is also shown.

## 2.2 Mathematical description of continuum solid deformation

After reviewing the problem of ductile damage to fracture transition from both physical and numerical perspectives, it seems logical to introduce the main concepts in continuum mechanics. In order to model the deformation of a continuum body, three descriptions should be adopted: (i). kinematic description: a study of the motion of material points without considering the forces that caused this motion; (ii). kinetic description: a study of the effect of forces on the motion of material points; (iii). constitutive model: a model that relates the motion (or deformation in the continuum sense) of the material points to the forces (stresses).

### 2.2.1 Kinematic description

A continuum body is composed of a continuous distribution of material points in the whole domain. Each material point has a set of physical properties such as the mass, density and micro-structural composition that give each material its unique properties. The study of continuum mechanics employs the concept of representative volume element (RVE) in order to define the mechanical and thermal properties of the material. This implies that the information at the lower scale are homogenized within a representative unit of a body on a macro-scale.

Fig. 2.1 shows the deformation process of a body starrting from the reference configuration $\Omega$ to a current configuration $\omega$ through a continuous and differentiable deformation map $\Phi_t$. The deformation map is defined so such that it keeps the same topological structure of the body after deformation. Each material point $P$ in the reference configuration with a position vector $X_i$ is transformed to $x_i$ in the current configuration through the following relationship (Einstein notation is used in all the following expressions)

$$x_i = \Phi(X_i, t) = \Phi_t(X_i), \tag{2.1}$$

and the displacement vector $u_i$ is defined as follows

$$u_i = x_i - X_i. \tag{2.2}$$

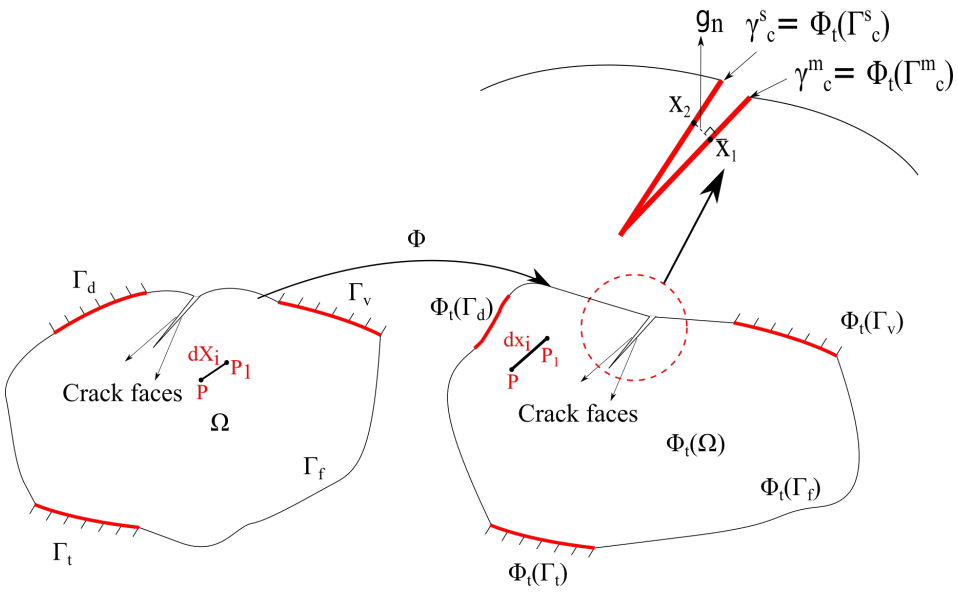


**Fig. 2.1** Deformation process of a continuum body.

An infinitesimal segment $dx_i$ between points $P$ and $P'$ in the current configuration with a length $l'$ can be expressed in terms of an infinitesimal segment $dX_i$ that connects the same points $P$ and $P'$ in the reference configuration with a length $l$ as follows

$$dx_i = F_{ij} dX_j \tag{2.3}$$

where $F_{ij}$ is called the deformation gradient that can be expressed as

$$F_{ij} = \delta_{ij} + \frac{\partial u_i}{\partial X_j} \tag{2.4}$$

where $\delta_{ij}$ is the dirac delta function. The Doyle-Ericksen family of strain tensors can be defined as follows

$$\boldsymbol{\varepsilon}_{ij} = \frac{1}{2m}(\boldsymbol{C}^{\boldsymbol{m}}_{\boldsymbol{ij}} - \delta_{ij}) \tag{2.5}$$

where $m$ determines the type of strain tensor definition, $\boldsymbol{C_{ij}}$ is the left Cauchy-Green deformation tensor defined as follows

$$\boldsymbol{C_{ij}} = F_{ki} F_{kj}. \tag{2.6}$$

Similarly, the right Cauchy-Green deformation tensor $\boldsymbol{b}_{ij}$ can be defined as follows

$$\boldsymbol{b}_{ij} = F_{ik} F_{jk}. \tag{2.7}$$

Table 2.1 list some of the common strain tensor definitions.

**Table 2.1** Different definitions of a strain tensor

| Model | Expression |
|---|---|
| Green-Lagrange | $\frac{1}{2}(\boldsymbol{C_{ij}} - \boldsymbol{I}_{ij})$ |
| Almansi | $\frac{1}{2}(\boldsymbol{I}_{ij} - \boldsymbol{b_{ij}^{-1}})$ |
| Hencky (true) | $\frac{1}{2}\, ln(\boldsymbol{C}_{ij})$ |

where $\boldsymbol{I}_{ij}$ is the second order identity tensor. It should be also noted that the constitutive models can also depend on the rate of strain tensor. The strain rate tensor is then defined as the symmetric part of the velocity gradient tensor $\boldsymbol{L}^g_{ij}$ as follows

$$\dot{\boldsymbol{\varepsilon}}(v) = \frac{1}{2}(\boldsymbol{L}^g_{ij} + \boldsymbol{L}^g_{ji}) \tag{2.8}$$

where the velocity gradient tensor is defined as follows

$$\boldsymbol{L^g_{ij}} = v_{i,j} = \dot{x}_{i,j}. \tag{2.9}$$

The rate of strain tensor can be identified as the rate of Hencky (true) strain tensor when expressed in 1D as follows

$$\dot{\boldsymbol{\varepsilon}} = \frac{\partial v}{\partial x} \tag{2.10}$$

integrating both sides leads to the following

$$\boldsymbol{\varepsilon} = ln(\lambda_S) \tag{2.11}$$

where $\lambda_S$ is the stretch in 1D which is defind as the ratio between the new element length $l^{'}$ to the initial element length $l$.

## 2.2.2 Kinetic description

### 2.2.2.1 Strong formulation

The strong form of mechanical equations used to describe a continuum body can be written as follows [102]

$$\begin{cases} \rho\dfrac{\partial \vec{v}}{\partial t} = \vec{\nabla}\cdot\boldsymbol{s} - \vec{\nabla}p + \rho\vec{g} \text{ (Conservation of linear momentum)} & \text{(2.12a)} \\ \boldsymbol{\sigma} = \boldsymbol{\sigma}^T \text{ (Conservation of angular momentum)} & \text{(2.12b)} \\ \vec{\nabla}\cdot\vec{v} = -\dfrac{\dot{p}}{\kappa} \text{ (Conservation of mass)} & \text{(2.12c)} \end{cases}$$

$\boldsymbol{\sigma}$ is the Cauchy stress tensor, $\rho$ is the material density, $\kappa$ is the bulk's modulus and $\vec{g}$ is the body force vector per unit mass. It should be noted that the conservation of angular momentum leads

to the symmetry of stress tensor. Cauchy stress tensor maps a unit vector $\boldsymbol{n}$ that is perpendicular to an imaginary surface of a material element in the current configuration to the traction vector $\boldsymbol{t}$ in the current configuration through the following relation

$$\boldsymbol{\sigma}_{ij}\boldsymbol{n}_j = \boldsymbol{t}_i. \tag{2.13}$$

Cauchy stress tensor defines the true stress state as it is entirely defined in the current configuration. Another stress measure known as first Piola–Kirchhoff stress can be also defined as follows

$$\boldsymbol{P}_{iJ} = \boldsymbol{\tau}_{ij}\,\boldsymbol{F}^{-1}_{jJ} \tag{2.14}$$

where $\boldsymbol{\tau}_{ij}$ is the Kirchhoff stress which can be defined as $\boldsymbol{\tau}_{ij} = det(\boldsymbol{F})\,\boldsymbol{\sigma}_{ij}$. The first Piola–Kirchhoff stress tensor is non-symmetric as it maps an area element in the reference configuration to a traction vector in the current configuration. A symmetric second Piola–Kirchhoff stress tensor can be then defined as

$$\boldsymbol{S}_{IJ} = \boldsymbol{F}^{-1}_{Ij}\,\boldsymbol{P}_{jJ}. \tag{2.15}$$

The second Piola–Kirchhoff stress tensor is fully defined in the reference configuration as it maps an area element in the reference configuration to a traction vector pulled back to the reference configuration. It should be noted that second Piola–Kirchhoff stress has no physical meaning, however, its mathematical nature can be useful in the context of continuum mechanics. It should be noted that Cauchy stress will be used in the following analysis.

The boundary conditions defined in the current configuration can be expressed as

$$\begin{cases} \vec{v} = \vec{\bar{v}}_0 \text{ on } \Gamma_v \text{ (Dirichlet boundary condition)} & \text{(2.16a)} \\ \vec{t} = \vec{\bar{t}}_0 \text{ on } \Gamma_t \text{ (Neumann boundary condition)} & \text{(2.16b)} \\ \vec{t} = 0 \text{ on } \Gamma_f \text{ (Free boundary condition)} & \text{(2.16c)} \end{cases}$$

where $\vec{\bar{t}}$ is the traction vector.

In addition to the mentioned boundary conditions, the treatment of contact boundary conditions by enforcing the non-penetration between bodies in contact is essential. A detailed description of the contact problem can be found in appendix B.1.

#### 2.2.2.2 Material constitutive law

Generally, linear elastic constitutive laws are used to describe the stress-strain relationship in the field of metal forming. This choice can be justified by the fact that the magnitude of reversible elastic strains is negligible with respect to the plastic strain contribution. An isotropic

elastic material (or Cauchy elastic material) is defined such that the stress tensor can be uniquely defined in terms of the current state of elastic strain $\boldsymbol{\varepsilon}^e$ as follows

$$\boldsymbol{\sigma} = \boldsymbol{\sigma}(\boldsymbol{\varepsilon}^e). \tag{2.17}$$

The assumption of the dependency of the stress tensor on the elastic strain tensor satisfies the objectivity condition of the constitutive law which is independent on the rigid body rotation [102]. In the assumption of linear elasticity, Hooke's law is adopted as follows

$$\boldsymbol{\sigma} = \boldsymbol{C} : \boldsymbol{\varepsilon}^e \tag{2.18}$$

where $\boldsymbol{\sigma}$ is Cauchy stress tensor and $\boldsymbol{C}$ is the fourth order elasticity tensor calculated at a zero strain state. Assuming that there is no residual stress, Hook's law can be also derived from a quadratic elastic strain energy density as follows

$$\boldsymbol{\sigma} = \frac{\partial W_e}{\partial \boldsymbol{\varepsilon}^e} \tag{2.19}$$

where $W_e = \frac{1}{2}\boldsymbol{C} : \boldsymbol{\varepsilon}^e : \boldsymbol{\varepsilon}^e$. The elasticity tensor exhibits major and minor symmetry characteristics because of the symmetry of both stress and strain tensors. Symmetry reduces the number of elasticity tensor components from 81 to 27 that are needed to fully characterize an anistropic material behavior. For an isotropic material behavior, the stress tensor can also be expressed in terms of two material parameters known as Lamé parameters $\lambda$, $\mu$ as

$$\boldsymbol{\sigma} = \lambda\, \boldsymbol{I}\, tr(\boldsymbol{\varepsilon}^e) + 2\mu\, \boldsymbol{\varepsilon}^e \tag{2.20}$$

and the elastic energy density can be then expressed as

$$W_e(\boldsymbol{\varepsilon}^e) = \frac{\lambda}{2} tr(\boldsymbol{\varepsilon}^e)^2 + \mu\, \boldsymbol{\varepsilon}^e : \boldsymbol{\varepsilon}^e. \tag{2.21}$$

The strain and stress tensors can be divided into two parts as follows

$$\boldsymbol{\sigma} = \boldsymbol{s} + p \tag{2.22}$$

$$\boldsymbol{\varepsilon}^e = \boldsymbol{\varepsilon}^e_{dev} + \frac{tr(\boldsymbol{\varepsilon}^e)}{3} \tag{2.23}$$

where $\boldsymbol{s}$ is the deviatoric stress tensor, $\boldsymbol{\varepsilon}^e_{dev}$ is the deviatoric strain tensor and the pressure $p = \frac{\boldsymbol{\sigma}_{kk}}{3}$. The elastic stress energy can be then defined in terms of the deviatoric strain tensor as follows

$$W_e(\boldsymbol{\varepsilon}^e) = \frac{\kappa}{2} tr(\boldsymbol{\varepsilon}^e)^2 + \mu\, \boldsymbol{\varepsilon}^e_{dev} : \boldsymbol{\varepsilon}^e_{dev} \tag{2.24}$$

where $\kappa = \frac{E}{3(1-2\nu)}$ and $\mu = \frac{E}{2(1+\nu)}$.

An elasto-plastic material behaviour is usually assumed during the cold forming processes when the viscous effects of the material are neglected. In this context, two approaches are used to decompose the total strain increment: (i) additive decomposition of the elastic and plastic strain increments [103]; (ii) multiplicative product of the elastic and plastic deformation gradients [104].

In the first approach, the total strain increment can be expressed as

$$\Delta\boldsymbol{\varepsilon} = \Delta\boldsymbol{\varepsilon}^e + \Delta\boldsymbol{\varepsilon}^p \tag{2.25}$$

where $\Delta\boldsymbol{\varepsilon}$, $\Delta\boldsymbol{\varepsilon}^e$ and $\Delta\boldsymbol{\varepsilon}^p$ are the total, elastic and plastic strain increments, respectively. It can be expected that the assumption of linearity of strain increments is no longer valid in case of finite strain increments. In this case, finite strains are non-linear in the displacement so that the linear addition is no longer valid. In such cases, the second approach of multiplicative product is adopted. The total deformation gradient $F$ is then expressed as

$$\boldsymbol{F} = \boldsymbol{F}^e \boldsymbol{F}^p \tag{2.26}$$

where $\boldsymbol{F}^e$ and $\boldsymbol{F}^p$ are the elastic and plastic deformation gradients, respectively. In this case, the constitutive law is expressed in terms of the deformation gradient tensor. In the field of metal forming, negligible elastic strain increments are usually assumed. In consequence, the additive decomposition is usually adopted. Moreover, equations are usually expressed in a rate form in order to reflect the incremental nature of the plastic flow as follows

$$\dot{\boldsymbol{\varepsilon}} = \dot{\boldsymbol{\varepsilon}}^e + \dot{\boldsymbol{\varepsilon}}^p. \tag{2.27}$$

Furthermore, the plastic strain is considered to be nearly incompressible, this can be mathematically expressed as follows

$$tr(\dot{\boldsymbol{\varepsilon}}^p) \approx 0. \tag{2.28}$$

The return mapping algorithm is used to update the equivalent plastic strain and deviatoric Cauchy stress tensor through the $J_2$-plasticity theory. With the assumption of no plastic strain increment, the resulting equations can be written as

$$\boxed{\boldsymbol{s}^{trial} = 2\,\mu(\boldsymbol{\varepsilon}_{n+1} - \boldsymbol{\varepsilon}_n^p)} \tag{2.29}$$

$$\boxed{f_p^{trial} = \sqrt{3\,J_2(\boldsymbol{s}_{n+1}^{trial})} - \boldsymbol{\sigma}_y(\bar{\boldsymbol{\varepsilon}}_n) \leq 0} \tag{2.30}$$

where $\boldsymbol{s}^{trial}$ is the trial deviatoric stress and $n$ is the increment number. If condition 2.30 is not

satisfied, a new plastic deformation increment is calculated by finding the root of the following equation

$$\boxed{f_p = \sqrt{3\, J_2(\boldsymbol{s}_{n+1}^{trial})} - \boldsymbol{\sigma}_y(\bar{\boldsymbol{\varepsilon}}_{n+1}) - 3\mu\Delta\lambda_p = 0} \tag{2.31}$$

where $\lambda_p$ is the plastic multiplier. The plastic strain update at a new time increment $n+1$ is written as

$$\bar{\boldsymbol{\varepsilon}}_{n+1} = \bar{\boldsymbol{\varepsilon}}_n + \Delta\lambda_p. \tag{2.32}$$

Finally, the update of the deviatoric stress tensor is expressed as follows

$$\boxed{\boldsymbol{s}_{n+1} = \frac{\boldsymbol{s}_{n+1}^{trial}}{1 + \frac{3\mu\Delta\lambda_p}{\boldsymbol{\sigma}_y(\bar{\boldsymbol{\varepsilon}}_{n+1})}},} \tag{2.33}$$

and the plastic energy density $W_p$ can be then defined as

$$W_p = \int_0^T \bar{\boldsymbol{\sigma}}\, \dot{\bar{\boldsymbol{\varepsilon}}}\, dt. \tag{2.34}$$

When the phase field model is used, another important feature can be added to the formulation by degrading the yield surface in order to ensure the continuous dependence of the phase field evolution on the plastic deformation. It was shown in [56] that without degrading the plastic yield surface, spurious elastic deformations start to develop and dominate the evolution of the phase field. This result is inconvenient for the cases where the effective plastic deformations is more significant than the elastic deformations. In order to resolve this problem, a plastic degradation function $g_p$ is used to degrade the yield surface. For the sake of simplicity, the plastic degradation function is chosen the same as the elastic degradation function $g_e$ that appears in equation 1.39 . The resulting modification leads to the following yield surface equation

$$\boxed{f_p = \sqrt{3\, J_2(\boldsymbol{s}_{n+1}^{trial})} - g_p(d_n)\, \boldsymbol{\sigma}_y(\bar{\boldsymbol{\varepsilon}}_{n+1}) - 3\,\mu\Delta\lambda_p = 0.} \tag{2.35}$$

In the coupled Lemaitre model, a similar behaviour can be expected since the effective stress tensor is used to calculate the von Mises stress. The yield surface can then expressed as follows

$$\boxed{f_p = \frac{\sqrt{3\, J_2(\boldsymbol{s}_{n+1}^{trial})}}{1 - \bar{D}_n} - \boldsymbol{\sigma}_y(\bar{\boldsymbol{\varepsilon}}_{n+1}) - 3\mu\Delta\lambda_p = 0.} \tag{2.36}$$

#### 2.2.2.3 Weak formulations

In order to build a finite element model, a weak formulation should be developed. Before choosing an appropriate weak formulation, it is important to have a look at the relationship

between the pressure and the strain tensor as follows

$$\dot{p} = \kappa \, tr(\dot{\boldsymbol{\varepsilon}}). \tag{2.37}$$

As a consequence of the incompressibility condition, the pressure cannot be calculated anymore using velocity field since $\kappa \approx \infty$. In the finite element setting, this condition can be seen as enforcing the incompressibility constraint at each point in the domain. As a result, the element will suffer from a volumetric locking in which the computed stress field will oscillate and the whole solution becomes unstable. The penality method has been widely used to ensure the stability of the finite element solution under the incompressibility condition [105]. Another efficient strategy to get rid of such oscillations is to assume a strain field independently from the computed strain field (or equivalently strain rate) from the assumed displacement field (or equivalently velocity). An essential component in this type of formulations is the so-called Hu-Washizu variational principle that can be expressed as

$$\boldsymbol{\pi}_{HW}(u, \boldsymbol{\varepsilon}, \boldsymbol{\sigma}) = \int_{\omega} \boldsymbol{\phi}_{HW}(\boldsymbol{\varepsilon}) + \boldsymbol{\sigma} : (\boldsymbol{\varepsilon} - \nabla_s u) \; d\omega + \boldsymbol{\pi}_{ext} \tag{2.38}$$

with the optimally condition

$$\delta_{u,\boldsymbol{\varepsilon},\boldsymbol{\sigma}} \boldsymbol{\pi}_{HW} = 0 \tag{2.39}$$

where $u, \boldsymbol{\varepsilon}, \boldsymbol{\sigma}$ are the assumed displacement, assumed strain and assumed stress fields, respectively and $\nabla_s u$ is the symmetric part of the displacement gradient. $\boldsymbol{\phi}_{HW}(\hat{\varepsilon})$ is the strain energy functional of assumed strain field that can be expressed as

$$\boldsymbol{\phi}_{HW} = \int_{\omega} C_{ijkl} \; : \boldsymbol{\varepsilon} : \; \boldsymbol{\varepsilon} \; d\omega, \tag{2.40}$$

and $\boldsymbol{\pi}_{ext}$ is the energy functional of external loading. The main advantage of Hu-Washizu variational principle is that it provides a freedom of the choice for three independent fields, displacement, strain and stress, without any constraints. Simo et al. have presented in [106] an assumed strain finite element formulation which is based on Hu-Washizu variational principle. It has been demonstrated that the stability of the problem is ensured by the choice of a proper displacement gradient operator that relates the assumed strain to the assumed displacement fields. In addition, the satisfaction of the LBB condition [107] is also essential for the stability of the discrete system of equations. Simo and Hughes have shown in [108] that the ad-hoc **B**-bar method proposed in [109] can be variationally recovered under some orthogonality conditions. In the **B**-bar approach the strain-displacement matrix **B** is assumed to be equal to the summation of deviatoric and dilatational parts. The dilatational part is manipulated such that the results are improved. The new dilatational part components can be then computed using selective/reduced integration schemes. Likewise, Herrmann proposed a mixed displacement-

pressure weak formulation where the displacement is assumed to be linear over the element and the pressure to be constant in the element [110]. It has been shown in [111] that the bi-linear displacement based finite element with a single point reduced integration scheme is equivalent to Herrmann formulation. A mixed velocity-pressure weak formulation was used in [112] in order to derive the so-called MINI element. In order to satisfy the LBB condition, a bubble function stabilization technique [113] has been adopted by enriching the velocity field. The advantage in this case is that the number of incompressibility constraints (represented by the number of pressure DOFs) is reduced with respect to the number of velocity DOFs so that a stable solution is obtained. It has been shown in [114] that the velocity-pressure formulation is a special case of Hu-Washizu functional where both velocity and pressure are assumed. The last assumptions result in the modified Hellinger–Reissner functional which can be expressed in the rate form as follows

$$\boldsymbol{\pi}_{HR,_m}(v,p) = \int_{\omega} 2\,\mu\,\boldsymbol{\varepsilon} : \dot{\boldsymbol{\varepsilon}} - \frac{p\,\dot{p}}{k} + p\,\nabla\cdot v\;d\omega - \int_{\partial\omega} \vec{t}\cdot v\,d\partial\omega \tag{2.41}$$

with the following optimality condition

$$\delta_{v,p}\boldsymbol{\pi}_{HR,_m} = 0. \tag{2.42}$$

The resulting weak form of the velocity/pressure in the current configuration $\omega$ in addition to the phase field formulation can be expressed as follows (assuming that the body forces are neglected and a contact between crack faces is only assumed to exist for simplicity)

$$\begin{cases} \displaystyle\int_{\omega} \Big(\boldsymbol{s}(v) : \dot{\boldsymbol{\varepsilon}}(\delta v) - p\nabla\cdot\delta v\Big)\,d\omega = \int_{\partial\gamma_t} \vec{t}\cdot\delta v\,d\partial\omega - \overbrace{\int_{\partial\gamma_c} \vec{t}\cdot(\delta v_2 - \delta\bar{v}_1)\,d\partial\omega}^{\text{where } \delta\boldsymbol{\pi}_{LM}} & (2.43a) \\ \displaystyle\int_{\omega} \delta p\,\nabla\cdot v + \frac{\delta p\,\dot{p}}{\kappa}\,d\omega = 0 & (2.43b) \\ \displaystyle\int_{\omega} \frac{G_c}{l_c}\,[\delta\bar{D},\delta d]\,[\bar{D},d] + \int_{\omega} G_c\,l_c\,\nabla[\delta\bar{D},\delta d]\;\cdot\nabla[\bar{D},d]\,d\omega + \mathcal{F} = 0 & (2.43c) \\ \forall \delta v,\delta p,[\delta\bar{D},\delta d] \in \mathcal{V}^0\;\otimes\mathcal{P}^0\;\otimes\mathcal{D}^0 & (2.43d) \end{cases}$$

$$\mathcal{V} = \Big\{\delta v \in (H^1)^{dim(\omega)}\Big\}$$

$$\mathcal{P} = \Big\{\delta p \in (\mathcal{C}^0)^{dim(\omega)} \cap L^2\Big\}$$

$$\mathcal{D} = \Big\{\delta d \in (\mathcal{C}^0)^{dim(\omega)} \cap H^1\Big\}$$

$$\mathcal{V}^0 = \Big\{\delta v \in \mathcal{V}, \delta v = 0 \text{ on } \partial\omega_v\Big\}$$

$$\mathcal{P}^0 = \Big\{\delta p \in \mathcal{P}, \delta p = 0 \text{ on } \partial\omega_t\Big\}$$

$$\mathcal{D}^0 = \left\{ \delta d \in \mathcal{D},\ [\bar{D}, d]_{n+1} \geq [\bar{D}, d]_n, \nabla \cdot [\bar{D}, d] = 0 \,\text{on}\, \partial\omega \right\}$$

where

$$\mathcal{F} = \begin{cases} \int_\omega \delta\bar{D}\, D\, d\omega & \text{Non-local gradient damage} \\ -2\int_\omega \delta d\,(1-d)\ \mathcal{H}\, d\omega & \text{Phase field} \end{cases}$$

*the bracket $[\bar{D}, d]$ is used to indicate that either the non-local damage or the phase field is used in the calculations*. It should be noted here that the MINI element will be used in this work for the FE computations.

In order to deal with the problem of large plastic strains, an updated lagrangian formulation coupled with adaptive remeshing is used. In the updated lagrangian formulation, the new reference configuration is set to be the deformed configuration of the last time step [115]. In consequence, a continuous update of the geometry coordinates requires an adaptive remeshing operation in order to conserve the quality of elements used throughout the simulation.

For the modeling of thin structures in sheet metal forming, structural element are preferred over solid elements as they produce accurate results with a dramatic decrease in the computation time. Triangular shell elements have been proposed in [116] and quadrilateral shell elements in [117] where Hu-Washizu variational principle was adopted. In these element formulations, membrane strains, bending strains and transverse shear strains can be all be taken into account through the variational statement. In addition, these formulations prevent the shear locking since the shear strain is independently assumed from the displacement field. The so-called solid shell element has been proposed in [118] based on a hexaheral element with eight nodes. The main advantage of this element over classical shell elements is the ability to use 3D constitutive laws because the plane stress condition is not considered. Reduced/selective integration schemes can be also used to construct the $\boldsymbol{B}$ matrix that relates the strains and displacements. It was shown that the use of a single quadrature point is insufficient for elasto-plastic materials because the behaviour of the material in this case is fully dependent on the behaviour of the calculated point. Thus, a multi-points calculation is required in order to give a better accuracy. In addition, the contact treatment becomes more convenient with the existence of two contact surfaces.

Different methods exist in the literature to transform the constrained optimization form of the contact problem to an unconstrained one. The objective here is to enforce the non-violation of the non-penetration constraint in a weak sense with the assumption of frictionless contact between the crack surfaces (refer to Appendix B.1 for more details). In the Lagrangian multiplier method, the contact contribution to the virtual power shown in equation 2.43a is replaced by the following

$$\delta\boldsymbol{\pi}_{LM} = \int_{\partial\gamma_c} \delta(\lambda_T\ \dot{g}_n)\, d\partial\omega = \int_{\partial\gamma_c} \delta\lambda_T\, \dot{g}_n + \lambda_T\, \delta\dot{g}_n\, d\partial\omega \tag{2.44}$$

where $\lambda_T$ is the Lagrange multiplier. An additional cost is added to this formulation since new DOFs are introduced to the system in order to solve for the unknown Lagrange multiplier. Nitsche method was adopted to the contact formulation in [119]. It has been shown that the method is more computationally efficient for linear problems than the Lagrangian multipliers method. However, the application of the method to non-linear problem is difficult because of the difficulty of computing the traction variation. The penalty method can be also used to enforce the non-penetration condition in the weak formulation. The last integral in equation 2.43a can be then computed as follows

$$\int_{\partial\gamma_c} \vec{t} \cdot (\delta v_2 - \delta \bar{v}_1)\, d\partial\omega = \int_{\partial\gamma_c} \sigma_n\, \delta\dot{g}_n\, d\partial\omega \rightarrow \int_{\partial\gamma_c} \epsilon_n \langle \dot{g}_n \rangle_-\, \delta\dot{g}_n\, d\partial\omega \tag{2.45}$$

where

$$\langle \dot{g}_n \rangle_- = \begin{cases} 0 & \dot{g}_n \geq 0 \\ \dot{g}_n & \dot{g}_n < 0 \end{cases}, \delta\dot{g}_n = (\delta v_2 - \delta \bar{v}_1) \cdot \bar{\boldsymbol{n}} \tag{2.46}$$

$\epsilon_n$ is the penalization parameter that is used to add artificial stiffness to the system in order to prohibit the violation of the non-penetration condition. It can be shown that the solution of the unconstrained problem with penalization converges to the solution of the original constrained problem as $\epsilon_n \rightarrow \infty$. However, the stiffness matrix becomes ill-conditioned as the value increases, so there should be a trade-off between accuracy and robustness. In the current work, the penalty method is used because the choice of the penalization parameter provides a good compromise between computational cost and accuracy.

#### 2.2.2.4 Finite element formulation

Returning back to the MINI element formulation as it will be adopted in this work. The approximate velocity and pressure variables can be expressed as

$$v_h = v_l + v_b = \sum_{k=1}^{N_n} N_l^k v_l^k + \sum_{j=1}^{N_e} N_b^j v_b^j \tag{2.47a}$$

$$p_h = \sum_{k=1}^{N_n} N_l^k P^k. \tag{2.47b}$$

In addition to that, the non-local gradient damage $\bar{D}_h$ and phase field $d_h$ variables can be also defined as follows

$$[\bar{D}_h, d_h] = \sum_{k=1}^{N_n} N_l^k [\phi_{\bar{D}}^k, \phi_d^k] \tag{2.48}$$

where $N_l^k$ and $N_b^j$ are basis functions associated with node $k$ and element $j$, respectively. $N_e$ and $N_n$ are the number of elements and nodes respectively. $\bar{v}_l$ and $\bar{v}_b$ are the linear and bubble DOFs, respectively. $P^k$ is the pressure DOF, $\phi_{\bar{D}}^k$ and $\phi_d^k$ are the DOFs of the non-local damage and phase field variables, respectively. In our model, four-node tetrahedral elements are used for the FE discretization. More details about the element interpolation functions can be found in [22].

Assuming that the body forces are neglected, the resulting system of equations can be expresses as

$$\begin{cases} \displaystyle\int_{\omega_h} \rho \frac{\partial v_l}{\partial t} \cdot \delta v_l + \boldsymbol{s}(v_l) : \dot{\boldsymbol{\varepsilon}}(\delta v_l) - p_h \nabla \cdot \delta v_l \, d\omega_h = \mathcal{R}_h & \text{(2.49a)} \\ \displaystyle\int_{\omega_h} \rho \frac{\partial v_b}{\partial t} \cdot \delta v_b + \boldsymbol{s}(v_b) : \dot{\boldsymbol{\varepsilon}}(\delta v_b) - p_h \nabla \cdot \delta v_b \, d\omega_h = \int_{\omega_h} \rho g \cdot \delta v_b \, d\omega_h & \text{(2.49b)} \\ \displaystyle\int_{\omega_h} \delta p_h \, \nabla \cdot (v_l + v_b) + \frac{\delta p_h \, \dot{p}_h}{\kappa} \, d\omega_h = 0 & \text{(2.49c)} \\ \displaystyle\int_{\omega_h} \frac{G_c}{l_c} [\delta \bar{D}_h, \delta d_h] \, [\bar{D}_h, d_h] d\omega_h - \int_{\omega_h} G_c \, l_c \, \nabla [\delta \bar{D}_h, \delta d_h] \cdot \nabla [\bar{D}_h, d_h] \, d\omega_h + \mathcal{F}_h = 0 & \text{(2.49d)} \end{cases}$$

where

$$\mathcal{R}_h = \int_{\partial \gamma_{th}} \vec{t} \cdot \delta v_l + \int_{\partial \gamma_{ch}} \epsilon_n \, \langle \dot{g}_n \rangle_- \, \delta \dot{g}_n \, d\partial\omega$$

and

$$\mathcal{F}_h = \begin{cases} \int_{\omega_h} \delta \bar{D}_h \, D_h \, d\omega_h & \text{Non-local gradient damage} \\ -2 \int_{\omega_h} \delta d_h (1 - d_h) \, \mathcal{H} \, d\omega_h & \text{Phase field} \end{cases}$$

$\omega_h$ is the volume of a finite element mesh at the current configuration expressed as follows

$$\omega_h = \bigcup_e \omega_e \, (e \in N_e).$$

The following properties are taken into account: $\int_{\partial \gamma_{th}} \vec{t_0} \cdot \delta v_b \, d\omega_h = 0$ since the bubble function vanishes at the boundaries. The inertial contribution of the bubble part is vanished so that $\int_{\omega_h} \rho \frac{\partial \boldsymbol{v}_l}{\partial t} \cdot \delta v_b \, d\omega_h = \int_{\omega_h} \rho \frac{\partial v_b}{\partial t} \cdot \delta v_l \, d\omega_h = 0$ and $\int_{\omega_h} \boldsymbol{s}(v_b) : \dot{\boldsymbol{\varepsilon}}(\delta v_l) \, d\omega_h = \int_{\omega_h} \boldsymbol{s}(v_l) : \dot{\boldsymbol{\varepsilon}}(\delta v_b) \, d\omega_h = 0$ due to the orthogonality property of the bubble and nodal spaces. The time derivative of the velocity is approximated as follows

$$\frac{\partial v_{l,b}}{\partial t} = \frac{v_{l,b}^{t+\Delta t} - v_{l,b}^t}{\Delta t} \tag{2.50}$$

where $\Delta t$ is the time step.

The next step is to transform the contact problem to a discretized form. The NTS (node to

segment) method is a simple but robust technique that can be used to enforce the satisfaction of the contact constraints [120]. For each slave node, the contact constraints are imposed to the projection point on the master surface as can be seen in Fig. 2.2. The discretized form of contact contribution in the weak form for each element can be shown as follows

$$\int_{\partial\gamma_{elem}} \epsilon_n \langle \dot{g}_n \rangle_- \delta\dot{g}_n \, d\partial\omega \approx \sum_{i}^{n_s} \epsilon_n \langle \dot{g}_n^i \rangle_- \delta\dot{g}_n^i S_i \tag{2.51}$$

where $g_n^i$ is the value of the gap function calculated at node $i$, $n_s$ is the number of slave nodes that are in the active area of contact and $S_i$ is the surface area of the contact face in contact with node $i$. Although the NTS method is very efficient in terms of numerical computation, pathological cases of non-physical gaps between the master and slave faces that can lead to stress singularities can exist. This is due to the fact that the discretization is $\mathcal{C}^0$ continuous so that the curvatures are not accurately modeled. A smoothing algorithm described in [121] is used in order to have a higher order interpolation of the surface discretization without significantly affecting the computation time.

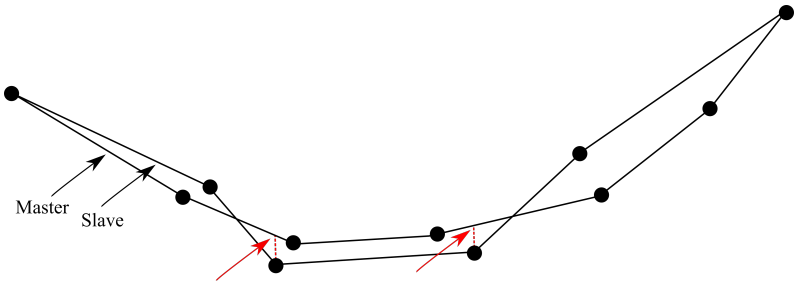


**Fig. 2.2** Master-slave contact in a discretized setting where the contact constraints are enforced using the NTS (node to segment) approach.

Another discretization approach called the QSTS (quadrature segment to segment) has been proposed in [120]. In this approach, the contact constraints are satisfied in an integral rather than a collocated approach. This can be satisfied by enforcing the contact constraints on a given set of quadrature points at the contact surface. This can be mathematically given by (assuming frictionless contact surfaces)

$$\int_{\partial\gamma_{elem}} \epsilon_n \langle \dot{g}_n \rangle_- \delta\dot{g}_n \, d\partial\omega \approx \sum_{i}^{n_s} \sum_{k}^{n_q} \epsilon_n \langle \dot{g}_n^k \rangle_- \delta\dot{g}_n^k w_k \, J_k \tag{2.52}$$

where $n_s$ is the number of slave segments, $n_q$ is the number of quadrature points per element used for the enforcement of contact constraints, $w_k$ is a quadrature weight and $J_k$ is the Jacobian of transformation. It can be observed that a fewer number of elements can be used in this approach to enforce the contact constraints which makes it very efficient. However, a similar problem of non-physical gaps can be also seen similar to the NTS method. This can be explained by the non exact matching between all quadrature points at slave and master segments.

In addition, it is well known that the LBB stability condition is not satisfied in this case due to the high number of applied constraints. Temizer et al. in [122] applied a KTS (knot to segment) strategy within the framework of NURBS discretization. An oscillatory behaviour was observed in the solution in which appropriate relaxation techniques are needed. Authors also showed that a mortar KTS approach gives superior results over the classical KTS method as it lead to a non-local satisfaction of the constraints. Mortar methods are also known to be very robust when applied within the Lagrangian framework [123]. More details about the discretization methods can be found in [124]. In this work, the NTS method will be used due to its simplicity and robustness which makes it suitable for industrial codes. The final form of the residual equations can be found in [22].

## 2.3 Numerical validation of the phase field model

In this section, numerical validation of the phase field implementation of Borden et al. [56] is carried out with **FORGE ®**[1]. Fig. 2.3 shows the geometry and boundary conditions of a symmetrically notched tension test along with the mesh of the discretized domain. The material properties are shown in Table 2.3. The local energy functional $\mathcal{H}$ that is adopted in the validation step can be expressed as follows [56]

$$\boxed{\mathcal{H} = \frac{l_c}{G_c}\Big(\beta_1 \max_n W_e(\boldsymbol{\varepsilon}^e(x, d_n)) + \beta_2 \ < W_p(\bar{\boldsymbol{\varepsilon}}) - W_0 > \Big)} \tag{2.53}$$

where $W_e$ and $W_p$ are the elastic and plastic energy densities, respectively. The plastic energy density can be calculated using equation 2.34. An anistropic energy decomposition shown in Appendix A.2.2 has been used in order to calculate the elastic energy density. $\beta_1$ and $\beta_2$ are two weighing coefficients that control the contributions of the elastic and plastic energies in the phase field evolution and $W_0$ is a plastic energy threshold that delays the effect of plastic deformation in the phase field evolution.

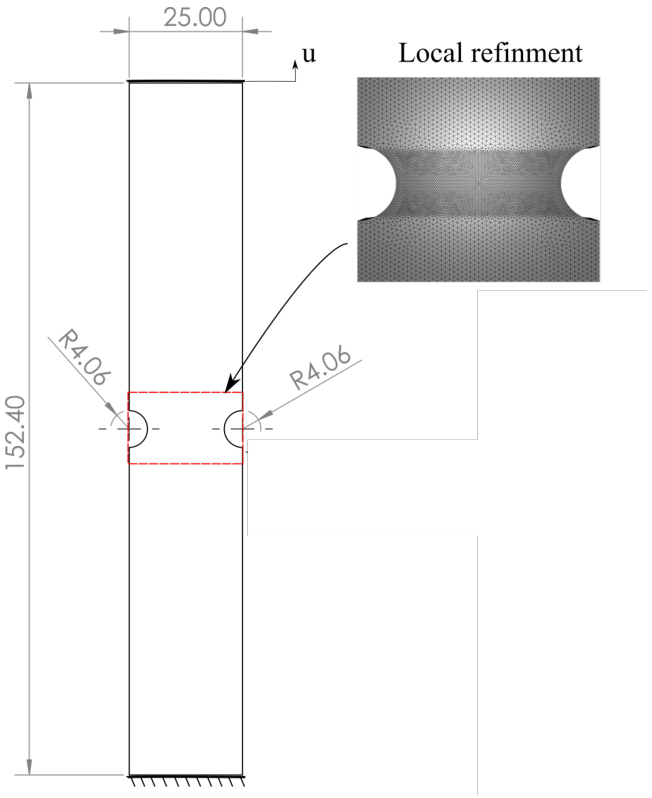


**Fig. 2.3** The representation of the tension test geometry and boundary conditions of a reference case [56]. The mesh is illustrated with the local refinement. The thickness of the specimen is 2.37 mm where all dimensions are in mm. The minimum mesh size is set to 0.1613 mm.

[1]FORGE ® is a finite element software specialized in material forming simulation.

**Table 2.2** Material and model parameters [125]

| Quantity | Value | Unit |
|---|---|---|
| Young's modulus, E | 68.8 | GPa |
| Poisson's ratio, $\nu$ | 0.33 | |
| Yield stress, $\boldsymbol{\sigma}_y$ | $\sigma_0 + H\bar{\varepsilon}$ | MPa |
| $\sigma_0$ | 320 | MPa |
| $H$ | 688 | MPa |
| $\beta_1$, $\beta_2$ | 1 | |
| $l_c$ | 0.6452 | mm |
| $G_c$ | 60 | MPa mm |

A time convergence study with a plastic energy threshold $W_0 = 10$ MPa is carried out in order to confirm the convergence of the solution with the solution reported in [56]. For the reference case, the computations were performed using a quadratic NURBS isogeometric formulation [126] which is known to give a better accuracy of the mechanical resolution. In addition, an adaptive time stepping was used to ensure a good convergence during the simulation.

Fig. 2.4 shows the Normalized stress vs. Normalized strain curves for different time steps. Normalized stress refers to the applied force divided by the initial area of the narrowest cross section and normalized strain is the total displacement divided by the initial length of the specimen. A convergence behaviour is clearly observed when the time step is reduced.

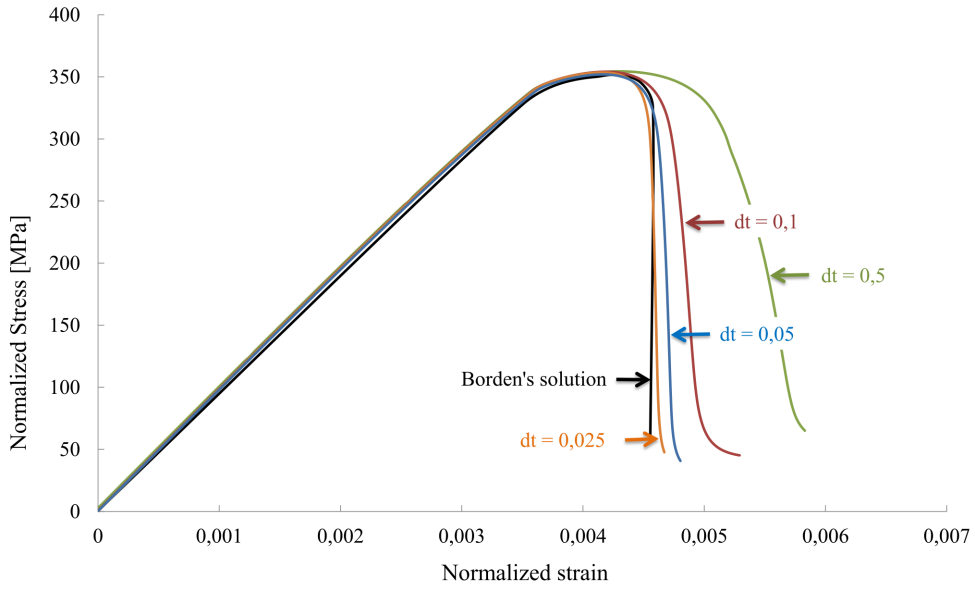


**Fig. 2.4** Study of the time step convergence for the Normalized Stress vs. Normalized Strain curves. Time increments are in seconds.

In addition, one can observe that in the linear and non-damaged elasto-plastic regimes, the Normalized stress vs. Normalized strain curves are almost identical to the reference solution and hence a larger time step can be used without loosing the solution accuracy.

Fig. 2.5 also shows the crack evolution for different values of the plastic threshold. Results are shown on the crass section cutting the specimen between the notches. One can clearly observe that the phase field profile at the initiation instant depends on the threshold and hence it should be well calibrated in order to accurately track the crack evolution.

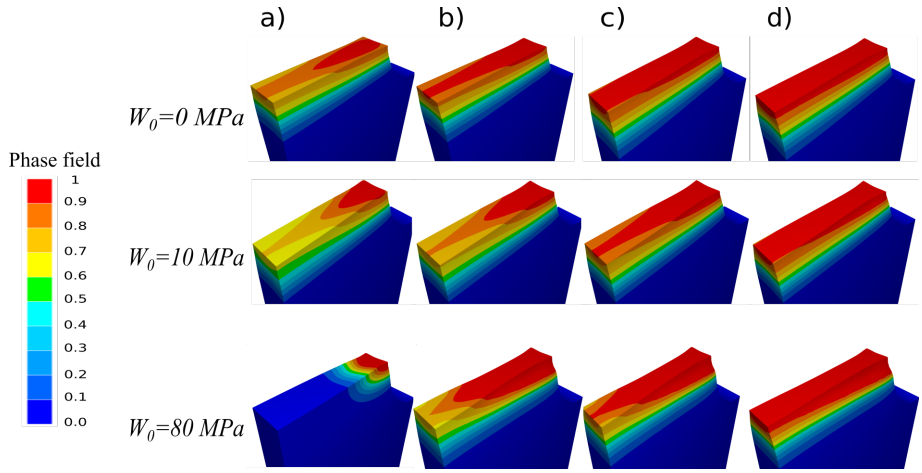


**Fig. 2.5** Contour plots of the phase field evolution for three different values for the plastic threshold $W_0$. Four different deformation states are illustrated starting from crack initiation at a) until the final failure at d).

## 2.4 Phase field vs. gradient-based non-local damage models

In order to see the main features of both the phase field and the gradient-based non-local damage model, a 1D infinite bar with a fully formed crack shown in Fig. 2.6 in the middle is analyzed using both models.

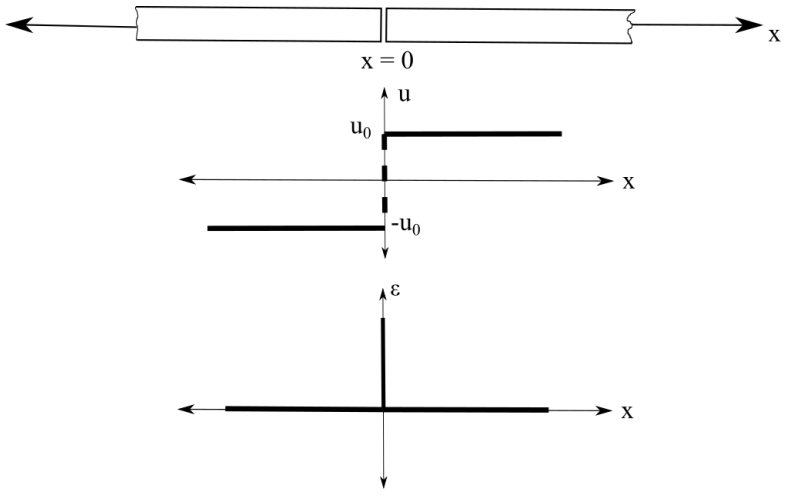


**Fig. 2.6** Description of the displacement and strain fields for a 1D bar with a discontinuity.

The displacement field is described using a Heaviside function as follows

$$u(x) = \begin{cases} u_0 & \text{if } x > 0 \\ -u_0 & \text{if } x \leq 0 \end{cases}$$

where $u_0$ is the crack opening displacement. The strain field is described by a Dirac delta function as follows

$$\varepsilon(x) = u_0\, \delta(x).$$

In order to simplify the analysis, a non-local strain field is used in the analysis where similar solution features are expected if the non-local model is formulated with respect to the damage variable. The non-local strain and phase field variables can be then obtained by solving the following differential equations

$$\bar{\varepsilon} - l_c^2 \nabla^2 \bar{\varepsilon} = \varepsilon \text{ (Non-local gradient damage model)} \tag{2.54a}$$

$$d - l_c^2 \nabla^2 d = 2(1-d)\,\mathcal{H}. \text{ (Phase field model)} \tag{2.54b}$$

The local history functional $\mathcal{H}$ that drives the crack evolution in the phase field equation is chosen as the local strain field. This can be expressed mathematically as follows

$$\varepsilon(x) = u_0\ \delta(x) \text{ (Non-local gradient damage model)} \tag{2.55a}$$

$$\mathcal{H}(x) = u_0\ \delta(x). \text{ (Phase field model)} \tag{2.55b}$$

Applying Fourier transform to equations 2.54a and 2.54b leads to the following expressions

$$\mathcal{F}(\bar{\varepsilon}) = \frac{u_0}{1 + l_c^2\, k^2} \text{ (Non-local gradient damage model)} \tag{2.56a}$$

$$\mathcal{F}(d) = \frac{2u_0(1 - d(0))}{1 + l_c^2\, k^2} \text{ (Phase field model)} \tag{2.56b}$$

where $k$ is the angular frequency. The final solutions of both equations after applying the inverse Fourier transform can be shown as follows

$$\bar{\varepsilon} = \frac{u_0}{2\, l_c} e^{-\frac{|x|}{l_c}} \tag{2.57a}$$

$$d = \frac{u_0}{l_c + u_0} e^{-\frac{|x|}{l_c}}. \tag{2.57b}$$

Fig. 2.7 shows the plots of both the phase field and non-local damage solutions for different values of crack opening and a constant length scale $l_c = 0.5$ mm. It can be shown that the phase field profile does not lead to a significant diffusion in the regions far from the crack when the crack opening $u_0$ increases. In addition, it converges to the crack homogenized solution presented in equation 1.45 in the following sense

$$\lim_{u_0 \to \infty} \frac{u_0}{l_c + u_0} e^{-\frac{|x|}{l_c}} = e^{-\frac{|x|}{l_c}}.$$

On the other hand, the increase of the crack opening displacement in the non-local damage model leads to a significant diffusion in the strain field over the regions far from the crack. This result confirms that the non-local damage models with constant length scale are not very suitable for representing the sharp crack interface especially in the framework of large strains. The same conclusion was found in [127] where a variable length scale model was proposed to resolve this issue.

Fig. 2.8 shows the effect of length scale on the results of both models while the crack opening displacement is kept constant. It can be observed that the length scale in the phase field model plays the role of controlling the width of the transition zone between the intact and fully damaged material points. In other words, the homogenized crack converges to the discontinuous crack interface when the length scale vanishes in the sense of $\Gamma$-convergence. On the other hand, smaller values of the length scale lead to two contrary effects in the non-local damage models, a sharpening at the crack surface associated with broadening in the zones far the cracked zone. This broadening effect is related to the coefficient $\frac{u_0}{l_c}$ that is multiplied by the crack homogenized function in equation 2.57a which leads to an amplification effect with the reduction of $l_c$. On the contrary, the multiplying coefficient in the phase field equation 2.57b which is $\frac{u_0}{l_c+u_0}$ converges to unity when $l_c = 0$.

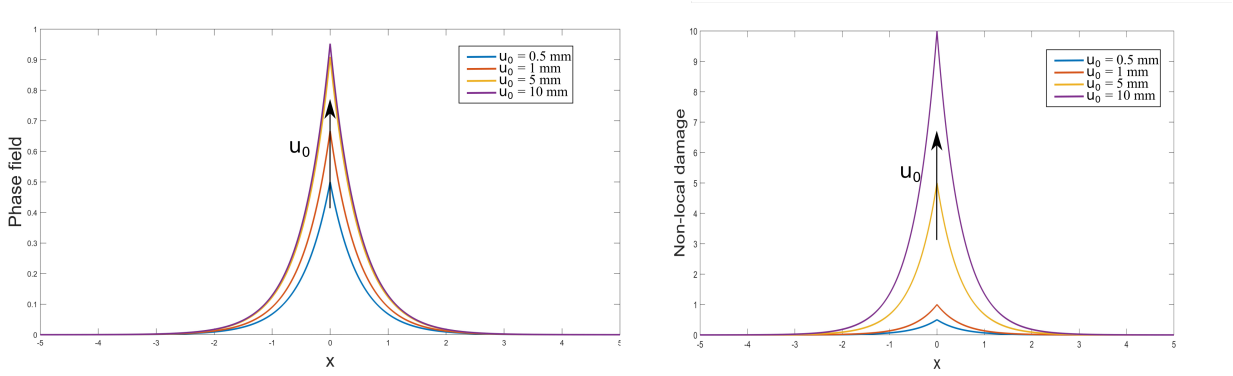


**Fig. 2.7** The effect of the crack opening displacement $u_0$ on the phase field profile (left) and non-local strain profile (right).

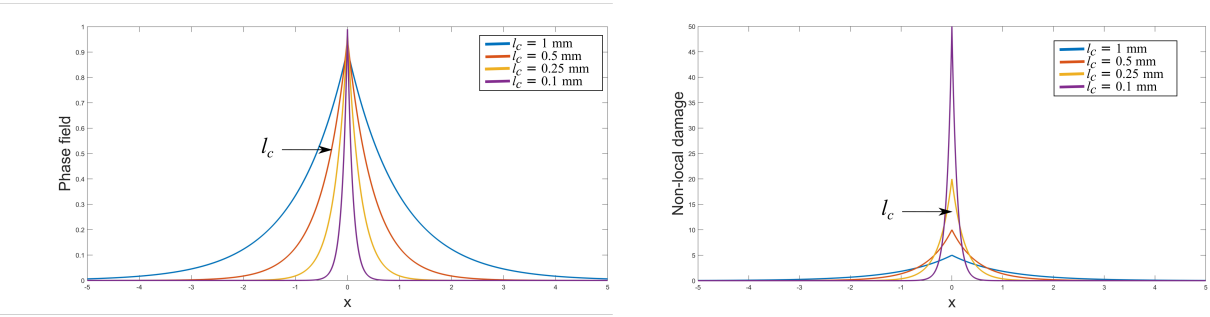


**Fig. 2.8** The effect of the characteristic length scale $l_c$ on the phase field profile (left) and non-local strain profile (right).

The previous analysis can be also extended to 2D and 3D cases. Fig. 2.9 shows a double notched asymmetric specimen where a mixed-mode fracture is expected to occur. The mesh in the whole domain in set to 0.4 mm and only refined in the zone where the crack is expected to propagate with a minimum size $h_{min}$. The material and model parameters can be found in Table 2.3. The characteristic length scale $l_c$ is chosen as $2h_{min}$ in all cases for both models. For the purpose of illustration, a simple form of a phenomenological local damage variable $D$ is chosen as only dependent on the plastic energy density $W_p$ and normalized by a plastic threshold $W_0$ that is expressed as follows

$$D = \langle \frac{W_p}{W_0} - 1 \rangle \tag{2.58}$$

with the condition that $0 \leq \bar{D} \leq 1$.

Likewise, the local history functional in the phase field model is chosen to be only dependent on the plastic energy as follows

$$\mathcal{H} = \frac{l_c}{G_c} \langle W_p - W_0 \rangle, \tag{2.59}$$

**Table 2.3** Material and model parameters

| Quantity | Value or expression | Unit |
|---|---|---|
| Young's modulus, $E$ | 180000 | MPa |
| Poisson's ratio, $\nu$ | 0.28 | |
| Yield stress, $\boldsymbol{\sigma}_y$ | $300(1.477 + \bar{\boldsymbol{\varepsilon}})$ | MPa |
| Plastic energy density, $W_p$ | $\int_0^{\bar{\boldsymbol{\varepsilon}}} \boldsymbol{\sigma}_y \, d\bar{\boldsymbol{\varepsilon}}$ | MPa |
| Characteristic length scale $l_c$ | 0.1/0.2/0.4 | mm |
| Fracture toughness $G_c$ | 5 | MPa mm |
| Plastic threshold $W_0$ | 10 | MPa |

we recall the main equations that will be solved for each model:

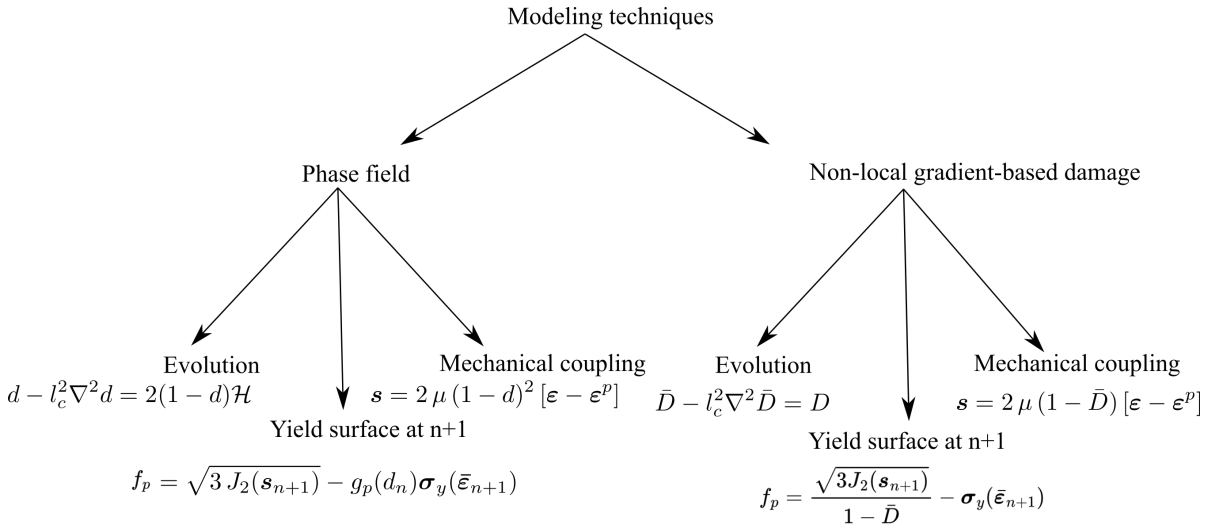


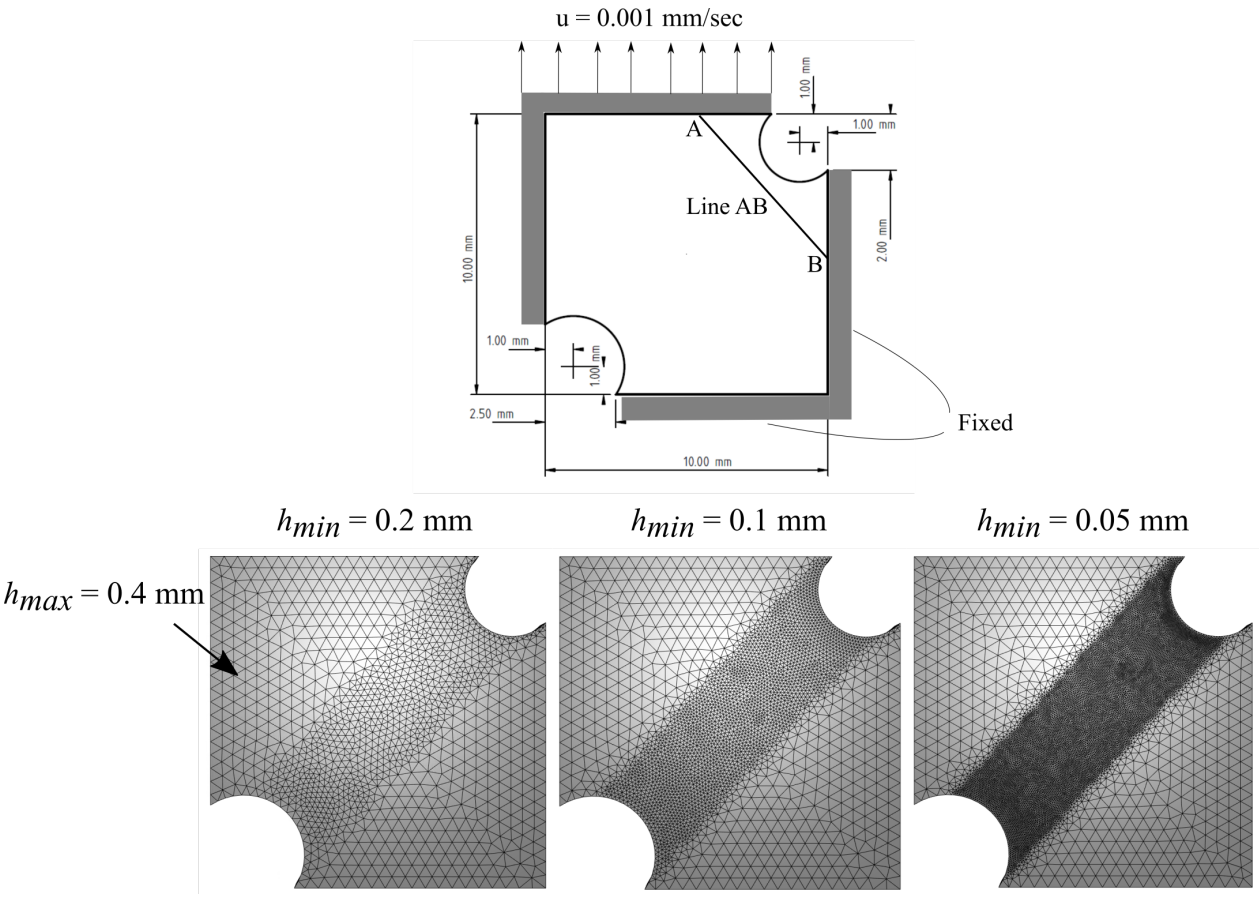


**Fig. 2.9** Geometry and boundary conditions of a double notched asymmetric specimen [88].

Fig. 2.10 shows the final crack paths obtained with the non-local gradient damage and phase field models. It can be clearly seen that a broadening effect is always associated with the non-local damage field while the phase field is very concentrated in the damaged zone which is consistent with the results published in [87]. This feature is important for the accurate determination of the crack surface intersection with the mesh edges.

Fig. 2.11 shows the evolution of phase field and non-local damage profiles along the line AB shown in Fig. 2.10. It can be observed that both fields are very similar at the beginning of damage evolution. While approaching the crack initiation moment, the phase field profile becomes highly concentrated in the cracked zone with no further diffusion far from the crack path. On the other hand, the non-local damage field continues to diffuse outside the cracked zone where it reaches a plateau as damage continues to progress. In order to see the effect of length scale on the results, Fig. 2.12 shows the non-local damage and phase field profiles for different length scales computed along the line AB. It can be seen that the non-local damage model leads to a diffused profile near the cracked zone where the width of the damage plateau decreases with the finer meshes. On the other hand, the phase field leads to an accurate representation of the crack profile even with the coarse mesh. The in-plane gradient components of each field are plotted along the AB line for the case of the fine mesh. It can be clearly seen that a unique local maximum, with vanishing gradient components, can be identified with the phase field model. On the other hand, the non-local damage does not lead to a unique point due to the field diffusion near the crack intersection point. This conclusion makes the detection of local maxima of a given damage field difficult. In consequence, the phase field model represents a suitable choice for representing the regularized crack surface for the modeling of damage to fracture transition.

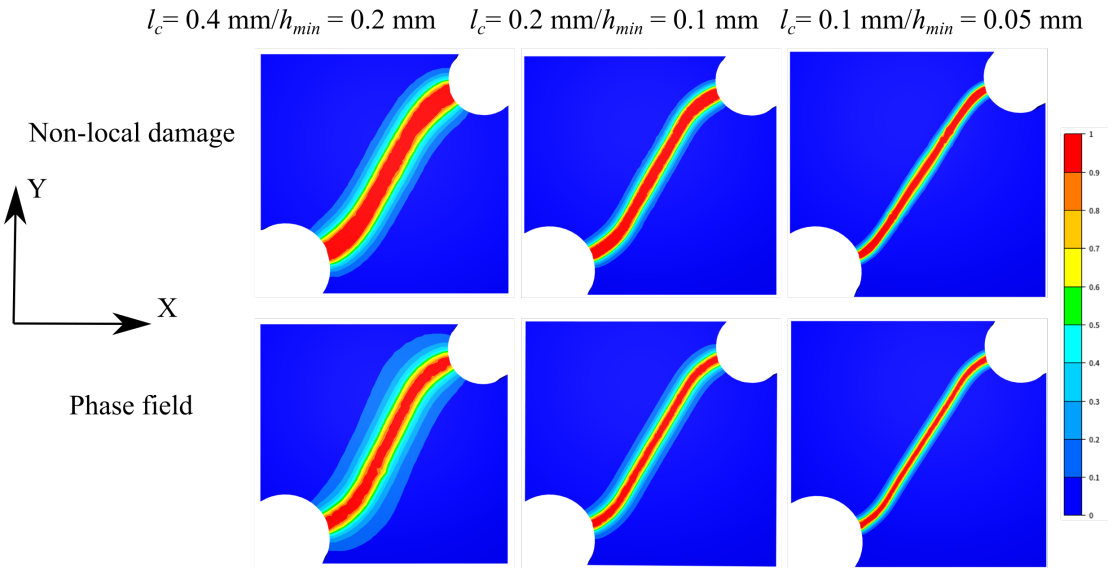


**Fig. 2.10** Evolution of the non-local damage vs. phase field for different values of the characteristic length scale $l_c$.

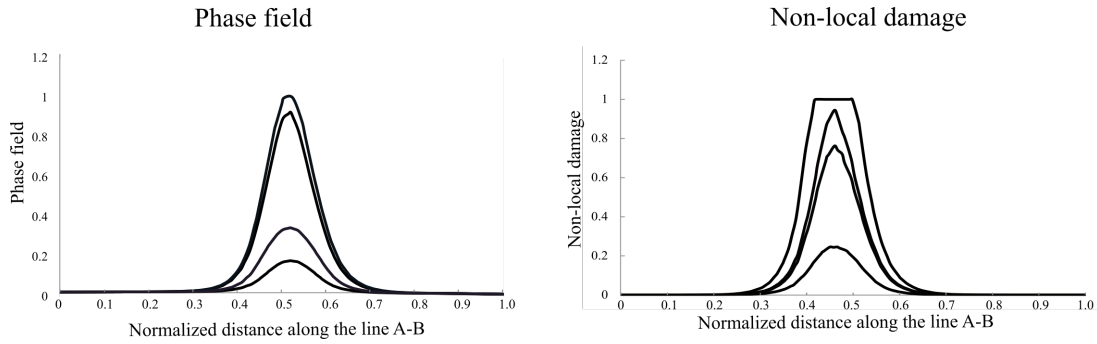


**Fig. 2.11** Evolution of the phase field and non-local damage profiles along the line AB shown in Fig. 2.9. Results are shown for a fine mesh with $h_{min} = 0.05$ mm

The previous analysis suggests that the only possibility to use a non-local damage model for the study of damage to fracture transition is to frequently insert the real crack increments before reaching the state of a fully damaged material ($\bar{D} = 1$). On the other hand, the phase field model gives the possibility to insert a fewer number of real crack increments with larger distances during the simulation since the field does not diffuse once it reaches a value of 1. This emerging feature leads to a reduction in computational cost since a fewer number of remeshing operations is needed in the modeling of damage to fracture transition as will be shown in chapter 4.

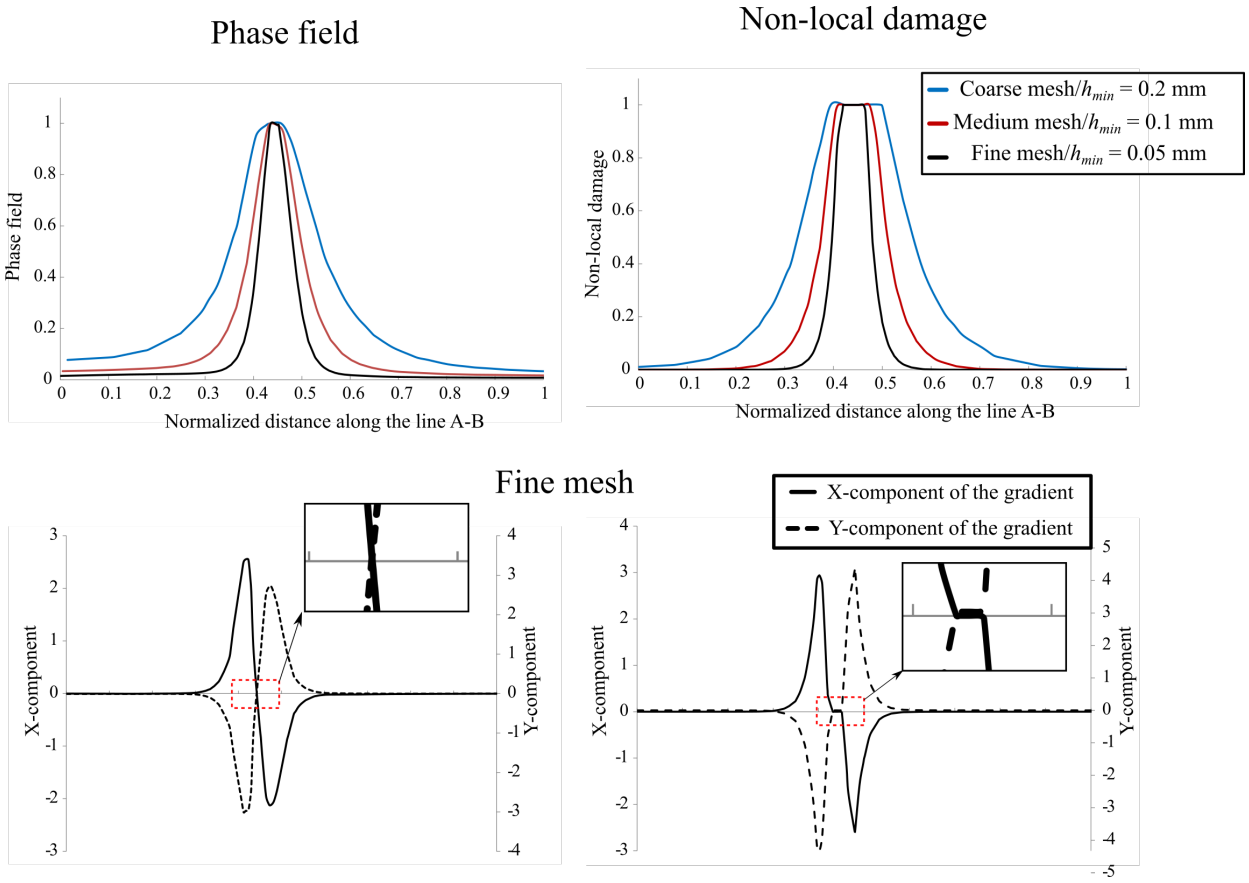


**Fig. 2.12** Phase field vs. non-local damage profiles along the line AB (up) in addition to the X and Y components of the phase field gradient for the fine mesh (bottom).

The conclusion is that, the phase field model can be efficiently adopted for the simulation of crack initiation and propagation when coupled with an appropriate crack driving force through the local history functional $\mathcal{H}$. Although both non-local gradient-based damage and phase field models are very similar, a thorough analysis of both models shows the ability of the phase field model to give a better representation of the crack surface topology.

Based on the previous analysis, the phase field model will be adopted in this work to predict the initiation and propagation of cracks. This choice can be justified by the model features that enable a proper modeling of damage to fracture transition. The aim is to investigate the ability of the phase field to model the ductile fracture problem once coupled with an appropriate discontinuous model.

## 2.5 Summary

The first part of this chapter is dedicated to presenting a literature review about the main mathematical formulations used in the current work. This review started with kinematic and kinetic descriptions of the motion of a continuum body in which different strain and stress measures are presented. Then, elasto-plastic constitutive laws are also shown. Finally, different forms of the weak formulation are presented that can all be derived from the Hu-Washizu variational principle.

In the second part of this chapter, a phase model validation with the literature in order to test the phase field model implementation in **FORGE ®**. A time step convergence analysis is used to confirm the convergence of the solution with the reduction of time step.

Next, a detailed comparison between the phase field and non-local gradient models is presented both analytically and numerically. An analytical solution is obtained of a problem of an infinite 1D bar with a crack at the center using Fourier transform. In this case, analytical expressions are obtained for the phase field and non-local gradient damage models. Results show that the phase field model gives a suitable approximation of the discrete crack surface with the property of $\Gamma$-convergence. On the other hand, the non-local damage models leads to a damage diffusion far from the crack path that increases with the crack opening which is confirmed with the literature.

Finally, A numerical study is presented to show the evolution of both fields along a line perpendicular to the crack path. It has been shown that the phase field profile becomes very concentrated when it approaches the limit of crack initiation ($d$ = 1) with no further diffusion. On the other hand, the non-local damage field diffuses laterally near the critical point ($\bar{D}$ = 1) where the identification of a crack point is not possible. This result is confirmed with the plot of gradient components along the perpendicular line to the crack path. The non-diffusive property of the phase field model makes it efficient in the accurate identification of a crack surface when the material is fully damaged. This will lead to the modeling of the damage to fracture transition with minimal computation cost.

## 2.6 Résumé en français

La première partie de ce chapitre est dédiée à la validation du modèle avec la littérature afin de tester la mise en œuvre du modèle de champ de phase dans **FORGE ®**. une analyse de convergence du pas de temps est utilisée pour confirmer la convergence de la solution avec la réduction du pas de temps.

Ensuite, une comparaison détaillée entre le champ de phase et les modèles d'endommagement non-locaux à base de gradient est présentée à la fois analytiquement et numériquement. Une solution analytique est obtenue pour le problème d'une barre infinie 1D avec une fissure au centre à l'aide de la transformation de Fourier. Dans ce cas, des expressions analytiques sont obtenues pour le champ de phase et les modèles d'endommagement non locaux. Les résultats montrent que le modèle de champ de phase donne une approximation appropriée de la surface de fissure discrète avec la propriété de $\Gamma$-convergence. D'autre part, les modèles d'endommagemnt non-local conduisent à une diffusion du champ d'endommagment loin du chemin de la fissure. De meme, cette diffusion augmente avec l'ouverture de la fissure comme indiqué précédemment dans la littérature.

Enfin, une étude numérique est présentée pour montrer l'évolution des deux champs le long d'une ligne perpendiculaire au chemin de la fissure. Il a été montré que le profil de champ de phase devient très concentré lorsqu'il s'approche de la limite d'amorçage de la fissure ($d$ = 1) sans autre diffusion. D'autre part, le champ de l'endommagement non-local diffuse latéralement près du point critique ($\bar{D}$ = 1) où l'identification d'un point de fissure devient plus difficile. Ce résultat est confirmé au travers de la courbe de composants gradient le long de la ligne perpendiculaire au chemin de la fissure. La propriété non diffusive du modèle de champ de phase le rend efficace dans l'identification précise d'une surface de fissure lorsque le matériau est entièrement endommagé. Celui permettra de modéliser la transition endommagement-rupture avec un coût minimal de calcul.

# Phase field model with adaptive remeshing

## Contents



*This chapter is an extended version of the following published paper:*

**H. Eldahshan, P.-O. Bouchard, J. Alves, E. Perchat, D.P. Munoz, "Phase field modeling of ductile fracture at large plastic strains using adaptive isotropic remeshing", Computational Mechanics 67 (2021), 763–783.**

## 3.1 The role of adaptive remeshing in ductile fracture simulations

The widely used technique in the literature to perform the phase field computations is to fix the mesh size in the zone where the crack is expected to propagate before starting the computations. The minimum element size $h_{min}$ should be properly chosen in order to describe the damage zone. However, a larger element size can be used at the beginning of the simulation before starting the phase field evolution. As recommended by Miehe et al. [81], $h_{min}$ in the critical zones where the crack is expected to propagate is chosen to be at least two times less than the length scale $l_c$. Performing the phase field computations on fixed meshes have two major disadvantages: (i). the refinement region might be unknown before starting the computations which contradicts the purpose of our model which is to predict the location of crack initiation and propagation; (ii). high computational cost is expected since the higher element size can be used before the onset of crack initiation and also in the slightly damage zones.

The main objective of this work is to provide an adaptive refinement scheme in order to get an accurate resolution of the mechanical and phase field equations with lowest possible computational cost.

## 3.2 Mesh refinement criteria

Different mesh refinement techniques were proposed in the literature based on a posteriori error estimations. The aim is to estimate the difference between the computed finite element and exact solutions and construct a refinement map that changes the elements size according to the computed error. As mentioned in [128], the following characteristics assess the quality of an a posteriori error estimator: (i). the predicted error should be close to the unknown actual error and should converge to zero with the same rate as the actual error; (ii) the error estimator should be robust and easy to compute in order to refine the mesh in the zones where the computed solution deviates from the actual one. Error estimators can be divided into explicit, implicit and recovery-based estimators. In explicit method, an accurate computation of the residual at the element level is necessary to find the error bounds. On the other hand, implicit methods tend to compute the error by solving an auxiliary problem where its solution can be used to estimate the actual error for the original problem due to the problem similarity. In the third category, the error estimator $E_h$ is constructed by comparing the smoothed gradient field by the finite element approximated gradient field. This can be shown mathematically as follows

$$E_h^2 = \int_{\Omega_h} \mid \nabla u_h^{smooth} - \nabla u_h \mid^2 \, d\Omega \tag{3.1}$$

where $\nabla u_h^{smooth}$ is the smoothed gradient solution and $\nabla u_h$ is the approximated gradient obtained from the finite element solution. In order to calculate the smoothed solution of the

gradient, Zienkiewicz and Zhu proposed a gradient smoothness criterion that uses the same interpolation functions as the original solution [129]. The method is known to be superconvergent in the sense that the computed error converges in a quadratic order with respect to the mesh size. It should be noted that there is not yet available anderror estimator that gives exact error bounds for all types of problems. Each proposed error estimator has pros and cons that makes it suitable for specific category of problems.

In this work, a simple and efficient mesh adaptation strategy is proposed to refine the mesh according to a given field of interest. In order to prevent the excessive mesh refinement that leads to a considerable numerical diffusion, a volume quality metric is defined in order to stop the remeshing operations once a given threshold is reached. In other words, once the damaged zone is well refined. Three main steps are followed in the remeshing strategy: (i). the choice of an appropriate indicator function that triggers the remeshing process; (ii). to have a control of the number of remeshing operations; (iii) the choice of a consistent field transfer operator that minimizes the numerical diffusion after each remeshing operation.

The general idea is that elements are refined upon reaching a given threshold for a given indicator function. A tag for each element is used to know whether or not it needs to be refined during the computations so that a size map is built for the whole mesh. Before carrying out the refinement step, a quality metric is calculated for all elements in order to ensure that each tagged element has not been previously refined. The remeshing operation is triggered only if there is at least one tagged element that is not yet refined. The main objective of the proposed strategy is to minimize the numerical diffusion due to remeshing by stopping the remeshing operations once the whole damaged zone is well refined.

## 3.3 Transport of mechanical fields

Field transfer operation refers to the transport of mechanical fields between two different meshes occupying the same topological space. Regardless of the method used in this step, an amount of data is always lost due to the non-exact transfer of fields. The important features of a conservative remeshing-transfer operator are: (i). minimizing the numerical diffusion; (ii). preserving the mechanical equilibrium after the transfer step. Two types of fields can be transferred: element fields (P0 fields) that are stored at the integration points and nodal fields (P1 fields). For the sake of demonstration two categories of transfer operator will be used, however, more advanced techniques can be used in the current strategy once established: (i). P0 transfer: each integration point in the new mesh takes the value of its nearest neighbourhood in the old mesh; (ii). P1 transfer: a three-step procedure is carried out as follows: (a). a smoothing operator transforms the P0 field to a P1 field; (b). a direct interpolation maps the nodal fields of the old mesh $\mathcal{T}_0$ to the new mesh $\mathcal{T}$; (c). the nodal field at the new mesh is remapped to the integration points [130, 131].

Different remeshing transfer operators have been introduced in the literature and vary in

the degree of accuracy and robustness. Kumar et al. [132] presented a comparison between a wide range of recovery methods by element patches or by nodal patches. Other important aspects related to the parallel implementation and managing the transport for the nodes at the surface should be taken into consideration. Zienkiewicz and Zhu presented in [133] the SPR (Super convergent Patch Recovery) method which is based on retrieving a mapped stress field using a patch of elements sharing a common node. In order to ensure the equilibrium after each remeshig operation, a few Newton-Raphson iterations should be carried out as suggested in [88]. A simpler approach was proposed in [100] which is to use a very small time step ( order of $10^{-9}$) in the next solution step in order to ensure that the obtained solution after remeshing satisfies the equilibrium. Authors in [134] proposed to divide the loading step into two steps in order to increase the convergence rate of the solution. Another proposition in [132, 135] is to ensure that the transferred field preserves the equilibrium at the new mesh by ensuring the satisfaction of the smoothed solution of the equilibrium equation. In this work, two field transfer operators are used: (i). nearest point interpolation method; (ii). P1 transfer by Galerkin smoothing method.

### 3.3.1 P0 transfer method (Nearest point interpolation)

This method is the simplest among the other field transfer operators. However, it lacks a proper mathematical consistency when compared to other methods so that it can be very diffusive if the mesh is not very refined. The values at the integration point of the old mesh are transferred to the nearest possible integration point in the new mesh as shown in Fig. 3.1. This method preserves the values of the transferred field when the changes in the mesh topology are very small. However, the remapping error is proportional to the field gradient, i.e., when the gradient of a given field is very high, it becomes very difficult to recover the fields with high accuracy. This technique also has the advantage of a low computational costs ince no additional operations are done except for locating the nearest neighbourhood of each integration point in the mesh. Fig. 3.1a summarizes the steps of this method.

### 3.3.2 P1 transfer with Galerkin smoothing

The Galerkin smoothing method is referred to the smoothing of discontinuous P0 fields per element in order to build another continuous P1 field per node. The P0 fields are transformed to be P1 fields followed by a direct nodal interpolation using the same interpolation functions used for the finite element solution as shown in Fig 3.1b. Finally, a P0 field is recovered from the constructed P1 field. This method is expected to be more conservative than the nearest point interpolation method when the old and new mesh typologies are very different. On the contrary, it should always be expected to have an amount of data loss due to the P0-P1-P0 transformations even if the mesh topological changes are small. The weak form of the field

type transformation applied over an element gives

$$\int_{\Omega} \phi_h \, f_{P1} \, d\Omega = \int_{\Omega} \phi_h \, g_{P0} \, d\Omega \tag{3.2}$$

where $g_{P0}$ is the P0 type field, $f_{P1}$ is the transformed field of type P1 and $\phi_h$ is a test function. The functions $f_{P1}$ and $\phi_h$ are defined as follows

$$f_{P1} = \sum_{k=1}^{N_n} N_l^k \hat{f}_{P1}^k \tag{3.3a}$$

$$\phi_h = \sum_{k=1}^{N_n} N_l^k \hat{\phi}^k \tag{3.3b}$$

where $N_l^k$ are the same basis functions used in the finite element model.

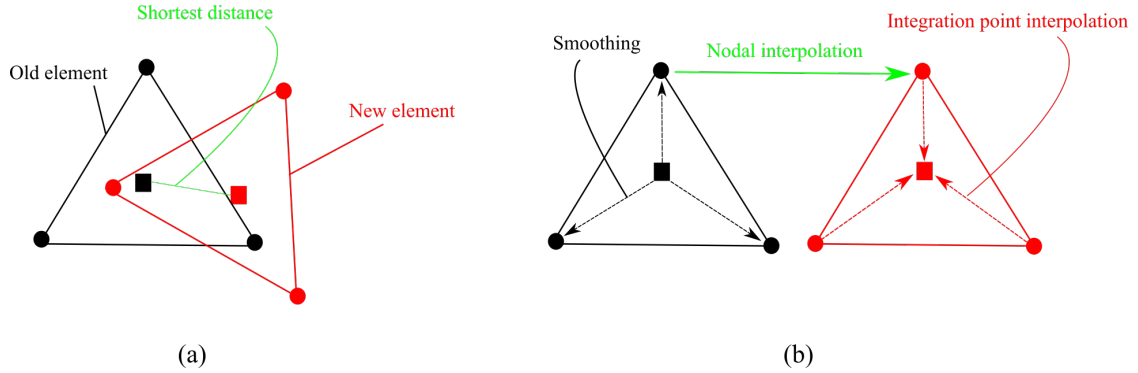


**Fig. 3.1** Field interpolation method: a. P0 transfer (Nearest point interpolation). b. P1 transfer with Galerkin smoothing.

## 3.4 Minimization of the numerical diffusion

Numerical diffusion during remeshing is inevitable. When the local error estimators are adopted, the refinement process is terminated once a given error between the computed and exact solution is reached. Another criterion is implemented in the current strategy in order to stop the remeshing operations once the element size is reduced. Here it is assumed that the error in the computed solution is minimized when the mesh is properly refined.

In order to achieve that objective, a volume quality metric is proposed in this work. Fig. 3.2 illustrates the way of calculating the element size in the case where the phase field is used as an indicator function for the refinement process. It should be noted here other variables that are essential in the ductile damage process can be used for the mesh refinement such as the equivalent plastic strain and equivalent plastic strain rate. The size related to each node is determined based on the value of the phase field, i.e., the size only changes if the phase field value exceeds the pre-set threshold. At each increment, a volume quality metric $\mathcal{B}$ is calculated

for each element $T$ as follows

$$\mathcal{B}(T) = min\Big(\big(\frac{l_{new}}{l_{old}}\big)^3, \big(\frac{l_{old}}{l_{new}}\big)^3\Big) \tag{3.4}$$

where $l_{new}$ is the average length of a tetrahedron in the new mesh in case of remeshing and $l_{old}$ is the average length of a tetrahedron in the old mesh. Both lengths are calculated as follows

$$l_{new} = \frac{h^1_{new} + h^2_{new} + h^3_{new} + h^4_{new}}{4} \tag{3.5}$$

$$l_{old} = \frac{\text{Perimeter of the old element}}{6} \tag{3.6}$$

The mesh quality threshold can be chosen to be as follows

$$\text{Mesh quality threshold} = \Big(\frac{l_{new}}{\eta_v\, l_{old}}\Big)^3 \tag{3.7}$$

where $h^i_{new}$ is the pre-set element size associated with the node $i$ in the refined zone in which the phase field is expected to propagate, $l_{new}$ is the average element size after the mesh refinement step, $l_{old}$ is the average element size before refining the mesh and $\eta_v$ is a numerical parameter that varies between $0.6$ and $1.4$. This artificial parameter $\eta_v$ is a tolerance for the remeshing initiation process as the initial element size distribution is heterogeneous. The threshold gives an upper bound for the ratio of element volume between the old and new meshes.

Fig. 3.3 illustrates the mesh refinement process where the chosen indicator function is the equivalent plastic strain with a threshold of 0.01 and the mesh quality threshold is calculated as 0.0156. First, all the elements that reach a value of the equivalent plastic strain of 0.01 are tagged. Second, the volume quality metric is calculated for all the tagged elements as seen in Fig. 3.3a. A remeshing step is carried then out in order to reduce the size of the tagged elements that have a mesh quality value less than the mesh quality threshold as seen Fig. 3.3b. After the mesh refinement step, no further remeshing is carried out since the value of the mesh quality metric exceeds the threshold value so that the numerical diffusion is minimized.

This proposed strategy is essential in limiting data diffusion due to remeshing. In other words, the rule here is that: once the region in which the crack is expected to propagate is remeshed and all the elements in the refined zone have a good quality for the phase field resolution, the remeshing is terminated.

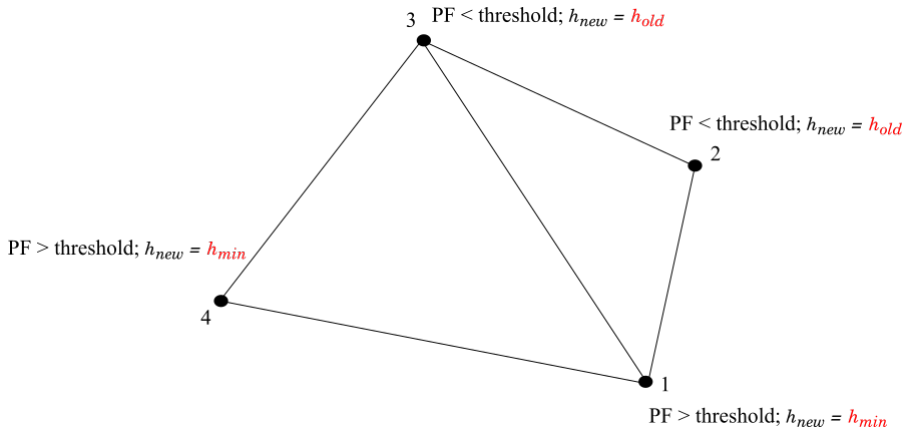


**Fig. 3.2** Calculating the new element size based on the phase field values at the nodes.

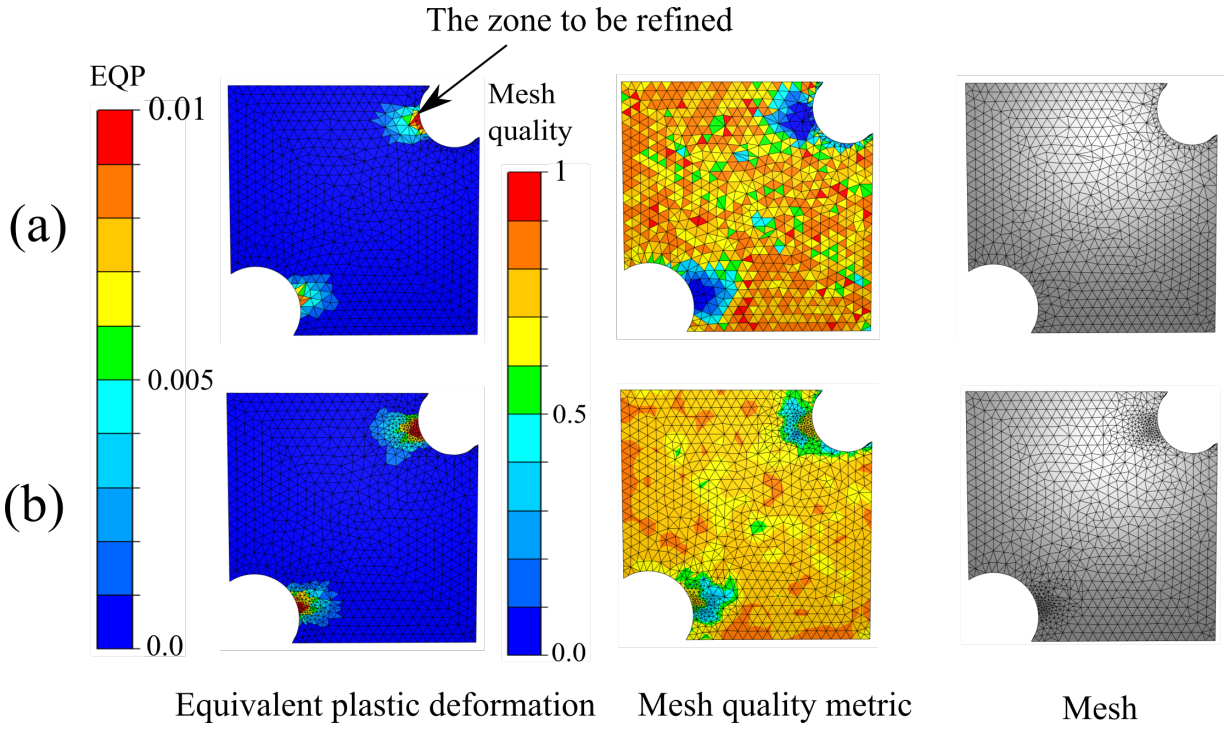


**Fig. 3.3** Illustration of the mesh refinement procedure.

## 3.5 Numerical examples

Two numerical examples are demonstrated in this section. The aim is to show the ability of the developed algorithm to deal with the crack initiation and propagation under different loading conditions. In the following two examples, the following form of the local energy functional $\mathcal{H}$ that is used to drive the phase field evolution is used

$$\boxed{\mathcal{H} = \frac{l_c}{G_c}\Big(\beta_1 \max_n W_e(\boldsymbol{\varepsilon}^e(x, d_n)) + \beta_2 \ < W_p(\bar{\boldsymbol{\varepsilon}}) - W_0 > \Big)} \tag{3.8}$$

### 3.5.1 Double-edge symmetric specimen under traction

In this example, we show the numerical results of the phase field model obtained with the developed isotropic remeshing strategy. When remeshing is used, a constant mesh size is used in the whole initial domain. Then, a mesh refinement process is carried out in order to have a small enough element size in the regions in which the crack is expected to propagate. Two different base element sizes are compared for the values 0.5 mm and 1.25 mm. Base element size is referred to the pre-set element size in the whole domain before starting the computations. The aim is to illustrate the accuracy of the two field transfer operators. The geometry and boundary conditions are shown in Fig. 3.4. The material and model parameters are also shown in Table 3.1. Two fixed size meshes, mesh 1 and mesh 2, are used to compare the results with the cases where remeshing is adopted. Mesh 1 and mesh 2 have sizes of 0.5 mm and 1.25 mm in the domain, respectively, except in the zone where the crack is expected to propagate. A minimum mesh size of 0.1613 mm is used in the region where the crack is expected to propagate. The specimen is fixed from the bottom and displaced from the upper end with a constant velocity of 0.0042 mm/s. The phase field is used as an indicator function in this example. Two different thresholds of the indicator function are used: 0.025 and 0.075. A value of $\eta_v = 1$ is used in all the upcoming simulations.

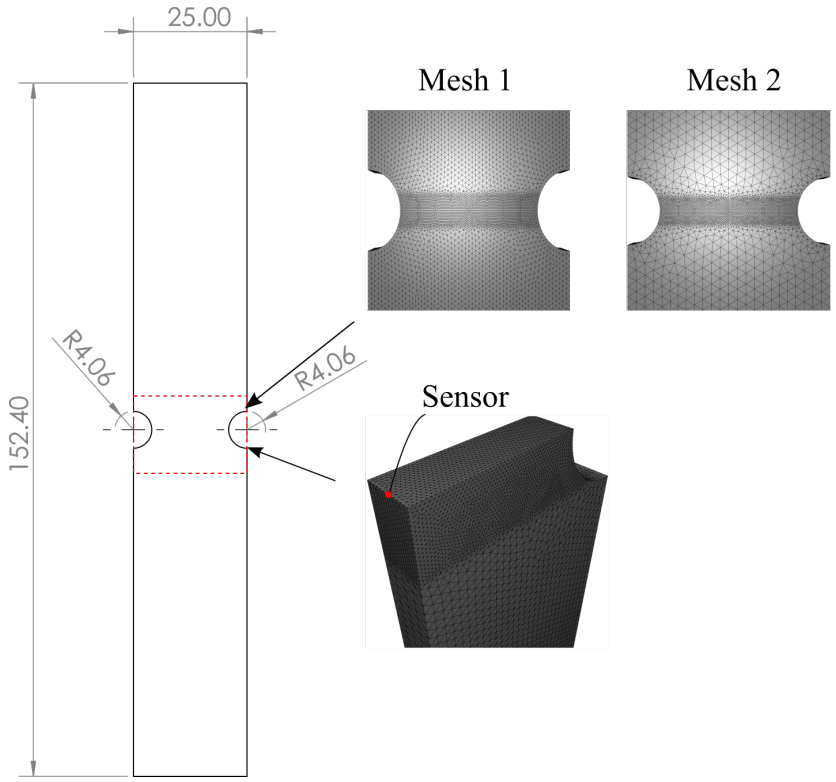


**Fig. 3.4** The representation of the tension test geometry and boundary conditions of a reference case [56]. The mesh is illustrated with the local refinement. The thickness of the specimen is set to 2.37 mm where all the other dimensions are in mm.

**Table 3.1** Material and model parameters

| Quantity | Value | Unit |
|---|---|---|
| Young's modulus, $E$ | 68.8 | GPa |
| Poisson's ratio, $\nu$ | 0.33 | |
| Yield stress, $\boldsymbol{\sigma}_y$ | $\sigma_0 + H\bar{\boldsymbol{\varepsilon}}$ | MPa |
| $\sigma_0$ | 320 | MPa |
| $H$ | 688 | MPa |
| $\beta_1$, $\beta_2$ | 1 | |
| $l_c$ | 0.6452 | mm |
| $G_c$ | 60 | MPa mm |
| $W_0$ | 10 | MPa |

Fig. 3.5 shows the phase field evolution at four different displacement states with the phase field threshold value equals to 0.025 and base mesh size set to 0.5 mm. The time step is set to 0.5 s for the first 125 increments since accurate results can be obtained in the linear regime with a large time step and then 0.05 s for the rest of the simulation. The choice of the time step is concluded from the time step convergence study in the previous chapter which gives a good compromise between accuracy and low computation time. The results are plotted on the current configuration where the mesh at the different displacement states is shown. In Fig. 3.5a, the remeshing is not yet initiated since this is an early deformation state, i.e., the same phase field distribution is obtained. Then, the remeshing step is initiated with both transfer operators as shown in Fig. 3.5b.

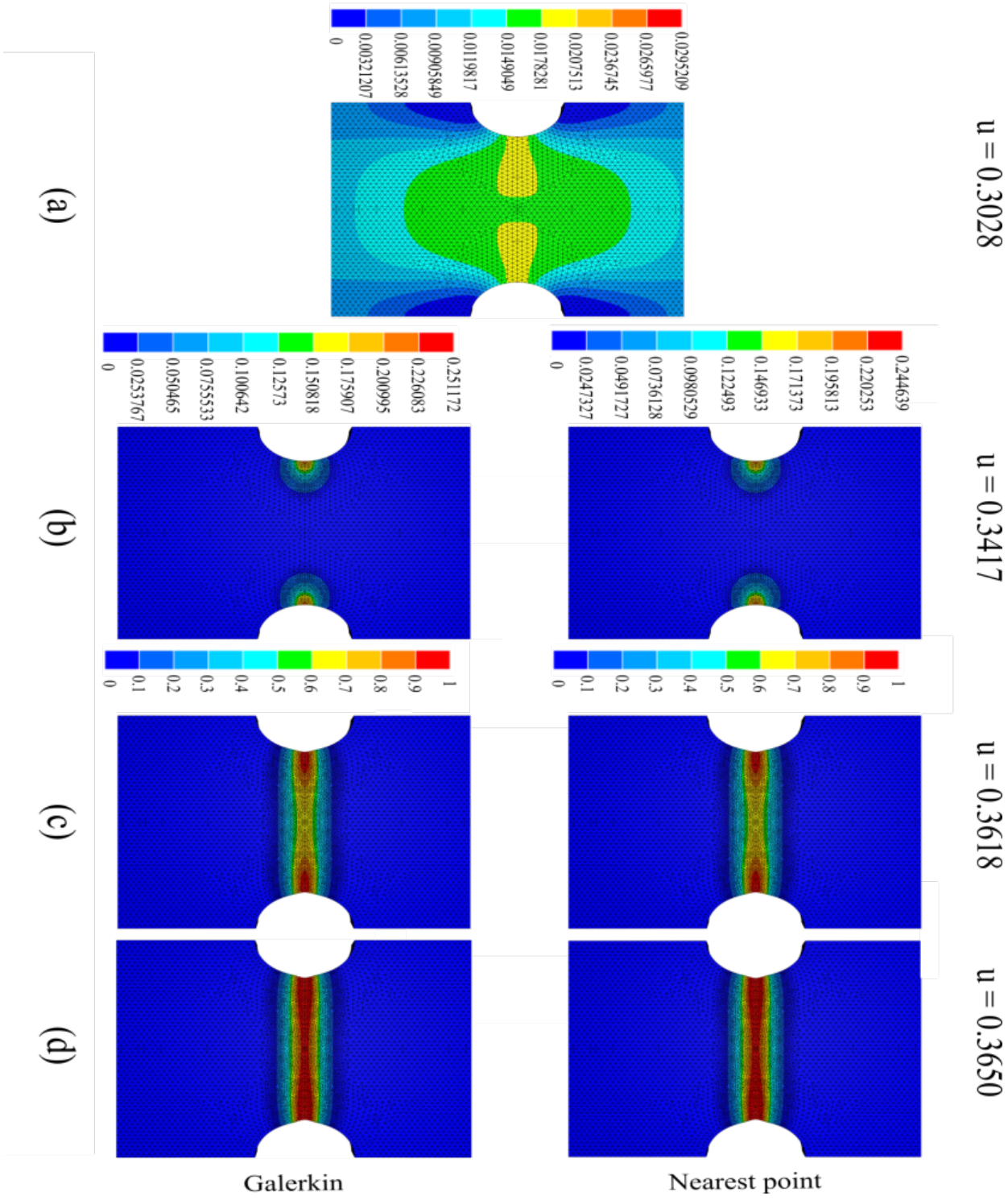


**Fig. 3.5** Evolution of phase field at different displacements where the phase field threshold is set to 0.025 and the average element size of the base mesh is set to 0.5 mm.

The phase field profiles with a threshold value of 0.075 are shown in Fig. 3.6. Comparing Figs. 3.5c and 3.6c shows that when the phase field threshold is 0.075, the crack initiates and propagates at a larger displacement than the case with a threshold of 0.025. This can be explained by the fact that when the element size in the damaged region is not sufficiently small, the accuracy of the mechanical resolution is affected. This means that when the remeshing

initiation is slightly delayed, the exact moment of crack initiation is not accurately captured. In consequence, the full crack is formed at a displacement $u = 0.3671$ mm which is also higher than the case when the threshold is 0.025 which is reported as $u = 0.3650$ mm.

It can also be shown in Fig. 3.6c that the crack front propagates for a longer distance toward the center at the same displacement when the Galerkin smoothing method is used. This can be also referred to the field transfer step that affects the accuracy of the transported fields. Fig. 3.7 shows the Normalized Stress vs. Normalized Strain curves for different threshold values.

Normalized stress refers to the applied force divided by the initial area of the narrowest cross section and normalized strain is the total displacement divided by the initial length of the specimen. Results are obtained for both field transfer operators and compared with the case of an initial fixed mesh. When the value of the threshold is increased to 0.075, the coarse mesh topology before the initiation of remeshing steps does not capture the localized plastic strains at an early stage of the deformation which in turn leads to a delay in the crack initiation. Fig. 3.8 shows the local phase field evolution at a sensor location shown in Fig. 2.3. A small difference in the phase field evolution between the remeshing and the reference cases can be seen. The number of elements and run time are reported in Table 3.2.

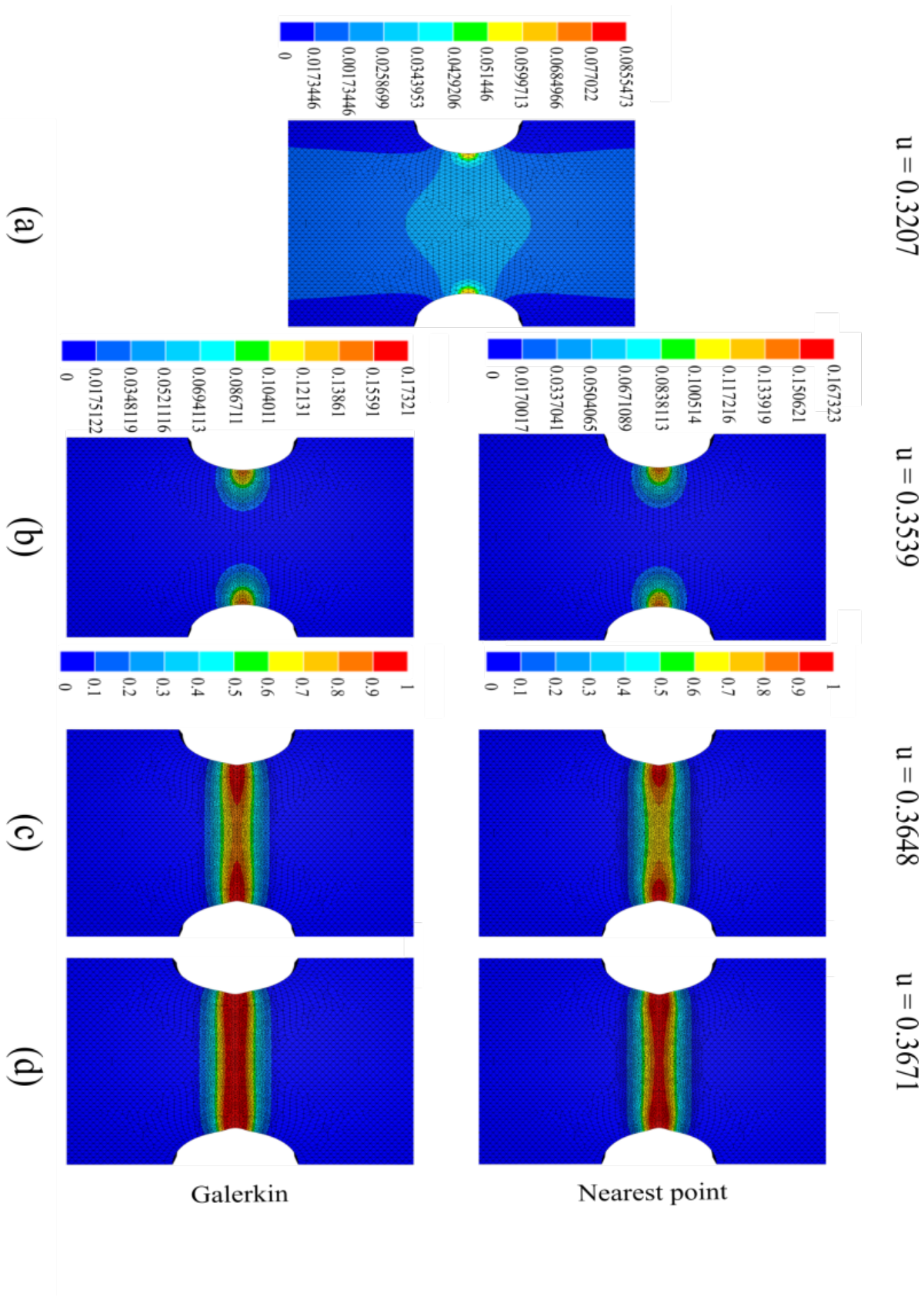


**Fig. 3.6** Evolution of phase field at different displacements where the phase field threshold is set to 0.075 and the average element size of the base mesh is set to 0.5 mm.

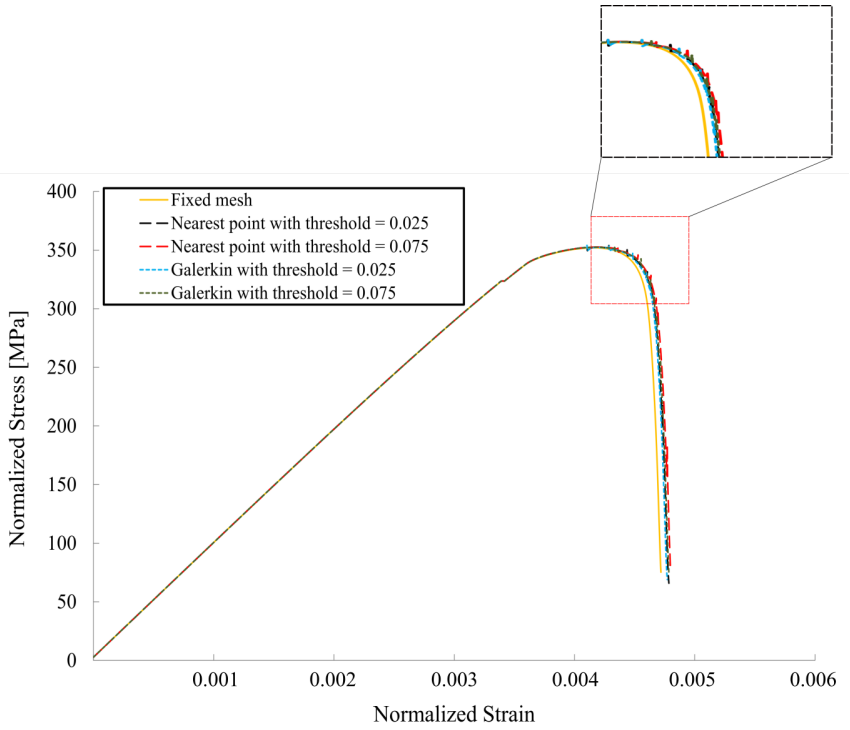


**Fig. 3.7** Normalized Stress vs. Normalized Strain curves for two different values for the phase field threshold. The base element size = 0.5 mm.

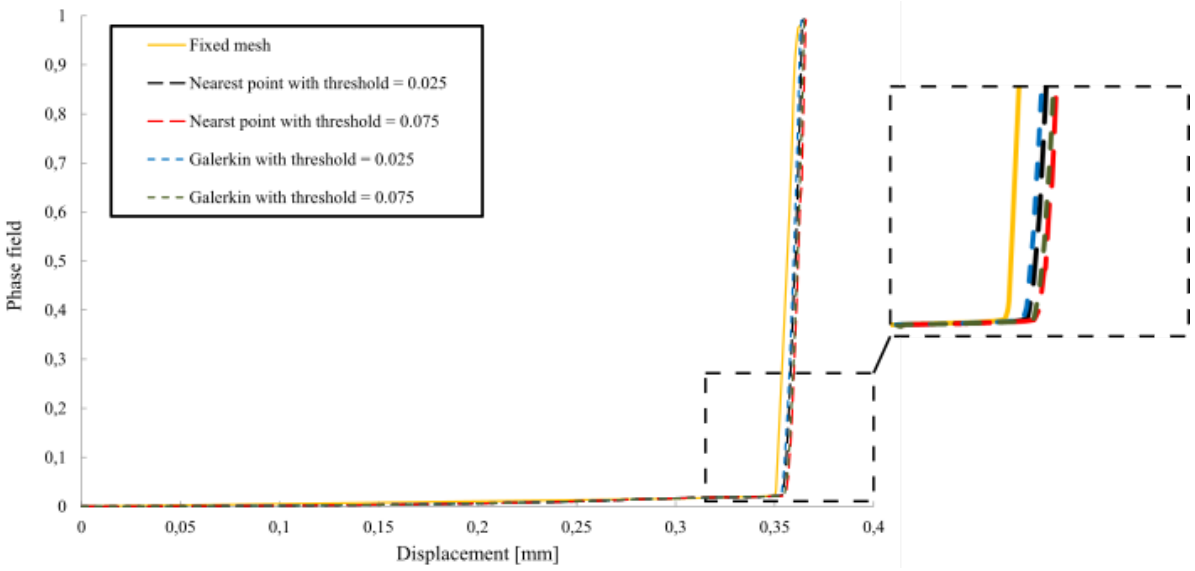


**Fig. 3.8** Comparison between the phase field evolution for a fixed mesh and with remeshing with a base element size = 0.5 mm

The developed adaptive remeshing strategy results in a very accurate prediction of the crack initiation and propagation with a significant reduction in the computation time. It should be noted that the reduction factor in the element size from the beginning to the end of the computations was about 3. The next step is to test the model validity with a higher reduction ratio in order to test the limits of the computational strategy. A base element of size 1.25 mm is used

with a reduction ratio to the final element size of about 7.75. Figs. 3.9 and 3.10 show the phase field evolution profiles for two threshold values of 0.025 and 0.075, respectively.

In a general sense, for both threshold values the crack is initiated at a larger displacement than the cases with a base element size equals to 0.5 mm.

**Table 3.2** Symmetrically notched tension test with base element size = 0.5 mm

| Operator | Threshold | Nb. of remeshing operations | Initial number of elements | Final number of elements | CPU time [h] |
|---|---|---|---|---|---|
| Fixed mesh | | | 112080 | 112080 | 1.09 |
| Galerkin | 0.025 | 6 | 82477 | 125550 | 0.85 |
| Galerkin | 0.075 | 6 | 82477 | 111800 | 0.79 |
| Nearest point | 0.025 | 7 | 82477 | 130800 | 0.77 |
| Nearest point | 0.075 | 6 | 82477 | 117780 | 0.71 |

It can be observed again that displacements starting at the crack initiation until the complete failure are higher when the threshold 0.075 is used. The same conclusion is drawn regarding the two field transfer operators; the crack propagates for a longer distance at the same displacement when the Galerkin smoothing method is used as shown in Figs. 3.9c and 3.10c.

The Normalized Stress vs. Normalized Strain curves are shown in Fig. 3.11. From a global view, there is a noticeable shift between the curves of fixed mesh and remeshing cases as compared to the case with a base element size of 0.5 mm. It can be also observed that when a threshold of 0.025 is used, closer results to the reference solution are obtained. The behavior of the global response can be clearly explained by tracing the local evolution of the phase field as shown in Fig. 3.12 which confirms the same result.

To conclude, a significant decrease in the computation time is possible by using the remeshing strategy. However, the solution accuracy with remeshing is reduced when the reduction ratio in the element size is increased. The results are also improved when the phase field threshold is reduced since the localization of plastic strain is well captured with the small element size, but the computation time is increased. In consequence, the developed computational framework can be adopted to have a good compromise between solution accuracy and computation time. Regarding the field transfer operators, the results show that the data diffusion is very similar for the two cases with a slight improvement observed when the Galerkin smoothing method is used.

The initial and final number of elements along with the CPU run time are reported in Table 3.3. It can be clearly seen that the initial and final number of elements are less than the case with a base element size of 0.5 mm, i.e., the computation time has drastically been reduced by a factor of nearly 4 in average. It can also be observed that the number of elements in the end of

simulations is even lower than the reference case since it is difficult to know where exactly the refinement should take place so we tend to enlarge the region when the size of the refinement zone is controlled by the user.

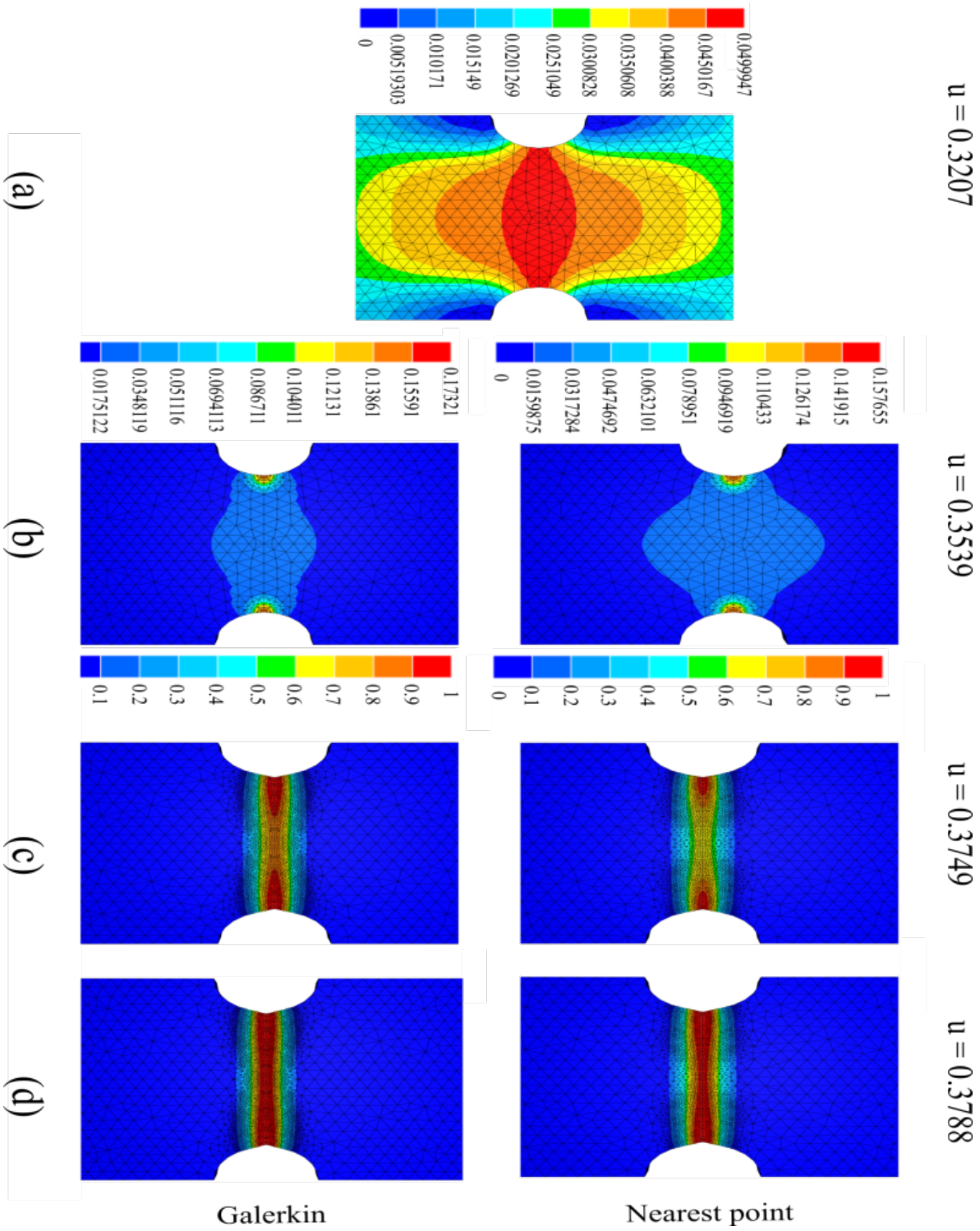


**Fig. 3.9** Evolution of phase field at different displacements where the phase field threshold is set to 0.025. The average element size of the base mesh is set to 1.25 mm.

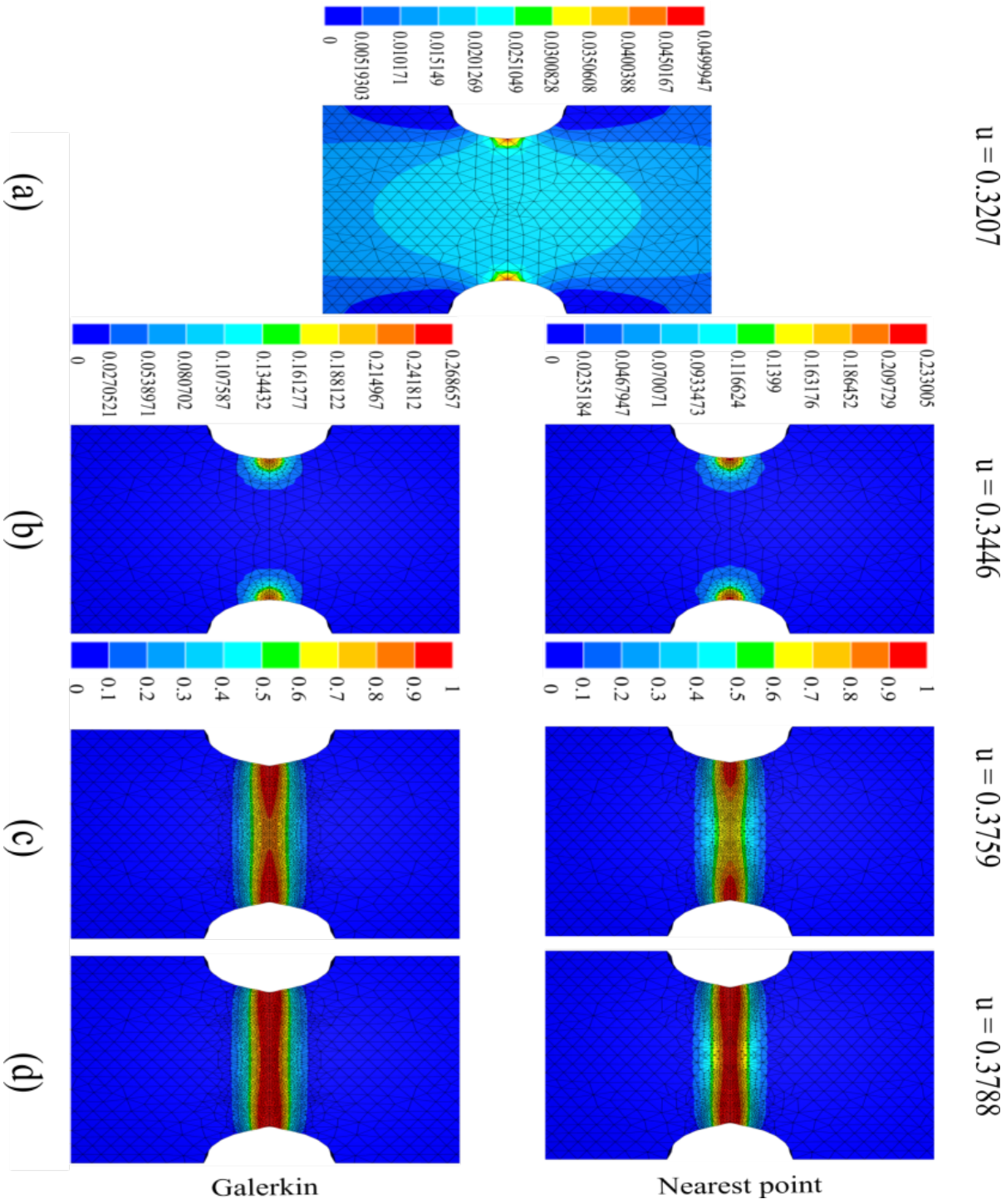


**Fig. 3.10** Evolution of phase field at different displacements where the phase field threshold is set to 0.075. The average element size of the base mesh is set to 1.25 mm.

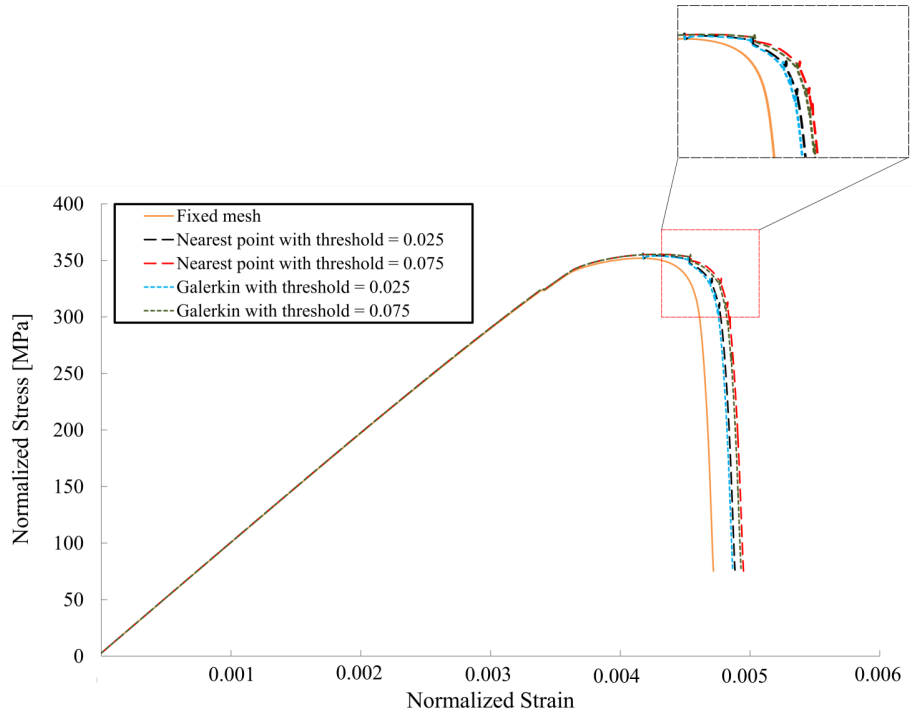


**Fig. 3.11** Normalized Stress vs. Normalized Strain curves for two different values of the phase field threshold. The average element size of the base mesh is set to 1.25 mm.

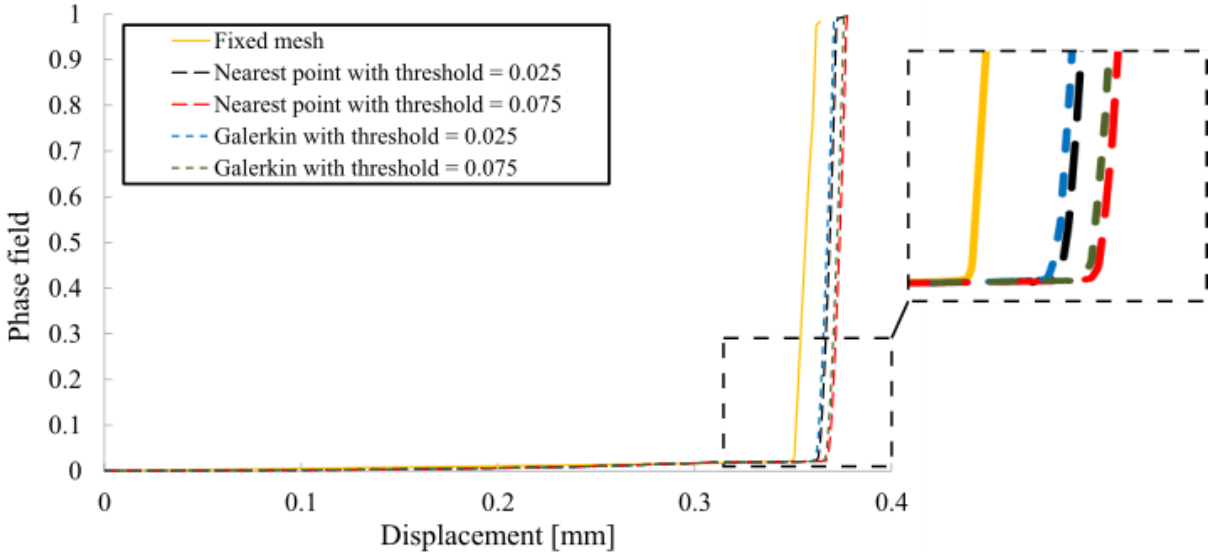


**Fig. 3.12** Comparison between the phase field evolution for a fixed mesh and with remeshing with a base element size = 1.25 mm.

**Table 3.3** Symmetrically notched tension test with base element size = 1.25 mm.

| Operator | Threshold | Nb. of remeshing operations | Initial number of elements | Final number of elements | CPU time [h] |
|---|---|---|---|---|---|
| Fixed mesh | | | 52278 | 52278 | 0.57 |
| Galerkin | 0.025 | 7 | 7023 | 43688 | 0.15 |
| Galerkin | 0.075 | 5 | 7023 | 34618 | 0.14 |
| Nearest point | 0.025 | 4 | 7023 | 38326 | 0.15 |
| Nearest point | 0.075 | 4 | 7023 | 26119 | 0.11 |

In the following numerical example, the Galerkin smoothing method is adopted for all cases.

## 3.5.2 Double notched specimen

In this example, a double notched thin specimen is used to prove the ability of the developed algorithm to deal with complex crack paths efficiently. The geometry and boundary conditions of the specimen are shown in Fig. 3.13 [86] along with the mesh size distribution. The thickness of the specimen is chosen to be 0.2 mm so the problem can be considered as a plane stress case. A quasi static loading is assumed, i.e., inertial effects are neglected. The material properties and model parameters are listed in Table 3.4. The loading velocity is set to 0.05 mm/s. The time step is set to 0.01 s in the first 200 steps since the level of the damage is still low and 0.002 s for the rest of simulations in order to properly track the crack evolution.

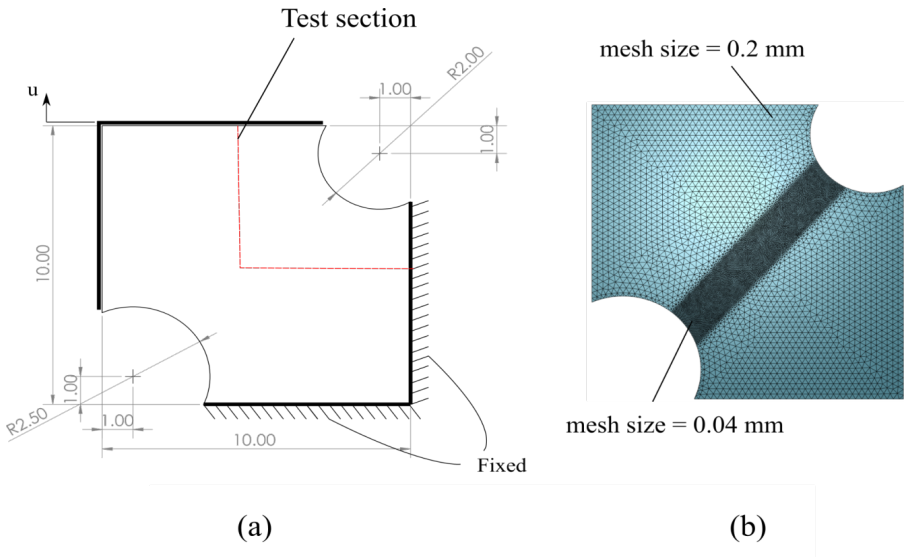


**Fig. 3.13** (a). Geometry and boundary conditions of a double notched specimen. (b). The mesh size of the reference case without remeshing. The thickness of the specimen is 0.2 mm. All dimensions are in mm.

**Table 3.4** Material and model parameters

| Quantity | Value | Unit |
|---|---|---|
| Young's modulus, $E$ | 180 | GPa |
| Poisson's ratio, $\nu$ | 0.28 | |
| Yield stress, $\boldsymbol{\sigma}_y$ | $\sigma_0 + H\bar{\varepsilon}$ | MPa |
| $\sigma_0$ | 443 | MPa |
| $H$ | 300 | MPa |
| $\beta_1$, $\beta_2$ | 1 | |
| $l_c$ | 0.08 | mm |
| $G_c$ | 20 | MPa mm |
| $W_0$ | 80 | MPa |

Fig. 3.14 shows the phase field evolution for a base element size of 0.2 mm where the phase field threshold is chosen to be 0.06.

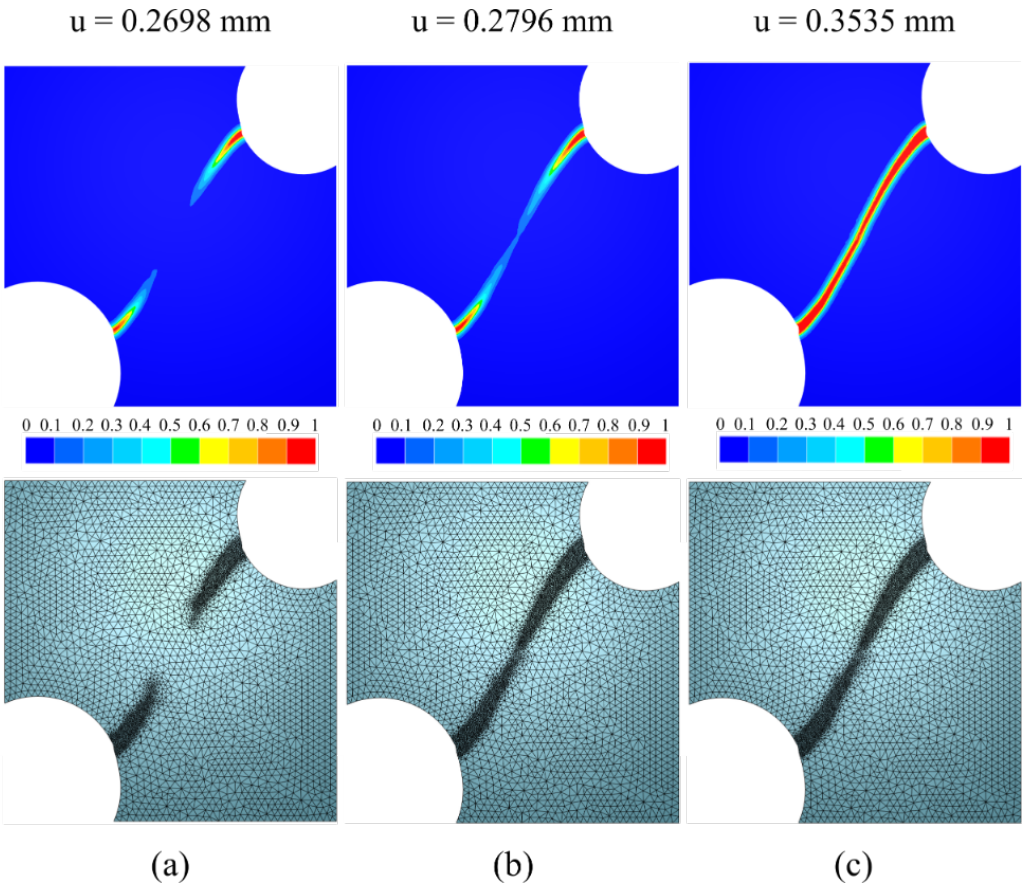


**Fig. 3.14** Phase field evolution at various deformation stages on the deformed configuration for a fine mesh with base element size 0.2 mm. The phase field is used to trigger the remeshing with a threshold of 0.06.

It should be noted that the choice of the numerical parameter $\eta_v$ that is defined in equation

3.7 is tailored manually in all the following examples in order to obtain a similar number of remeshing operations i.e., the effect of data diffusion due to remeshing is eliminated. It can be shown that two cracks are initiated at the two notches which is the same observation as the reference case with a fixed mesh (the reference case is considered as the most accurate). Then, the two crack branches propagate toward the center until merging and leading to the final failure. It can also be observed that the evolution of the refined zone in the mesh follows the phase field evolution starting from the crack initiation until the complete failure.

Fig. 3.15 shows the evolution of the crack and mesh size distribution with a base element size of 0.15 mm. The obtained cracking sequence is very similar to the case of a 0.2 mm mesh. However, the specimen is completely fractured at a lower displacement value as compared to the case of a 0.2 mm mesh size. The Force vs. Displacement curve for two base element sizes of 0.2 mm and 0.15 mm with a phase field threshold of 0.06 are shown in Fig. 3.18.

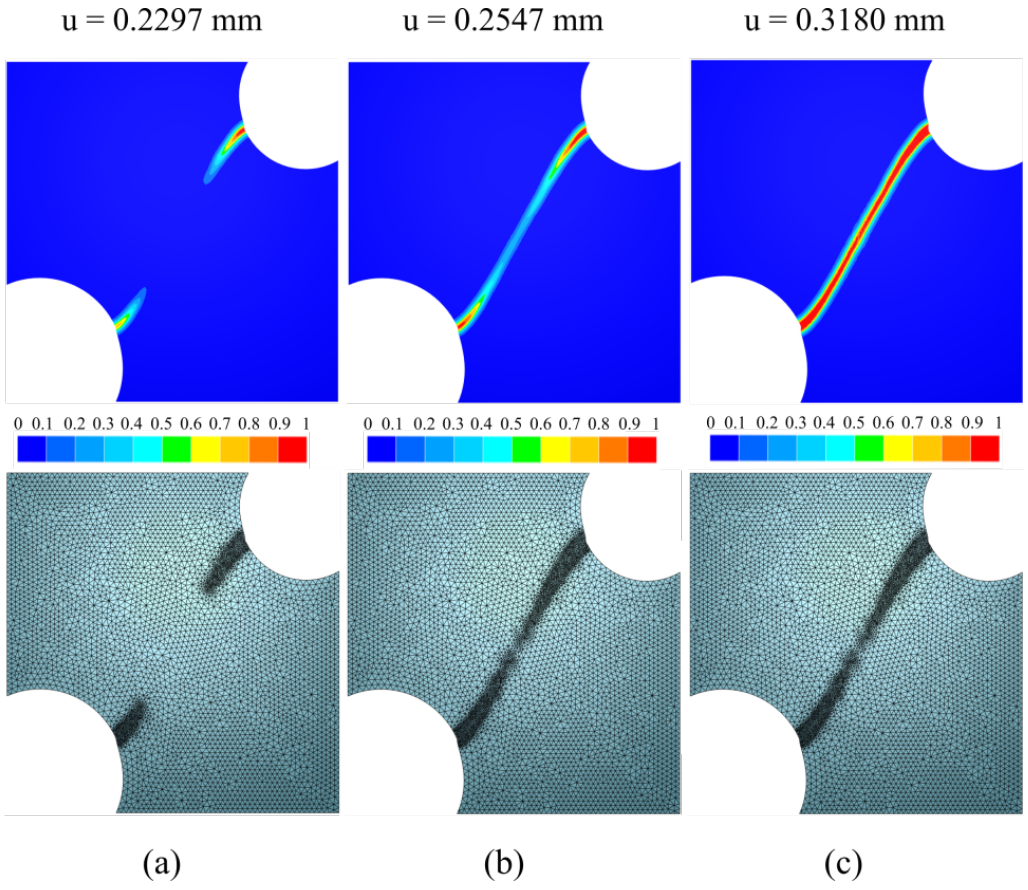


**Fig. 3.15** Phase field evolution at various deformation stages on the deformed configuration with base element size 0.15 mm. The phase field is used to trigger the remeshing with a threshold of 0.06.

A significant shift between the adaptive remeshing results and the fixed mesh result is observed for the two mesh sizes. The explanation here is that the mesh in the damaged region will be only refined once the plastic energy exceeds the threshold $W_0$ when the phase field evolution is initiated. This is due to the dominant contribution of plastic deformation in the crack

evolution. Hence, the mechanical equations are solved on a relatively coarse mesh which led to inaccurate computation of the equivalent plastic strain.

In order to improve the results, new remeshing indicator functions that are related to the evolution of plastic strain are tested in this example. Fig. 3.16 shows the evolution of the phase field and the mesh size distribution where the equivalent platic strain is used as an indicator for the mesh refinement. A threshold value equals to 0.06 with an initial element size is 0.2 mm are used in this example. It can be observed that remeshing is initiated at an early stage in which the zone where the crack is expected to propagate is fully refined before the crack initiation, i.e., the maximum value of the phase field is not yet equal to 1. It can be also observed that the refined zone is wider than the cases where the phase field is used as an indicator function. This observation is confirmed with the difference between the initial and final number of elements which is reported in Table 3.5 when compared to the case where a phase field remeshing indicator function is used with the same initial element size. The Force vs. Displacement curves for two different threshold values of 0.06 and 0.001 are shown in Fig. 3.18. It can be confirmed that the results are closer to the reference case than the previous choice of the phase field as an indicator to the refinement especially when the small threshold of 0.001 is used. However, it can be observed that there is still a delay in the softening and fracture compared to the reference case with a fixed mesh.

The normalized yielding function NYF defined in equation 3.9 is used as another remeshing indicator function.

$$\text{NYF} = \frac{f_p^{trial}}{\bar{\boldsymbol{\sigma}}} \tag{3.9}$$

where $f_p^{trial}$ is the trial yield function. The aim of this choice is that the refinement process becomes more predictive since all the elements that are expected to develop the plastic deformation are refined a priori. This confirms that all the plastic strain increments are calculated on a sufficiently refined mesh. The other advantage of this function is that, the elements far from the crack zone are coarsened once the crack is initiated since the stress far from the crack lips (damaged region) is degraded due to the creation of the crack surface as shown in Fig 3.17. It can be shown in Fig. 3.18 that the Force vs. Displacement curve of the NYF function is very close to the reference case solution.

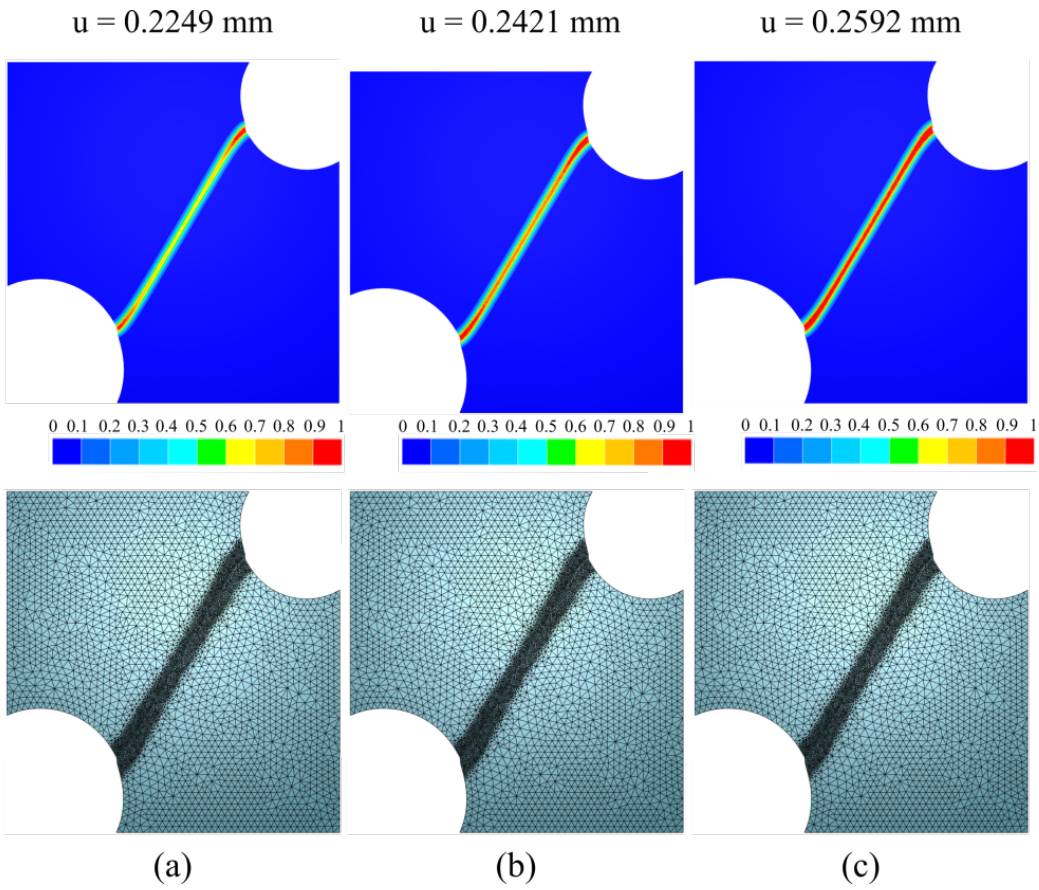


**Fig. 3.16** Phase field evolution at various deformation stages on the deformed configuration with base element size 0.2 mm. The equivalent plastic strain is used to trigger the remeshing with a threshold of 0.06.

Fig. 3.19 shows the evolution of the equivalent plastic strain at two different displacements where three remeshing indicator functions are used: phase field, equivalent plastic strain and normalized yielding functions. It can be observed that the error of the equivalent plastic strain with respect to the reference case is reduced when either the equivalent plastic strain or the NYF indicator functions are used. This can be related to the fact that when the mesh size is reduced earlier, more accurate calculation of the equivalent plastic strain is obtained since the strain localization is properly captured; hence the phase field evolution becomes more accurate.

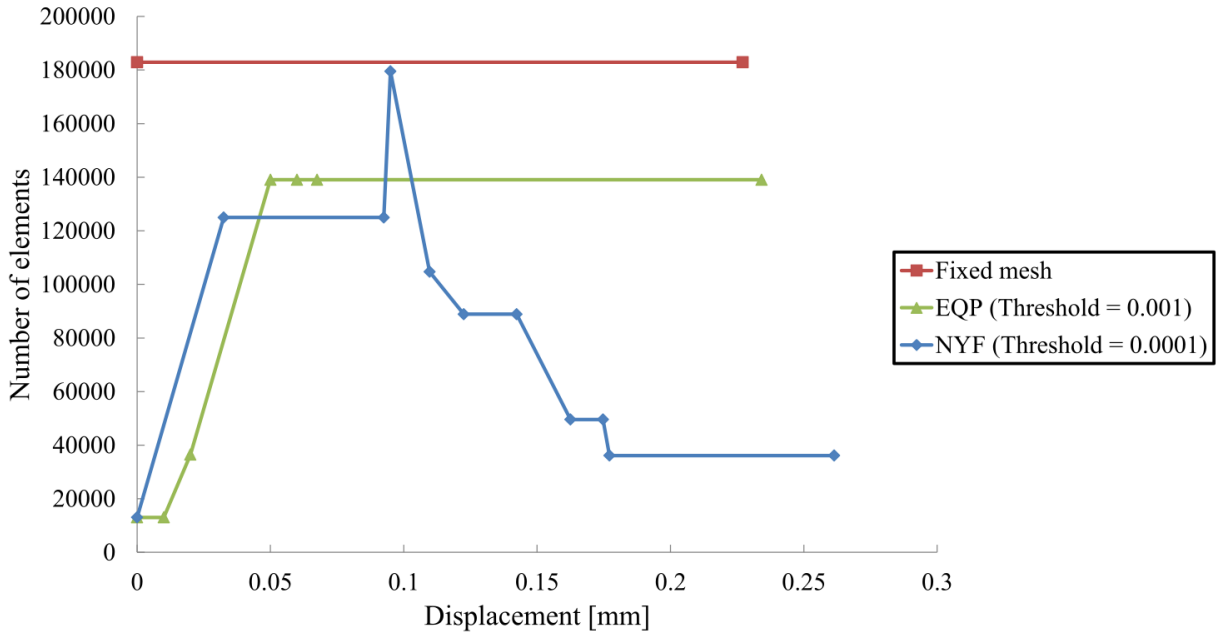


**Fig. 3.17** Evolution of number of elements for different remeshing cases along with the reference case (Fixed mesh).

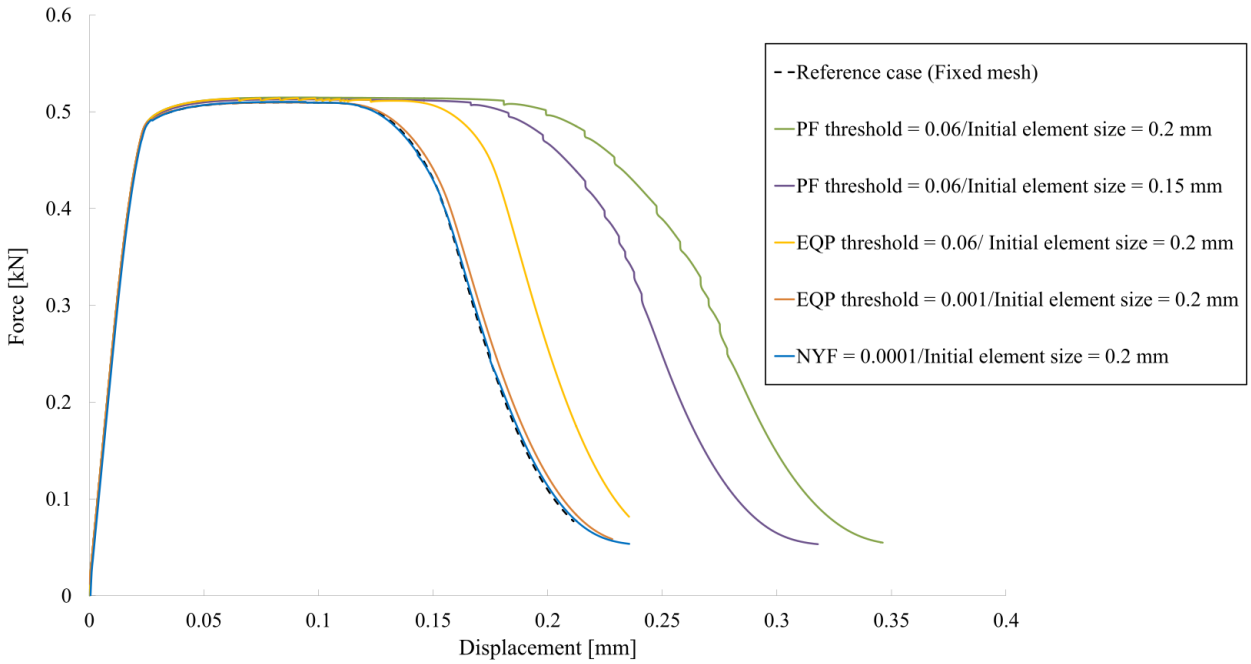


**Fig. 3.18** Force vs. Displacement curves for different remeshing cases along with the reference case (Fixed mesh). NYF is the normalized trial yield function.

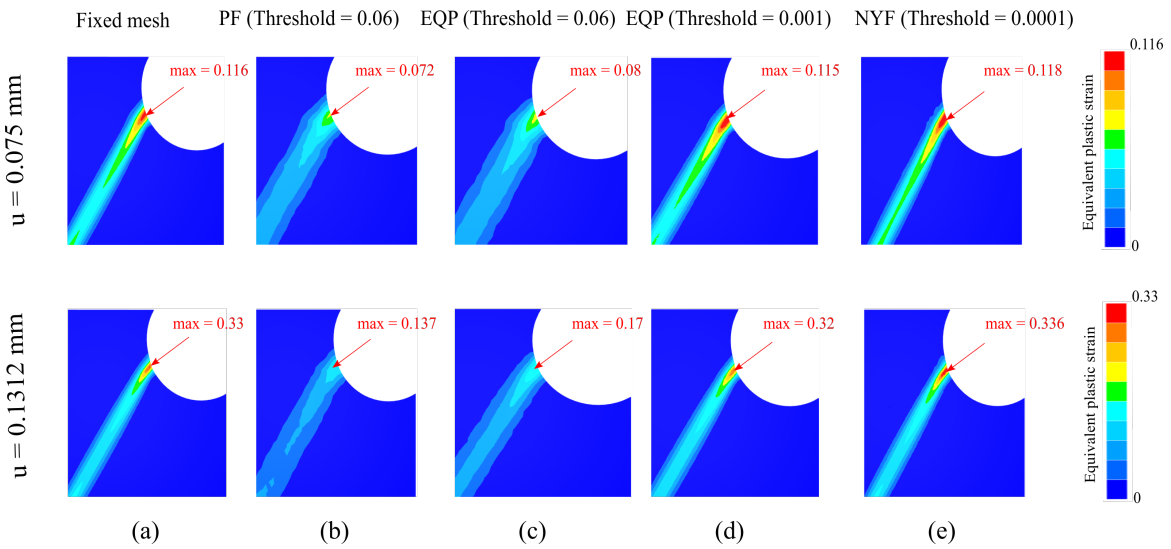


**Fig. 3.19** Evolution of equivalent plastic strain at two different displacements. Comparison is carried out between the reference case with no remeshing, remeshing with phase field (PF) threshold, two equivalent plastic strain thresholds (EQP) and normalized yielding function (NYF).

Table 3.5 shows the performance analysis for different cases along with the fixed mesh case. It can be seen that a reduction of the equivalent plastic strain threshold to 0.001 leads to results very close to the reference case with a fixed mesh at a computational cost reduced by about 12%. In addition, when the normalized yielding function is used, the computation time is reduced by 59 % while the results are very close to the reference case with a fixed mesh. In addition, an energy error is found in the same table for each threshold type. The energy error is calculated as follows

$$\text{Energy error } \% = \frac{\int_0^{r_{max}} (F_{remesh} - F_{ref})\, dr}{\int_0^{r_{max}} F_{ref}\, dr} \tag{3.10}$$

where $F_{remesh}$ is the force obtained with remeshing, $F_{ref}$ is the force obtained from the reference case with a fixed mesh, $r$ is the displacement and $r_{max}$ is the maximum displacement. The energy error helps in quantifying the energy loss for each method. It can be seen that the normalized yielding function gives the lowest possible energy loss among the others which proves its accuracy.

The proposed adaptive remeshing strategy provides a flexible compromise between accuracy and computational cost. Depending on the application, the choice of refinement indicator function can be related to either the phase field or the equivalent plastic strain. When the normalized yielding function is used, the obtained results are very close to the reference case with a significant reduction in the computation time. It should be also noted that the main inconvenience in the presented strategy is the choice of the refinement threshold and especially for the NYF which is not straight forward and depends on the type of problem. If the value of the NYF threshold is not well chosen, this might lead to an over estimation of the size of the refined

zone.

**Table 3.5** Double notched specimen performance analysis

| Threshold $\eta_v$ | Value | Initial size [mm] | Initial nb. of elements | Final nb. of elements | CPU time [h] | Energy error % |
|---|---|---|---|---|---|---|
| Fixed mesh | | | 182900 | 182900 | 2.25 | |
| PF 1 | 0.06 | 0.15 | 23663 | 48193 | 0.8 | 50.7 |
| PF 0.8 | 0.06 | 0.2 | 13046 | 41904 | 0.7 | 54.86 |
| EQP 0.8 | 0.06 | 0.2 | 13046 | 70677 | 1.05 | 20 |
| EQP 0.8 | 0.001 | 0.2 | 13046 | 148300 | 1.97 | 4.9 |
| NYF 1.2 | 0.0001 | 0.2 | 13046 | 36113 | 0.93 | 2.7 |

## 3.6 Summary of chapter 3

The main objective of this chapter is to develop an adaptive remeshing strategy coupled with the phase field model. The proposed strategy offers a robust tool for predicting initiation and propagation of complex crack path in highly ductile materials. This chapter analyzed both qualitatively and quantitatively two applications with different levels of complexity: a straight crack path between two notches having the same sizes and a diagonal crack formed in a non symmetric notched specimen. In both cases, it is evident that the developed strategy offers a good compromise between computational cost and accuracy of the results.

Two different field transfer operators are used in order to efficiently remap the mechanical fields: (i). the nearest point interpolation; (ii). the Galerkin smoothing method. The former is considered as the simplest approach since a direct interpolation is done for each integration point, however its accuracy is dependent on the size of mesh and the gradient of remapped field. While the latter is more computationally expensive since a smoothing step is needed to transform the P0 field to a P1 field, but it gives a relatively better accuracy according to the numerical results presented in this work.

In order to minimize the numerical diffusion during the transfer process, two different metrics are introduced in the algorithm: (i). a remeshing indicator function that is used to identify the regions where the mesh should be refined; (ii). a volume quality metric that stops the remeshing operations once the zone of interest is sufficiently refined so that the numerical diffusion is minimized.

A comparison is carried out between the results when the indicator function is based on the phase field or another criterion based on the equivalent plastic strain. Results have shown that in some cases where the contribution of the plastic strain in the phase field evolution is

delayed, the mesh in the damaged region will not be refined at an early stage; the evolution of the plastic strain will not be accurate. This results in a bad resolution of the phase field which leads to inaccuracy in predicting the crack initiation and propagation. On the other hand, when the equivalent plastic strain is used to trigger the remeshing, the mesh will be refined earlier so the evolution of the plastic strain will be accurately captured. The main disadvantage with the choice of the equivalent plastic strain is that the refined region becomes wider with higher number of elements in the beginning since the crack is not yet localized; the computation time is increased. In order to reduce the size of the refined zone once the crack is initiated, a third criterion based on the yielding function is introduced. The main advantage of this proposition is the ability to coarsen the elements far from the highly damaged zone once the crack is initiated since they do not develop further plastic strains. However, the choice of the remeshing triggering threshold becomes difficult for a general type of application. In consequence, the industrial use of this third criterion might not be preferred.

## 3.7 Résumé en français

L'objectif principal de ce chapitre est de développer une stratégie de remaillage adaptatif couplée au modèle de champ de phase "Phase field". La stratégie proposée offre un outil robuste pour prédire l'amorçage et la propagation des chemins complexes de fissure dans les matériaux ductiles. Ce chapitre a commencé par l'analyse qualitative et quantitative de deux cas test avec des niveaux de complexité différents: un chemin de fissure rectiligne entre deux entailles ayant les mêmes tailles et une fissure diagonale formée dans une éprouvette entaillée non symétrique. Dans les deux cas, il est évident que la stratégie développée offre un bon compromis entre coût de calcul et précision des résultats.

Deux opérateurs de transfert de champ sont utilisés afin de transporter efficacement les champs mécaniques : (i). l'interpolation du point le plus proche "Intérpolation par parachutage"; (ii). la méthode de lissage Galerkin. La première est considérée comme l'approche la plus simple puisqu'une interpolation directe est effectuée pour chaque point d'intégration, cependant sa précision dépend de la taille de maille et du gradient du champ à transporter. Alors que la seconde approache est plus coûteuse en calcul car une étape de lissage est nécessaire pour transformer le champ P0 en un champ P1, mais elle donne une précision relativement meilleure selon les résultats numériques présentés dans ce travail.

Afin de minimiser la diffusion numérique pendant le processus de transfert, deux métriques différentes sont introduites dans l'algorithme: (i). une fonction indicateur de remaillage qui permet d'identifier les régions où le maillage doit être affiné; (ii). une métrique de qualité volumique qui arrête les opérations de remaillage une fois que la zone d'intérêt est suffisamment affinée pour que la diffusion numérique soit minimisée.

Une comparaison est effectuée entre les résultats lorsque la fonction indicatrice est basée sur le champ de phase ou un autre critère basé sur les déformations plastiques équivalentes. Les

résultats ont montré que dans certains cas où la contribution de la déformation plastique dans l'évolution du champ de phase est retardée, le maillage dans la région endommagée ne sera pas raffiné à un stade précoce ce qui rend l'évolution de la déformation plastique imprécise. Il en résulte une mauvaise résolution du champ de phase qui conduit à une prédiction précise de l'amorçage et de la propagation des fissures. En revanche, lorsque la déformation plastique équivalente est utilisée pour déclencher le remaillage, le maillage sera affiné plus tôt afin que l'évolution de la déformation plastique soit capturée avec précision. Le principal inconvénient avec le choix de la déformation plastique équivalente est que la région raffinée devient plus large avec un nombre d'éléments plus élevé au départ puisque la fissure n'est pas encore localisée ce qui va augmenter le temps de calcul.

Afin de réduire la taille de la zone affinée une fois la fissure amorçée, un troisième critère basé sur la fonction d'écoulement est introduit. Le principal avantage de cette proposition est la possibilité de déraffiner le maillage loin de la zone fortement endommagée une fois la fissure amorçée car ils ne développent plus de déformation plastique. Cependant, le choix du seuil de déclenchement du remaillage devient difficile pour un type d'application général ce qui rend cette méthode difficile pour une utilisation industrielle.

# Crack insertion and propagation algorithm

## Contents



*This chapter is an extended version of the following published paper:*

**H. Eldahshan, J. Alves, P.-O. Bouchard, E. Perchat, D. P. Munoz, "CIPFAR: A 3D unified numerical framework for the modeling of ductile fracture based on the phase field model and adaptive remeshing", Computer Methods in Applied Mechanics and Engineering 387 (2021), 114171.**

## 4.1 Introduction

In this chapter, a crack initiation and propagation strategy is applied on 3D meshes using automatic remeshing. The choice of this technique among others is preferred for many reasons: (i). the volume and energy are conserved throughout the simulation which resolves the issues encountered with the element deletion technique (it should be noted that there is always an amount of energy loss associated with the field transfer operations that cannot be avoided); (ii). the crack path is independent on the mesh size given that the mesh size is sufficient for the mechanical resolution; (iii). the automatic remeshing toolbox in **FORGE ®** is used to ensure the good quality of elements through the ductile fracture simulation.

The main steps of the crack initiation and propagation algorithm using the phase field model and adaptive remeshing (CIPFAR) are illustrated in Fig. 4.1. First, the phase field is computed using the adaptive remeshing strategy described in chapter 3. Then, the intersection of the crack surface with the mesh edges is identified as the local maxima of the phase field function. Following that, new nodes are inserted in the identified locations and all the elements intersected by the crack are repartitioned by local remeshing operations in order to fit the crack topology within the mesh. Finally, the nodes that lie on the crack surface are duplicated in order to open the new crack surfaces while a subsequent remeshing operation is carried out in order to keep the good quality of elements throughout the simulation. In the next sections, all the algorithmic steps are discussed in details.

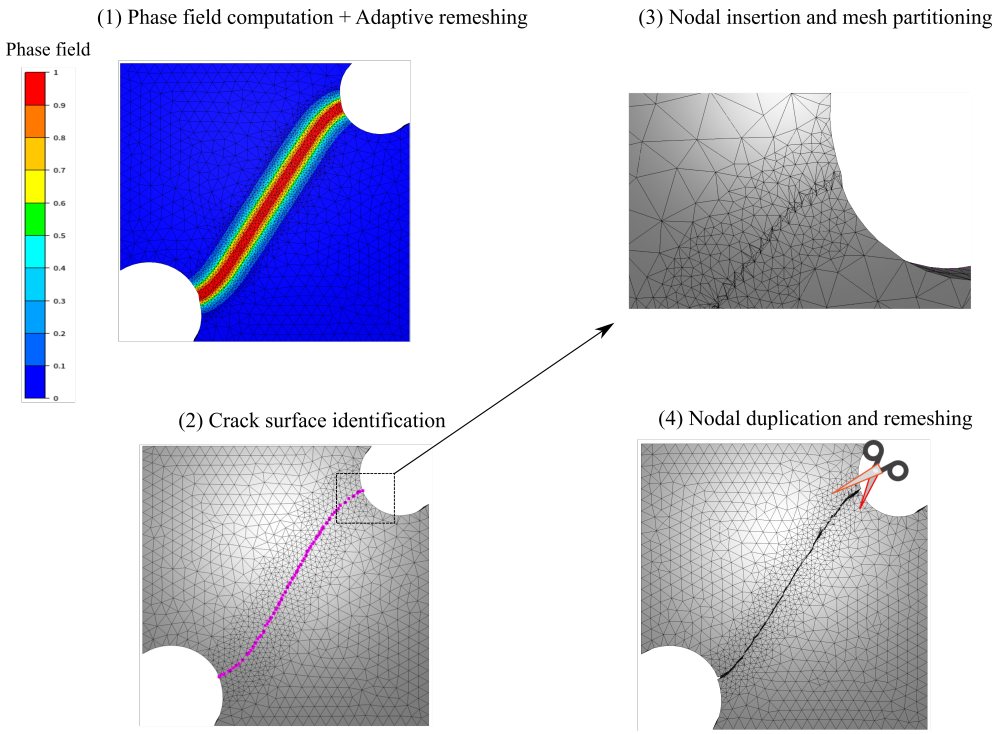


**Fig. 4.1** A summary of the main steps of crack initiation and propagation algorithm.

## 4.2 Discrete crack initiation

In order to conserve the energy release rate during the fracture process, a new crack increment is inserted only if all the material points are totally damaged, i.e., the phase field value becomes close to 1 (the maximum value is taken as 0.99 for the practical implementation). An infinitesimal crack area increment $dA$ can be calculated as follows [136]

$$dA = l_f \, da = \frac{d\psi_{frac}}{G_c} \tag{4.1}$$

where $l_f$ is the length of the crack front and $da$ is the crack increment length as shown in Fig. 4.2, $\psi_{frac}$ is the fracture energy which is defined in the regularized form as follows:

$$\psi_{frac}^{reg} = \int_\Omega \frac{G_c}{2l_c}(d^2 + l_c^2|\nabla d^2)| \, d\Omega. \tag{4.2}$$

The effective crack area increment can be then calculated as

$$\Delta A^{eff} = \frac{\psi_{n+1}^{reg} - \psi_n^{reg}}{G_c} \tag{4.3}$$

where the total effective crack area at increment $n+1$ can be calculated as

$$A_{n+1}^{eff} = A_n^{eff} + \Delta A^{eff}. \tag{4.4}$$

The condition at which a crack increment is inserted is defined as follows:

$$A_{n+1}^{eff} \geq A_{fixed} \tag{4.5}$$

where $A_{fixed}$ is a predefined parameter used to control the moment at which a crack increment is inserted.

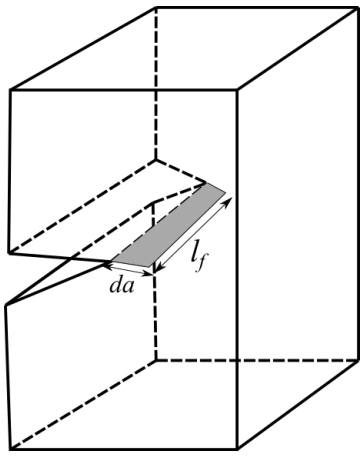


**Fig. 4.2** Illustration of the surface topology of a crack increment.

## 4.3 Crack surface identification

The phase field solution provides a highly concentrated damage field in which the crack surface can be identified as the points that have a phase field value of 1. However, due to the numerical approximation, the continuity condition of the phase field gradient [1] leads to a diffused zone of the crack, i.e., there is a finite zone that has a phase field value very close to 1 as can be seen in Fig. 4.3. In this work, we propose a strategy that is based on the phase field gradient in order to identify the crack surface by combining the phase field solution along with its gradient. The idea of our algorithm is to simplify the crack surface identification methodology for two main reasons: (i). the search process must be independent on the choice of model parameters such as the radius of the evaluation circle as presented in [91]; (ii). the algorithm should be independent on the starting point, in other words, an agnostic search of identifying the crack surfaces which allows to track multiple cracks propagation simultaneously.

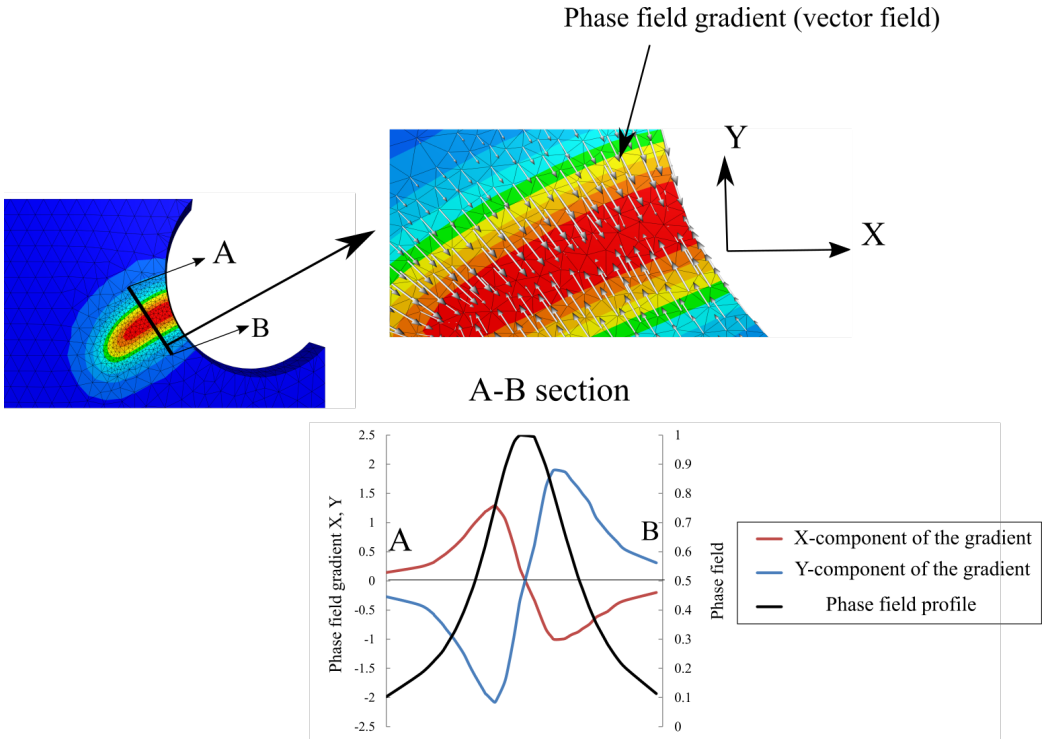


**Fig. 4.3** Phase field computation on a finite element mesh. The vector field of the phase field gradient is shown (top). The phase field along with the gradient components profiles projected on the X-Y plane are computed (bottom).

Starting with the continuous phase field $d$, a point is identified to lie on the crack surface if it satisfies the following two conditions:

$$\boldsymbol{V}^t \nabla d = 0 \tag{4.6a}$$

[1] The continuity of the phase field solution and its gradient within the elements are imposed in the weak formulation of the problem). However, the solution of the homogeneous differential equation of the phase field shows that the gradient is undefined at the crack interface.

$$\boldsymbol{V}^t Hess(d)\boldsymbol{V} = 0 \tag{4.6b}$$

where $\boldsymbol{V}$ is a $n \times k$ matrix in which $n$ is the dimension of the space and $k$ is the number of linearly independent vectors that span the search space. The second condition is automatically satisfied since the search process is limited in the region where the phase field is very close to 1 which is convex by definition. In consequence, the satisfaction of condition 4.6a requires at least the $C^1$ continuity of the phase field solution. This critical point represents a (n-1)-dimensional height ridge in a n-dimensional space according to the definition of Eberly et al. in [137]. In other words, the search space is restricted to a subspace spanned by a the unit vector connecting the edge nodes.

The crack surface identification algorithm can be explained in three main steps: (i). smoothing the phase field gradient on all the mesh nodes; (ii). calculating the projection of the phase field gradient along the vector connecting the two nodes (along the edge direction); (iii). identifying the location on the edge at which the gradient projection along the edge is vanished. The selection of an edge to be tested should satisfy a condition of having a value of phase field greater than a given threshold very close to 1 (normally the threshold is chosen to be 0.99) for at least one of its two nodes as shown in Fig. 4.4. The search direction is chosen to be the unit vector that is aligned along an edge in the mesh. The projection of the phase field gradient is calculated as follows:

$$\nabla d_{i,j}^{proj} = \nabla d_{i,j}^{nodal} \cdot \vec{\boldsymbol{r}} \tag{4.7}$$

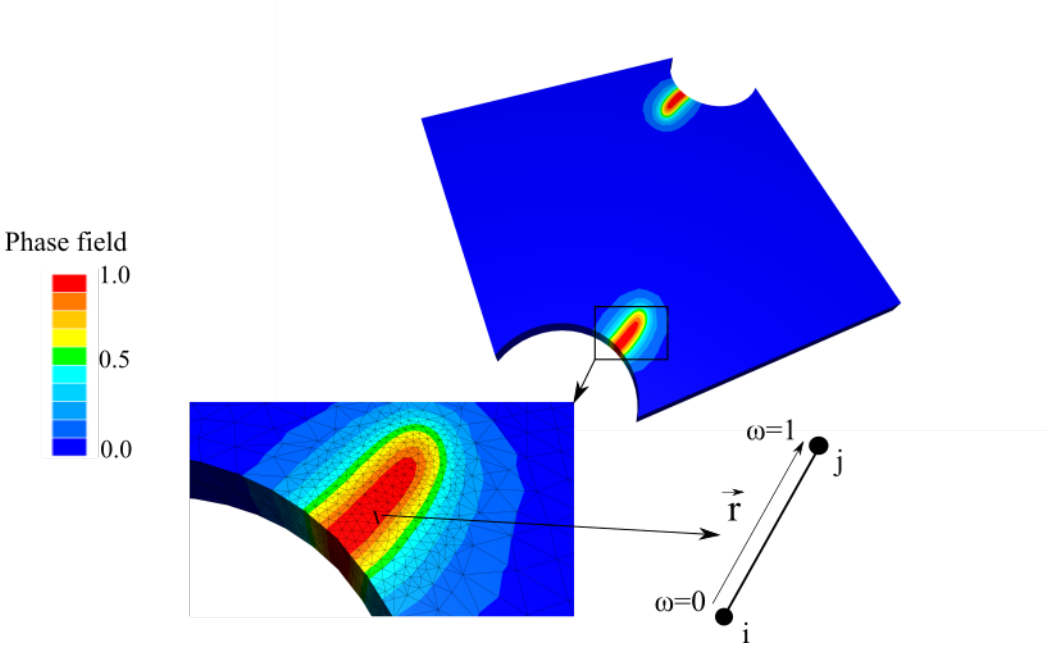


**Fig. 4.4** Selection of the candidate edges for the crack intersection.

where $i$ and $j$ are the node index, $\nabla d_{i,j}^{nodal}$ is the phase field gradient calculated at the nodes $i, j$, $\nabla d_{i,j}^{proj}$ is the projection of the phase field calculated at nodes $i, j$ and $\vec{\boldsymbol{r}}$ is the position unit

vector as shown in Fig. 4.4. A linear interpolation in terms of the non-dimensional parameter $\omega_c$ is given as:

$$\nabla d_i^{proj} + \omega_c \left(\nabla d_j^{proj} - \nabla d_i^{proj}\right) = 0 \tag{4.8}$$

where $\omega_c$ is a non-dimensional distance of the critical point calculated along the edge length. Solving equation 4.8 for $\omega_c$ with the condition that $0 < \omega_c < 1$ gives the intersection of the crack surface with the edge. Another condition is added to ensure that the material point at the selected $\omega_c$ has reached a maximum level of degradation as follows:

$$d_i^{nodal} + \omega_c \left(d_j^{nodal} - d_i^{nodal}\right) \geq 0.99. \tag{4.9}$$

In the next section, the smoothing operation that transforms the phase field gradient from a P0 (constant per element) to a P1 (nodal) field is presented.

## 4.3.1 Phase field gradient smoothness

In this section, a smoothing operation of the phase field gradient from a P0 field (which is constant per element) to a nodal P1 field is achieved. The gradient calculation represents an important part in the crack insertion algorithm as it is the essential component in the identification of the crack surface intersection with the mesh. The aim is to reduce the numerical error during the smoothing of fields in order to have a good resolution of the phase field gradient. Different smoothing methods can be found in the literature [132, 133] where two of them are explained here for the sake of demonstration: (i). average smoothing method; (ii). Galerkin's smoothing method.

### 4.3.1.1 Average smoothing method

This is the simplest method of a P0 field smoothing. The nodal phase field gradient $\nabla d_i^{nodal}$ is calculated as

$$\nabla d_i^{nodal} = \frac{\sum_{k=1}^{N_{ep}} V_{elem}^k \nabla d_k^{elem}}{V_{patch}} \tag{4.10}$$

where $\nabla d_k^{elem}$ is the phase field gradient calculated per element, $V_{elem}^k$ is the volume of the element $k$ and $V_{patch}$ is the total volume of the patch.

### 4.3.1.2 Galerkin's smoothing method

The weak form of the transformation of the phase field gradient from a P0 field to a P1 field (nodal) applied over an element gives

$$\int_\Omega \vec{\phi}_h \nabla d^{nodal}\, d\Omega = \int_\Omega \vec{\phi}_h \nabla d^{elem}\, d\Omega \tag{4.11}$$

The functions $\nabla d^{nodal}$ and $\vec{\phi}_h$ are defined as follows

$$\vec{\phi}_h(\mathrm{x}) = \sum_{k=1}^{N_n} N_k(\mathrm{x}) c_k \tag{4.12a}$$

$$\nabla d^{nodal}(\mathrm{x}) = \sum_{k=1}^{N_n} N_k(\mathrm{x})\, d_k \tag{4.12b}$$

where $\vec{\phi}_h$ are the test functions, $c_k$ and $d_k$ are the degrees of freedom of the test and trial functions, respectively. $N_k$ are the same basis functions used in the finite element model and $N_n$ is the number of basis functions.

It can be imagined that the average smoothing method is more computationally efficient than the Galerkin's method. This can be explained by the fact that the method is based of performing local computations. On the other hand, a system of linear equations should be solved for all degrees of freedom at each time step in the Galerkin's method.

In the current work, the average smoothing method will be adopted for all numerical examples for the sake of demonstration. A future exploration showing the effect of the gradient smoothing operator on the crack path detection is important. In this case, more advanced techniques can be tested and the results should be analyzed in terms of accuracy and computational efficiency.

## 4.4 Crack insertion into the mesh

### 4.4.1 A sequence agnostic partitioning strategy

First, the mesh is modified in order to insert new nodes at the identified locations of the crack surface intersection. A local partitioning strategy is used in order to fit the identified crack surface within the mesh topology, i.e., new nodes are added in the locations of the intersection between the crack surfaces and the mesh. The general sequence of partitioning operations that are carried out is explained in Fig. 4.5 as follows:

(i). the intersected non-partitioned element can be partitioned into four sub elements connected by a volume node where edge nodes are inserted at the positions of the crack intersection with the edges. The position of the volume node is calculated to be at the center of the crack surface that passes through the non-partitioned tetrahedron, i.e., its coordinates are calculated as the average of the coordinates of edge nodes.

(ii). additional face nodes are added on each face of the tetrahedron. The face nodes are added in order to ensure a unique partitioning scheme and to eliminate the possibility of having more than one admissible partitioning scheme. If two intersections are identified on one face, there will be two possibilities for the new mesh configuration. On the other hand, adding a face node gives a unique mesh topology as shown in Fig. 4.6. This partitioning strategy leads to a

total number of 24 new partitioned elements where all the added nodes lie on the crack surface.

In practice, the number of crack intersections for each edge in the mesh depends on the detected crack path. Therefore, the next step is to merge the edges that do not contain any intersection so that the two elements sharing these edges are compacted to one element. In addition, for the face that does not have any intersections on one of the edges, all the elements sharing this face are compacted to form only one element. The final topology of the patch will only have edge and face nodes where there is at least one edge intersection on the face.

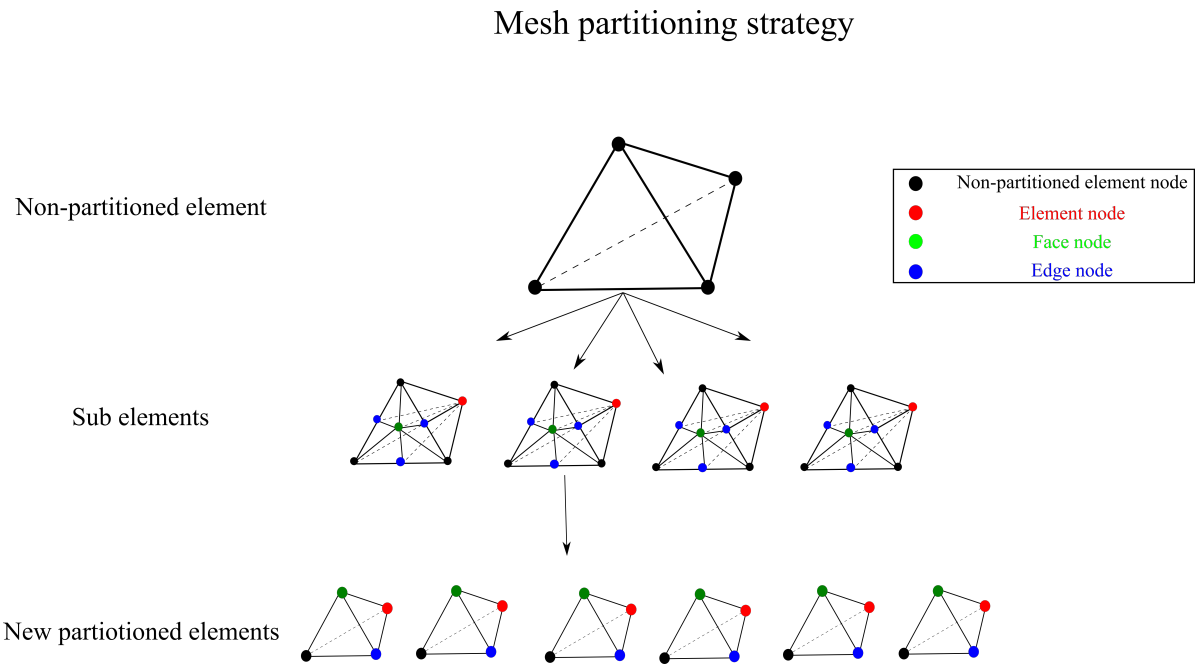


**Fig. 4.5** Mesh partitioning strategy used to fit the crack surface with the mesh.

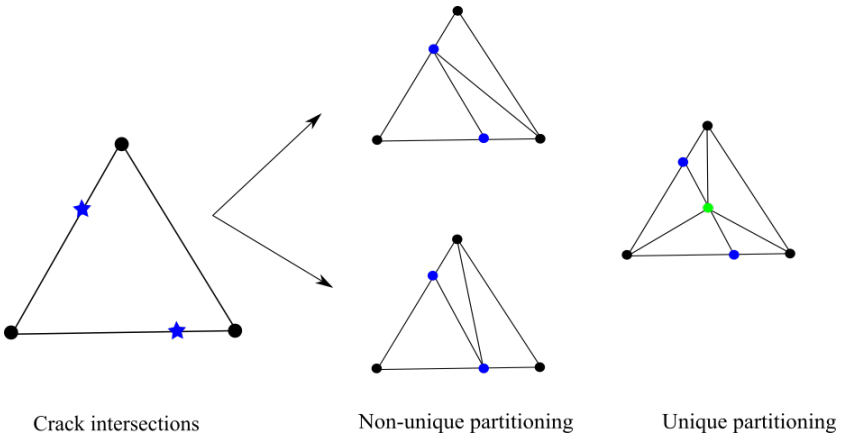


**Fig. 4.6** A comparison between the non-unique and unique face partitioning schemes.

In Fig. 4.7a, three intersections have been identified, the topology of the new partitioned elements is shown in Fig. 4.7b where the coordinates of face and element nodes are calculated according to the mentioned rules. Six crack faces are identified in this configuration where each face contains an edge node, face node and the volume node. The next step is the duplication of

nodes that belong to the crack faces in order to open the crack surfaces. It can be seen that each new partitioned element cannot have more than one crack face by construction. This feature is very important as it leads to a unique description of the crack surface in the case of crack bifurcation.

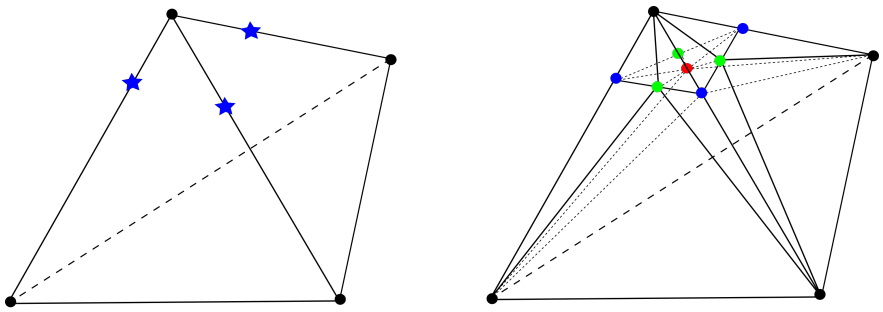

(a) (b)

**Fig. 4.7** The strategy of identifying the crack faces.

Fig. 4.9b shows how the mesh topology is modified in order to fit the crack surface within the mesh.

### 4.4.2 Introducing a topological discontinuity in the mesh

In this part, a discontinuity is introduced in the mesh by duplicating the new inserted nodes in the crack intersection locations. The nodes that belong to the crack faces should be duplicated except the crack front nodes. As described in the previous section, a crack face is identified as the surface that connects three nodes (an edge node, face node and a volume node) for a tetrahedral element in 3D as described by the sequence agnostic partitioning strategy. In order to achieve this objective, the graph coloring algorithm widely used in the graph theory is adopted for this purpose. In graph coloring, a vertex or face is assigned a unique color so that no adjacent one can have the same color, see [138]. In our case, the patch around each node that needs to be duplicated is analyzed. Each connected patch of elements should have the same color. The color is changed once a crack face separates two patches. Finally, each node is duplicated according to the number of colors associated to the patches connected to it.

Fig. 4.8 shows three mesh patches of triangular elements in 2D showing the three possible scenarios of nodal duplication where the generalization of the algorithm in 3D is straightforward. In the first patch 4.8a, one crack face is identified which leads to a partially cracked patch. Starting with a loop around each test node, it is found two elements are connected to the node having a crack face in common. Each element takes a different color leading to two copies of this node, one copy for each disconnected patch. The second test node is not duplicated since all the attached elements have the same color, so it represents the crack tip. The second patch as shown in Fig. 4.8b contains two crack faces. This results in having two copies of the first test node leading to a crack opening in the initial patch. Then, a second test node will also have two

copies leading to a second opening of the crack surfaces in the patch. The last test node is then duplicated in order to totally separate the two patches leading to a fully cracked patch. A third patch shown in Fig. 4.8c contains three crack faces leading to a bifurcation of the crack path. These faces contain four nodes that lie on the crack surface. Starting with an initial test node, the same initial crack path is obtained as the partially and fully cracked patches. However, the analysis of the second node leads to three different colors since there are two crack faces. Hence, three copies are made of this central node. Finally, the third and fourth test nodes are duplicated to two copies leading to a final crack bifurcation.

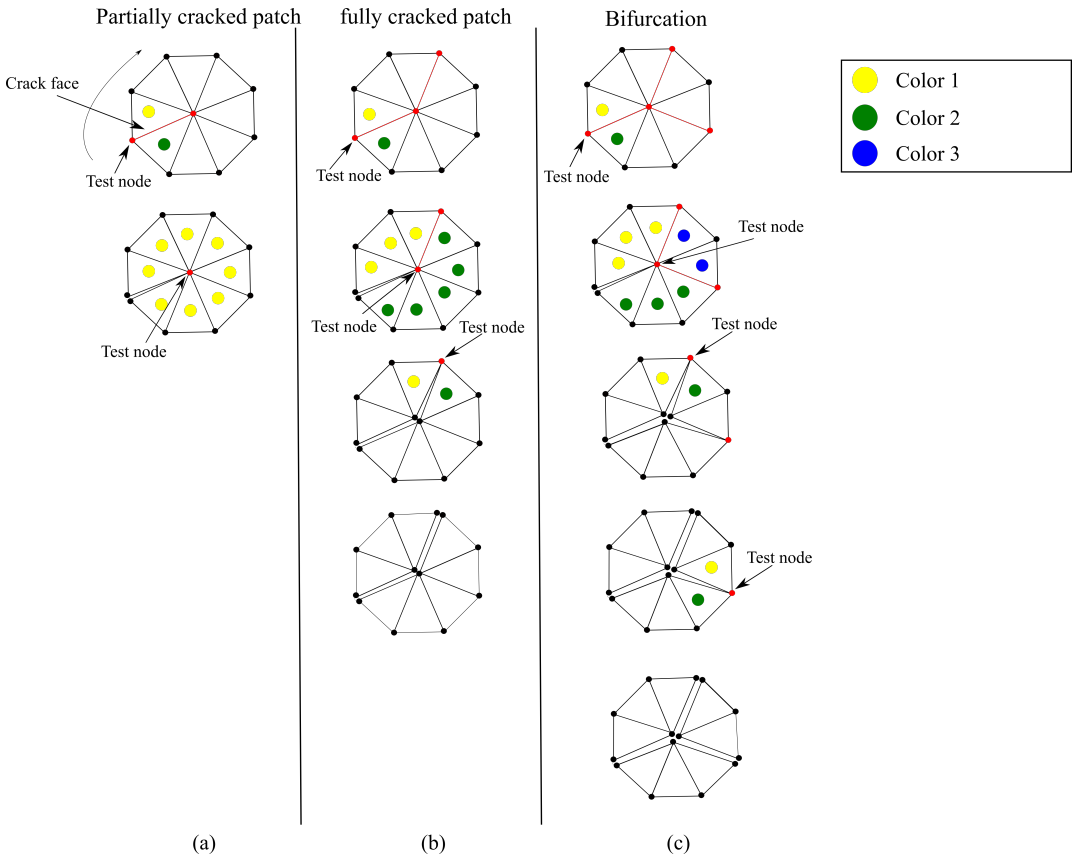


**Fig. 4.8** Illustration of the use of the coloring algorithm for the nodal duplication.

Fig. 4.9c shows an example of the use of the coloring algorithm for the nodal duplication and the opening of the crack surfaces.

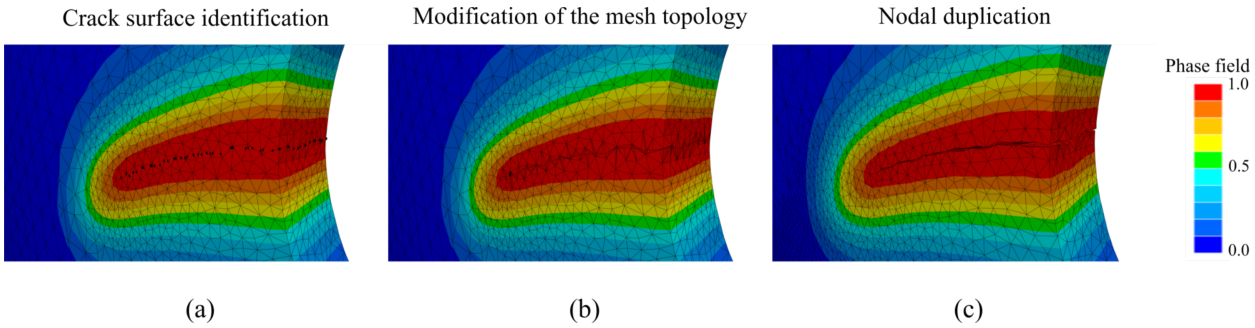


**Fig. 4.9** Illustration of the main operations of the crack insertion algorithm. Crack identification in (a), mesh modification in (b) and nodal duplication followed by a volume remeshing step in (c).

### 4.4.3 Convergence of the crack path detection with mesh refinement

The objective of this section is to prove the convergence of the crack path identification with the mesh refinement. Fig. 4.10 shows a 2D example of a crack path identification strategy using a triangular mesh topology. In order to insert a new crack increment, one needs to verify that the phase field value at the detected positions is close to 1 (here it is chosen to be greater than 0.99). However, since low order finite elements do interpolate the phase field values linearly over the edges, at least one nodal value of an intersected edge should have a phase field value greater than 0.99. However, it is very probable that the phase field value at some identified points (marked with a blue color) does not exceed the threshold of 0.99 because of the nature of the discretization and element type. On the other hand, the detected intersections on the edges that have at least one node close to the crack path (marked in green color) will have a phase field value greater than 0.99. Though, if some nodes are not to be duplicated at a time increment $n$, no doubt that they will be duplicated in the following time increment since that phase field value at both edges nodes will exceed the threshold value for a sufficiently fine mesh.

It can be imagined that with a finer mesh, the two identified locations marked in blue would have been identified so that the whole crack path is detected at the same time. This conclusion confirms that the crack identification strategy has the same convergence behaviour as the phase field solution. Thus, the solution converges with both h-refinement and p-refinement strategies.

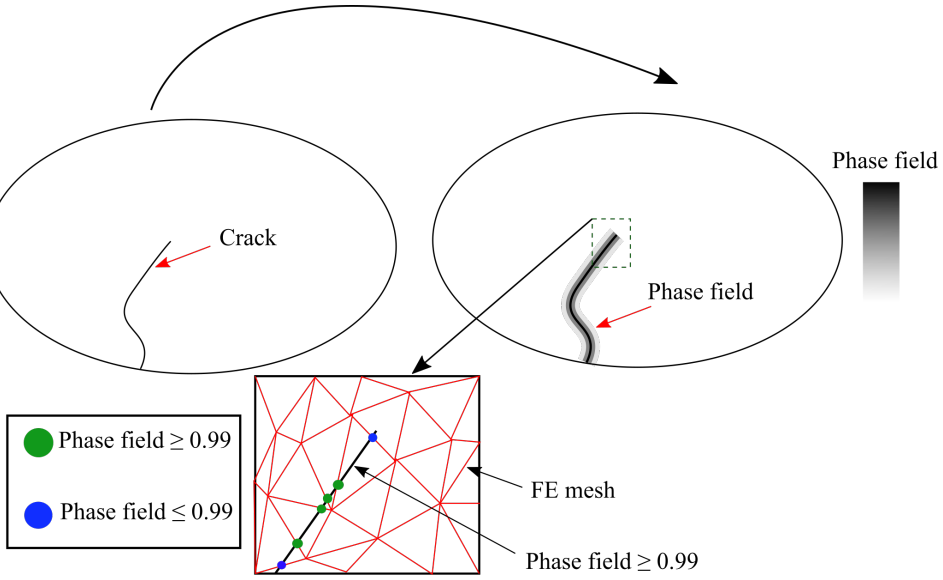


**Fig. 4.10** Convergence behaviour of the crack path identification process.

### 4.4.4 Propagating multiple cracks in a parallel framework

The parallel framework implemented in **FORGE ®** is known as SPMD (single program on multiple data) [139, 140]. Fig. 4.4 illustrates the basic idea of the framework where the mesh elements are divided to different partitions where each one is managed by a processing unit. This means that all processors see the same program instructions with different data inputs. The only constraint in this case is the compatibility of the mesh connectivity at parallel interfaces. At the interface between different processors, the following information is shared:

1. the number of neighbourhood interfaces;
2. an index for each neighbourhood partition;
3. the number of nodes at each interface;
4. an index for each node at the interface with its global numbering.

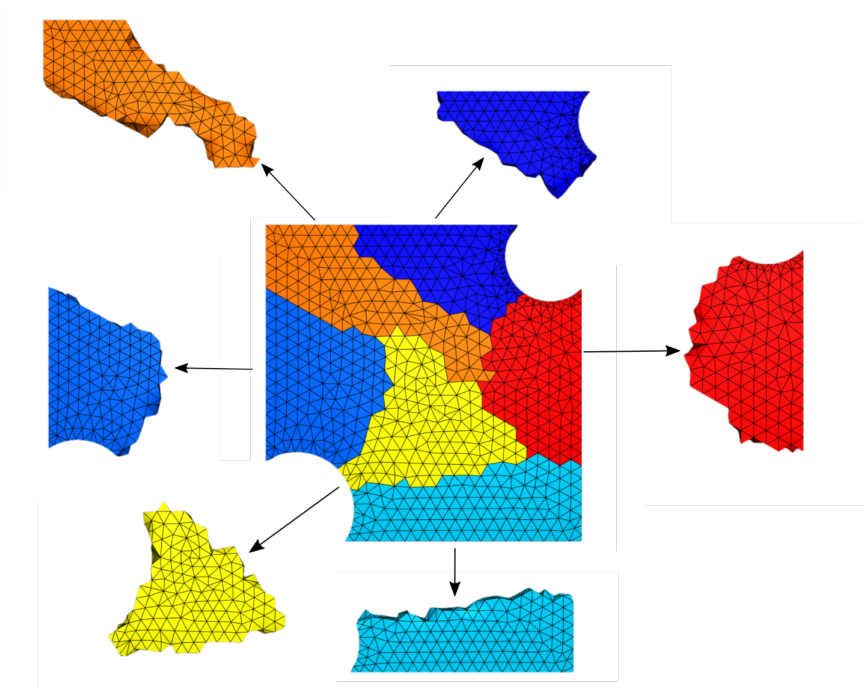

**Fig. 4.11** Illustration of the SMPD parallel framework.

In order to handle the crack propagation in parallel, each processor manages all algorithmic operations for the interior elements without a need for communicating with its neighbourhood. Interior elements are refereed to all the elements that do not have any shared face between two processors. The main advantage of the crack propagation algorithm appears when dealing with the elements that contain shared faces at the parallel interface. The unique element division strategy as proposed in Fig 4.6 will naturally lead to compatible elements connectivity without any communication between the processors as shown in Fig 4.12. It can be also shown that without applying this strategy, it is highly possible that non-unique partitions are produced which requires a communication between the processors in order to ensure a unique choice.

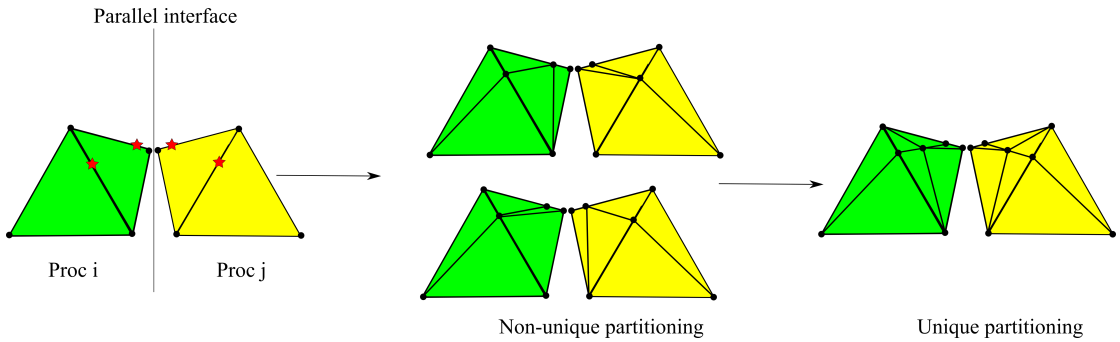


**Fig. 4.12** Partitioning of elements that share faces located at the parallel interface.

The proposed strategy leads to efficient element partitioning operations with low computational cost. This is the consequence that all algorithmic operations are local and no communication is needed between the different processors. The flow chart shown in Fig 4.13 summarizes the algorithmic steps used for the simulation of crack propagation.

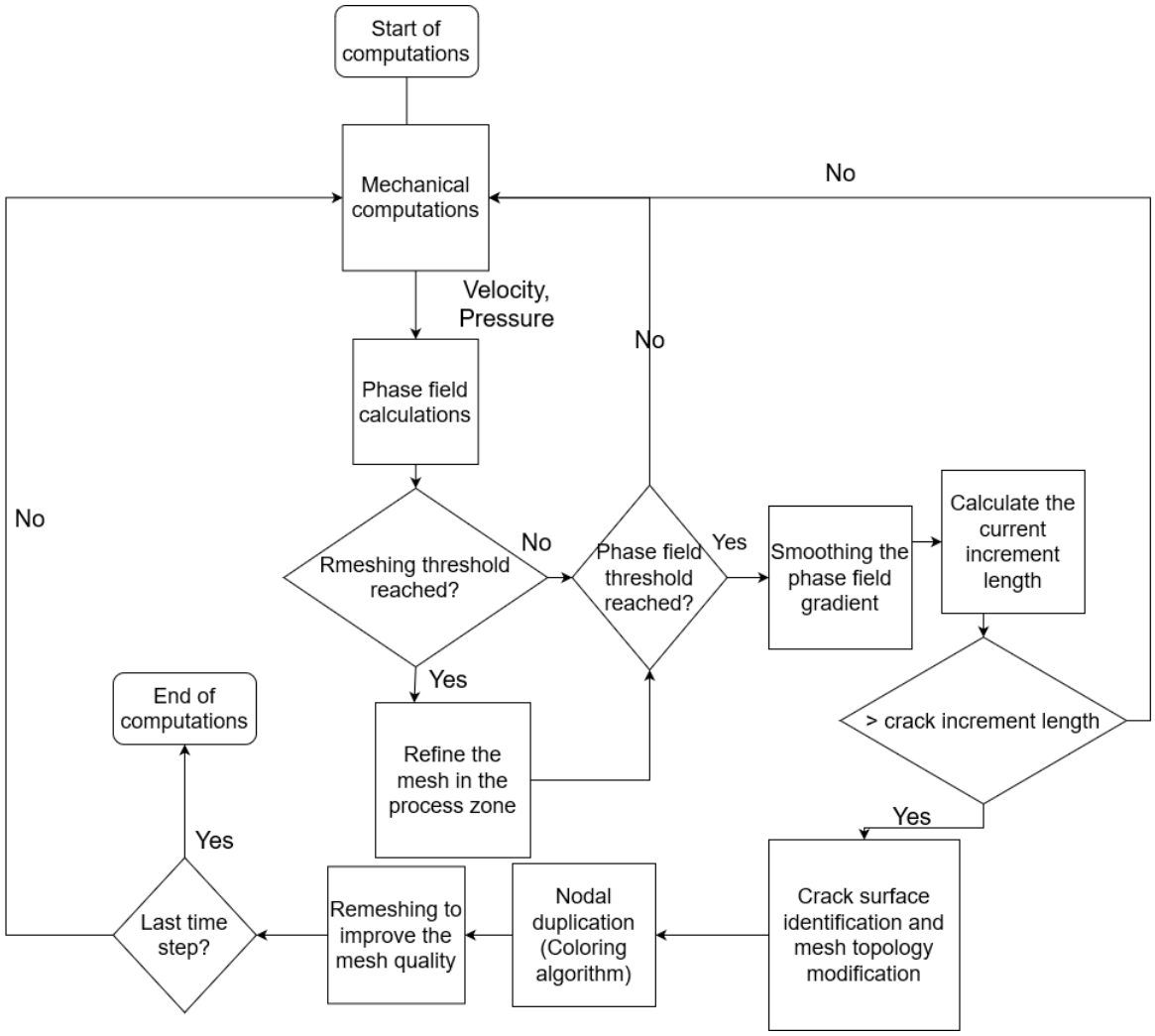


**Fig. 4.13** Flowchart describing the main operations of the CIPFAR algorithm.

## 4.5 Numerical validations

### 4.5.1 Double notched symmetric specimen

In this example, mode I of fracture is demonstrated using a symmetric specimen with double notches subjected to tensile loading. Fig. 4.14 shows the geometry and boundary conditions of the specimen where the thickness is 1 mm. The material and model parameters are listed in Table 4.1. The time step is set to 0.5 s until the maximum value of the phase field reaches 0.1 and 0.125 s for the rest of the simulation in order to ensure the convergence of the solution. An initial mesh size of 1 mm in used everywhere in the mesh. The mesh is refined in the damaged zone based on the equivalent plastic strain as described by the adaptive remeshing algorithm in chapter 3. A comparison is carried out between coarse and fine meshes with the smallest mesh sizes $h_{min}$ as 0.4 mm, 0.3 mm and 0.2 mm. The effective crack area $A_{fixed}$ is set to 0.5 mm$^2$ for all the examples.

The phase field evolution and discrete crack surfaces propagation at three different displace-

ments are illustrated in Fig. 4.15 for different mesh sizes. It can be observed that the actual crack path follows the implicit crack path predicted by the evolution of the phase field until the final rupture of the specimen. Although the intermediate crack evolution process is slightly different for the different mesh sizes, the same crack path is obtained at the final fracture for the three mesh sizes. These slight differences can be explained by the increase of the accuracy of mechanical and phase field resolutions with the mesh refinement.

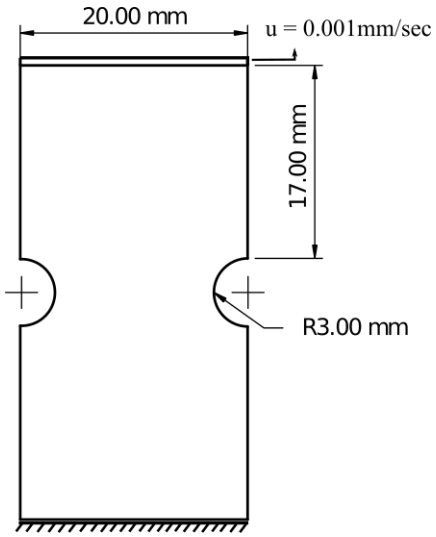


**Fig. 4.14** Geometry and boundary conditions of a double notched symmetric specimen.

**Table 4.1** Material and phase field model parameters for a double notched symmetric specimen

| Quantity | Value | Unit |
|---|---|---|
| Young's modulus, $E$ | 200 | GPa |
| Poisson's ratio, $\nu$ | 0.3 | |
| Effective stress, $\boldsymbol{\sigma_y}$ | $\sigma_0 + H\bar{\varepsilon}$ | MPa |
| Yield stress, $\sigma_0$ | 300 | MPa |
| Plastic modulus, $H$ | 600 | MPa |
| $\beta_1$ | 1.0 | |
| $\beta_2$ | 1.0 | |
| Plastic threshold, $W_0$ | 5 | MPa |
| Fracture toughness, $G_c$ | 5 | MPa mm |
| Characteristic length scale $l_c$ | 0.8 | mm |

Fig. 4.16 shows the force vs. displacement curves for different mesh sizes with a comparison between the discrete crack propagation and fixed mesh computations. Two main conclusions can be drawn: (i). a convergence behaviour is observed with the reduction of mesh size which is coherent with the characteristic features of the implicit gradient-based non-local dam-

age formulations; (ii). a numerical diffusion due to remeshing is also observed for the discrete crack propagation cases, however, a similar convergence behaviour with the reduction of mesh size is observed as the fixed mesh computations. It should be noted that the slight deviations from the equilibrium path after each remeshing step leads to a final deviation in the force vs. displacement curve. This numerical diffusion is due to the transport of mechanical fields after each remeshing operation.

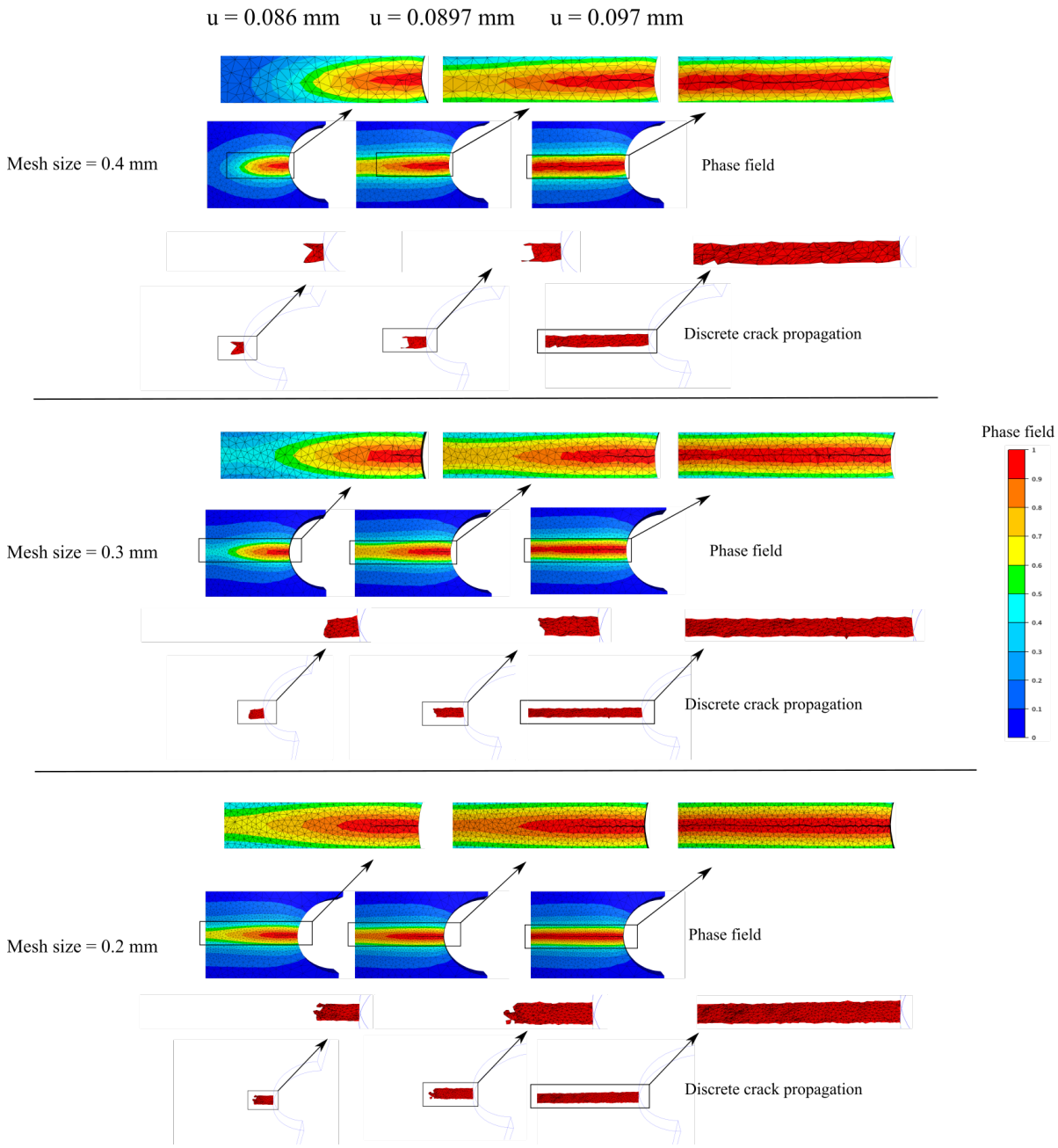


**Fig. 4.15** Phase field evolution showing the crack initiation, propagation until the final fracture.

The effect of adaptive remeshing threshold on the force vs. displacement curves is shown in Fig. 4.17 with a comparison with the fixed mesh computations without neither adaptive remeshing nor discrete crack propagation. It can be shown that when the remeshing threshold

is reduced, the deviation between the fixed mesh and discrete crack propagation solutions is reduced. This can be explained by the fact that when mesh refinement process is initiated earlier, the mechanical resolution becomes more accurate in capturing the moment of crack initiation. The deviation of the total strain energy in the case of discrete crack insertion as compared to the fixed mesh case is shown in Table 4.2. In the next presented cases, a remeshing threshold of 0.005 is used.

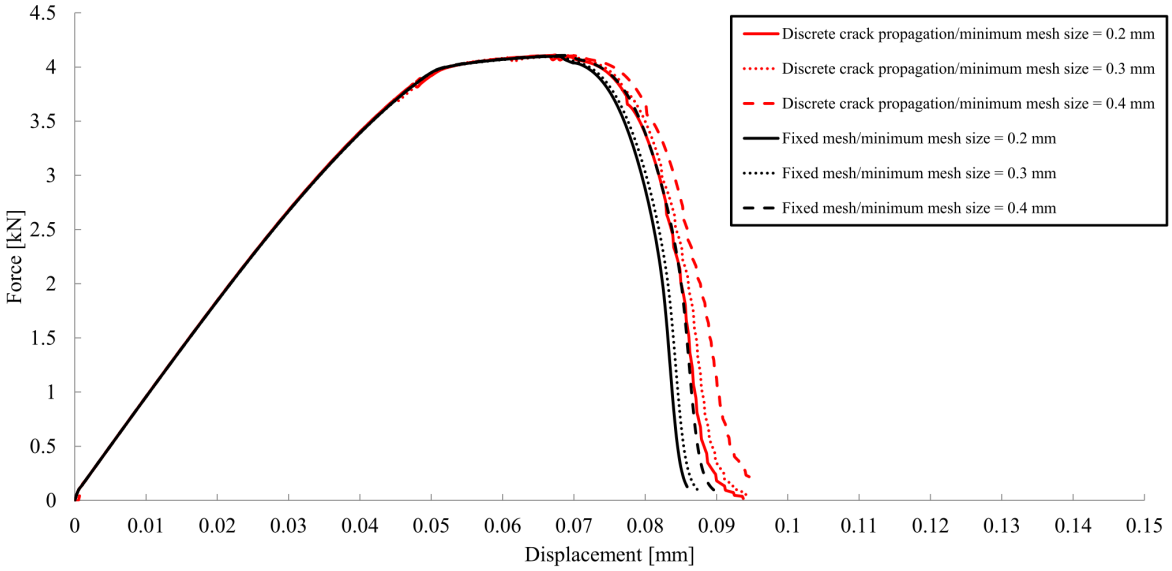


**Fig. 4.16** Force vs. displacement curves for different mesh sizes with a comparison with the fixed mesh computations.

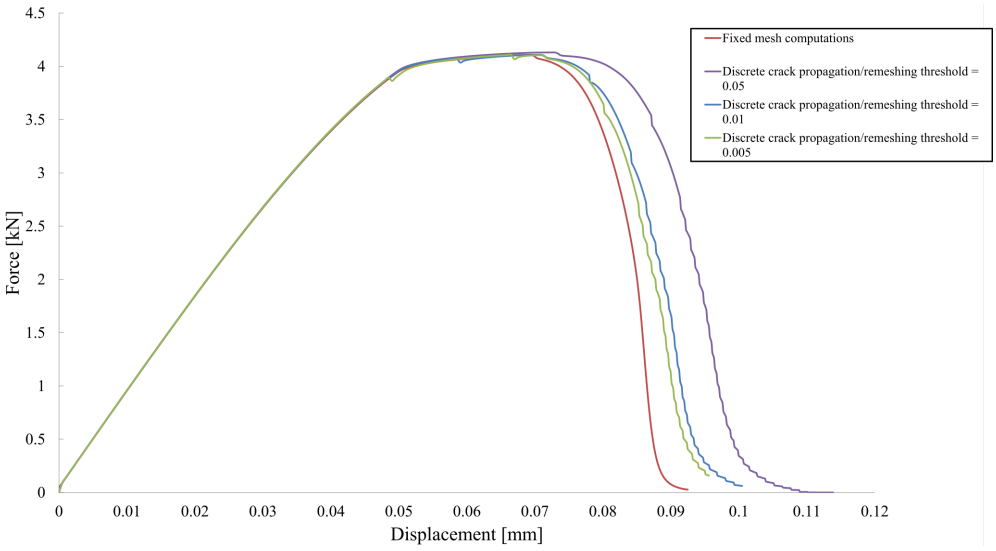


**Fig. 4.17** Force vs. displacement curves for different remeshing thresholds where the adaptive mesh refinement is based on the equivalent plastic strain.

**Table 4.2** The effect of remeshing threshold on the total strain energy

| Remeshing threshold | Total strain energy ($J$) | Deviation % |
|---|---|---|
| 0.05 | 0.281 | 12.75 |
| 0.01 | 0.263 | 6.67 |
| 0.005 | 0.259 | 5.1 |

The effect of crack increment length threshold on the force vs. displacement curves is shown in Fig. 4.18. Results are compared with pre-refined fixed mesh computations which is considered as the reference case. It is worth mentioning that the discrete crack insertion has a negligible effect on the mechanical resolution since the material is totally degraded before the insertion of the crack increment. Slight deviations between the curves are observed after the crack initiation point. This result is directly related to the numerical diffusion that increases with the increase of the number of remeshing operations as shown on the figure. It can be also shown in Fig. 4.19 that the final crack paths are very similar for the different crack increment lengths. This result is consistent with the fact that the discrete crack path follows the phase field evolution which is independent on the choice of the crack increment length threshold.

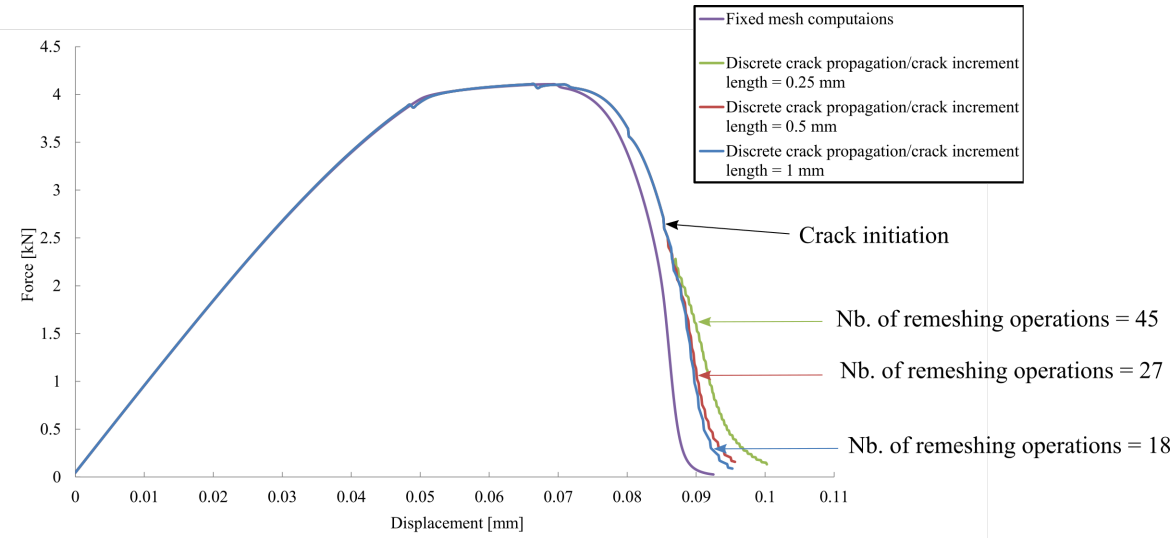


**Fig. 4.18** Force vs. displacement curves for different crack increment lengths.

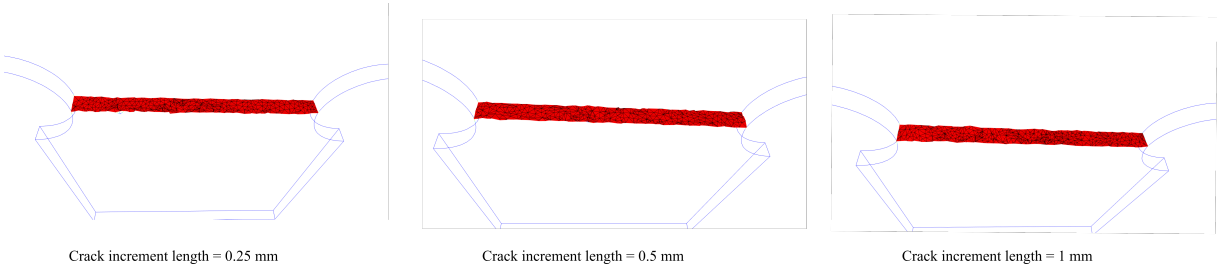


**Fig. 4.19** Final crack surface for different crack increment lengths.

As suggested in [125], the effect of stress triaxiality in the prediction of damage localization and hence the crack evolution is important. In order to test this effect, the same proposed modification is added to the plastic energy $W_p$ that appears in the local history functional by adding a stress triaxiality function $\phi(\eta)$. The rate form of the plastic strain energy becomes

$$\dot{W}_p^{eff} = \frac{\dot{W}_p}{\phi(\eta)} \tag{4.13}$$

where $W_p^{eff}$ is the effective plastic energy. For the sake of demonstration, the same form and parameters of the triaxiality function are taken from [125] which is shown as follows

$$\phi(\eta) = d_1 + d_2\, e^{d_3\,\eta} \tag{4.14}$$

with $d_1 = 0.1$, $d_2 = 3.8$ and $d_3 = -1.8$.

The local energy functional shown in equation 2.53 is then modified to be

$$\mathcal{H} = \frac{l_c}{G_c}\Big(\beta_1 \max_n W_e(\boldsymbol{\varepsilon}^e(\mathrm{x}, d_n)) + \beta_2 \; < W_p^{eff}(\bar{\boldsymbol{\varepsilon}}) - W_0 > \Big). \tag{4.15}$$

Fig. 4.20 shows the phase field evolution and discrete crack surface propagation without and with the effect of stress triaxiality, in other words, without adding the stress triaxiality function. All the material and model parameters are fixed for both cases except the effect of the stress triaxiality. When the effect of stress triaxiality is added, it also be shown that the internal crack initiation occurs close to the free surface but not at the notch boundary which is the location of maximum stress triaxiality. The same result was observed in [125] which was also qualitatively confirmed by the experimental observations reported in [141].

The developed algorithm is able to describe the full cracking process starting with the initiation at the expected locations until the formation of the complete crack surface leading to the separation of the initial specimen into two pieces. In addition, the final crack paths are independent on the mesh size given that the mesh size is small enough for a good resolution of the phase field equations.

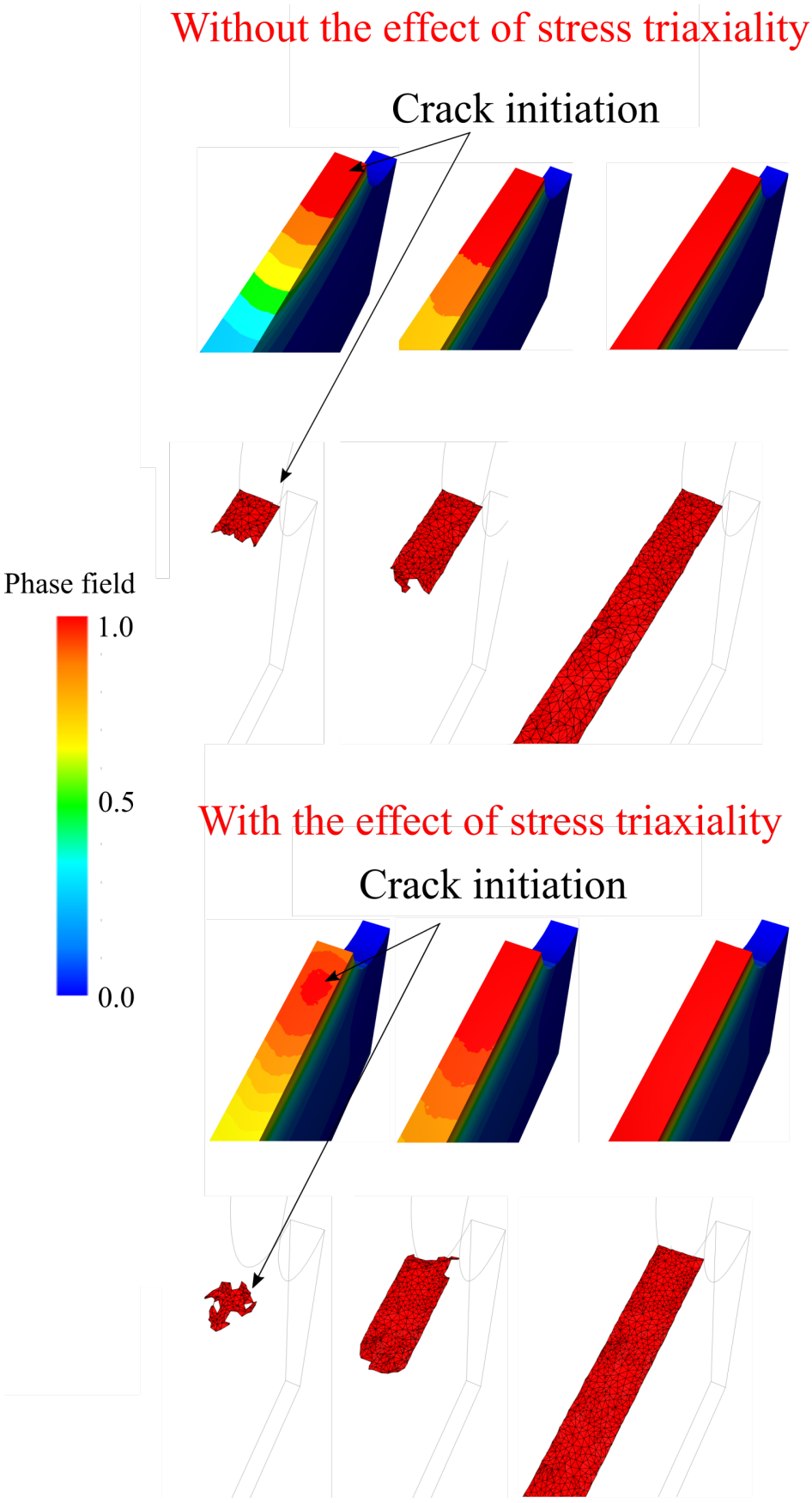


**Fig. 4.20** The effect of stress triaxiality function on the initiation and propagation of discrete crack surface.

### 4.5.2 Double notched asymmetric specimen

In this example, a mixed mode of fracture is simulated in order to prove the ability of the algorithm to deal with complex cracking pattern. The geometry and boundary conditions along with the initial mesh are shown in Fig. 4.21 as in [54, 88]. The initial mesh size is set to 0.4 mm. Using the adaptive remeshing algorithm, the mesh size is reduced to 0.2 mm in the regions where the crack is expected to propagate where the equivalent plastic strain is used as an indicator function with a threshold of 0.01. The material and model parameters are listed in Table 4.3. The time step is set to 0.01 s in the beginning of the simulation until and then reduced to a minimum time step $\Delta t_{min}$ once the maximum value of the phase field reaches 0.1. A time step convergence study is shown in Fig. 4.22 with the following model parameters $G_c = 5$ MPa mm and $W_0 = 10$ MPa. A convergence behaviour is observed with respect to the time step most notably for the values less than 0.00625 s which will be used in all the following simulations. The crack increment length is fixed at 0.5 mm in all the presented examples.

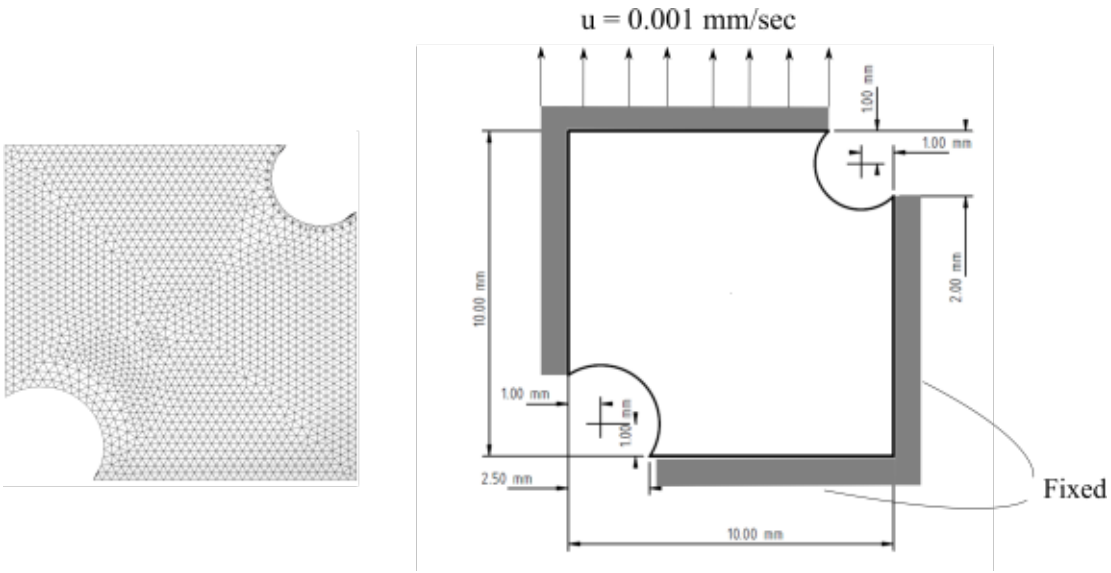


**Fig. 4.21** The geometry and boundary conditions along with the mesh of an asymmetric double notched specimen. The thickness of the specimen is set to 1 mm.

**Table 4.3** Material and phase field model parameters for a double notched asymmetric specimen.

| Quantity | Value | Unit |
|---|---|---|
| Young's modulus, $E$ | 180 | GPa |
| Poisson's ratio, $\nu$ | 0.28 | |
| Effective stress, $\boldsymbol{\sigma_y}$ | $\sigma_0 + H\bar{\varepsilon}$ | MPa |
| Yield stress, $\sigma_0$ | 443 | MPa |
| Plastic modulus, $H$, | 300 | MPa |
| $\beta_1$ | 0.0 | |
| $\beta_2$ | 1.0 | |
| Plastic threshold, $W_0$ | 10/20/40 | MPa |
| Fracture toughness, $G_c$ | 0.5/1/5/10 | MPa mm |
| Characteristic length scale $l_c$ | 0.4 | mm |

Figures 4.23 and 4.24 show the phase field evolution and discrete crack surface propagation at three different displacements for coarse and fine meshes of element sizes of 0.2 mm and 0.05 mm, respectively. From a global point of view, it can be shown that the crack initiation and propagation in both cases are very similar. However, a better resolution of the quality of the crack surface is observed with the fine mesh. This result is coherent with the fact that the order of approximation of the crack surfaces prediction follows the order of finite element approximation where linear elements are adopted in this case. Fig. 4.25 shows the force vs. displacement curves for three different mesh sizes where a convergence behaviour is observed when the mesh is sufficiently refined.

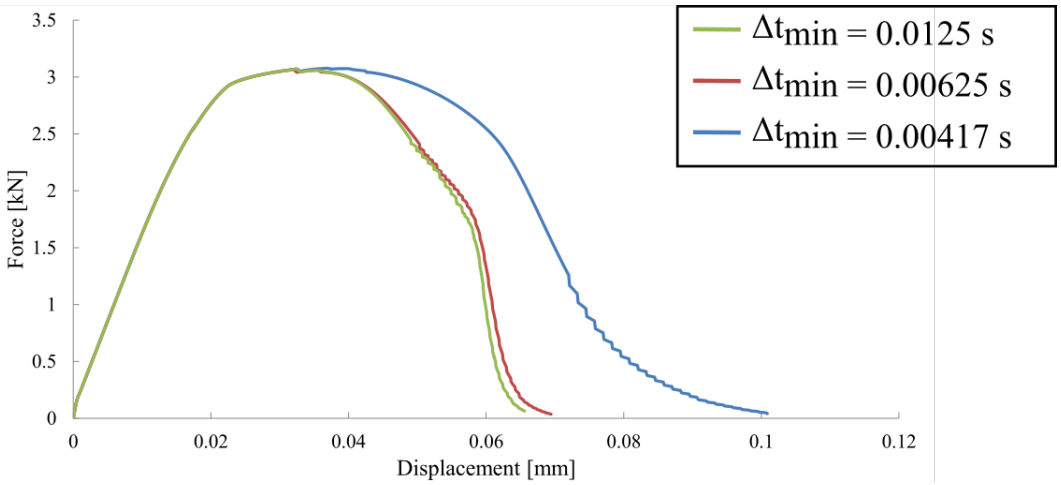


**Fig. 4.22** Convergence of the Force vs. displacement curve with respect to the reduction in the time step.

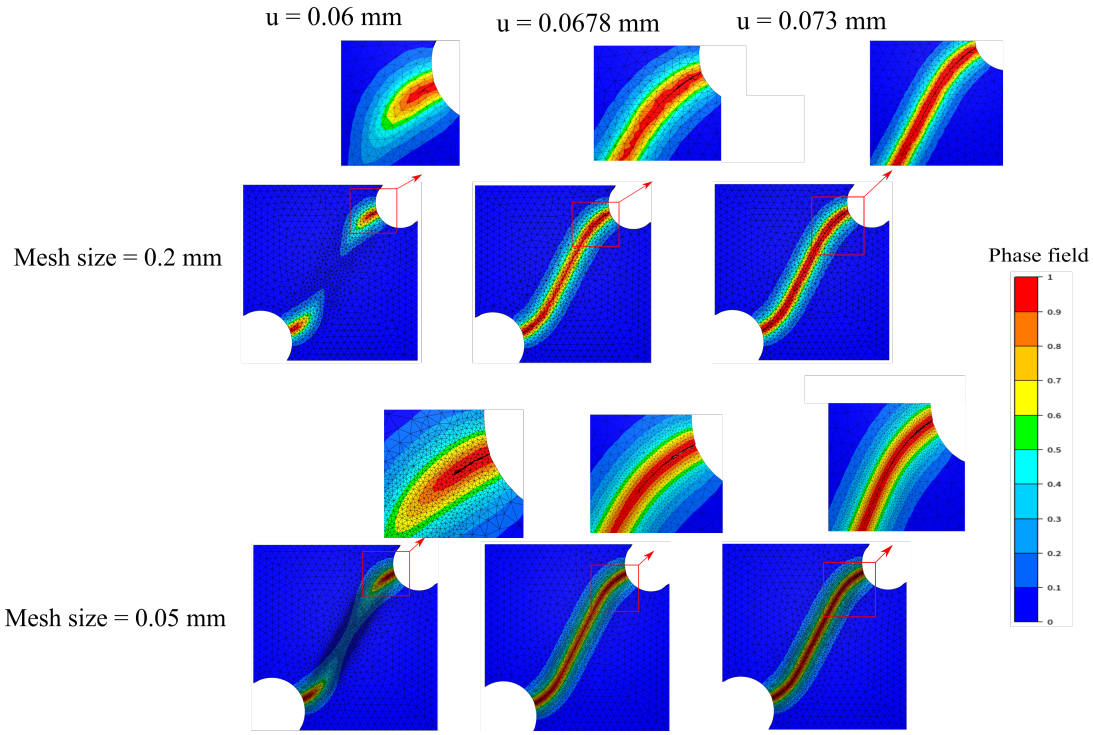


**Fig. 4.23** Phase field evolution accompanied with the crack path propagation at three different displacements using two different mesh sizes.


**Fig. 4.24** Crack surfaces evolution in 3D at three different displacements using two different mesh sizes.

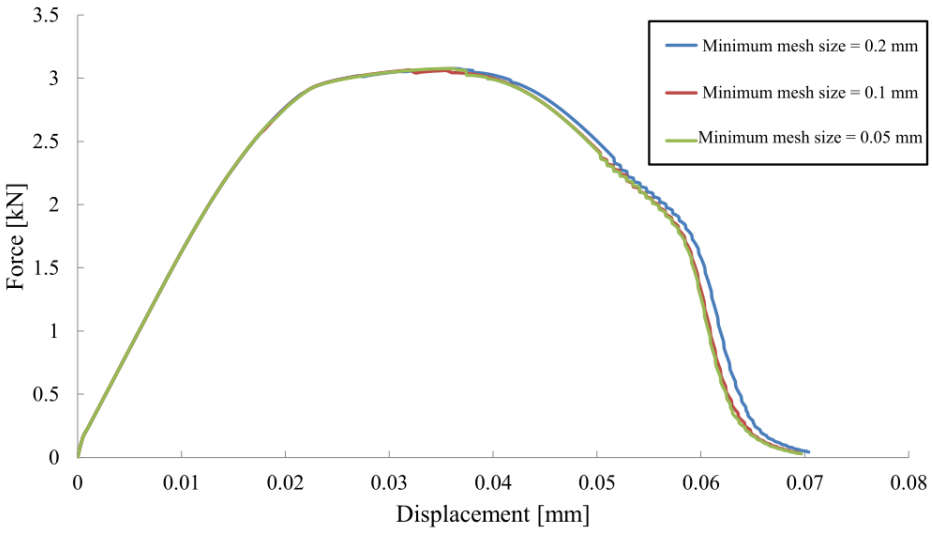


**Fig. 4.25** A comparison between three mesh sizes on the Force vs. displacement curves.

Fig. 4.26 shows the effect of stress triaxiality on the initiation of the phase field and hence the discrete crack surface at different values of the plastic threshold $W_0$. The phase field profile is shown at a cross section that cuts the upper notch of the specimen. The same modification to the local history functional $\mathcal{H}$ as in section 4.5.1 is done by adding a stress triaxiality function $\phi(\eta)$. It is clear that without adding the effect of stress triaxiality, the crack is always initiated at the boundary of the upper notch. On the other hand, an internal crack is initiated close to the free surface but not at the notch boundary when the stress tiaxiality is included in the phase field evolution.

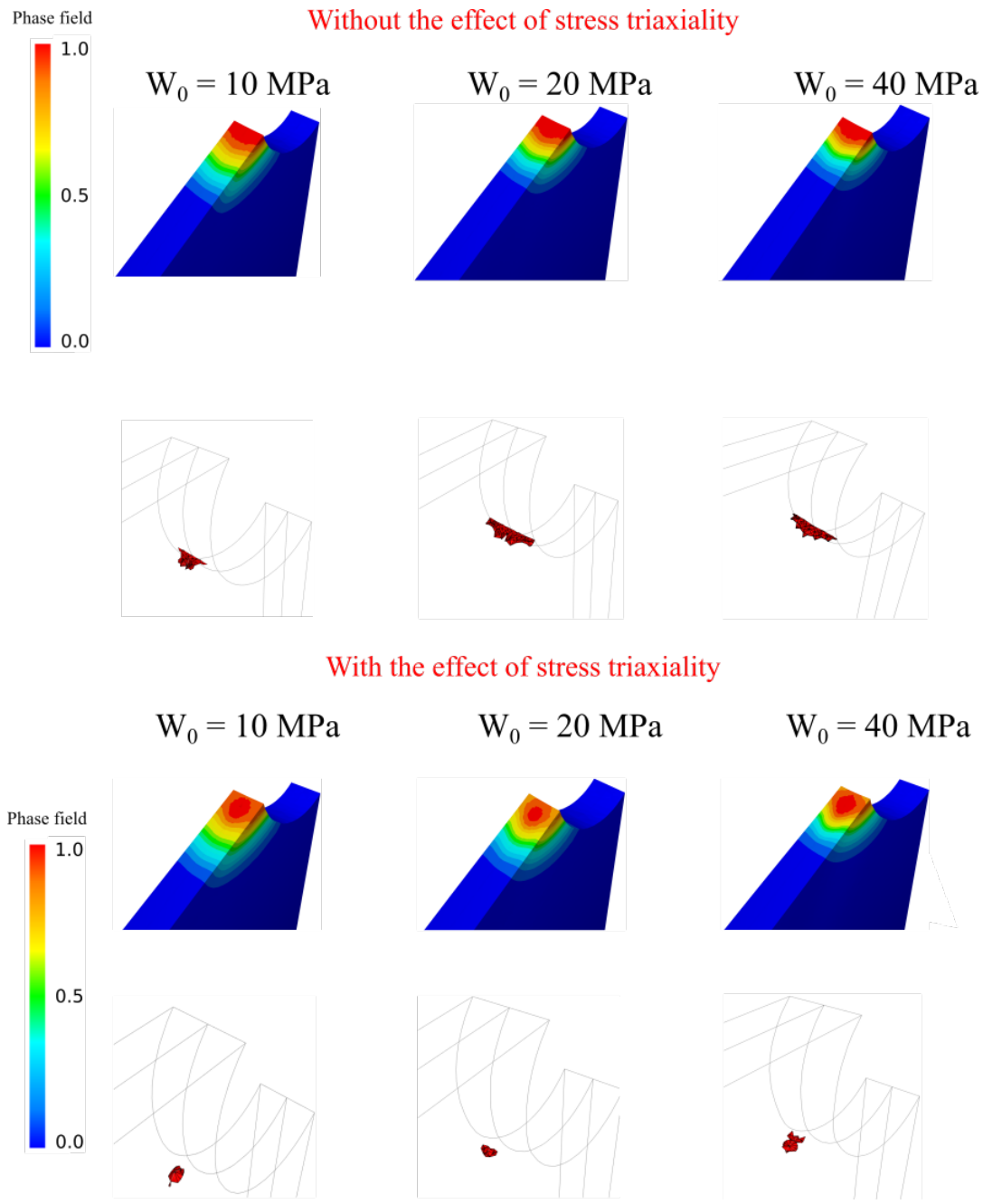


**Fig. 4.26** The crack initiation at different values of the plastic threshold $W_0$. Results are shown without the effect of stress triaxiality (up) and with the effect of stress triaxiality (bottom).

The force vs. displacement curves that show the effect of plastic threshold $W_0$ on the results are plotted in Fig. 4.27 where the effect of the parameter on the delay of crack initiation point is clearly demonstrated.

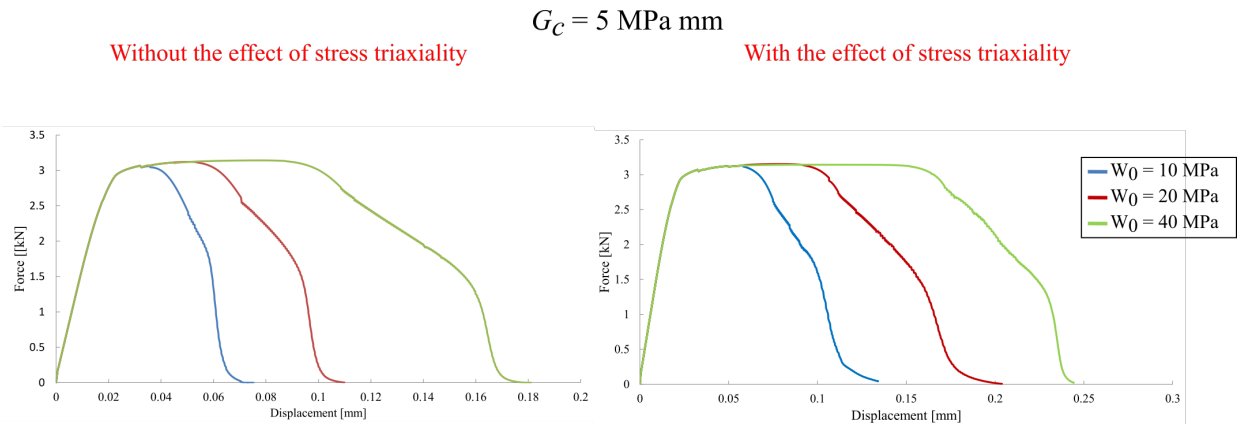


**Fig. 4.27** The force vs. displacement curves for different values of the plastic threshold $W_0$.

Another study is carried out in order to see the effect of the fracture toughness $G_c$ on the onset of crack initiation. Fig. 4.28 shows the force vs. displacement curves for different values of $G_c$ where crack initiation moments are identified by the arrows. It can be shown that when the value of the fracture toughness increases, which is typical in ductile materials, the crack initiation is slowed which is in contrast to brittle materials where the crack initiation happens just after reaching the peak stress. This can be explained by the fact that in ductile fracture, the amount of plastic energy dissipation is much larger than the amount of energy needed to create new crack surfaces. In other words, the crack is initiated at a high plastic strain level. In the current phase field model, this feature is related to the degradation of the yielding surface that appears in equation 2.30 so that the phase field evolution is dominated by the plastic strains. These results are confirmed with the experimental tests shown in [141].

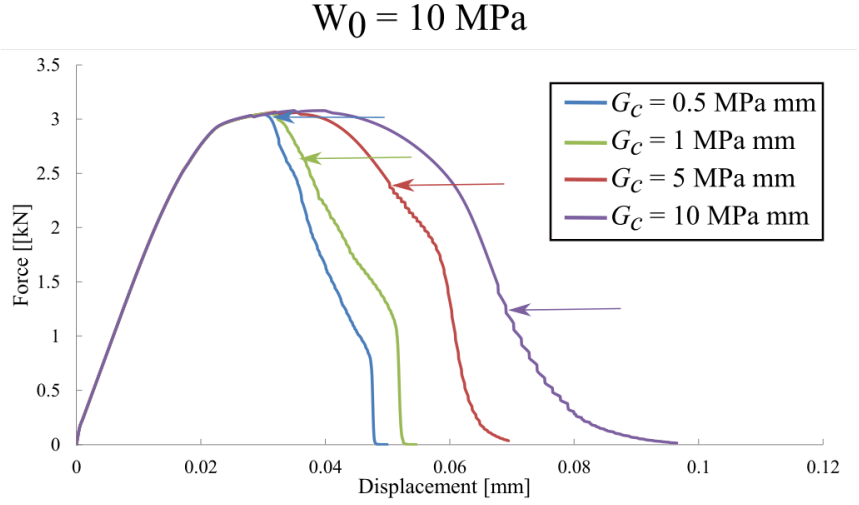


**Fig. 4.28** The force vs. displacement curves for different values of fracture toughness showing the onset of crack initiation using the crack insertion algorithm. The arrow indicates the instant of discrete crack initiation.

Fig. 4.29 shows the final discrete crack paths obtained for different values of the fracture toughness. The main observation is that the crack path becomes more straight for the ductile

fracture patterns, i.e., when $G_c$ increases. This can be explained by the fact that ductile materials fail in the zones of high plastic deformation which is the zone that connects the two notches by a straight path.

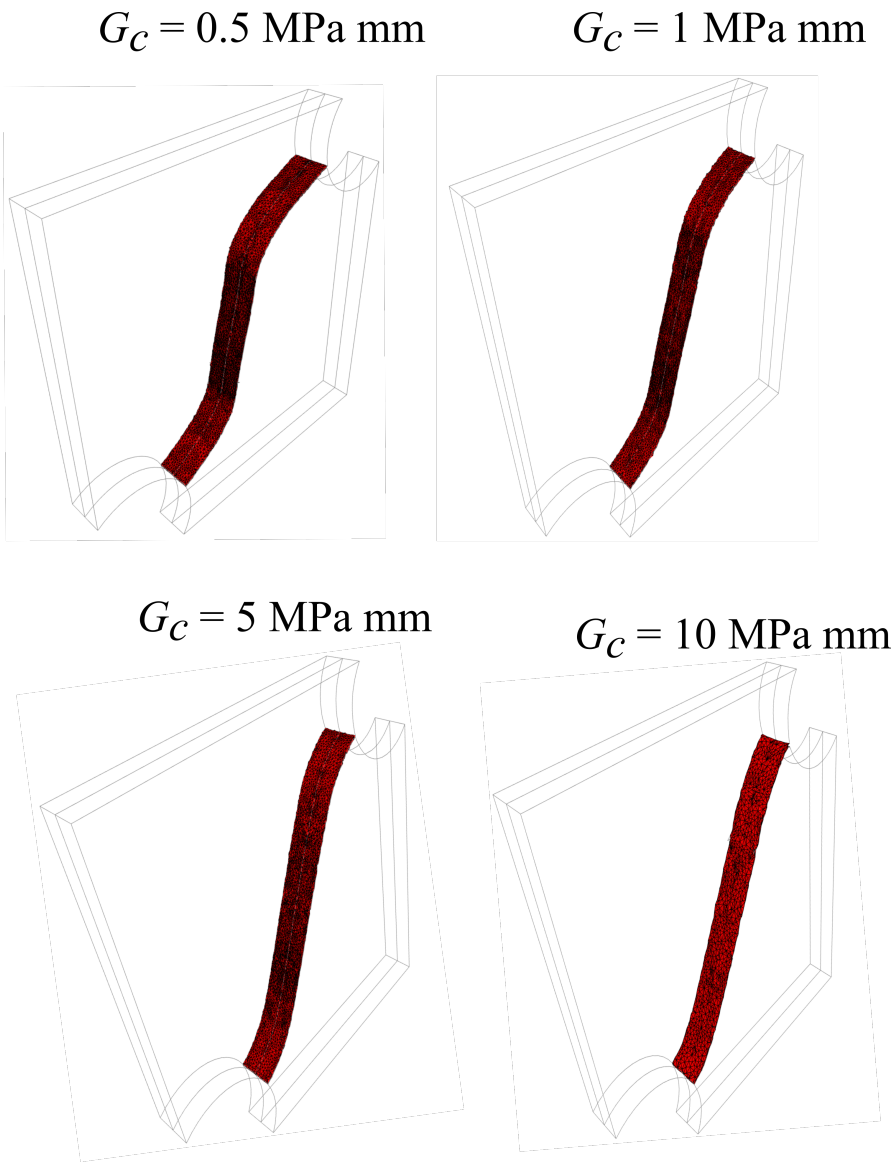


**Fig. 4.29** The final crack path obtained for different values of fracture toughness $G_c$.

Fig. 4.30 shows the final crack path and crack surfaces in 3D using different number of processors where each color indicates a different processor. It can be shown that the algorithm is able to predict the same crack path within a fully parallel framework. Table 4.4 shows the CPU time for the different cases along with the gain in computation time calculated as follows

$$\text{Gain for N processors} = \frac{\text{CPU time using 1 processor - CPU time using N processors}}{\text{CPU time using 1 processor}} \tag{4.16}$$

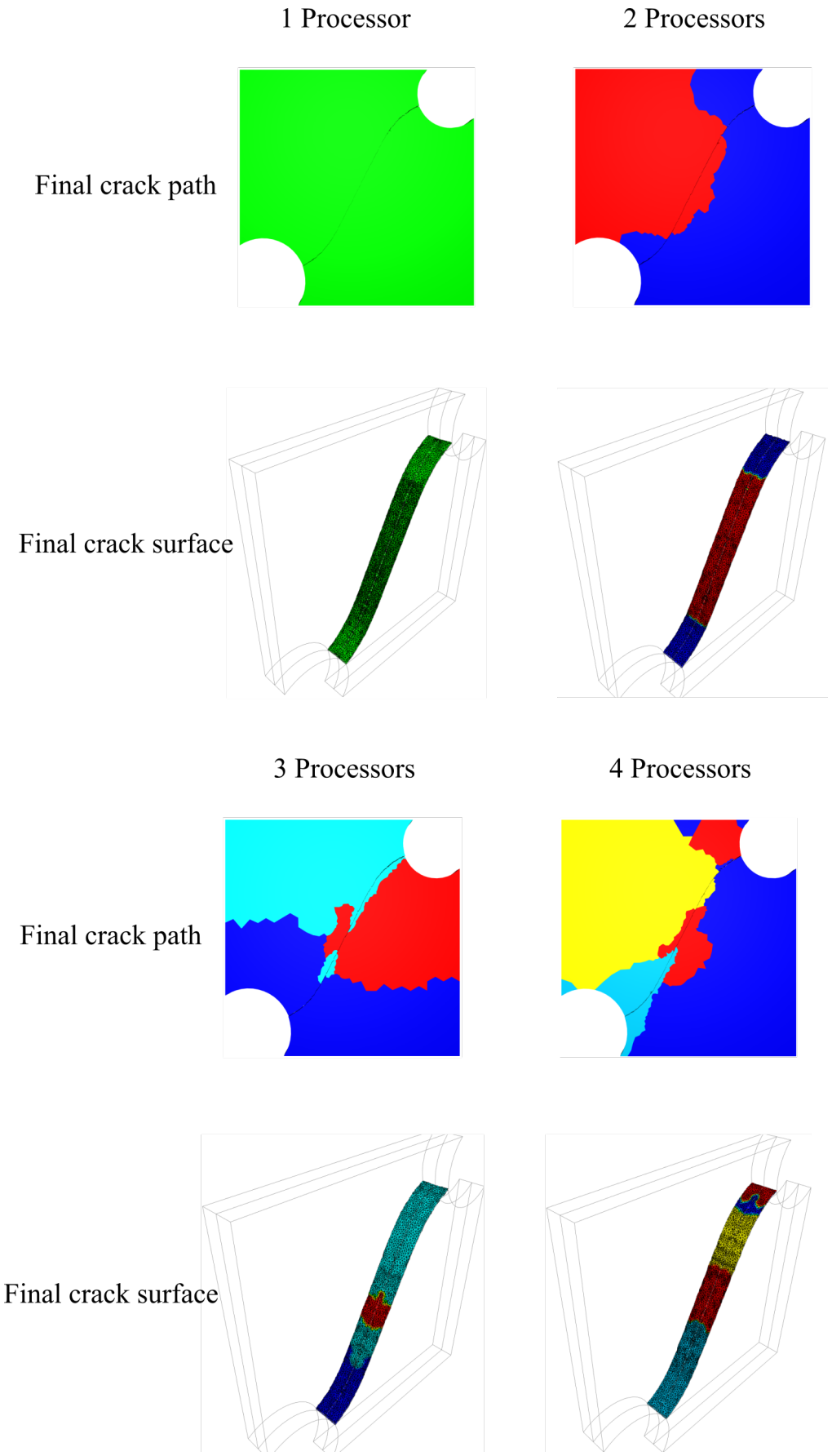


**Fig. 4.30** The final crack path obtained with 1, 2, 3 and 4 processors.

It can be observed that the algorithm maintains the same level of efficiency while increasing the number of processing units. The scalability of the algorithm makes it suitable for the 3D simulations of crack initiation and propagation with huge number of degrees of freedom.

**Table 4.4** Performance analysis of the crack insertion algorithm.

| Number of processors | CPU time [min] | Gain in computation time % |
|---|---|---|
| 1 processor | 170 | |
| 2 processors | 123 | 27.6 |
| 3 processors | 55 | 67.6 |
| 4 processors | 42.5 | 75 |

The developed strategy provides a robust numerical tool to handle the initiation and propagation of crack surfaces in 3D. All calculations are carried out within a fully parallel numerical framework which decreases the computation time drastically and renders it suitable for large scale simulations of discrete crack propagation.

### 4.5.3 Flat tensile specimen

In this example, the crack insertion algorithm is used to predict an internal crack initiation in a flat tensile specimen described in [55]. The geometry and boundary conditions are shown in Fig. 4.31 where the loading is carried out with a constant velocity of 0.01 mm/s.

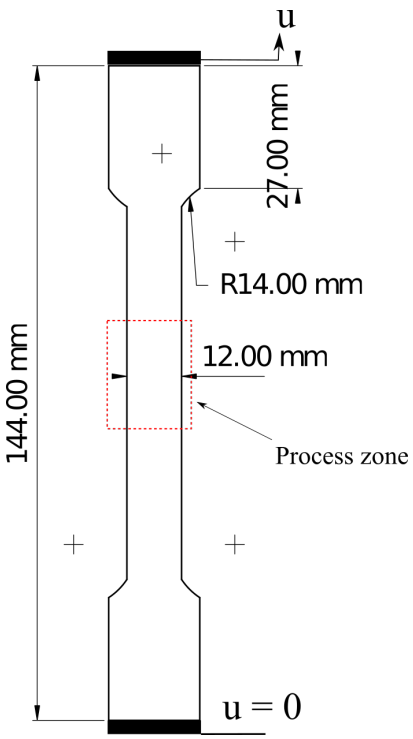


**Fig. 4.31** Geometry and boundary conditions of a flat tensile specimen [55].

A time step of 2 s is used until the maximum phase field value reaches 0.1 and reduced to 0.4 s for the rest of the simulation. The effective crack area $A_{fixed}$ is set to 0.5 mm$^2$ for all the simulations. The material and model parameters presented in Table 4.5 are used. The equivalent plastic strain is used as an indicator function for the mesh refinement with a threshold of 0.05. A fine mesh with smallest element size of 0.25 mm and a coarse mesh with a smallest element size of 0.5 mm are used for the comparison. The characteristic length scale $l_c$ is set as two times the minimum element length.

**Table 4.5** Material and phase field model parameters [55].

| Quantity | Value | Unit |
|---|---|---|
| Young's modulus, $E$ | 65200 | MPa |
| Poisson's ratio, $\nu$ | 0.26 | |
| Yield stress, $\boldsymbol{\sigma}_y$ | $\sigma_\infty + (\sigma_0 - \sigma_\infty)\boldsymbol{e}^{(-\delta\bar{\varepsilon})}$ | MPa |
| Initial yield stress, $\sigma_0$ | 209.6 | MPa |
| Ultimate strength, $\sigma_\infty$ | 62.6 | MPa |
| Saturation coefficient, $\delta$ | 38.81 | |
| Weighing parameters, $\beta_1, \beta_2$ | 1.0 | |
| Plastic threshold, $W_0$ | 10/15 | MPa |
| Fracture toughness, $G_c$ | 50 | MPa mm |
| Characteristic length scale $l_c$ | 0.5 or 1.0 | mm |

Fig 4.32 where the plastic threshold is set to 10 MPa shows the crack initiation at the center of the specimen which agrees with the experimental observation in [55] shown in Fig. 4.36. Then, the crack propagates in a direction perpendicular to the loading direction leading to the final failure of the specimen. A final curvature of the crack surface is also confirmed by the experiments. It is clear that the crack surface follows the evolution of the equivalent plastic strain which is expected in ductile fracture. The evolution of the crack surface can also be shown in Fig. 4.32. A full description of the crack initiation and propagation can be accurately described by the algorithm. Fig. 4.33 shows the evolution of the phase field along with the crack surface where the plastic threshold is set to 15 MPa. It can be observed the same cracking pattern as in the previous case with a similar evolution of the crack surface in 3D.

The cracking simulation on a coarse mesh is simulated in Fig. 4.34. The crack is initiated at the center of the specimen where the plastic deformation is localized. However, the final crack path is straight, contrary to what is observed with the fine mesh. The force vs. displacement curves for the three cases can be seen in Fig. 4.37. The increase in the plastic threshold leads to a crack initiation at a larger displacement.

Finally, another simulation is carried out in order to test the effect of the remeshing indicator function on the cracking process. The phase field is used as an indicator for the mesh refinement

process with a threshold of 0.05 and the results are reported in Fig. 4.35 where a minimum element size of 0.25 mm is used in the refined zone. It can be observed that the final crack path is inclined with respect to the horizontal path shown in Fig. 4.32. It can also be observed that the evolution of the crack path follows the evolution of the equivalent plastic strain as expected in the case of ductile fracture. The reason for this observation is that the phase field is updated once the plastic energy exceeds the plastic threshold. In consequence, using the phase field threshold leads to a delay in the mesh refinement in the damaged zone and hence an inaccurate resolution of the plastic strains.

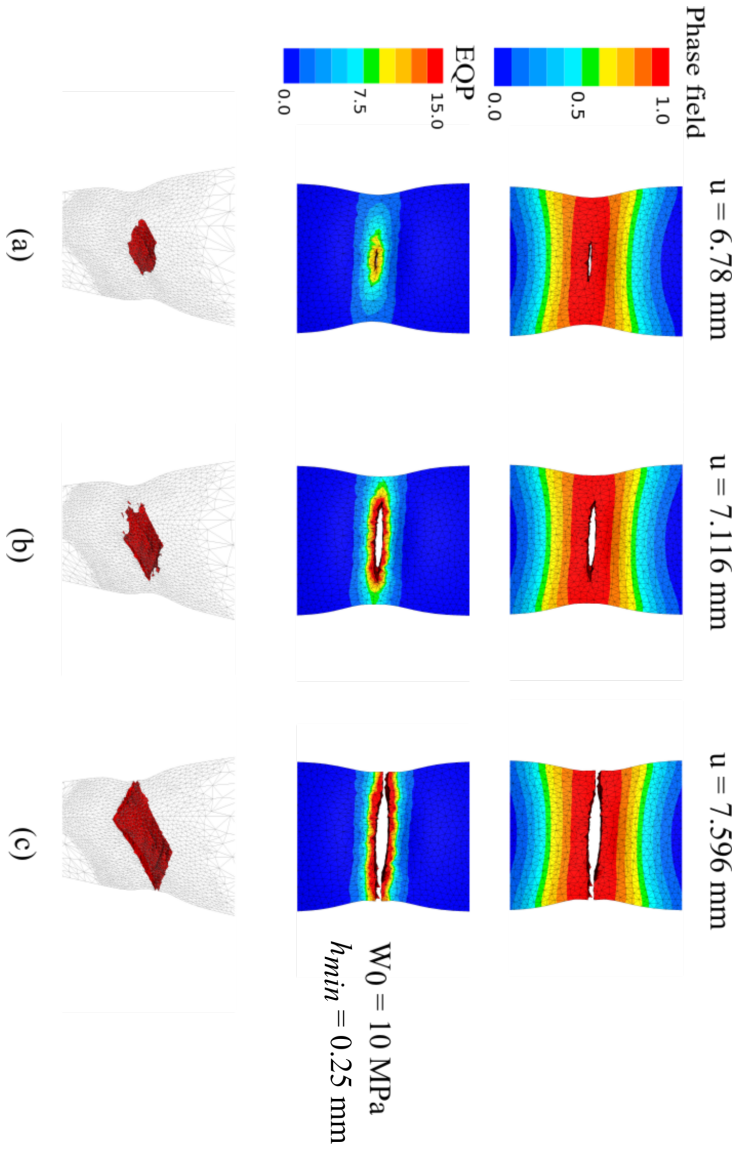


**Fig. 4.32** The evolution of phase field, equivalent plastic strain (EQP) and the crack surface evolution in 3D at three different different displacements. The minimum element size = 0.25 mm (fine mesh) with a plastic threshold = 10 MPa.

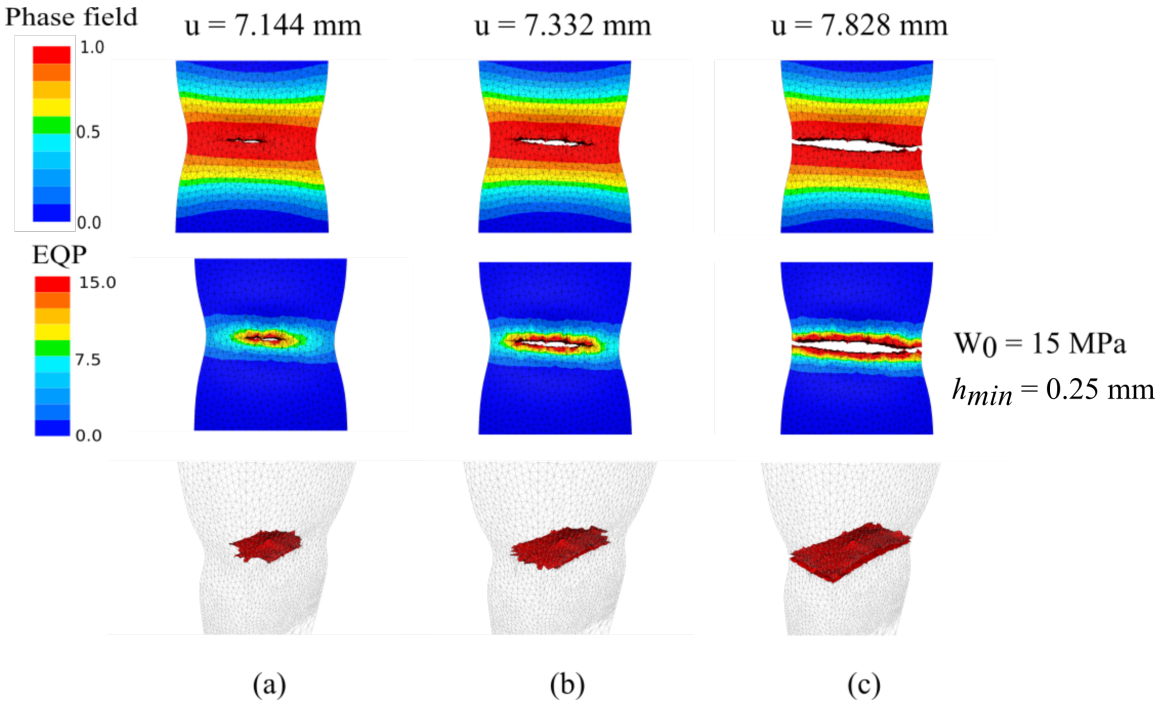


**Fig. 4.33** The evolution of phase field, equivalent plastic strain (EQP) and the crack surface evolution in 3D at three displacements. The minimum element size = 0.25 mm (fine mesh) with a plastic threshold = 15 MPa.

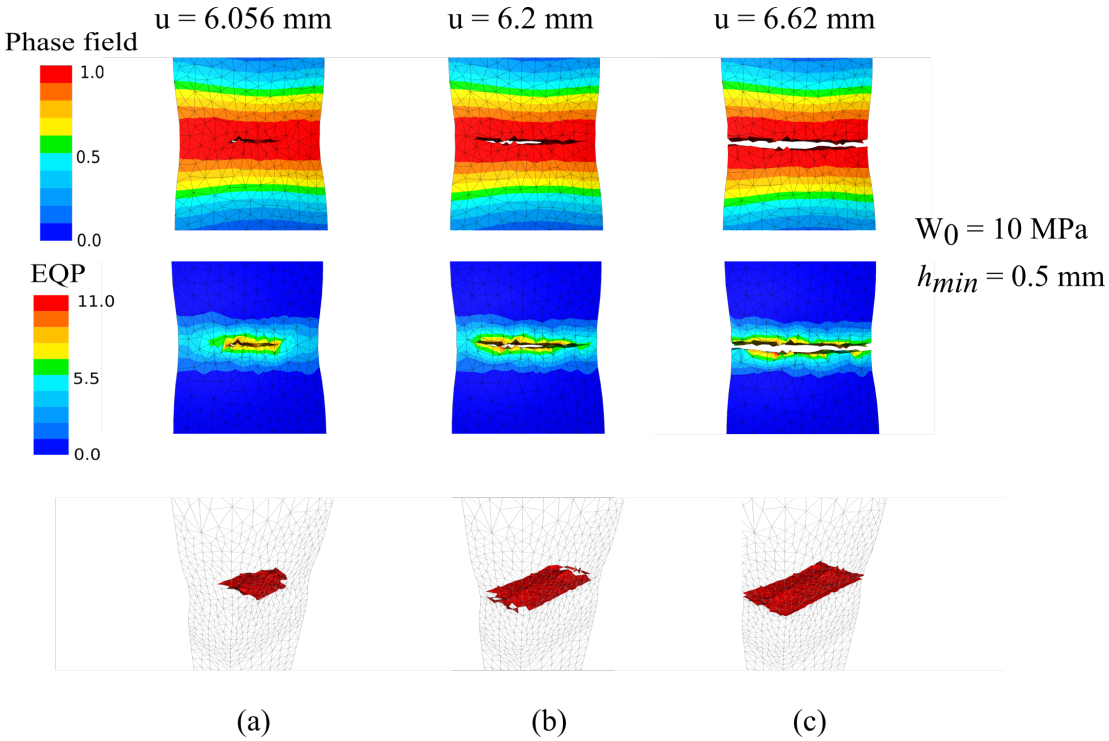


**Fig. 4.34** The evolution of phase field, equivalent plastic strain (EQP) and the crack surface evolution in 3D at three displacements. The minimum element size = 0.5 mm (coarse mesh) with a plastic threshold = 10 MPa.

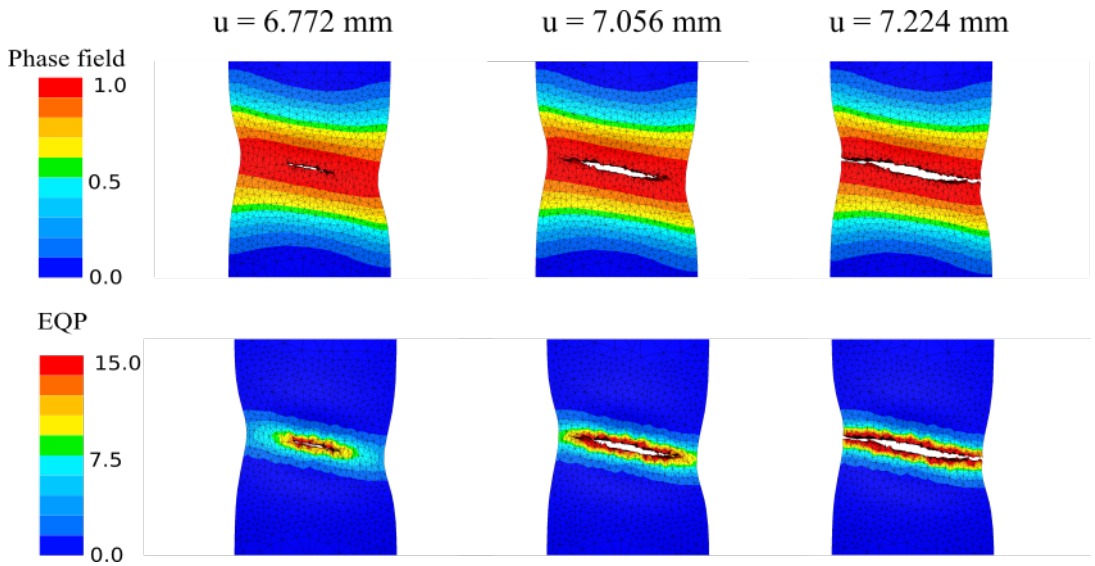


**Fig. 4.35** The evolution of phase field along with the effective plastic deformation EQP at three different displacements. The phase field is used an indicator function for the mesh refinement with a threshold of 0.05 as indicated in [57]. The final crack path is inconsistent with the experimental observations reported in [55].

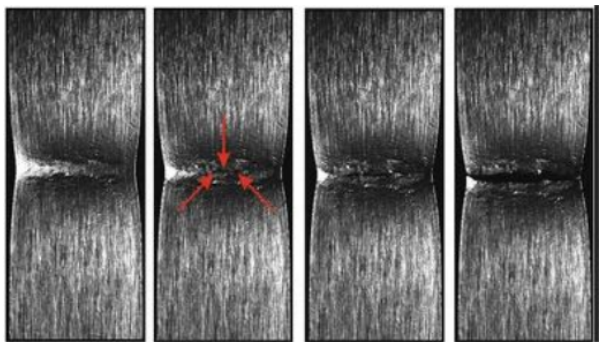

**Fig. 4.36** Experimental results showing the initiation and propagation of the crack until the final fracture [55].

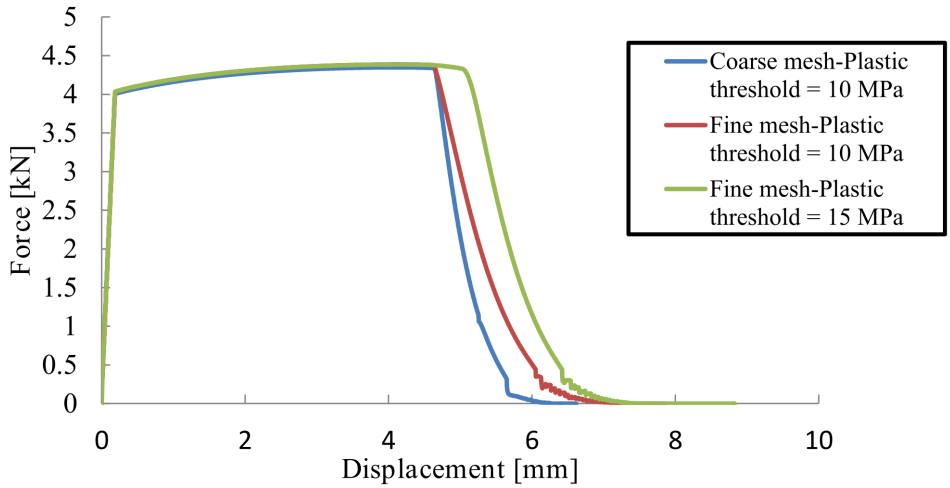


**Fig. 4.37** The force vs. displacement curves for fine and coarse meshes.

The developed algorithm is able to accurately predict the crack initiation location with good agreement with experimental observation. Once the phase field model parameters are well calibrated, a good matching in terms of final crack path and force vs. displacement response with the experiments can be achieved.

## 4.6 Summary of chapter 4

The main objective of this chapter is to introduce a fully parallel numerical algorithm for the modeling of crack initiation and propagation in ductile materials. The algorithm introduces a combination of the phase field model adapted for ductile fracture and adaptive remeshing tools. First, an adaptive remeshing strategy is used in order to sufficiently refine the mesh where the crack is expected to propagate. Then, an agnostic crack surface identification method is developed in order to find the intersection of the discrete crack surface with the mesh edges. Next, a mesh partitioning strategy is developed in order to divide an initial element where the crack surface is expected to cross. Many advantages arise from the proposed partitioning scheme: (i). the uniqueness of the partitioned elements facilitates the algorithm parallelization; (ii). the algorithm is highly efficient because the partitioning scheme has a linear proportionality to the number of intersected elements, making it perfectly scalable. The next step is the nodal duplication in order to simulate the decohesion of the crack surfaces. In this regard, a coloring algorithm is used in order to locally determine the number of new duplicated nodes and the elements sharing each copy. The same operations are repeated until the final crack path is obtained.

Three numerical examples are presented in this work. First, a symmetric double-notched specimen is used in order to simulate mode I of fracture. The results have shown that the crack is initiated at the two notches simultaneously and propagated toward the center until the specimen complete fracture is reached. Second, a mixed fracture mode is simulated through the ductile fracture simulation of an asymmetric double-notched specimen. It has been shown that two cracks initiate at the two notches and propagate in a curved path toward the center of the specimen which can be observed experimentally. When a stress triaxiality function is added to the crack driving force, cracks are initiated where the stress triaxiality is maximum close to the free surface but not at the notch boundary. Finally, a flat tensile specimen is tested and results are compared with experimental observations. The main aim of this example was to show the crack initiation at the center of the specimen and the propagation of the crack leading to a horizontal final path with some curvature of the crack surfaces.

In the three examples, parametric studies are carried out to see the effect of phase field and crack insertion models parameters, the effect of mesh size on the final crack path as well as the force vs. displacement curves. The three examples show the robustness of the developed strategy to handle damage to fracture transition in a 3D parallel environment.

## 4.7 Résumé en français

L'objectif principal de ce chapitre était d'introduire un algorithme numérique entièrement parallèle pour modéliser l'amorçage et la propagation de fissures dans les matériaux ductiles. L'algorithme introduit une combinaison du modèle de champ de phase de de techniques remaillage adaptatif. Tout d'abord, une stratégie de remaillage adaptatif est utilisée afin d'affiner suffisamment le maillage où la fissure va se propager. Ensuite, une méthode d'identification de surface de fissure agnostique est développée afin de trouver l'intersection de la surface de fissure discrète avec les bords du maillage. Une stratégie de partitionnement local du maillage est développée afin de diviser chaque élément tétrahedre initial où la surface de la fissure est prévu d'intersecter le maillage. Il y a de nombreux avantages au schéma de partitionnement proposé : (i). l'unicité des éléments partitionnés facilite la parallélisation de l'algorithme ; (ii). l'algorithme est très efficace car le schéma de partitionnement est linéarement proportionnel au nombre d'éléments intersectés, ce qui le rend parfaitement évolutif. L'étape suivante est la duplication nodale afin de simuler la décohésion des surfaces des fissures. Un algorithme de coloration locale est adapté pour déterminer localement le nombre de nouveaux nœuds dupliqués et les éléments partageant chaque copie. Les mêmes opérations sont répétées jusqu'à l'obtention du chemin final de fissure.

Trois exemples numériques sont présentés dans ce travail. Tout d'abord, une éprouvette symétrique à double encoches est utilisée afin de simuler le mode I de rupture. Les résultats ont montré que la fissure s'est amorçée aux deux entailles simultanément et se propage vers le centre jusqu'à ce que la rupture complète de l'éprouvette soit atteinte. Deuxièmement, un mode de rupture mixte est simulé à travers une éprouvette à double encoches asymétrique. Il a été montré que deux fissures s'amorcent au niveau des deux encoches et se propagent selon un trajet courbe vers le centre de l'éprouvette, ce qui peut être observé expérimentalement. Lorsqu'une fonction de triaxialité des contraintes est ajoutée à la "Crack driving force", les fissures se sont amorçées proches des bords des encoches mais pas vraiment en extrême surface des encoches où la triaxialité des contraintes est maximale. Enfin, une tôle mince est soumise à un essai de traction. Les résultats sont comparés aux observations expérimentales. L'objectif principal de cet exemple était de montrer l'amorçage de la fissure au centre de l'éprouvette et la propagation de la fissure menant à un chemin final horizontal avec une certaine courbure des surfaces de la fissure.

Dans les trois exemples, une étude paramétrique est réalisée pour voir l'effet du champ de phase et des paramètres des modèles d'insertion de fissure, l'effet de la taille de mailles sur le chemin final de la fissure ainsi que les courbes force vs déplacement. Les trois exemples montrent la robustesse de la stratégie développée pour gérer la transition endommagement-fracture dans un environnement parallèle 3D.

# Ductile fracture under complex loading conditions: application to metal forming processes

## Contents



*This chapter is an extended version of the following paper:*

**H. Eldahshan, D. P. Munoz., J. Alves, E. Perchat and P.-O. Bouchard, "3D crack initiation and propagation applied to metal forming processes", (Under review in International Journal of Material Forming), (2021).**

## 5.1 Introduction

In the previous chapter, it has been demonstrated that adding the effect of stress triaxiality to the crack driving force leads to an accurate description of the crack initiation and propagation. In consequence, the inclusion of other factors that represent the stress state in the material is essential. The main objective of this chapter is to propose a new form of the crack driving force through a coupled phase field-damage formulation. This model takes advantage of the accurate geometric representation of the crack topology offered by the phase field model. In addition, it makes use of the rich damage models that are presented in the literature.

The next analysis starts with an explanation of the main mathematical features of the proposed model in addition to its physical interpretation. Then, numerical analysis of a bar shearing problem is demonstrated where different damage models are used. The aim of this example is to show the ability of the proposed model to handle complex crack initiation and propagation patterns when different damage driving factors are used. Next, the model is used to predict multiple crack initiations followed by the merging of crack branches of a symmetrically notched specimen subjected to a tensile loading. The objective of the second example is to show that the numerical results obtained with the proposed model can be matched with the experimental observations.

The next part of this chapter is dedicated to applying the model on different metal forming processes. The first example deals with the initiation of internal cracks during the bar extrusion process that need to be avoided. Then, inducing fracture surfaces during blanking processes is also demonstrated. Finally, a multi-stages production process is analyzed in order to see the effect of each stage on the following ones. In this case the proposed model is used to simulate the creation of crack surfaces in the first two stages and then to predict a possible crack initiation that should be avoided in the last stage.

## 5.2 Coupling the phase field model with continuous damage models

In order to simulate the different damaging mechanisms in the metal forming applications while taking advantage of the mathematical features of the phase field formulation, a coupling between the phase field and a local damage variable is presented through the crack driving force as follows

$$\begin{cases} d - l_c^2 \nabla^2 d = 2(1-d)\,\mathcal{H}(\underline{\mathrm{x}}, t) \text{ (Evolution of the phase field)} & \text{(5.1a)} \\ \mathcal{H} = \eta_c \left\langle D - D_{thresh} \right\rangle \text{ (Local history functional)} & \text{(5.1b)} \\ \boldsymbol{\sigma} = (1-d)^2 \dfrac{\partial W_e}{\partial \boldsymbol{\varepsilon}^e} \text{ (Stress tensor degradation)} & \text{(5.1c)} \end{cases}$$

$D$ is a local damage field, $\eta_c$ is a material parameter used to control the post-peak stress response of the material by controlling the amount of effective energy needed to create the crack surfaces once the crack is initiated and $D_{thresh}$ is a damage threshold value. This model is motivated because it benefits from the rich formulations of damage models in the literature which can be easily coupled in any numerical code. Second, it benefits from the phase field model characteristics such as the non-dependency of the solution on the mesh size and the high localization of the field in the cracked zone. It should be noted that the introduction of two new model parameters would need a re-calibration of the model and thus more experiments should be carried out.

The effect of the model parameters on the phase field evolution can be demonstrated in a one dimensional case with a homogeneous solution of the equation 5.2, i.e., the Laplacian term is set to zero.

$$d = \frac{2\eta_c \langle D - D_{thresh} \rangle}{1 + 2\eta_c \langle D - D_{thresh} \rangle}. \tag{5.2}$$

The effect of each parameter on the evolution of the phase field variable is demonstrated in Fig. 5.1. It can be noticed that an increase in the damage threshold $D_{thresh}$ leads to a delay in the phase field triggering. On the other hand, an increase in the fracture parameter $\eta_c$ increases the rate of phase field evolution due to the void coalescence.

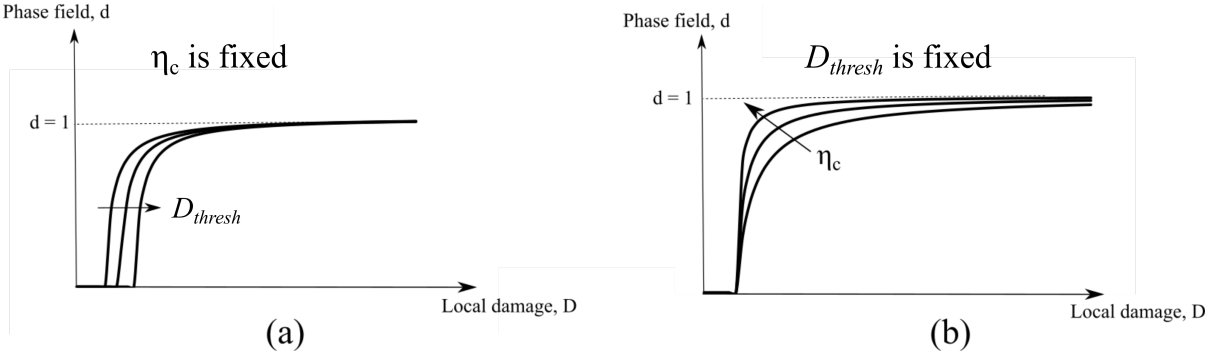


**Fig. 5.1** The effect of model parameters on the evolution of the phase field in a 1D homogeneous solution. The effect of $D_{thresh}$ is shown in (a) and the effect of $\eta_c$ is shown in (b).

A similar form for the local history functional $\mathcal{H}$ was proposed in [84] where a quadratic function of the equivalent plastic strain is used to drive the crack evolution. It should be noted that more complex formulas of $\mathcal{H}$ can be also proposed in the future.

### 5.2.1 Physical interpretation of the model

The physical sense of the phase field evolution can be justified as follows: during the void nucleation and growth phases, i.e., before reaching the damage threshold value $D_{thresh}$, the effect of void nucleation and growth on the material softening behaviour is not taken into account through the phase field variable. Then, the phase field is triggered when $D = D_{thresh}$ which

represents the beginning of the void coalescence phase. The fracture parameter $\eta_c$ controls the rate at which the void coalescence affects the material behaviour, in particular, Young's modulus and the yield surface. When $d = 1$, a crack is initiated at the macro-scale in which the material has lost its load carrying capacity.

Conceptually, ductile damage $D$ can be either an uncoupled damage variable (fracture criterion) if the softening effect due to damage evolution is neglected. It can also be a continuum damage variable (such as the Lemaitre model) or a void volume fraction such as the one offered by the Gurson's model if the softening effect should be taken into account. Therefore, *from now on, the word "damage" is referred to the local damage field that is used in the local history functional which can be either an uncoupled damage model, a continuum damage mechanics model, or a micro-mechanics porosity function.*

In the following analysis, a schematic representation of a 1D tension case is used to illustrate the main features of the proposed model for each category of damage models. The effect of coupling the phase field model with an uncoupled damage criteria can be explained by Fig. 5.2. In the phase **A**, it is assumed that no mechanical softening exists (this assumption is adopted in many metal forming processes). In this case, the effect of void nucleation and growth on both the Young's modulus and yield surface is not taken into account. Once the damage value reaches the limit $D = D_{thresh}$, the softening phase **B** begins by triggering the phase field variable. Once the maximum value of the phase field reaches a value of one, a full crack is formed and the material loses its load carrying capacity. Most importantly, the fracture parameter $\eta_c$ can be tailored such that the softening rate matches the experimental observation.

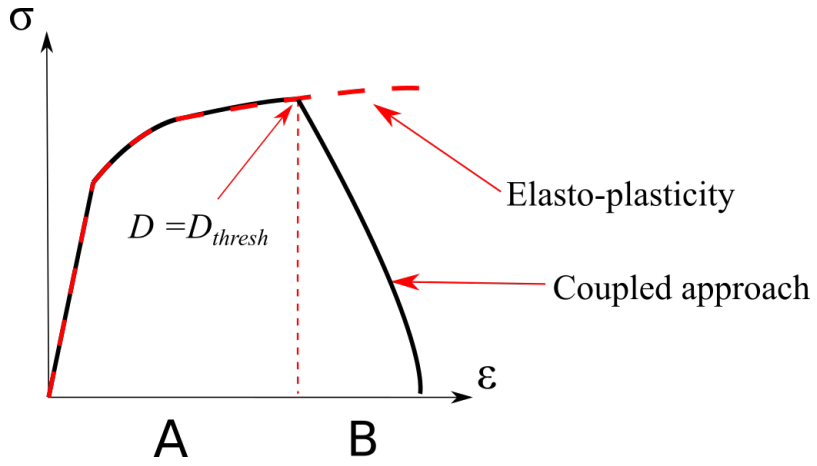


**Fig. 5.2** Illustration of the effect of coupling the phase field with an uncoupled damage model on the Stress vs. Strain curve.

In order to show the effect of coupling the phase field with a micro-mechanics porosity model, Aldakheel et al. proposed a similar coupling strategy between the GTN plasticity model with the phase field model through the use of the void volume fraction in the local history functional as follows [68]

$$\mathcal{H} = \zeta\langle\frac{f}{f_{cr}} - 1\rangle \tag{5.3}$$

with

$$f = f_{nucleation} + f_{growth} \tag{5.4}$$

where $f_{cr}$ is a critical void volume fraction and $\zeta$ is a fracture parameter used to control the post-critical range once the phase field evolution is triggered. Fig. 5.3 explains the idea of the proposed coupling methodology using the force vs. displacement curve. The **A** phase represents the elastic regime with the assumption of no void nucleation. Then, the void nucleation and growth mechanisms lead to a softening behaviour which can be seen in the phase **B**. This is due to the degradation of the yield surface predicted by the GTN model (without any effect from the phase field). Once the point at which $f = f_{cr}$ is reached, the phase field evolution is triggered in order to represent the void coalescence phase at the macro-scale. The fast drop in the load carrying capacity as seen in the phase **C** is explained by combined effect of the degradation of Young's modulus due to the phase field evolution and the degradation of yield surface due to the evolution of void volume fraction. The model is able to reproduce the well known cup-cone fracture pattern with an excellent agreement of the obtained force vs. displacement curve [68].

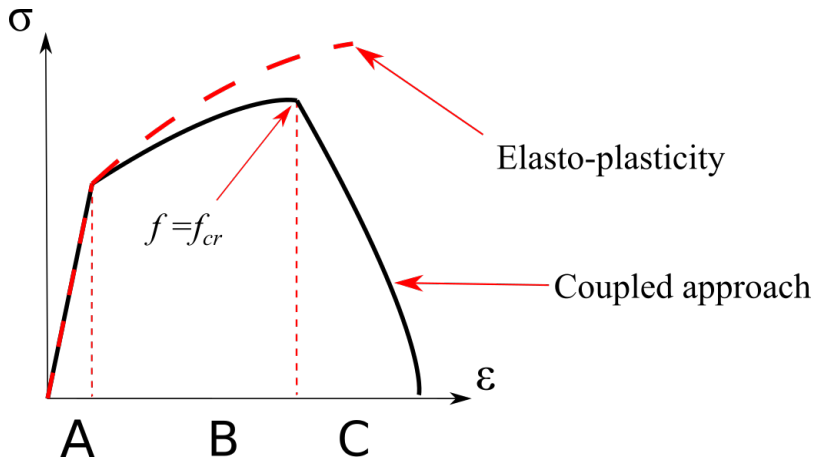


**Fig. 5.3** Stress vs. Strain curve showing the coupling between GTN plasticity and phase field models proposed in [68].

In order to illustrate the ability to use a continuum damage mechanics model such as the Lemaitre damage model to drive the phase field evolution, Fig. 5.4a shows the relationship between the local Lemaitre variable $D$ and the equivalent plastic strain $\varepsilon$ in 1D. The damage evolution is triggered when $\varepsilon = \varepsilon_D$ where $\varepsilon_D$ is the equivalent plastic strain at damage initiation and it is treated as a material parameter. It can be seen on the force vs. displacement curve in Fig. 5.4c that the damage variable is not updated in the elastic domain denoted by **A** and in the first part of the plastic domain denoted by **B** that is associated with void nucleation. In consequence, the phase field variable is not yet updated until this moment. Then, the damage

variable is updated when $\varepsilon = \varepsilon_D$ due to the void growth in which a softening behaviour can be seen in the phase **C** in the plastic domain as shown in Fig. 5.4c. Until this moment, the phase field is not yet initiated as seen in Fig. 5.4b. However, the effect of material softening can be taken into account by degrading the stress tensor with the linear degradation function used in the Lemaitre model as follows

$$\boldsymbol{\sigma} = (1 - D)\, \mathcal{C}_0 : \boldsymbol{\varepsilon}^e \tag{5.5}$$

where $\mathcal{C}_0$ is the initial stiffness tensor. Once the damage reaches the value $D_{thresh}$ which corresponds to a plastic strain value $\varepsilon_{thresh}$, the phase field is triggered in order to represent the void coalescence phase in the material. At this moment, the mechanical coupling is now carried out through the quadratic degradation function of the phase field (the damage variable $D$ has no effect on the material behaviour at this point) as follows

$$\boldsymbol{\sigma} = (1 - d)^2\, \mathcal{C}^* : \boldsymbol{\varepsilon}^e \tag{5.6}$$

where $\mathcal{C}^*$ is the degraded stiffness tensor at the beginning of the void coalescence phase which can be expressed as follows

$$\mathcal{C}^* = (1 - D_{thresh})\, \mathcal{C}_0. \tag{5.7}$$

The phase field variable with quadratic degradation rate for both Young's modulus and the yield surface reflects the impact of the void coalescence at the micro-scale to the crack initiation at the macro-scale. This softening phase can be seen in the final phase **D** on the force vs. displacement curve in Fig. 5.4c. The rate of phase field evolution can be then controlled by changing the parameter $\eta_c$ as seen in Fig. 5.4b. Finally a crack at the macro-scale is initiated when $d \to 1$ which corresponds to the complete loss of the load carrying capacity of the material. This point can be also linked to the critical damage value $D_c$ predicted by the Lemaitre model.

A 1D test case under tensile loading is used in order to show the effect of the model parameters on the behaviour of the material. The Lemaitre damage variable with a constant stress triaxiality ratio of $\frac{1}{3}$ in 1D can be written as [62]

$$D = D_c \frac{\varepsilon - \varepsilon_D}{\varepsilon_R - \varepsilon_D}, \tag{5.8}$$

in order to get an initial estimation about the values of two model parameters $D_{thresh}$ and $\eta_c$, the following condition should be satisfied

$$D = D_c \to d \geq d^*, \tag{5.9}$$

this condition means that the phase field $d$ should attain a value of $d^*$ close to one (almost

broken material) when the local damage $D$ reaches the critical value $D_c$ that can be obtained experimentally. In the following calculations, $d^*$ is chosen to be 0.95. Substituting the previous condition in equation 5.2 leads to

$$\eta_c \geq \frac{d^*}{2(D_c - D_{thresh})(1 - d^*).} \tag{5.10}$$

The material and model parameters can be found in Table 5.1.

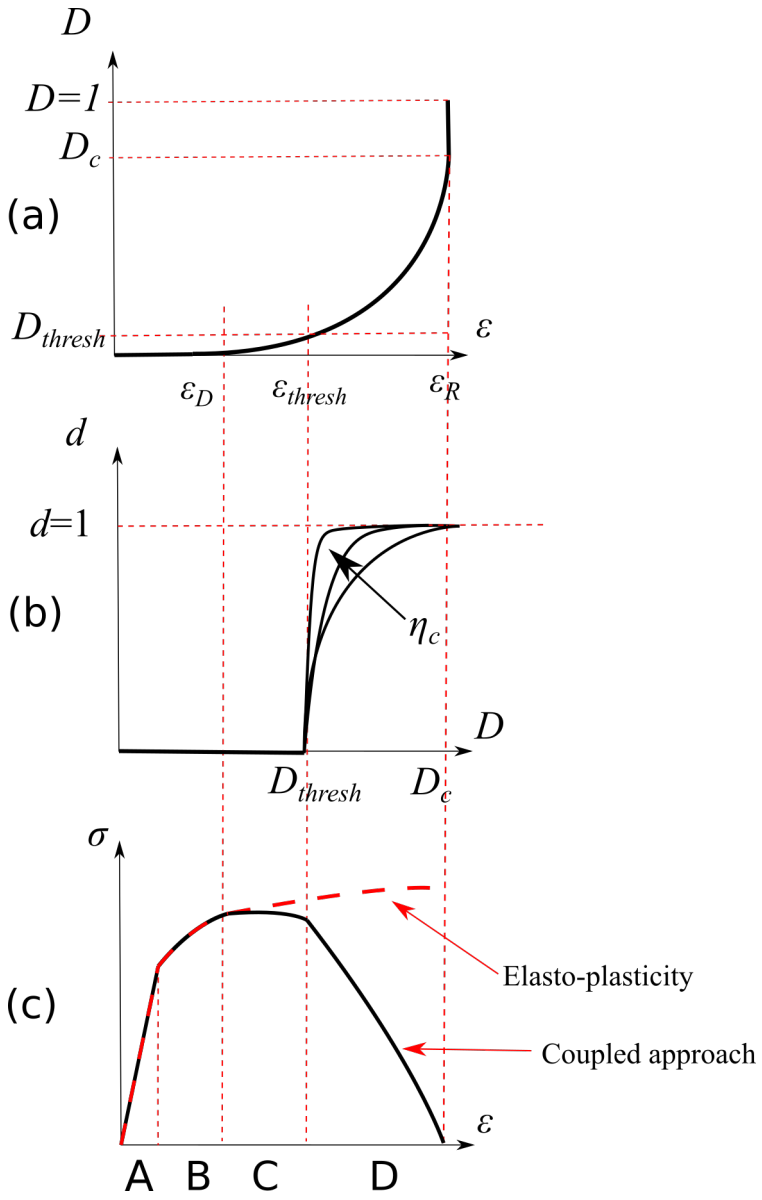


**Fig. 5.4** The relationship between a continuum damage mechanics (CDM) variable $D$ and equivalent plastic strain $\varepsilon$ is shown in (a). The relationship between the phase field $d$ and the damage variable is shown in (b). The Stress vs. Strain diagram is shown in (c).

**Table 5.1** Material and model parameters

| Quantity | Value | Unit |
|---|---|---|
| Young's modulus, $E_0$ | 200000 | MPa |
| Poisson's ratio, $\nu$ | 0.3 | |
| Yield stress, $\boldsymbol{\sigma}_y$ | $200(\varepsilon + 0.1)^{0.8}$ | MPa |

Fig. 5.5 shows the effect of $D_{thresh}$ on the phase field, the material degradation ratio of both Young's modulus and the yield surface and the Stress vs. Strain curve. It can be shown in Fig. 5.5a that the phase field variable is not initiated when $D \leq D_{thresh}$ as expected by the model. However, the linear degradation starts at an earlier stage when $\varepsilon = \varepsilon_D$ as shown in 5.5b in order to reflect the effect of void growth on the material behaviour.

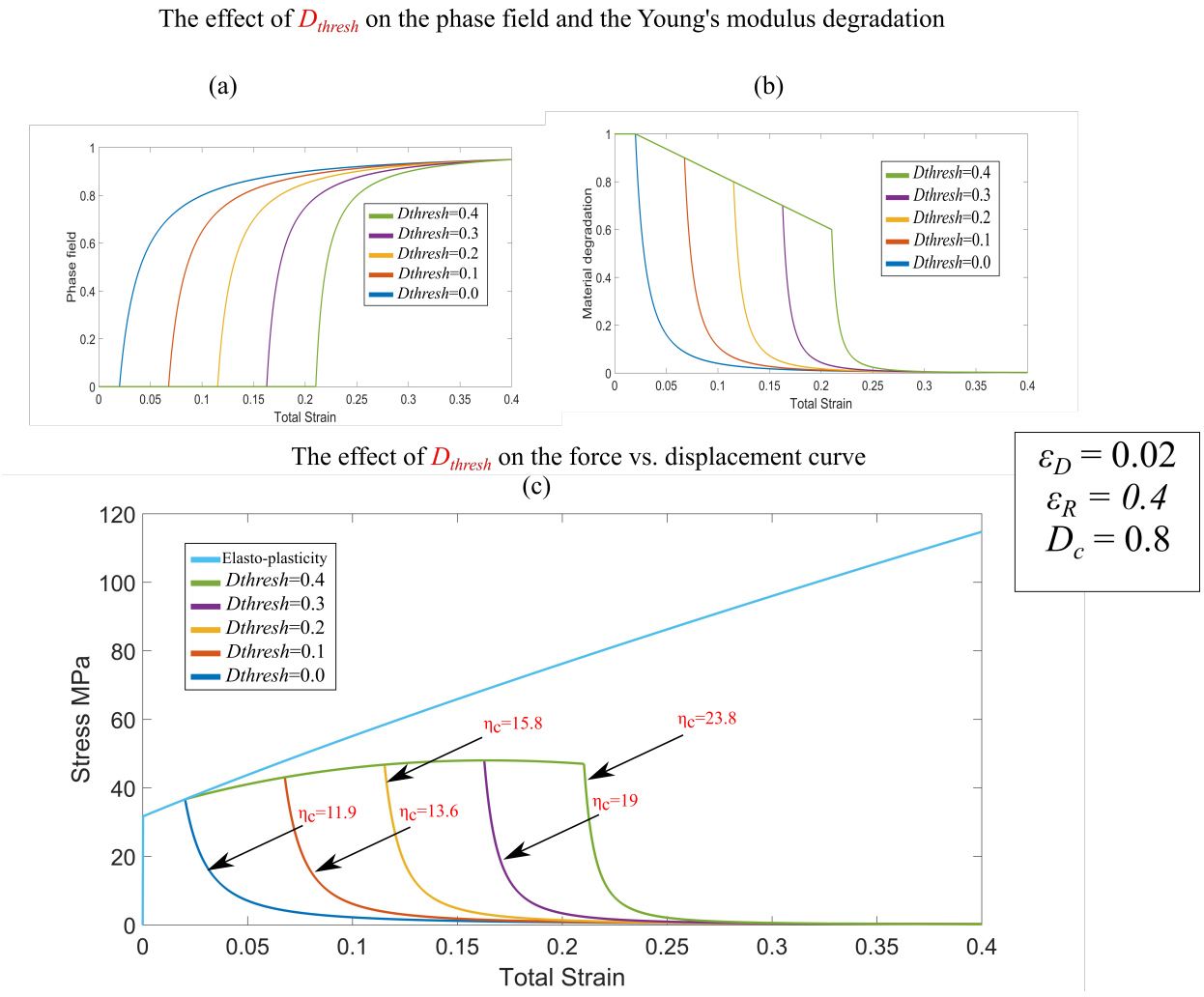


**Fig. 5.5** The effect of $D_{thresh}$ on the phase field evolution is shown in (a). The material degradation for different values of $D_{thresh}$ is shown in (b). The Stress vs. Strain curves for different values of $D_{thresh}$ is show in (c) where the corresponding values of $\eta_c$ are plotted for each curve.

Once the condition of $D = D_{thresh}$ is reached, the phase field is triggered with a fast drop

in the material degradation in order to reflect the effect of void coalescence. Fig. 5.5c shows the Stress vs. Strain curves for different values of $D_{thresh}$ where the calculated values of $\eta_c$ from equation 5.30 are plotted.

It can be observed that the model is able to predict the coupled effect of material softening due to void growth followed by a fast drop in the load carrying capacity as the phase field is triggered. It is also clear that the stress drop in post-critical regime is accelerated with the increase of $\eta_c$ so that the final failure occurs when $D = D_c$ regardless of the value of $D_{thresh}$.

Fig. 5.6a shows the Lemaitre damage evolution for different values of $D_c$ where all the other parameters are kept fixed. It can be observed that the damage evolution rate in this case increases with the increase in $D_c$ since the strain value at fracture $\varepsilon_R$ is fixed. As seen in Fig. 5.6 the phase field is triggered earlier with the increase of $D_c$ even if $D_{thresh}$ is fixed.

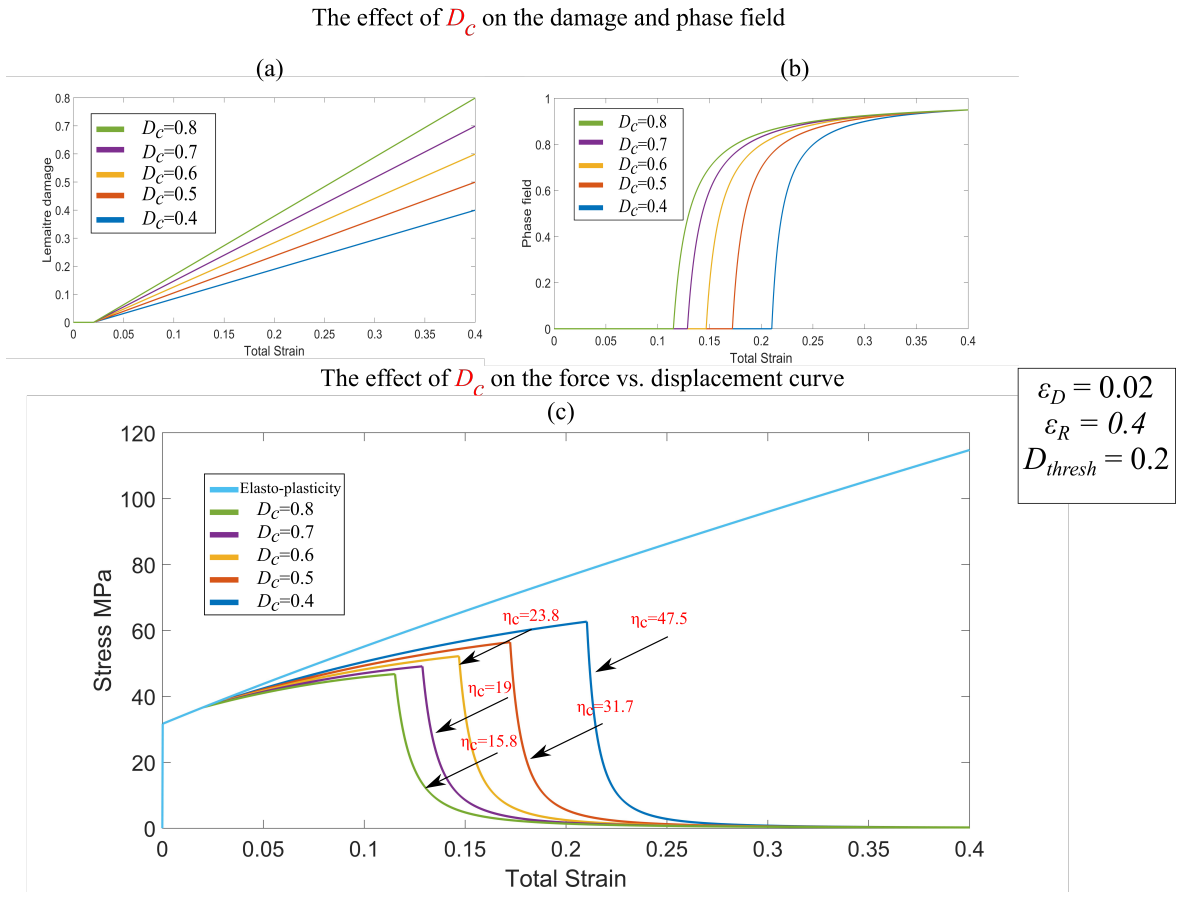


**Fig. 5.6** The effect of $D_c$ on the damage evolution is shown in (a). The phase field evolution for different values of $D_c$ is shown in (b). The Stress vs. Strain curves for different values of $D_c$ is show in (c) where the corresponding values of $\eta_c$ are plotted on the each curve.

This conclusion can be physically explained as follows: the higher rate of void growth results in triggering the void coalescence at a lower strain value. However, the material has lost its load carrying capacity at the same strain value since $\varepsilon_D$ is the same for all cases. In reality, the value of $\varepsilon_D$ usually increases with the increase in $D_c$ so that the increase of $D_c$ delays the initiation of the softening phase.

The effect of the parameter $D_c$ on the Stress vs. Strain curves can be illustrated in Fig. 5.6c. As expected, the delay in the phase field initiation at low values of $D_c$ leads to a slow softening rate due to damage accumulation and a delay in the stress drop phase. However, the parameter $\eta_c$ is automaticall y set to a proper value so that the material failure occurs at the defined values of $D_c$. For example, for lower $D_c$ values, $\eta_c$ becomes larger because the void coalescence process occurs in shorter strain range.

It is worth noting that a damage field regularization is necessary in this case in addition to the phase field regularization. Thus, one can imagine a two-length scales model for the regularization of both the void growth phase (usually associated with a slow material softening) and void coalescence phase (associated with a fast drop in the load carrying capacity). Miehe et al. proposed in [142] a gradient plasticity model that defines two independent length scales for the phase field computations. The main advantage of this model is to ensure that the phase field evolution zone is always inside the plastic deformation zone. Thus, mesh independent solutions are guaranteed.

To conclude, the role of the phase field variable in the proposed model is to model the transition from the phase of void nucleation at the micro-scale to the formation of cracks at the macro-scale. This transition can be controlled through the parameter $\eta_c$ that only affects the post-critical regime in the Stress vs. Strain curve once the damage threshold is reached. The coupling with the different types of damage models enables a good prediction of the effect of micro-structural effects on the material behaviour before the void coalescence phase. In addition to that, the coupling with the phase field results in a controlled coalescence regime in the material.The most important advantage of the model is its ability to represent the sharp crack topology without a significant diffusion of the field when the phase field reaches a value of one.

The next important part is the experimental calibration of the model parameters. It is clear that the addition of two additional model parameters makes the calibration process more difficult than the case of classical non-local damage models. For the experimental calibration of the phase field model parameters, the curve fitting strategy proposed by Bouchard et al. in [75] can be adopted. Additional experiments with different loading conditions are carried out to obtain force vs. displacement curves. Then, the cost function is constructed to minimize the error between the force obtained in the experiment and the simulation results. In order to ensure the uniqueness of the predicted parameters, full field measurements such as the local displacement field can be used to improve the optimization process by obtaining a unique set of parameters.

## 5.3 The effect of damage model on crack initiation and propagation

In this section, different uncoupled damage models are tested with the phase field model presented in the previous section. The aim here is to show the capability of predicting complex

cracking patterns in the metal forming domain with the proposed model. Fig. 5.7 shows the geometry and boundary conditions of a bar subjected to shear loading. The initial mesh size is set to 1 mm and reduced to 0.4 mm in the regions where the equivalent plastic strain exceeds a given threshold. A time step of 0.001 s is used until the maximum value of the phase field reaches 0.1 and reduced to 0.0005 s for the rest of computations. The Coulomb limited by Tresca friction law is used for the tangential contact between the different dies and the billet. Four damage criteria are used to simulate the initiation and propagation of cracks during the shearing process. It was decided here to choose four different fracture criteria where the driving factor is either the maximum principal stress $\boldsymbol{\sigma}_1$ (only positive values), the von Mises equivalent stress $\bar{\boldsymbol{\sigma}}$ (only positive values), the stress triaxiality ratio $\eta$ (only positive values) or the maximum shear stress $\frac{\boldsymbol{\sigma}_1-\boldsymbol{\sigma}_3}{2}$.

It should be noted that the effect of the Lode angle parameter (or equivalently the Lode parameter) on the damage evolution is not discussed in the present work and left for a future exploration. The material and model parameters are listed in Table 5.3. It should be noted that the choice of all the model parameters here is based on the trial and error in order to give a similar crack initiation moment and propagation rate. The value of the effective crack area $A_{fixed}$ is chosen as two times the minimum mesh size in all the following cases.

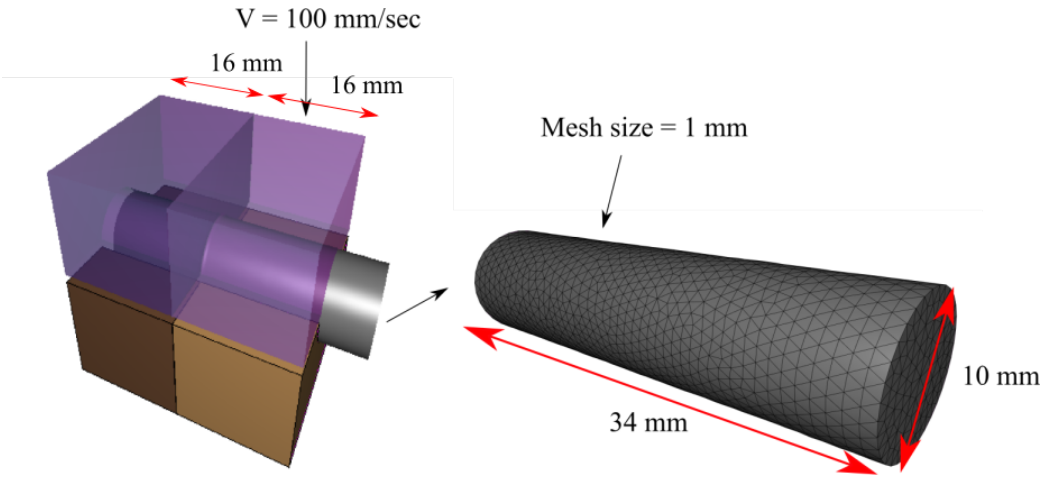


**Fig. 5.7** Geometry and boundary conditions of a bar subjected to shear loading.

**Table 5.2** Damage models used for the coupled phase field simulations

| Model number | Damage model | Driving parameter |
|---|---|---|
| 1 | $D = \int_0^{\bar{\varepsilon}} \frac{\langle \boldsymbol{\sigma}_1 \rangle}{\bar{\boldsymbol{\sigma}}} \, d\bar{\varepsilon}$ (Normalized Latham-Cockcroft) | Maximum principal stress $\boldsymbol{\sigma}_1$ |
| 2 | $D = \int_0^{\bar{\varepsilon}} \frac{\bar{\sigma}}{A} \, d\bar{\varepsilon}$ | von Mises stress $\bar{\boldsymbol{\sigma}}$ |
| 3 | $D = \int_0^{\bar{\varepsilon}} C_1 e^{C_2 \langle \eta \rangle} \, d\bar{\varepsilon}$ (Generalized Rice-Tracey) | Stress triaxiality $\eta$ |
| 4 | $D = \int_0^{\bar{\varepsilon}} \frac{\boldsymbol{\sigma}_1-\boldsymbol{\sigma}_3}{\bar{\boldsymbol{\sigma}}} \, d\bar{\varepsilon}$ | Maximum shear stress $\boldsymbol{\sigma}_1 - \boldsymbol{\sigma}_3$ |

**Table 5.3** Material and model parameters

| Quantity | Value | Unit |
|---|---|---|
| Young's modulus, $E$ | 200000 | MPa |
| Poisson's ratio, $\nu$ | 0.3 | |
| Yield stress, $\boldsymbol{\sigma}_y$ | $A\,\bar{\boldsymbol{\varepsilon}}^{0.1845}\,\dot{\bar{\varepsilon}}^{0.012}$ | MPa |
| $A$ | 818 | MPa |
| Characteristic length scale $l_c$ | 0.5 | mm |
| Damage model 1 | | |
| Damage threshold, $D_{thresh}$ | 0.1 | |
| Fracture parameter, $\eta_c$ | 200 | |
| Damage model 2 | | |
| Damage threshold, $D_{thresh}$ | 0.1 | |
| Fracture parameter, $\eta_c$ | 50 | |
| Damage model 3 | | |
| Damage threshold, $D_{thresh}$ | 0.05 | |
| Fracture parameter, $\eta_c$ | 200 | |
| $C_1/C_2$ | 2/1 | |
| Damage model 4 | | |
| Damage threshold, $D_{thresh}$ | 0.2 | |
| Fracture parameter, $\eta_c$ | 100 | |
| Coulomb/Tresca friction coefficient | 0.2/0.4 | |
| Penalisation parameter $\epsilon_n$ | 100 | |
| Mesh adaptation threshold (EQP) | 0.05 | |

Fig. 5.8 shows the phase field evolution and the crack surfaces propagation for the different damage models. Different observations can be found from the results. Starting with the first damage model, it can be seen in Fig. 5.8a that two cracks are initiated at the left and right boundaries of the sheared zone. The two crack branches continue to propagate perpendicular to the loading direction. The two branched cracks are merged at the upper and lower boundaries leading to the formation of the full crack surface. Fig. 5.9 shows the phase field evolution at two points A and B. The results here are shown for the first damage model that is driven by the maximum principal stress. The two points are chosen such that points A and B are placed at the upper and left boundaries of the sheared zone (the lower and right boundaries are expected to have the same results due to symmetry). It can be shown that the phase field evolution is initiated at point B earlier than point A since the damage evolution is faster at this point. This evolution finally results in a crack initiation at the left and right boundaries before the initiation at the upper and lower boundary. This result is confirmed in Fig. 5.11. It can be shown that

the evolution of maximum principal stress at point B starts from the beginning and continues to increase until the crack is initiated. On the other hand, the maximum principal stress evolution at point B starts at a very late stage which then leads to the crack initiation at the upper and lower boundaries.

When the second damage model is adopted, it can be shown in Fig. 5.8b that the crack branches are initiated at the upper and lower boundaries in contrast to to what was observed with the first damage model. This is explained by the fact that the von Mises stress at point A is always higher than point B as shown in Fig. 5.11. This implies that the evolution of plastic deformation at point A is responsible for the crack initiation (this conclusion is due to the fact that von Mises stress is responsible for the evolution of plastic strain according to the $J_2-$ plasticity theory that is adopted here).

Fig. 5.10 shows the loading path for points A and B when the first damage model is used. Plotting the equivalent plastic strain vs. stress triaxiality evolution curve, it can be observed that point A is always under compression during the loading process with relatively high negative values of stress triaxiality. On the other hand, point B is subjected to a tensile loading with a value of $\eta \sim 0.2$. If the crack is initiated at the position of maximum stress triaxiality, it is suggested to use a damage model that is based on the positive stress triaxiality values. As shown in Fig. 5.8c, the third damage model leads to a crack initiation at the upper and lower boundaries of the sheared zone as expected. However, it can be also observed that a crack is initiated at the upper boundary far from the sheared zone. Fig. 5.12 shows the stress triaxiality evolution at points A (placed at the upper sheared zone boundary) and C (placed at a distance far from the upper boundary) as shown in Fig. 5.8c. It is clear that the stress triaxiality at point A is always negative. On the other hand, point C has a positive stress triaxility that led to the damage accumulation and hence a crack initiation in this zone.

Finally, a fourth damage field based on the normalized maximum shear stress is used as a source term for the phase field evolution. This choice is motivated by the shear dominant loading. As can be observed in Fig. 5.8d, the phase field evolution indicates that two crack branches are initiated at the upper and lower boundaries of the sheared surface. The two crack branches continue to propagate toward the center until the full crack surface is formed.

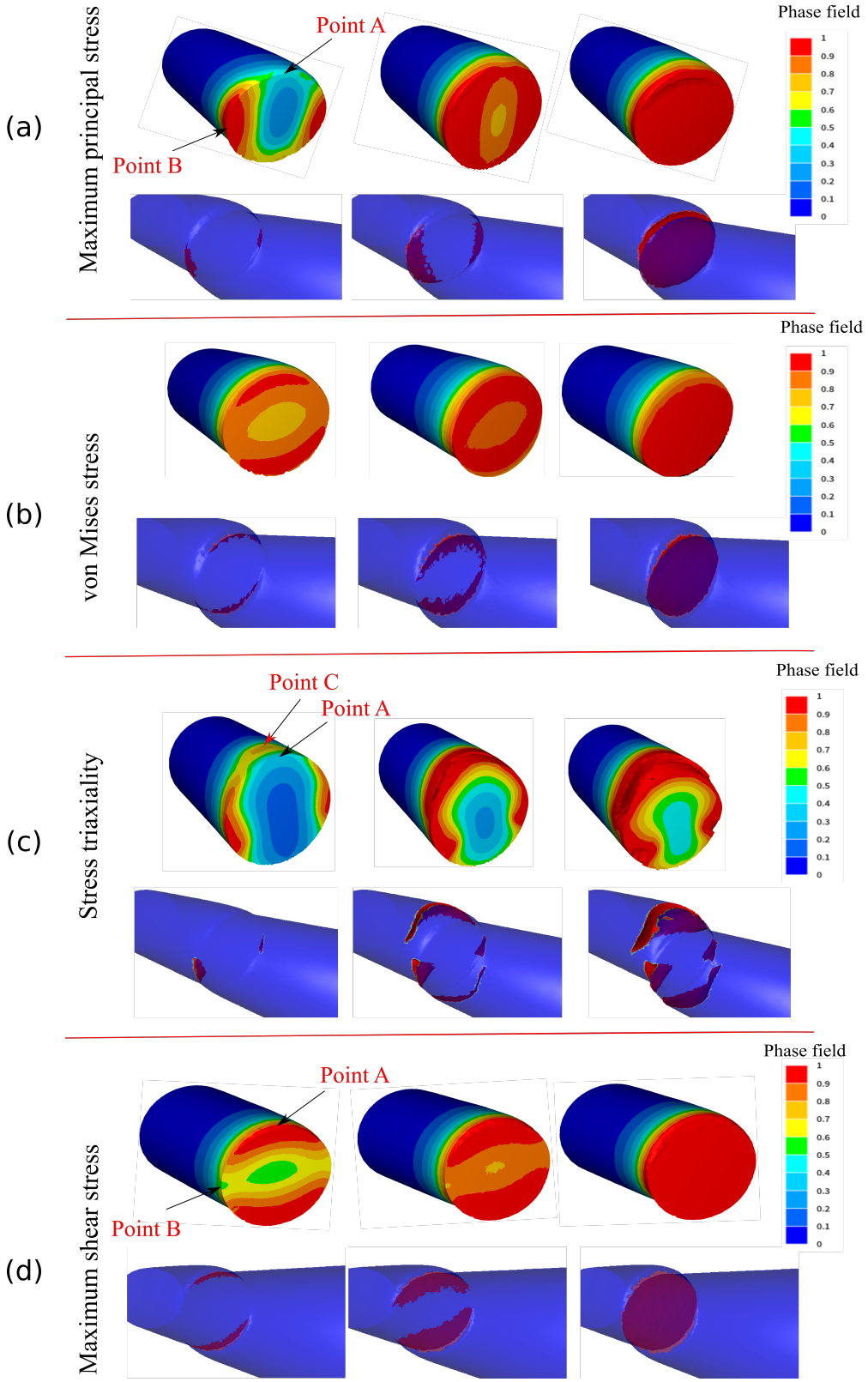


**Fig. 5.8** Illustration of the phase field evolution accompanied with the crack surfaces propagation where four different damage models are tested.

It can be also observed that the cracking pattern is very similar to the results of the second damage model that is based on the equivalent von Mises stress. This conclusion can be ex-

plained by the fact that the von Mises stress is proportional to the shear stress in the case of a pure shear loading. This can be mathematically expressed as follows

$$\bar{\boldsymbol{\sigma}} \approx \sqrt{3}\,|\sigma_{shear}| \tag{5.11}$$

where $\sigma_{shear}$ is the dominant shear stress component in the stress tensor. Fig. 5.13 shows the damage field evolution at two sensor locations A and B. It is evident that the damage field evolution is initiated at point A earlier than point B due to the concentration of maximum shear stress at this location.

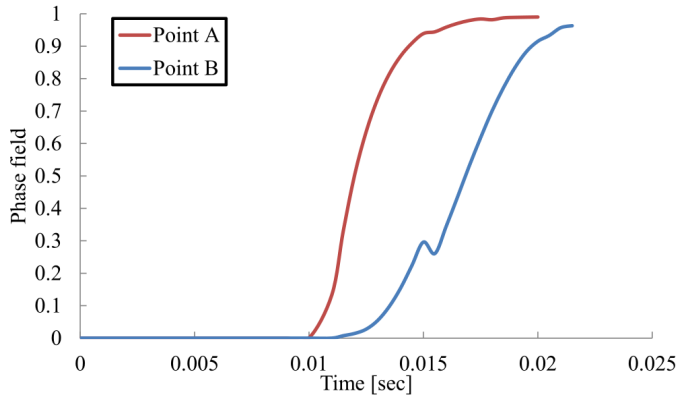


**Fig. 5.9** Phase field evolution at points A and B shown in Fig. 5.8a. Results are plotted for the first damage model.

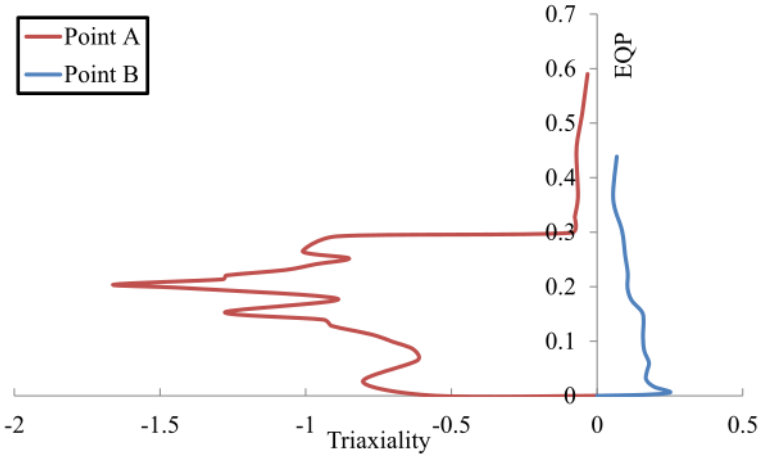


**Fig. 5.10** Loading path to fracture plotted for points A and B shown in Fig. 5.8a. Results are plotted for the first damage model.

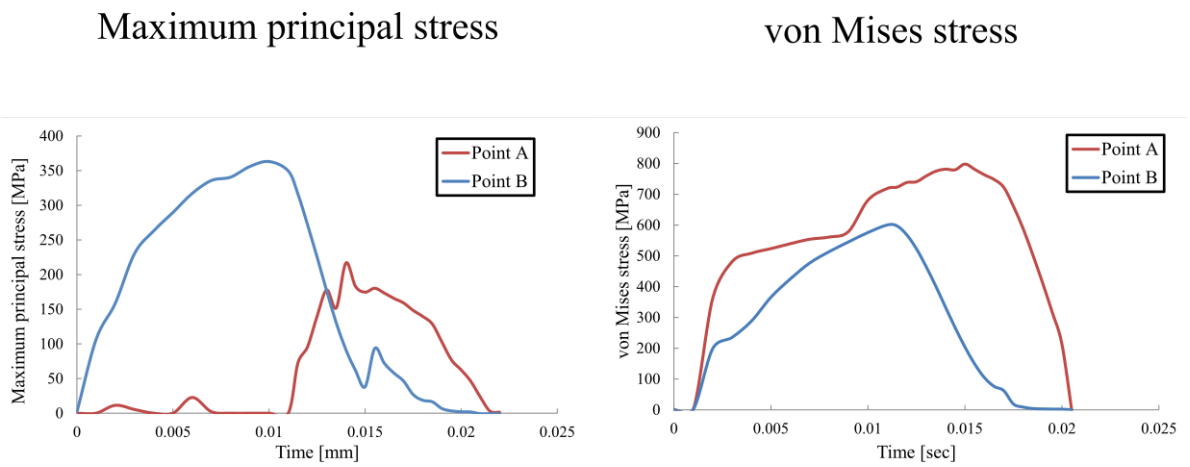


**Fig. 5.11** Evolution of maximum principal and von Mises stresses at points A and B shown in Fig. 5.8a. Results are plotted for the first damage model.

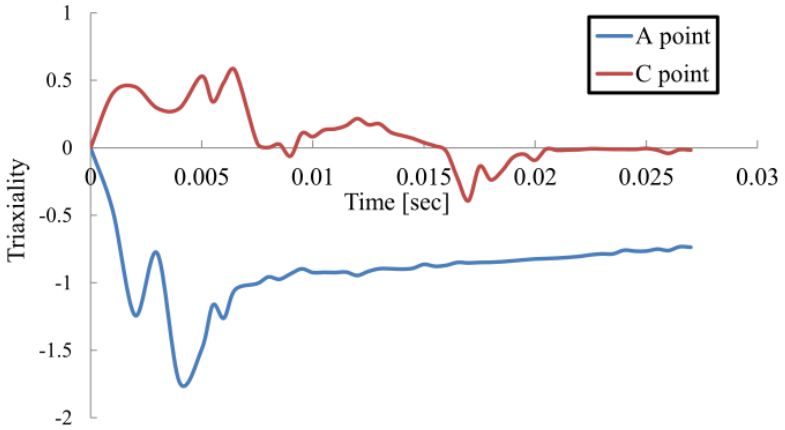


**Fig. 5.12** Loading path to fracture plotted for points A and C shown in Fig. 5.8c. Results are plotted for the third damage model.

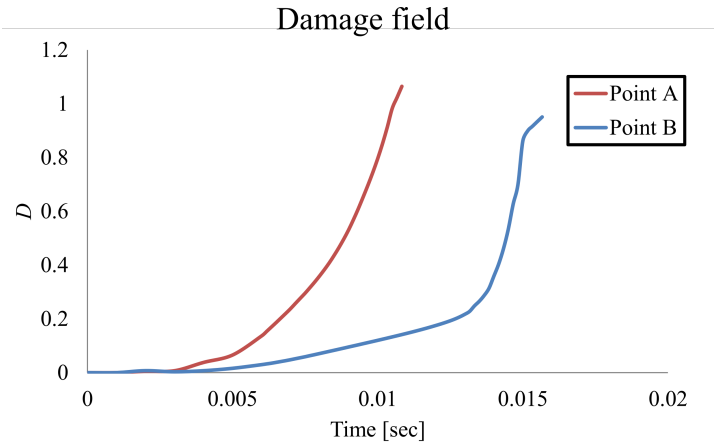


**Fig. 5.13** Evolution of a damage field based on the normalized maximum shear stress at two points A and B.

The phase field profile along with the final crack path obtained with the four damage criteria can be shown in Fig. 5.14 on a cross section. Two main observations can be made: (i). the phase field is very concentrated in the cracked zone at the end of the simulation which is an important feature in the analysis; (ii). Models 2 and 4 give very similar results with a flat crack surface which is usually a required result in bar cutting processes. The first model gives a curved crack path, however, it is difficult to confirm which crack path can be seen in reality without an experimental evidence. The third model results in an initiation of two crack branches at the locations of maximum positive stress triaxiality.

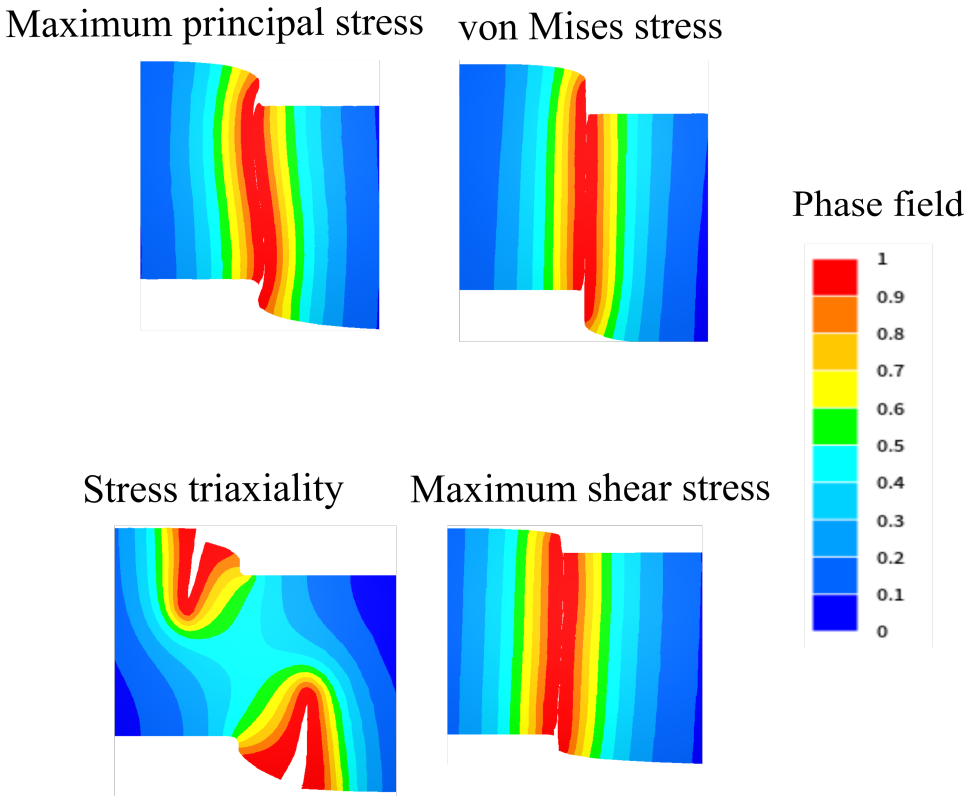


**Fig. 5.14** A cross section of the bar showing the final crack path for the different damage models.

A final comparison of the crack surfaces obtained at the end of the simulation for different mesh sizes is carried out between the CIPFAR method and the element deletion method where the results are shown in Fig. 5.15. The fourth damage model is used for all results for the sake of demonstration with a damage threshold of 0.8 for the element deletion criterion. It can be shown that the final crack path and quality of crack surfaces are completely independent on the mesh size when the CIPFAR method is adopted. This result is very important as it leads to a significant decrease in the computation time without sacrificing the accuracy of the results. On the other hand, the element deletion method is highly dependent on the mesh size. In other words, the quality of crack surfaces deteriorates with the increase of mesh size.

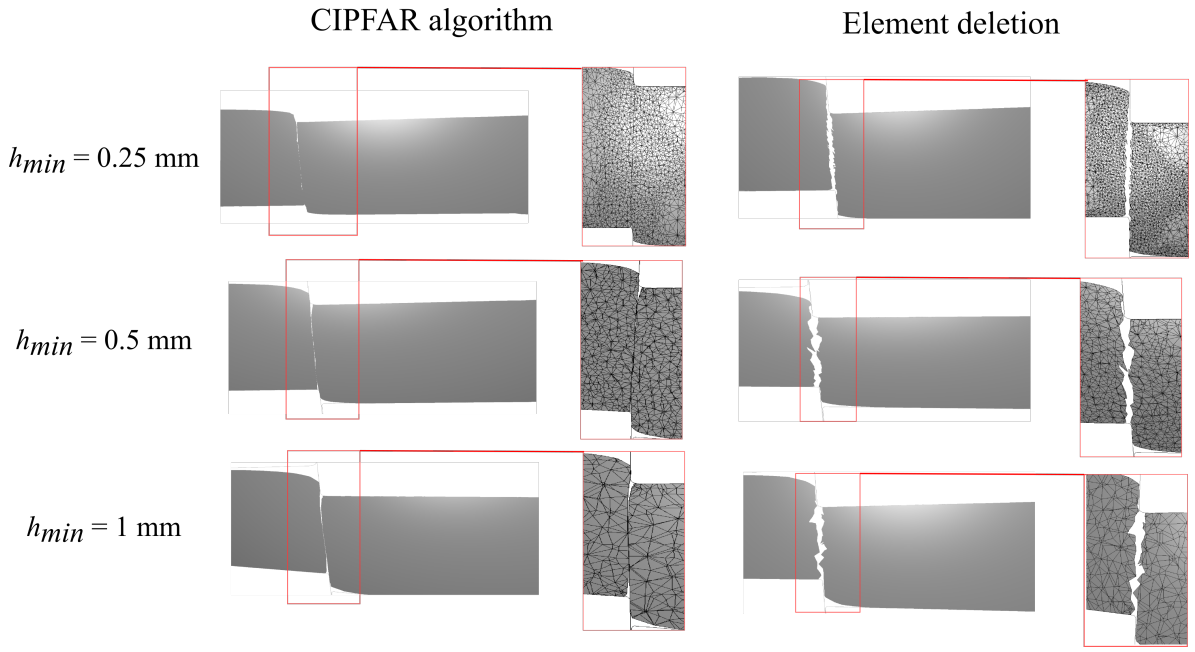


**Fig. 5.15** The final crack path shown for CIPFAR and the element deletion method for different mesh sizes.

To conclude, the presented examples confirm the ability of the proposed approach to accurately model the damage to fracture transition under different loading conditions. In addition, the model provides a general framework for crack initiation and propagation in 3D that can be adopted for different applications. Once the ductile damage mechanism that is responsible for the crack initiation is determined, an appropriate damage model is coupled with the phase field model in order to predict the evolution of crack surfaces that lead to the final fracture.

The main purpose of the next example is to test the ability of the model to predict multiples crack initiations followed by the merging of different crack branches. In addition, a comparison with experimental results is carried out in terms of both qualitative results (crack propagation) and quantitative results (force vs. displacement curve).

## 5.4 Multiple crack initiations in a notched specimen

In this example, a symmetrically notched specimen is subjected to tensile loading. The geometry and boundary conditions of the specimen are shown in Fig. 5.16 which are taken from the work of Davaze et al. [143].

Davaze et al. proposed to use the GTN model in order to describe the damage and fracture behaviours of the specimen under quasi-static/dynamic loading conditions. It was shown that the model is able to match the experimentally observed crack propagation and the Force vs. Displacement curve. It was shown that the effect of stress triaxiality is important in the accurate prediction of crack initiation and propagation. The same applications is modeled here using the coupled phase field-damage model to predict fracture under quasi-static conditions where the effect of strain rate and thermal softening on the damage mechanical behaviour are not

considered. It should be noted that a Drucker yield criterion was used in the work of Davaze et al.. However, the effect of $J_3$ (the third invariant of the deviatoric stress tensor) is not taken into account in the current study so that the $J_2$ yield criterion of von Mises is adopted. A time step of 0.2 s is used until the maximum value of the phase field in the domain equals 0.1 and then reduced to 0.1 s for the rest of the simulation. The initial mesh size in the process zone (shown in Fig. 5.16) is set to 0.6 mm. Then, adaptive remeshing is used to refine the mesh only in the zones where the crack is expected to propagate.

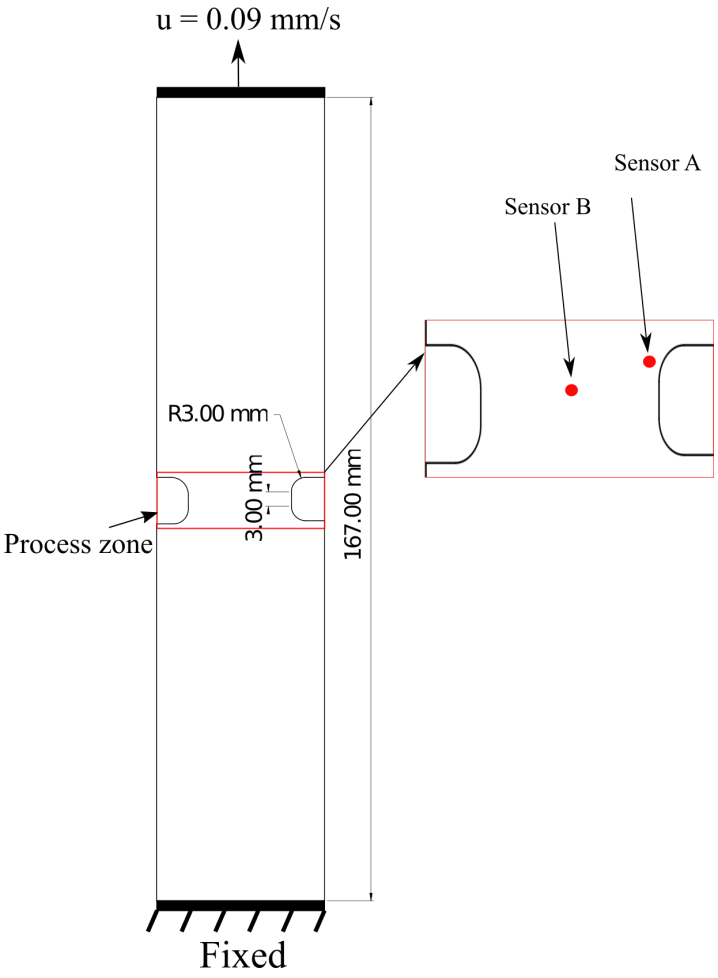


**Fig. 5.16** Geometry and boundary conditions of a symmetrically double notched specimen adopted from [143]. The thickness of the specimen is set to 1.18 mm.

The Rice-Tracey fracture criterion is used to drive the phase field evolution in order to include the effect of stress triaxiality on fracture. The damage variable can be expressed as

$$D = \int_0^{\bar{\varepsilon}_f} C_1 \, exp(C_2 \langle \eta \rangle) \, d\bar{\varepsilon} \tag{5.12}$$

In this case, the damage model parameters $C_1$ and $C_2$ are fixed where phase field model parameters $D_{thresh}$ and $\eta_c$ are varied in order to see their effect on fracture. However, a simultaneous experimental calibration of all parameters is required in order to represent the behaviour

of the material accurately. The material properties are shown in Table 5.4 where the Voce hardening law is used with an additional linear term. In addition, the phase field model parameters are also listed in the same table.

**Table 5.4** Material properties taken from [143] and the model parameters

| Quantity | Value | Unit |
|---|---|---|
| Young's modulus, $E$ | 192000 | MPa |
| Poisson's ratio, $\nu$ | 0.3 | |
| Yield stress, $\boldsymbol{\sigma}_y$ | $283 + 587\,\bar{\boldsymbol{\varepsilon}} + 208(1 - exp(-23.9\,\bar{\varepsilon}))$ | MPa |
| Damage threshold, $D_{thresh}$ | 0.13/0.15/0.17 | |
| $C_1$ | 0.2 | |
| $C_2$ | 2.2 | |
| Fracture parameter, $\eta_c$ | 10/15/20 | |
| Characteristic length scale, $l_c$ | 0.5 | mm |
| Minimum mesh size, $h_{min}$ | 0.25/0.15/0.1 | mm |

Fig. 5.17 shows the evolution of the equivalent plastic strain and stress triaxiality ratio at two locations shown in Fig. 5.16. It can be shown that a faster rate of plastic strain evolution is observed with sensor A than sensor B as shown in Fig. 5.17a. However, higher values of stress triaxiality are measured with sensor B than the ones measures with sensor A as shown in Fig. 5.17b. This observation means that a competition between the plastic strain and stress triaxiality determines the locations at which cracks are initiated in this case. In addition, it can be expected that the effect of model parameters is important as they give different weights for each damage driving factor.

The mesh is refined in the zones where the crack is expected to propagate with three different mesh sizes in the process zone: 0.25 mm (relatively coarse mesh), 0.15 mm (relatively medium mesh) and 0.1 mm (relatively fine mesh). The damage field is used as an indicator function for the mesh refinement in all the following simulations. This choice is made in order to ensure that the combined effects of plastic strain and stress triaxiality are taken into account in the refinement process.

Figs. 5.18 and 5.19 show the phase field evolution, in-plane crack propagation through the mesh and the evolution of crack surfaces in 3D for coarse and fine meshes. It can be seen that for both meshes, two cracks are initiated at the left and right notches and propagate toward the center. Then, a third crack branch is initiated at the center of the specimen and propagates toward the left and right notches until the three cracks are merged. The crack initiations at three different positions were also observed experimentally as shown in [144]. It can also be observed that the crack that is initiated at the center is slightly inclined compared to the other two crack branches that are initiated at the notches.

The results are very similar for both mesh sizes in terms of the crack propagation scenario. The Force vs. Displacement curves shown in Fig. 5.20 confirm the convergence of the solution with the reduction in the mesh size. In addition, a good matching with the experimental curve is also observed in the figure. It should be noted here that there is a small shift between the numerical and the experimental results which can be explained by the following reasons: (i). the use of $J_2$-plasticity theory instead of Drucker criterion as suggested in [143]. This choice leads to an underestimation of the hardening stress in the elasto-plastic and post-critical regimes; (ii). the damage and phase field model parameters are not calibrated in our analysis where the used values were chosen by the trial and error technique.

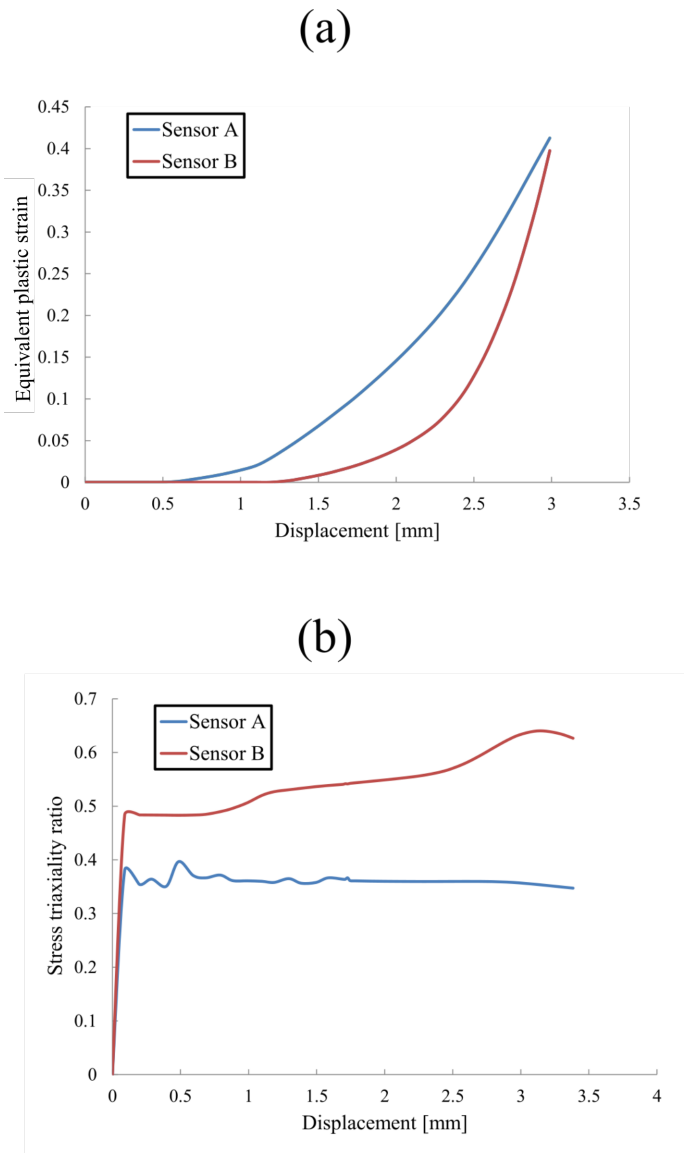


**Fig. 5.17** Evolution of the equivalent plastic strain (a) and stress triaxiality (b) measured with two sensors shown in Fig. 5.16.

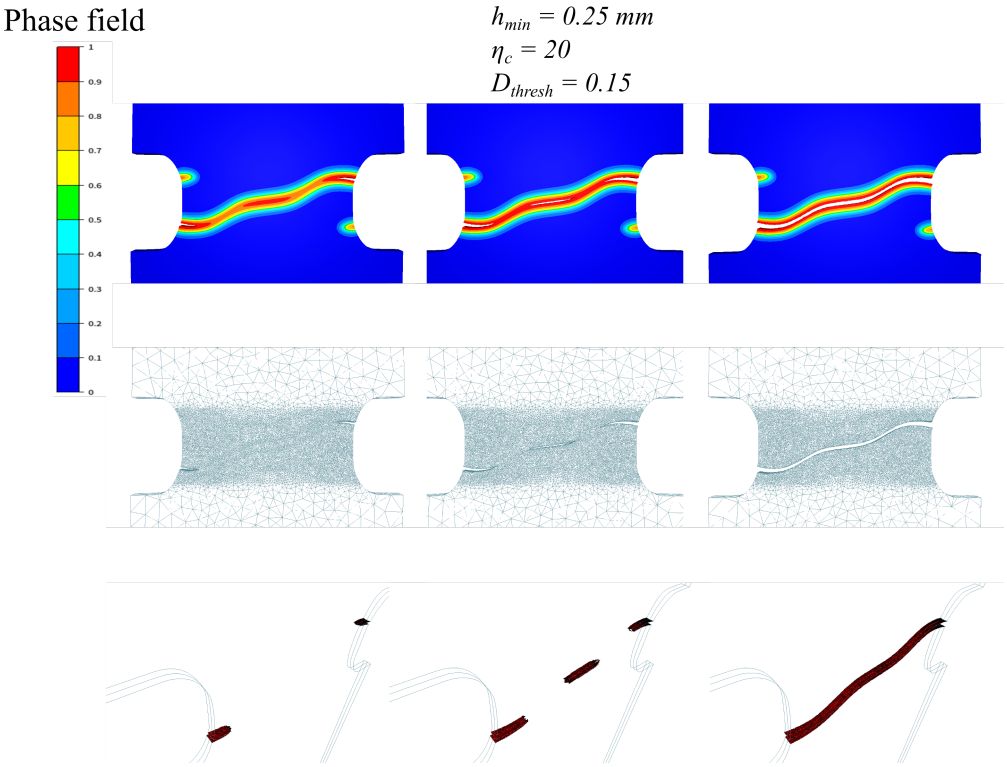


**Fig. 5.18** Initiation of two cracks at the left and right notches followed by a third crack initiation at the center of the specimen. Results are shown for $h_{min} = 0.25$ mm.

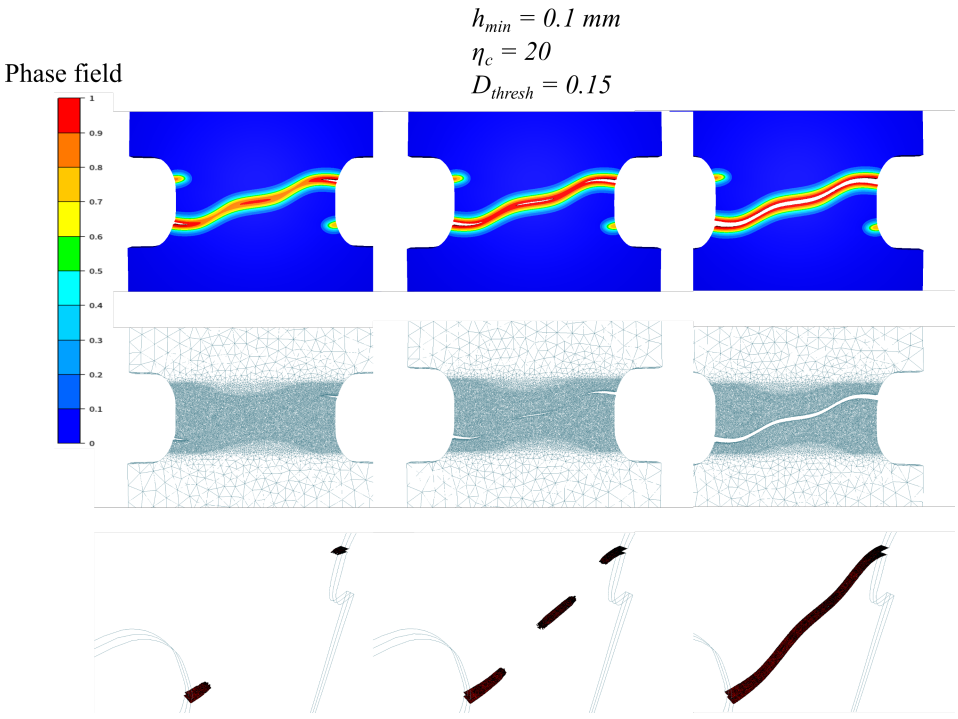


**Fig. 5.19** Initiation of two cracks at the left and right notches followed by a third crack initiation at the center of the specimen. Results are shown for $h_{min} = 0.1$ mm.

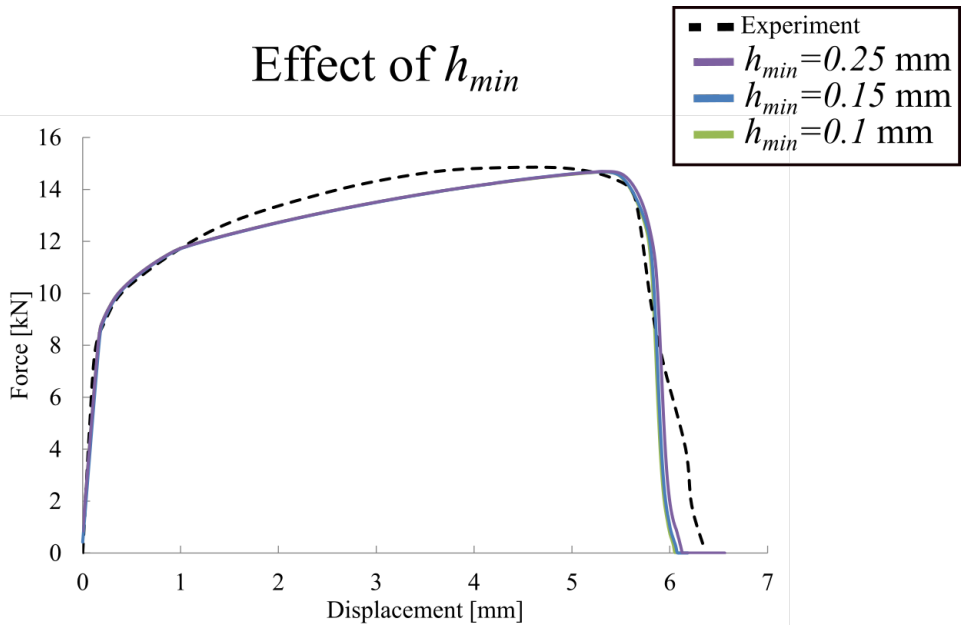


**Fig. 5.20** Force vs. Displacement curves for different mesh sizes. A comparison with the experimental result is also shown. The experimental curve is adopted from [143].

Fig. 5.21 shows the effect of the damage threshold $D_{thresh}$ on the final crack path where all the other parameters are fixed. It can be shown that the same crack path is obtained in all cases where the final crack connects the upper boundary of the right notch with the lower boundary of the left notch. However, it can also be observed that the decrease in $D_{thresh}$ may lead to two tiny crack initiations at the upper boundary of the left notch and the lower boundary of the right notch. These tiny cracks are not initiated with the highest value of $D_{thresh} = 0.17$.

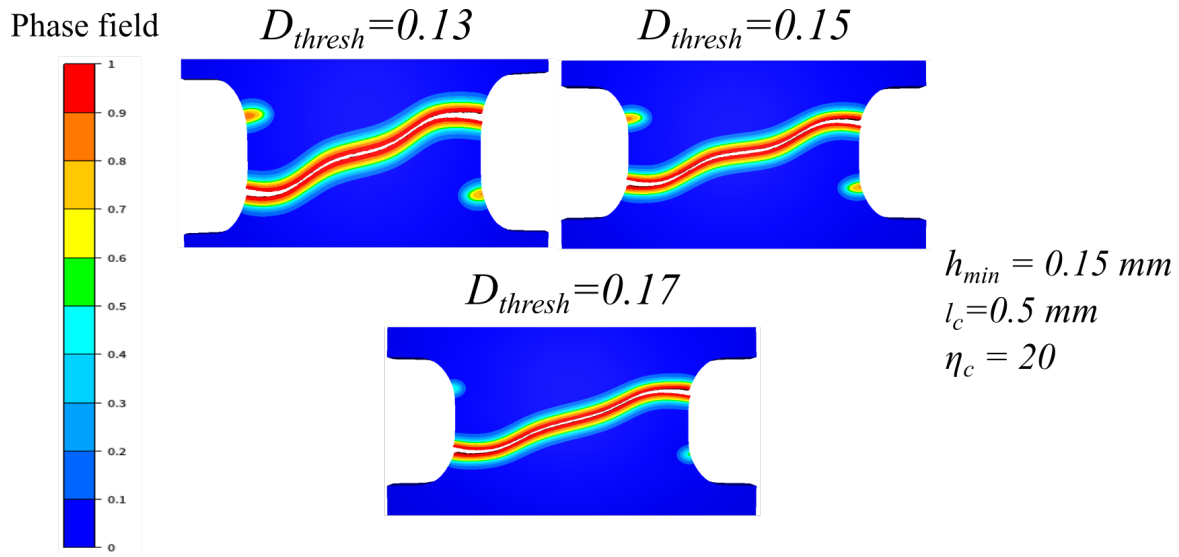


**Fig. 5.21** The effect of the damage threshold $D_{thresh}$ on the final crack path.

Fig. 5.22 shows the effect of $D_{thresh}$ on the Force vs. Displacement curve. As expected, the increase of the damage threshold leads to a delay in the fracture initiation. It can also be

observed that the rate of load drop in the post-critical regime is similar in all cases since $\eta_c$ is constant.

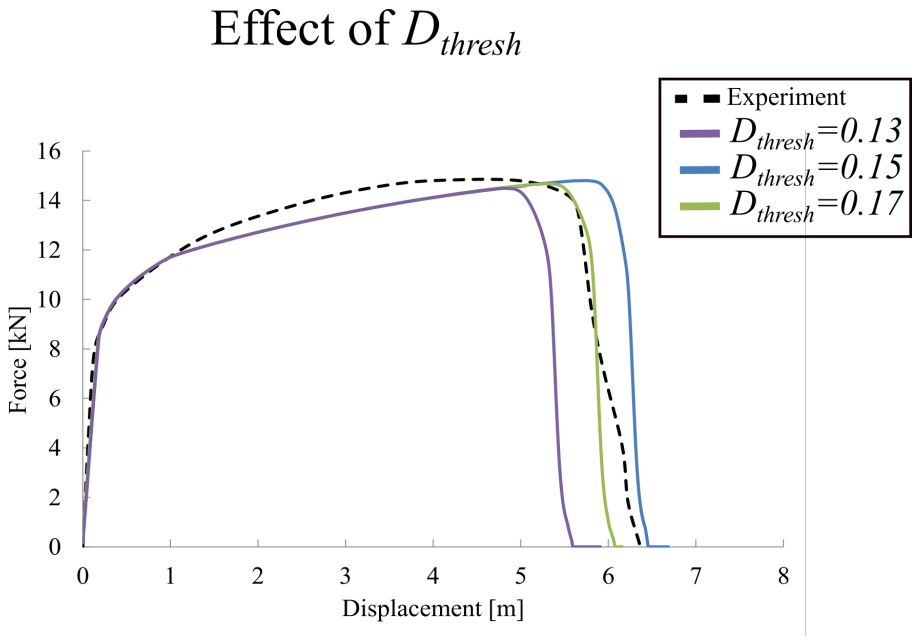


**Fig. 5.22** The effect of $D_{thresh}$ on the Force vs. Displacement curve.

The effect of $\eta_c$ on the crack propagation is shown in Fig. 5.23 where the results are shown for three displacement states: a, b and c for three different values of $\eta_c$. Two main observations can be made: (i). the reduction of $\eta_c$ leads to simultaneous crack initiations at the notches boundaries and at the center of the specimen; (ii). the inclination of the crack branch that is initiated at the center with respect to the horizontal axis is increased with the increase of $\eta_c$. Comparing the final crack paths with the experimental observation shown in the same figure proves that a very good matching between the numerical and experimental results can be obtained with a proper choice of $\eta_c$. The Force vs. Displacement curves that show the effect of $\eta_c$ are shown in Fig. 5.24 where the three displacements states are marked with different colors on each curve. It can be seen that the increase of $\eta_c$ leads to a faster rate of load drop as expected from the model.

The presented example has demonstrated the ability to model a relatively complex fracture phenomenon that is characterized by the following features: (i). multiple crack initiations simultaneously; (ii). automatic merging of crack branches without an ad-hoc criterion; (iii). a good matching with the experimental observations in terms of the crack propagation and the Force vs. Displacement curves.

The main advantage of the proposed model is the ability to capture the experimentally observed sequence of crack initiations with a simple fracture criterion (Rice-Tracey) which is important from an industrial point of view. The obtained results encourage the extension of the analysis toward more complex industrial processes which will be the scope of the upcoming numerical examples.

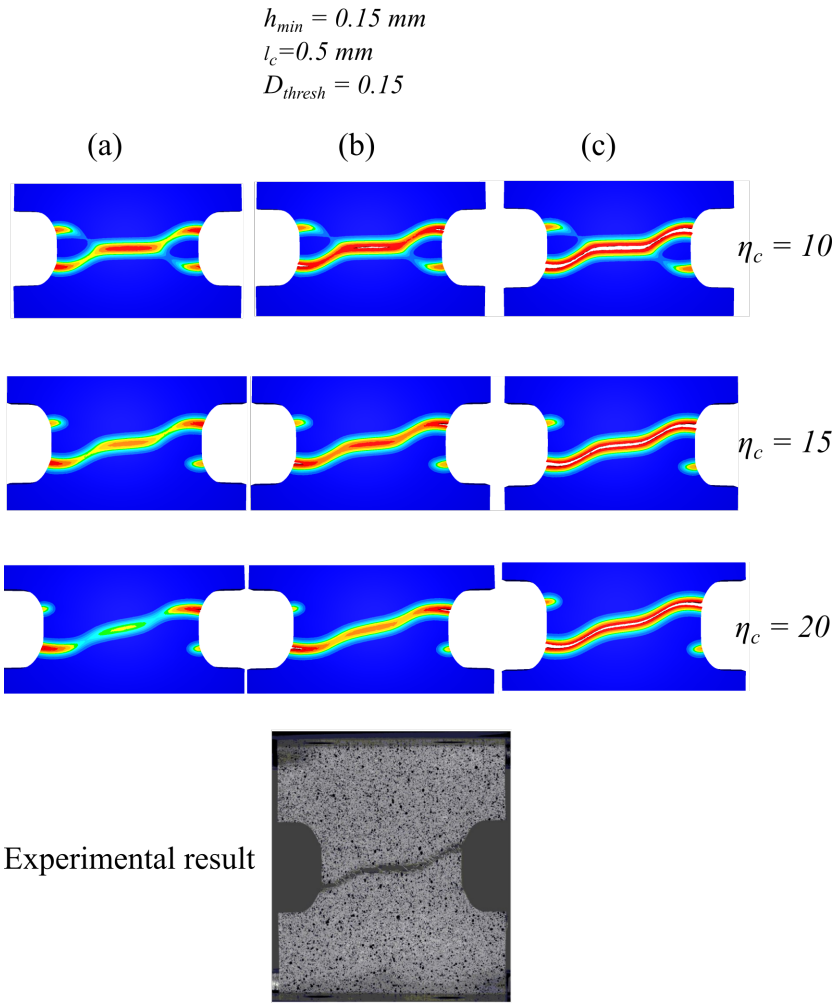


**Fig. 5.23** The effect of $\eta_c$ on the crack initiation and propagation is shown. Results are compared with an experimental observation (bottom). The experimental observation image is adopted from [143].

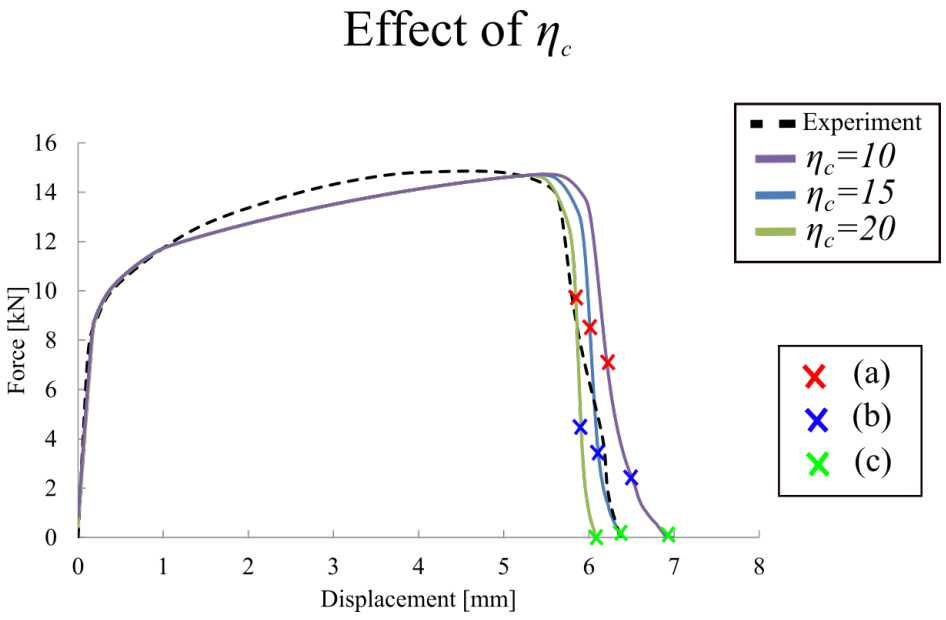


**Fig. 5.24** The Force vs. Displacement curves for different values of $\eta_c$.

## 5.5 The formation of chevron cracks

During the bar extrusion process, internal cracks known as "chevron cracks" may initiate in the core of the extruded bar as shown in Fig. 5.25. Such cracks lead to a major reduction in the effective stiffness and strength of the extruded bars. These internal cracks are difficult to inspect visually which requires the use of ultra-sonic scanning. The shape and number of the chevron cracks need to be properly inspected in order to optimize the quality of the output products. Authors in [9, 145] applied the finite element method on 2D axisymmetric geometries where the fracture analyses were carried out using the element deletion algorithm with the Latham-Cockcroft damage model. The aim of this study was to show the effect of different geometrical and mechanical parameters such as: the reduction area, semicone angle and friction on the number and shape of the formed cracks during the extrusion process. The normalized Latham-Cockcroft damage model is used in the local history functional $\mathcal{H}$ in order to drive the phase field evolution. This damage model was chosen because it is known that the apparition of the internal crack is highly driven by the stress state such as the maximum principal stress which drives the evolution of the damage. The normalized Latham-Cockcroft damage variable is defined as follows

$$D = \int_0^{\bar{\varepsilon}} \frac{\langle \boldsymbol{\sigma}_1 \rangle}{\bar{\boldsymbol{\sigma}}} \, d\bar{\boldsymbol{\varepsilon}} \tag{5.13}$$

**Fig. 5.25** Formation of chevron cracks in the core of an extruded bar taken from [12].

Fig. 5.26 shows the initial geometry, boundary conditions and initial mesh used for the calculations. The material and model parameters are detailed in Table 5.5 which are taken from [12]. The value of the effective crack area $A_{fixed}$ is chosen as two times the minimum mesh size. The semicone angle $\theta$ =18°, the initial and final radii are 25 mm and 21.75 mm, respectively. Adaptive remeshing is used to adapt the mesh in the regions where the crack is expected to propagate. The strategy of the adaptive mesh refinement is described in [57] where the adaptation is based on equivalent plastic strain in this example. The Latham-Cockcroft damage variable is used in this example as an indicator function for the mesh refinement process.

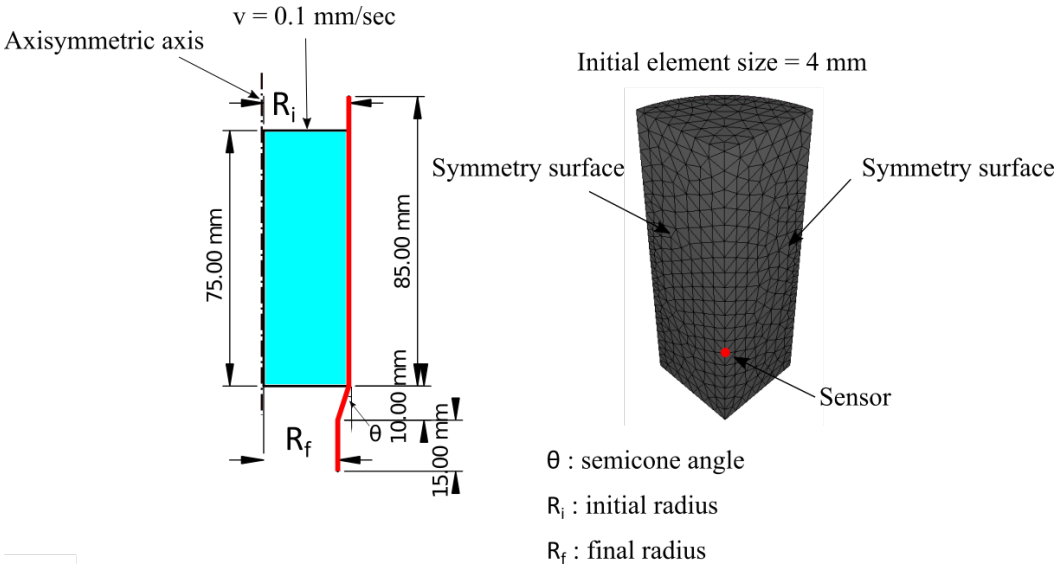


**Fig. 5.26** Geometry, boundary conditions and initial mesh size of the bar to be extruded taken from ref. [12].

**Table 5.5** Material and model parameters

| Quantity | Value | Unit |
|---|---|---|
| Young's modulus, $E$ | 200000 | MPa |
| Poisson's ratio, $\nu$ | 0.3 | |
| Yield stress, $\boldsymbol{\sigma}_y$ | $302(1 + 1.766\,\bar{\varepsilon})^{0.5465}$ | MPa |
| Damage threshold, $D_{thresh}$ | 0.15/0.2/0.25 | |
| Fracture parameter, $\eta_c$ | 100/200/500 | |
| Characteristic length scale $l_c$ | 2/4 | mm |
| Coulomb friction coefficient | 0.2 | |
| Penalisation parameter $\epsilon_n$ | 100 | |
| Mesh adaptation damage threshold | 0.1 | |

## 5.5.1 Effect of mesh size

A comparative study is carried out to analyze the effect of minimum mesh size $h_{min}$ on the shape and number of chevron cracks. Fig. 5.27 shows five different distances that are measured to describe the geometry of the specimen with each mesh size. It can be observed that the number of chevron cracks remains the same and geometrical shape is very similar with the different mesh sizes. The quantitative comparison of the effect of mesh size on the crack geometry is given in Table 5.6 where the distance between each chevron crack as well as the distance between the crack ends are reported. The comparison is carried out by comparing five distances that can characterize characterize the shape of chevron cracks. A convergence

behaviour can be observed in the sense that the differences between the measured distances are reduced with the reduction of mesh size. It should be noted that the resolution of the mechanical and phase field equations are also affected by the mesh size which in turn has a slight effect on the differences in the results. These results are encouraging since one of the main drawbacks in the element deletion algorithm is the dependency of the final crack path on the mesh size as clearly observed in this study [9].

### 5.5.2 Effect of model parameters

The effect of the damage threshold parameter $D_{thresh}$ is shown in Fig. 5.28. The main observation is that, not only the number of chevron cracks is affected by this parameter, but also the crack size and the distance between two consecutive cracks. When $D_{thresh} = 0.25$, one single crack is initiated with a relatively small size. On the other hand, three cracks are initiated for lower threshold values (damage threshold = 0.2 and 0.15 respectively).

Fig. 5.29 shows the local evolution of the phase field and equivalent stress for different values of $\eta_c$ at a sensor location shown in Fig. 5.26. It can be observed that the rate of the phase field evolution increases as $\eta_c$ increases which also leads to a quicker loss of the load-bearing capacity of the material as observed in the post-peak response of the von Mises stress.

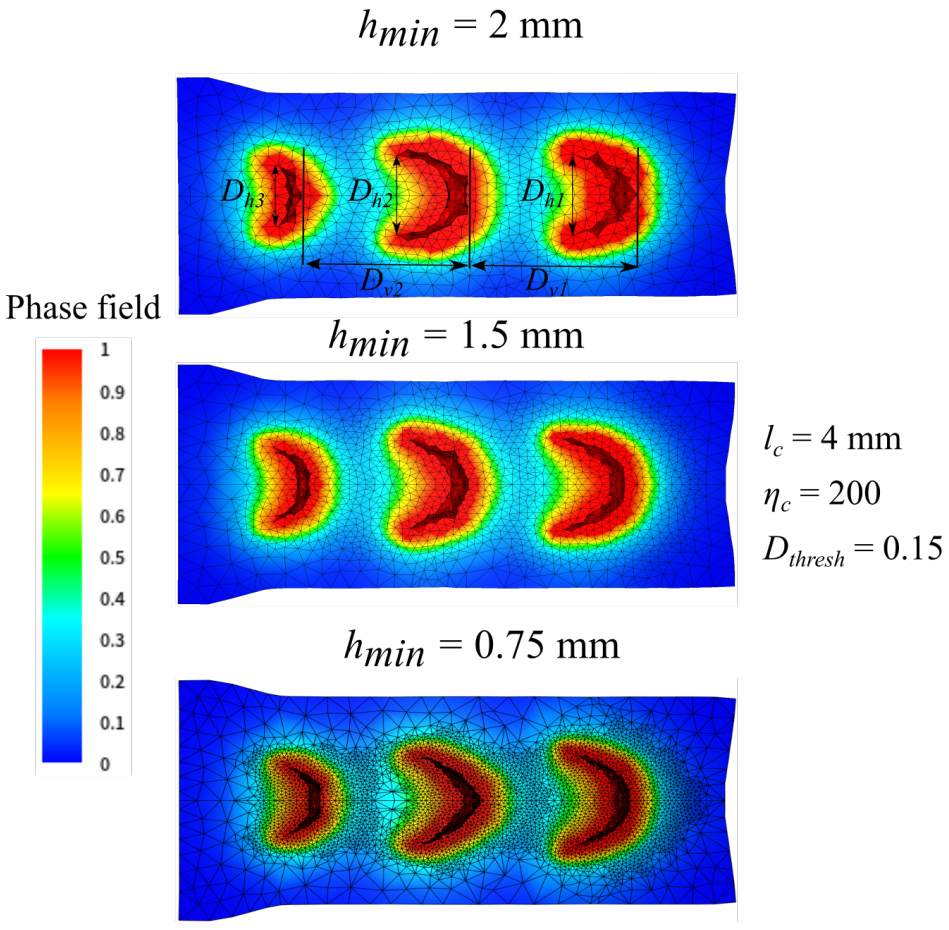


**Fig. 5.27** The effect of mesh size on the formation of final cracks predicted by the CIPFAR method.

**Table 5.6** Analysis of chevron cracks. All dimensions are in mm

| Mesh size | Number of cracks | $D_{v1}$ | $D_{v2}$ | $D_{h1}$ | $D_{h2}$ | $D_{h3}$ |
|---|---|---|---|---|---|---|
| 2 | 3 | 29.4 | 28.5 | 17.16 | 16.7 | 14.4 |
| 1.5 | 3 | 27.2 | 27.6 | 18.86 | 18.3 | 15.18 |
| 0.75 | 3 | 26.4 | 27.6 | 20.4 | 17.6 | 14.9 |

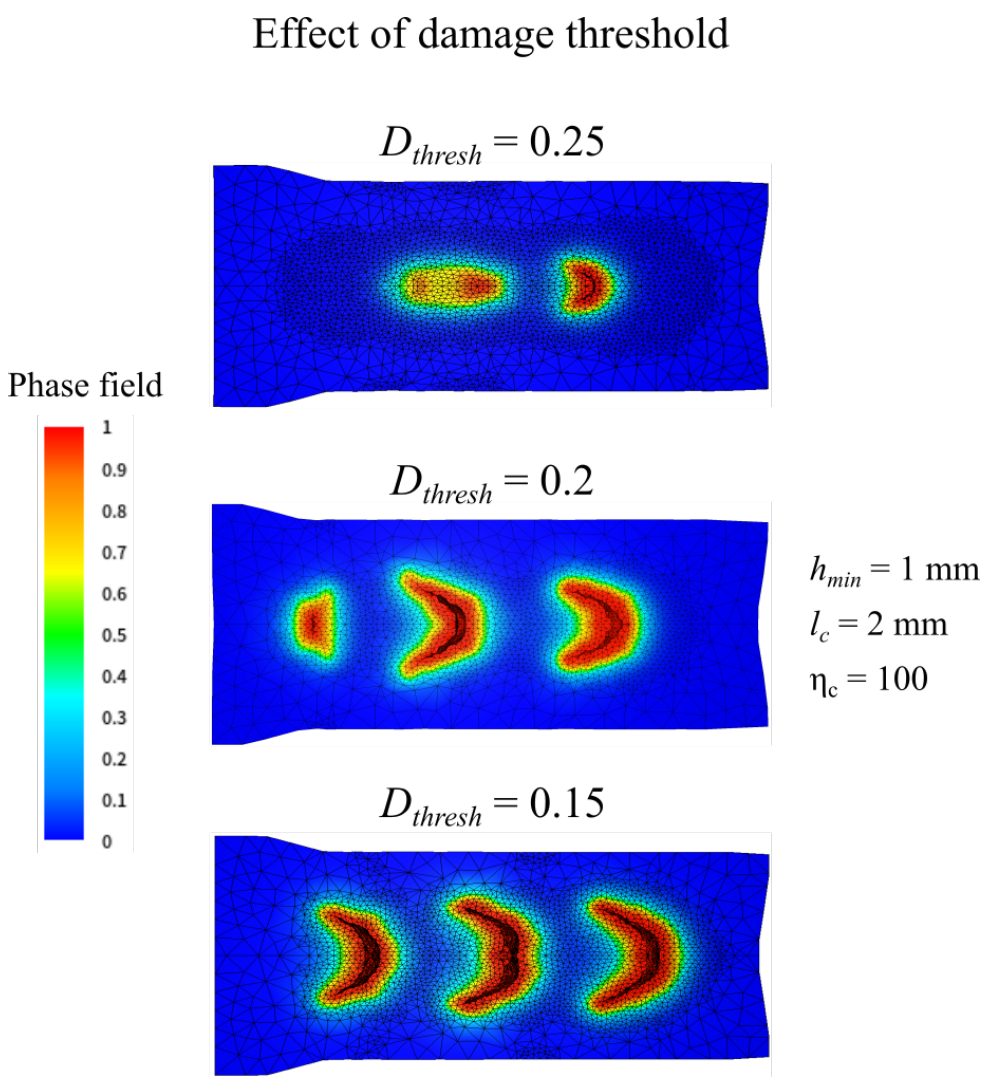


**Fig. 5.28** The evolution of the phase field for different damage threshold values $D_{thresh}$.

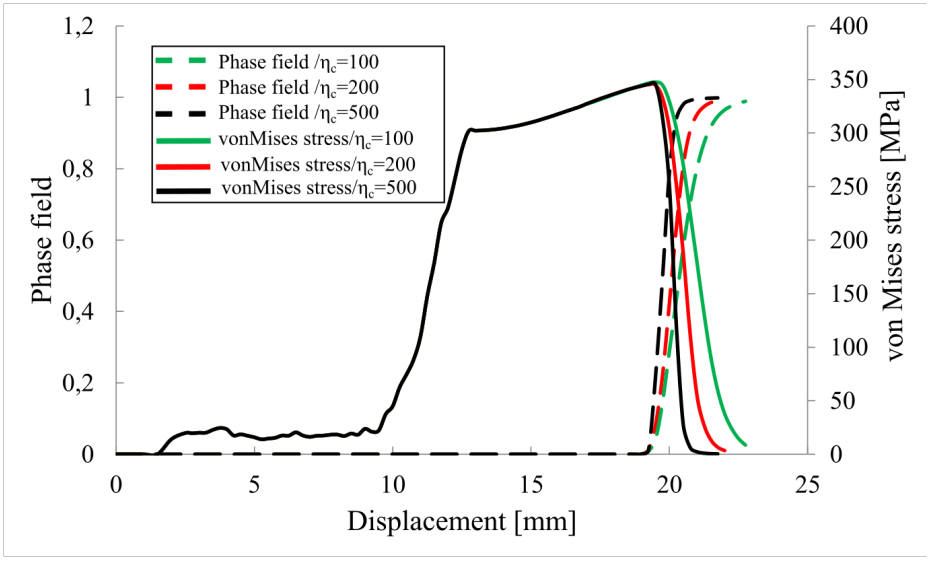


**Fig. 5.29** Evolution of the phase field and von Mises stress locally at a sensor location shown in Fig. 5.26 with $D_{thresh} = 0.15$.

### 5.5.3 Comparison with the element deletion method

A comparison with the element deletion technique is demonstrated in Fig. 5.30 where the elements are deleted from the mesh upon reaching a critical damage value of 0.15 without coupling to the material behaviour. It can be observed that the shape of the cracks with the element deletion algorithm are similar to those obtained with high values of $\eta_c$, most notably in the case of $\eta_c = 500$. This can be related to the fact that the increase of the fracture parameter $\eta_c$ increases the rate of stress softening which is expected to lead to an instantaneous loss of the load carrying capacity as the case of the element deletion when $\eta_c \to \infty$. Finally, the final chevron crack surfaces along with the amount volume loss are shown in Fig. 5.31 with a comparison with the element deletion algorithm. Two main observations can be made: (i). the element deletion algorithm leads to a considerable loss of the crack surfaces smoothness which is known to be highly dependent on the mesh size. Conversely the crack insertion algorithm leads to a rigorous definition of the crack surfaces with a proper quality according to the predicted crack path; (ii). the element deletion algorithm leads to a considerable amount of nonphysical volume loss which is also mesh dependent, i.e., it increases with the increase of mesh size. It should be also noted that a small amount of volume loss of about 0.8 % that is associated with the crack insertion simulation is directly related to the global remeshing operations that ensure the good quality of mesh elements. After each global remeshing operation, a small amount of the volume is lost due to the fact that the new geometry is slightly different from the old one. These two improvements are highly important in ductile fracture simulations in the domain of metal forming where the quality of each product in the fabrication cycle affects the final product.

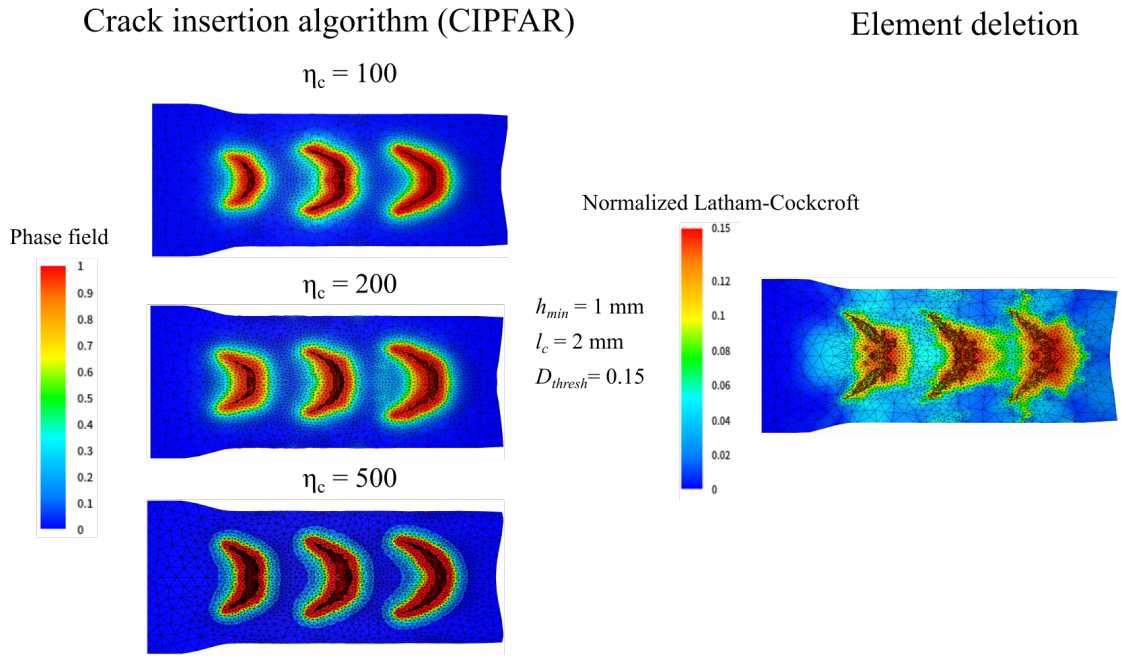


**Fig. 5.30** The evolution of the phase field for different fracture parameter values $\eta_c$ and comparison with the element deletion technique.

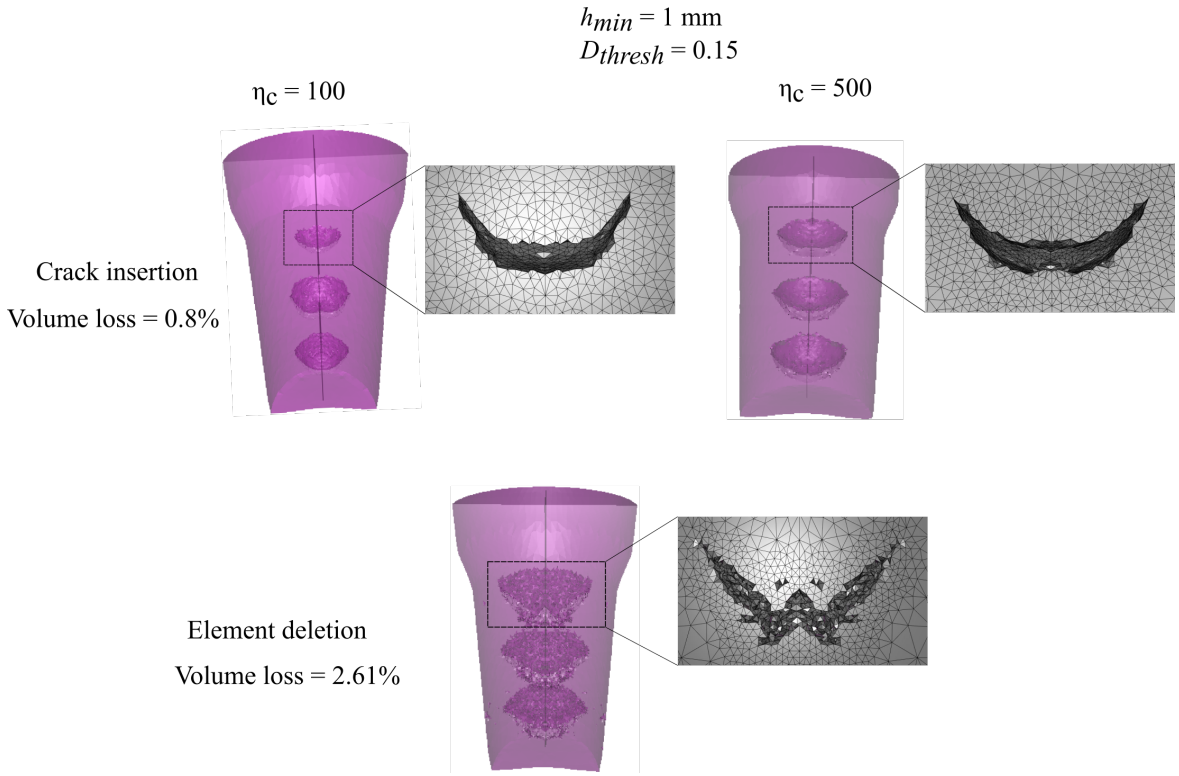


**Fig. 5.31** A comparison between the crack insertion algorithm (CIPFAR) and the element deletion algorithm. The crack insertion algorithm improves the quality of the crack surfaces and does not lead to a significant volume loss.

Last, a qualitative comparison between the experimental and numerical results of the crack insertion and element deletion algorithms is shown in Fig. 5.32. The material properties are

taken from [145] with a Coulomb friction coefficient of 0.1 and damage threshold $D_{thresh}$ of 0.1. The semicone angle $\theta = 30°$, the initial and final radii are 35 mm and 31.5 mm, respectively. For the element deletion method, elements are removed from the mesh when the damage value reaches a threshold value of 0.15. It can be seen that the crack insertion algorithm results in a better description of the material separation due to the formation of chevron cracks than the element deletion method where a considerable volume loss can be also observed. However, it is also clear that the distances between the cracks predicted by the CIPFAR algorithm are different from those seen in the experiment. For example, the crack initiation locations are slightly shifted upward with respect to the experimental ones. This result is mostly related to the adopted damage model and the phase field parameters that determine the crack initiation location. Thus, a comparison between different damage models accompanied with the experimental calibration of the model parameters is essential.

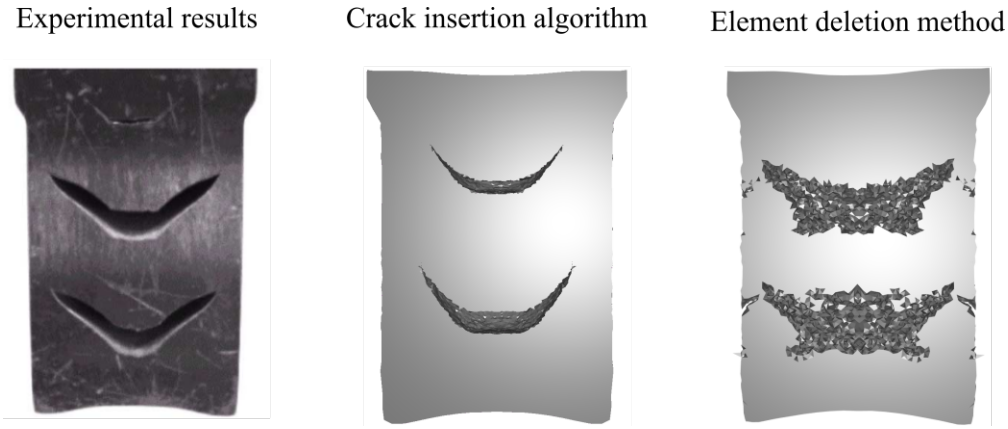


**Fig. 5.32** A comparison between the experimental and numerical results for the formation of chevron cracks.

To conclude, the presented phase field model provides a general framework to use a suitable damage model that is able to accurately predict the initiation and propagation of cracks in ductile media. The effect of numerical parameters introduced in the model is shown to be important in terms of the prediction of the number, size and shape of chevron cracks. The crack insertion and propagation algorithm (CIPFAR) results in a major improvement in the quality of the crack surfaces and prevents the non-physical volume loss when compared with the element deletion algorithm which is widely used for the modeling of ductile fracture applied to metal forming processes.

## 5.6 Simulation of blanking processes

Contrary to the formation of chevron cracks during extrusion, blanking is a manufacturing process based on ductile fracture for which the good prediction of the fracture surfaces is crucial. Fig. 5.33 shows the geometry and boundary conditions of the blanking simulation used in this example taken from [5]. Fig. 5.34 shows the different zones on the external surface of the

sheared work piece. The product quality can be assessed by the smoothness of the fracture surfaces and the burr height. A burr is an extension over the edge of the work piece that deteriorates the surface quality. Authors in [146] used the element deletion algorithm in 2D in order to study the effect of different geometrical parameters and friction coefficient on the characteristic features of the edge. However, a very fine mesh was adopted around the damaged zone in order to accurately predict the surface features.

The main objective of this example is to assess the ability of the crack initiation and propagation algorithm to predict the crack path and accurately define the characteristic features of the crack surfaces with relatively coarser meshes. The material properties and model parameters are shown in Table 5.7 and taken from [6]. The mesh is coarsened everywhere at the beginning of the simulation and refined only in the zone where the crack is expected to initiate with a minimum size $h_{min}$. Adaptive remeshing based on the equivalent plastic strain is used to preserve the mesh quality in the damaged zone while keeping the mesh size fixed. The Lemaitre damage model is used in this study as used in [6, 69]. The local Lemaitre damage variable can be expressed as follows

$$D = \int_0^{\bar{\varepsilon}} \frac{D_c}{\varepsilon_R - \varepsilon_D} \Big[\frac{2}{3}(1+\nu) + 3(1-2\nu)\langle\frac{-p}{\bar{\sigma}}\rangle^2\Big] \bar{\varepsilon}^{\frac{2}{n}}\, d\bar{\varepsilon} \tag{5.14}$$

$D_c$ is the critical damage value at fracture which is chosen here according to the calibrated non-local Lemaitre model used in [147], $\varepsilon_D$ is the strain threshold at which the damage is initiated, $\varepsilon_R$ is strain value at fracture and $n$ is the hardening exponent. Lemaitre damage model has proven the ability to predict the fracture zone and a matching force vs. displacement curve with experiments. The dependence of the damage variable on the equivalent plastic strain makes it accurate in the blanking simulations as mentioned in [69] where the plastic strain is responsible for the failure process. It is assumed in this example that the softening effect due to the void nucleation and growth is neglected. Thus, softening effect only appears in the void coalescence phase (the Lemaitre damage variable acts as an uncoupled damage field in this case).

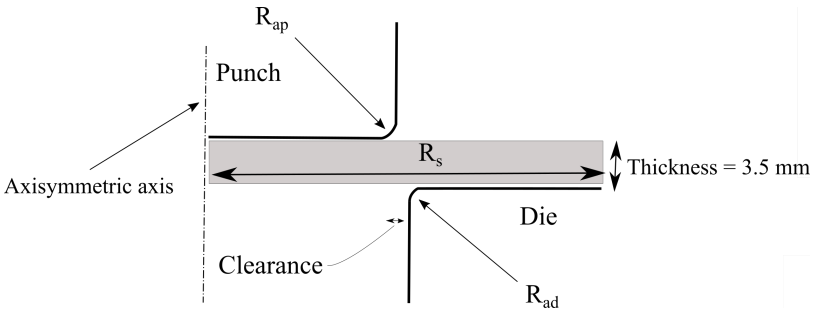


**Fig. 5.33** Geometry and boundary conditions of a blanking process. The dimensions are taken from ref. [5].

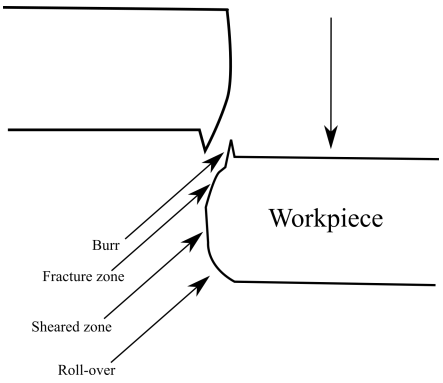


**Fig. 5.34** Geometry of a workpiece showing the characteristic features of the edge.

**Table 5.7** Material and model parameters

| Quantity | Value or expression | Unit |
|---|---|---|
| Young's modulus, $E$ | 210000 | MPa |
| Poisson's ratio, $\nu$ | 0.29 | |
| Yield stress, $\boldsymbol{\sigma}_y$ | $250 + 1048\,\bar{\varepsilon}^{0.2}$ | MPa |
| $D_c$ | 0.9 | |
| $\varepsilon_R$ | 0.8 | |
| $\varepsilon_D$ | 0 | |
| $n$ | 0.2 | |
| Fracture parameter, $\eta_c$ | 150/200 | |
| Damage threshold, $D_{thresh}$ | 0.6/0.8 | |
| Characteristic length scale, $l_c$ | 0.5 | mm |
| Mesh adaptation threshold | 0.05 | |
| Penalisation parameter $\epsilon_n$ | 100 | |
| Coulomb friction coefficient | 0.15 | |
| $R_s$ | 20 | mm |
| $R_{ap}$ | 0.1 | |
| $R_{ad}$ | 0.01 | |
| clearance $c$ | 10 % | |

Fig. 5.35 shows the phase field evolution along with the initiation and propagation of real cracks at different punch penetrations. It can be shown that cracks are initiated from the upper and lower edges and merged together until final failure. It should also be noted that the initiation and propagation zones are directly related to the choice of damage model that drives the phase field evolution where the role of the phase field model is to obtain a regularized crack interface that is used to insert real cracks.

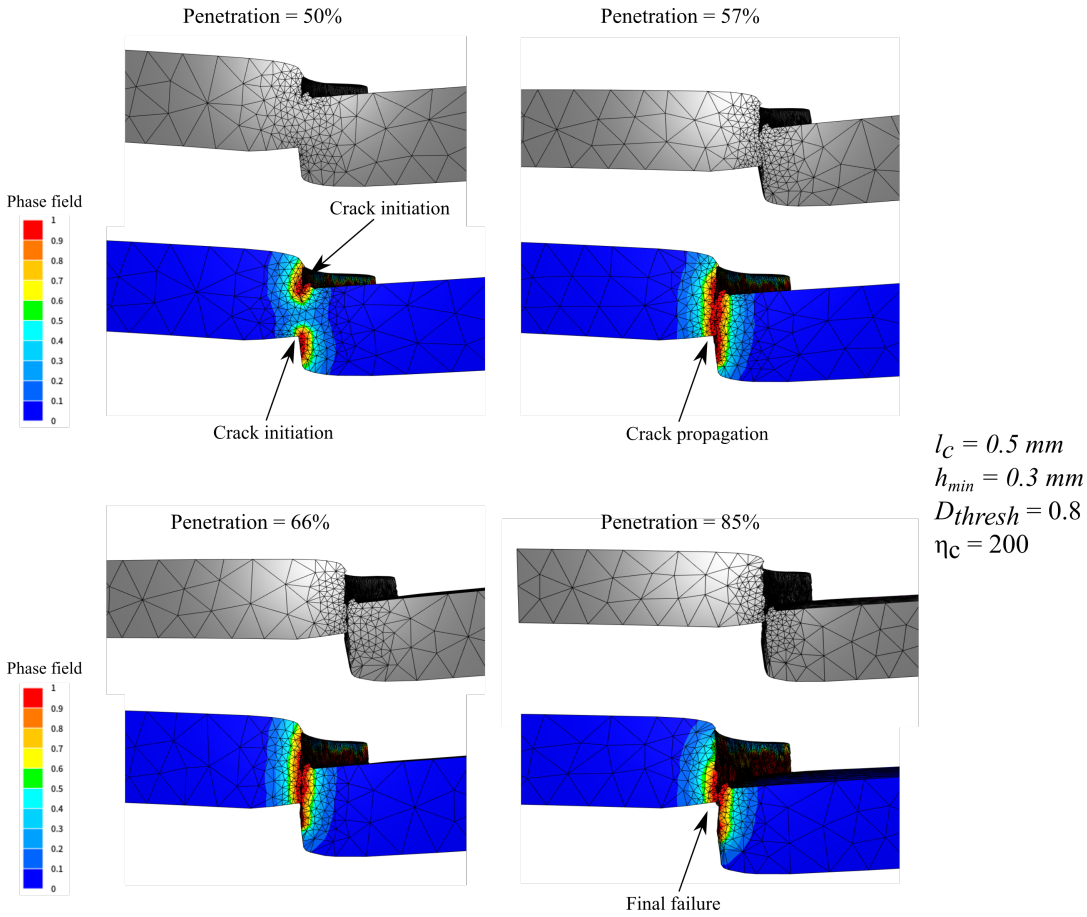


**Fig. 5.35** The initiation and propagation of the real crack and phase field at different penetration depths.

Fig. 5.36 shows the effect of each phase field parameters on the force vs. displacement curve compared with the experimental result taken from [69]. As expected, the damage threshold $D_{thresh}$ controls the moment at which the crack is initiated by delaying the softening due to damage accumulation as shown in Fig. 5.36 a. Likewise, The fracture parameter $\eta_c$ controls the post-peak behaviour once the damage threshold is triggered as shown in Fig. 5.36 b. The comparison reveals that a good quantitative matching with the experimental results is possible once the model parameters are calibrated with the experimental data. However, it can be observed that the softening behaviour in the experimental results cannot be accurately captured even with high values of the damage threshold. It should also be noted that a simultaneous calibration of the damage and phase field models is essential for an accurate prediction of the ductile damage to fracture transition.

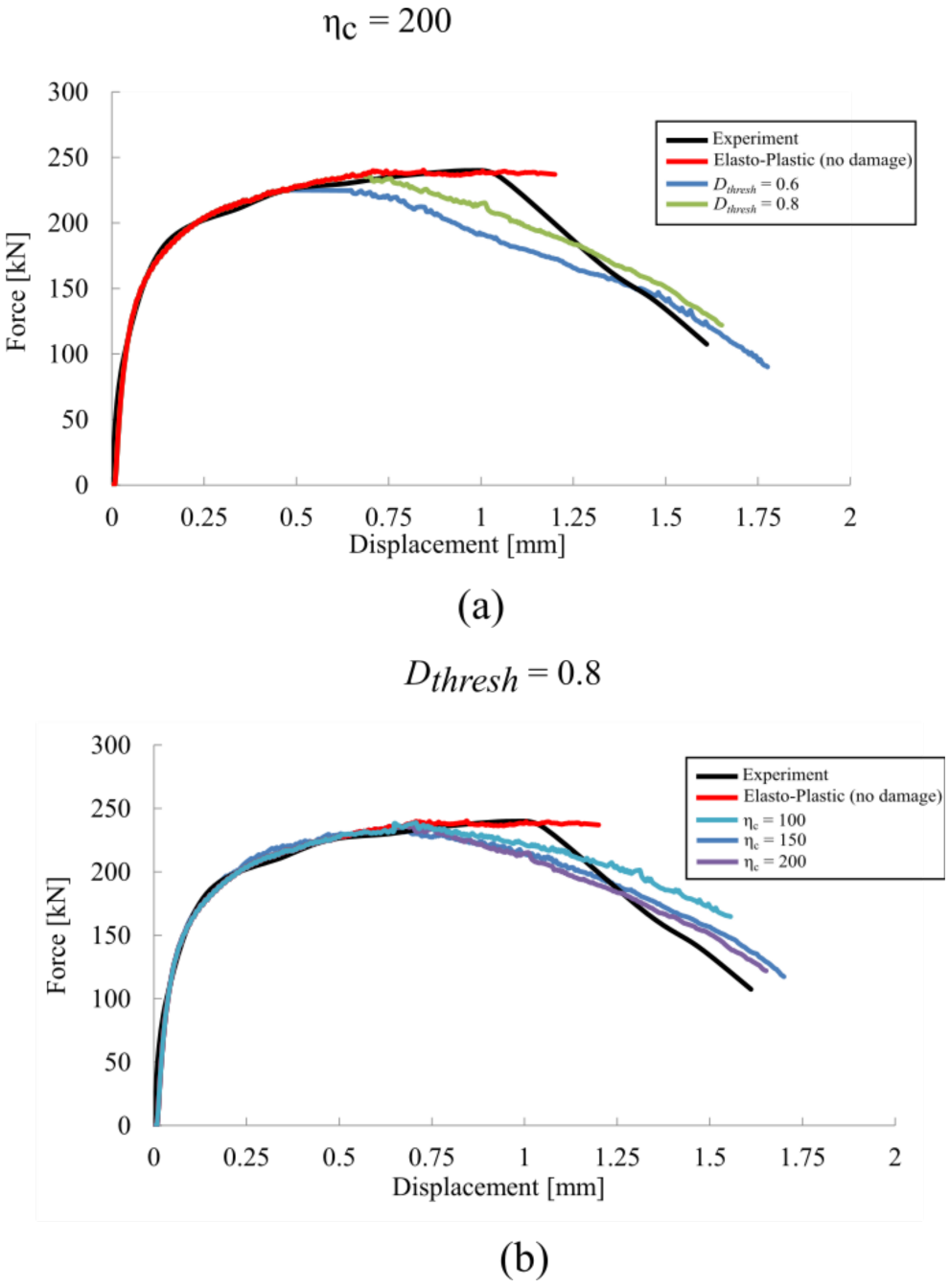


**Fig. 5.36** The effect of the damage threshold $D_{thresh}$ (a) and fracture parameter $\eta_c$ (b) on the force vs. displacement curves.

The effect of mesh size on the final crack path and phase field profile is shown in Fig. 5.37. It can be observed that the final crack path is relatively independent on the mesh size once a good resolution of the phase field is reached.

In order to have a quantitative comparison with the experimental results, box and whisker plots of the fracture zone length and burr height for different mesh sizes are shown in Figs. 5.38 and 5.39 where all lengths are normalized with respect to the workpiece thickness. The reported values are measured at twenty different equally-spaced locations around the circumference of the workpiece in order to give meaningful sampling. It can be shown that a convergence of

the fracture zone length is observed when the mesh size is reduced. In addition, the bur height measurements for coarse and fine meshes are similar in terms of the median. However a spread in the data is also observed. This spread can be related to different factors such as: (i). the approximations introduced to the contact problem; (ii). the numerical diffusion associated with the phase field gradient calculations especially near the surfaces as explained in [132]; (iii). the use of linear finite elements leads to a poor accuracy in the estimation of the phase field gradient; (iv). the remeshing operations used to improve the quality of the mesh elements might change the topology of external surfaces; (v). the imposed boundary condition stating that the phase field gradient is always perpendicular to the normal to the external surface ($\nabla d \cdot \boldsymbol{n} = 0$) enforces the crack path to be perpendicular to the external boundaries which might not be the true experimental observation.

The force vs. displacement curves for the different mesh sizes are also shown in Fig. 5.40 where a convergence is observed when the mesh size is reduced. This result is explained by the non-local effect introduced by adding the characteristic length scale $l_c$ in the phase field model.

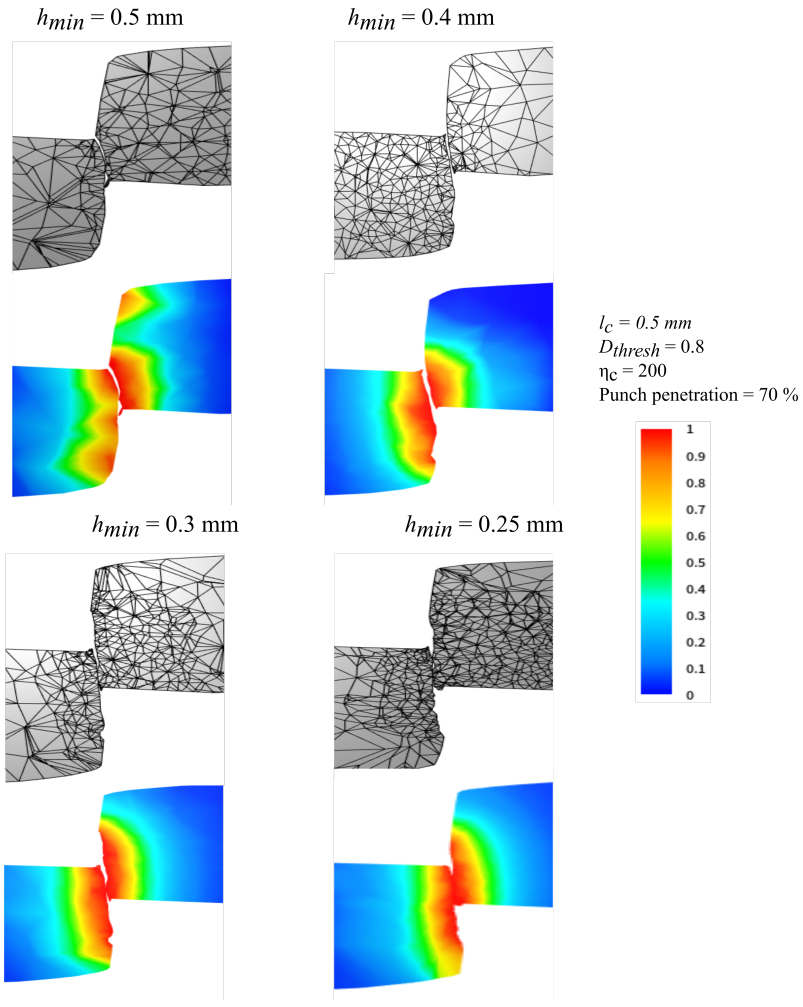


**Fig. 5.37** The effect of mesh size on the final crack path and phase field profile.

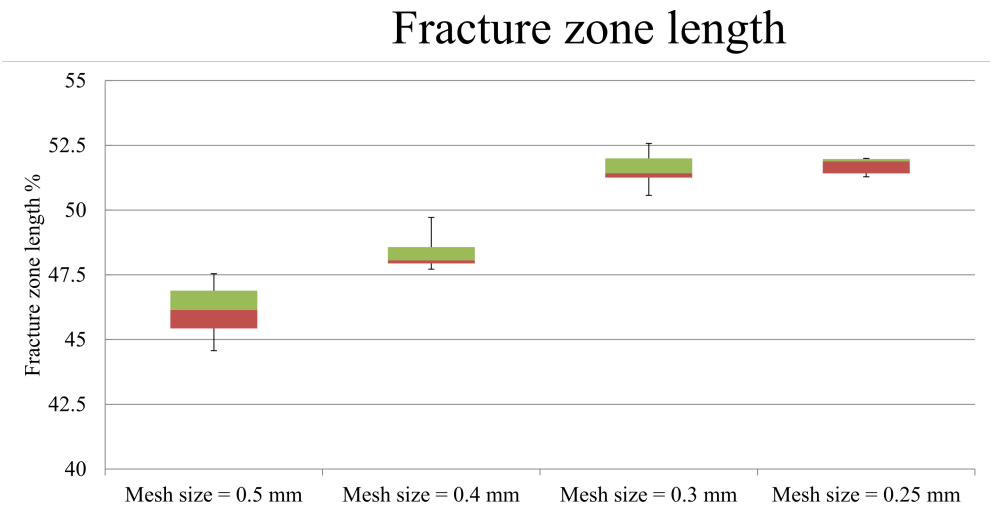


**Fig. 5.38** Box and whisker plot of the fracture zone length for different mesh sizes.

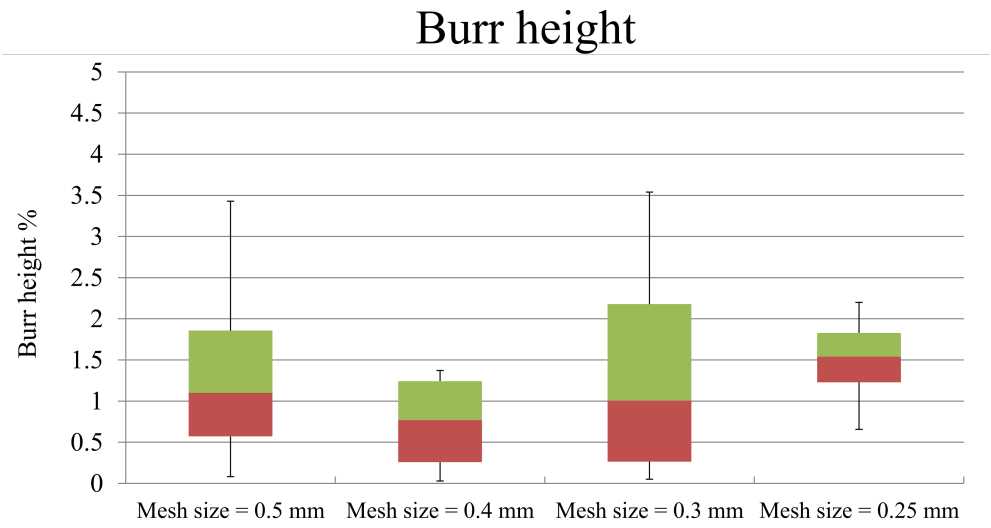


**Fig. 5.39** Box and whisker plot of the burr height for different mesh sizes.

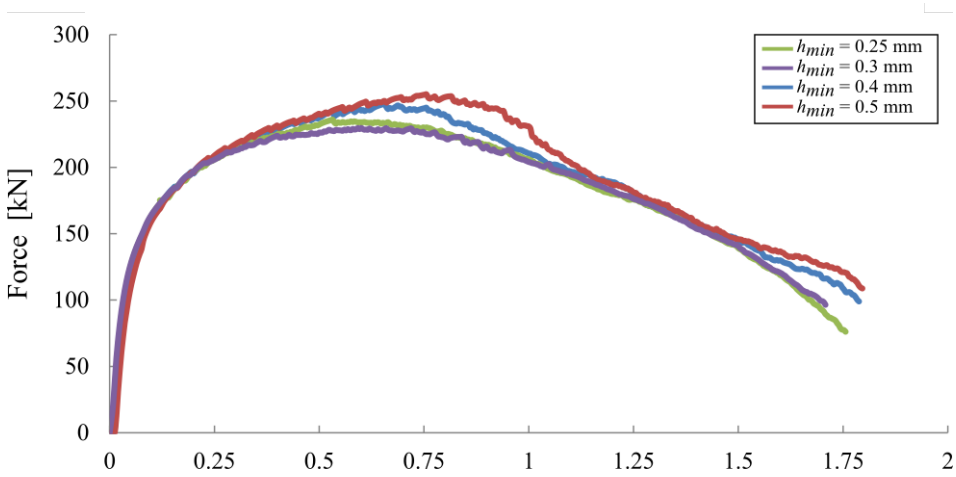


**Fig. 5.40** The force vs. displacement curves at different mesh sizes.

The presented results confirm that both qualitative and quantitative matching between the numerical and experimental results can be obtained with the insertion of real cracks. The crack initiation and propagation algorithm is able to predict the main features of the crack surfaces during cutting simulations with relatively coarse meshes while solving the issues of volume loss and dependency of the crack path on the mesh size. The algorithm presents a reliable and robust solution for the numerical simulation of metal cutting processes. However, an experimental investigation is essential for two main reasons: (i). to determine the main driving factor responsible for the ductile fracture so that a more appropriate damage model can be proposed; (ii). to have a better matching between the force vs. displacement curve obtained in the simulation with the experimental one.

## 5.7 Multi-stages process

In this example, the numerical simulation of a multi-stages process is shown. The main objective is to predict the mechanical behaviour of the final product in order to prevent the apparition of cracks. Fig. 5.41 shows the different stages that are used to form the final shape of the output product along with the velocity profiles adopted in the simulation. In the first and second stages, punches move downward with vertical velocities of 333 mm/s and 67 mm/s, respectively. In the third stage, two loading cases are used. Starting from the beginning, the vertical punch velocity is equal to 333 mm/s until the height reaches 51.6 mm. Then, a horizontal velocity component of 192 mm/s is added until the end of the simulation. In the first stage, a time step of 0.0001 s while a time step of 0.0004 s for the second and third stages in order to ensure the convergence of the solution

The material used in the simulations is a 36Mn5 steel grade. The material properties and model parameters are listed in Table 5.8. The Coulomb limited by Tresca friction law is used for the tangential contact between the different dies and the billet. The friction law parameters are found in Table 5.8. An initial mesh size of 1 mm is used in the whole domain. The adaptive remeshing strategy is used to refine the mesh in the regions where the equivalent plastic strain exceeds a threshold of 0.05. Two mesh sizes are used in the numerical simulations: (i). a coarse mesh with a minimum mesh size $h_{min} = 0.6$ mm; (ii). a fine mesh with $h_{min} = 0.3$ mm. For the crack propagation simulations, the effective crack area $A_{fixed}$ is chosen as two times the minimum mesh size.

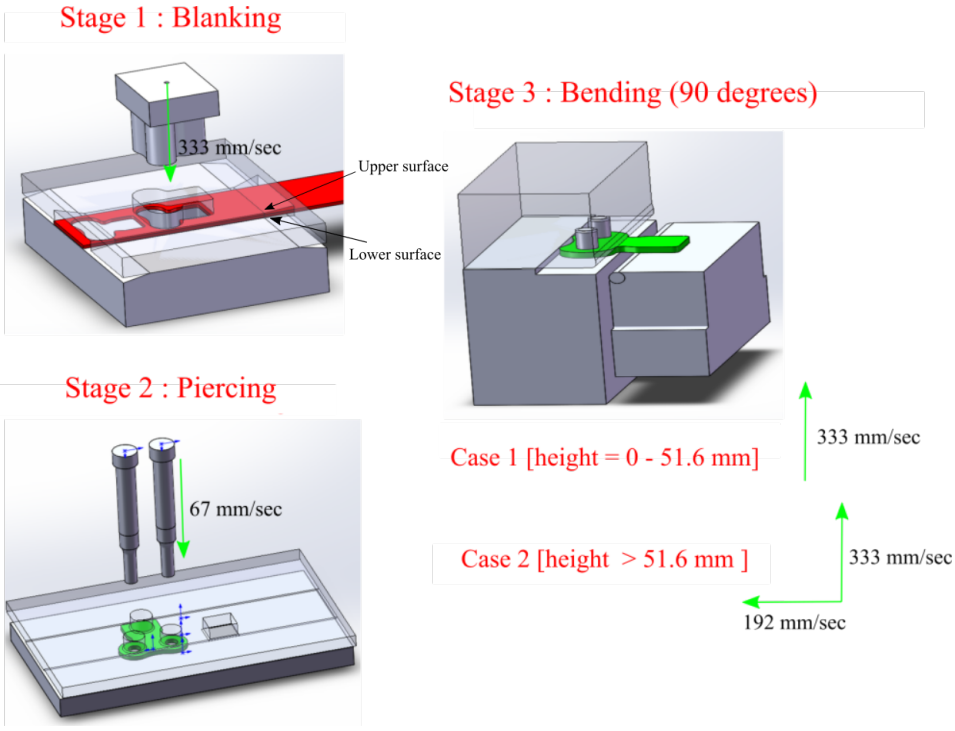


**Fig. 5.41** Industrial chain composed of three stages: (1). Blanking (external shape punching); (2). Piercing; (3). Bending.

Latham-Cockcroft damage model is used to drive the phase field evolution for the three stages. This damage model gives very satisfactory results in the metal forming domain especially in the blanking simulations. It can be assumed that the ratio of $\frac{\langle \boldsymbol{\sigma}_1 \rangle}{\bar{\boldsymbol{\sigma}}}$ is constant in the shear band formed during the blanking process [148]. The normalized Latham-Cockcroft variable can be then expressed as

$$D = \int_0^{\bar{\varepsilon}_f} \frac{\langle \boldsymbol{\sigma}_1 \rangle}{\bar{\boldsymbol{\sigma}}} \, d\bar{\boldsymbol{\varepsilon}} = C^* \bar{\varepsilon}_f \tag{5.15}$$

where $C^* = \frac{\langle \boldsymbol{\sigma}_1 \rangle}{\bar{\boldsymbol{\sigma}}}$ is assumed to be constant for each element in the shear band. This indicates that the material fails in the regions of maximum plastic deformation. It should also be noted that a damage criterion based on the maximum shear stress could also be adopted in order to add the effect of stress state on the ductile fracture process.

The accumulated plastic strain field is transferred from each step to the following one in order to reflect the effect of strain hardening on the material behaviour. However, the damage field is not transferred from each stage to the next one. Of course this assumption is unrealistic from the physical point of view since the regions close to the crack surface are partially damaged due to the growth of voids in the previous stages. However, cracks will be initiated instantaneously in this case since the damage variable will have a value greater than $D_{thresh}$ in these regions. This problem can be viewed as a consequence of the use of a coupled model to the material behaviour at the macro-scale that does not describe accurately the growth of voids near the cracked zone at the micro-scale. The size of this damaged zone should be much smaller

than the characteristic length scale (and hence the smallest element size) in order to accurately capture the size of the damaged zone. However, the problem will be computationally very expensive especially in 3D calculations. It should be noted that neglecting the effect of damage might lead to inaccurate results in the cases where the damaged surface is subjected to another shearing process in the following stages. Indeed, a future investigation of this assumption is needed to have a better understanding of its limitations.

In stage 1, a blanking operation is carried out in order to obtain a desired external shape of the material. The geometry of the punched cross sectional area is shown in Fig. 5.42.

**Table 5.8** Material and model parameters

| Quantity | Value or expression | Unit |
|---|---|---|
| Young's modulus, E | 210000 | MPa |
| Poisson's ratio, $\nu$ | 0.3 | |
| Yield stress, $\boldsymbol{\sigma}_y$ | $1011\ \bar{\varepsilon}^{0.317}\ \dot{\bar{\varepsilon}}^{\mathbf{0.012}}\ e^{\frac{0.018}{\bar{\varepsilon}}}$ | MPa |
| Fracture parameter, $\eta_c$ | 200 | |
| Minimum mesh size $h_{min}$ | 0.6/0.3 | mm |
| Characteristic length scale $l_c$ | 1.2 | mm |
| Penalisation parameter $\epsilon_n$ | 100 | |
| Coulomb friction coefficient | 0.2 | |
| Tresca friction coefficient | 0.4 | |
| Mesh adaptation threshold (EQP) | 0.05 | |

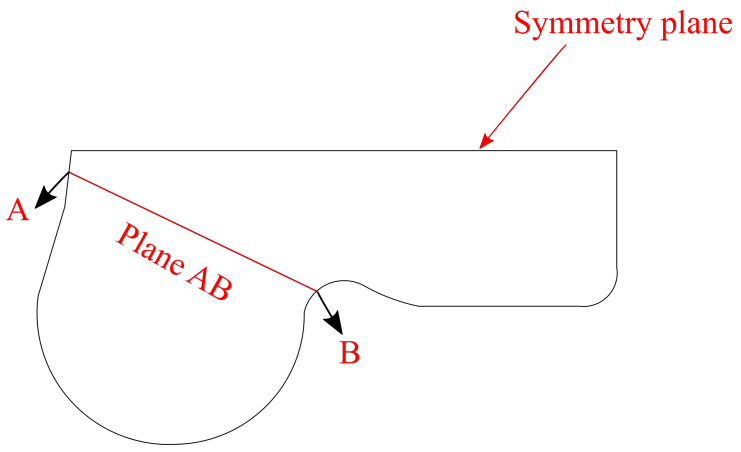


**Fig. 5.42** Geometry of a punch used in a blanking stage (the dimensions are not mentioned for confidentiality reasons).

Fig. 5.43 shows the propagation of crack surfaces in 3D for the coarse and fine meshes with a value of $D_{thresh} = 0.6$. Results are shown at three different punch penetrations (the punch penetration is defined as the ratio between the punch height and specimen thickness).

Starting with the coarse mesh, cracks initiate and propagate simultaneously from the lower and upper boundaries of the sheared zone. The upper and lower branches finally merge together leading to the total separation of the workpiece from the metal sheet. It can be observed that some crack segments are not connected as some nodes are not yet duplicated. This can be explained by the inability of low order finite elements to capture the crack surface intersection with coarse meshes. However, all the unduplicated nodes will be duplicated in the next few increments when the local phase field value approaches one. When a finer mesh is used, a better connectivity of the crack segments is observed with a more accurate resolution of the crack propagation details. Fig. 5.44 demonstrates the phase field evolution accompanied with discrete crack propagation on the plane **AB** shown in Fig. 5.42. Two observations can be made: (i). the characteristic features of sheared surfaces such as the burr height and fracture surface can be accurately captured for both coarse and fine meshes; (ii). a crack is initiated at point **A** before the initiation at point B for both coarse and fine meshes. The last observation can be explained by the fact that the maximum principal stress near the geometric curvature at point **B** is lower than the one at point **A**.

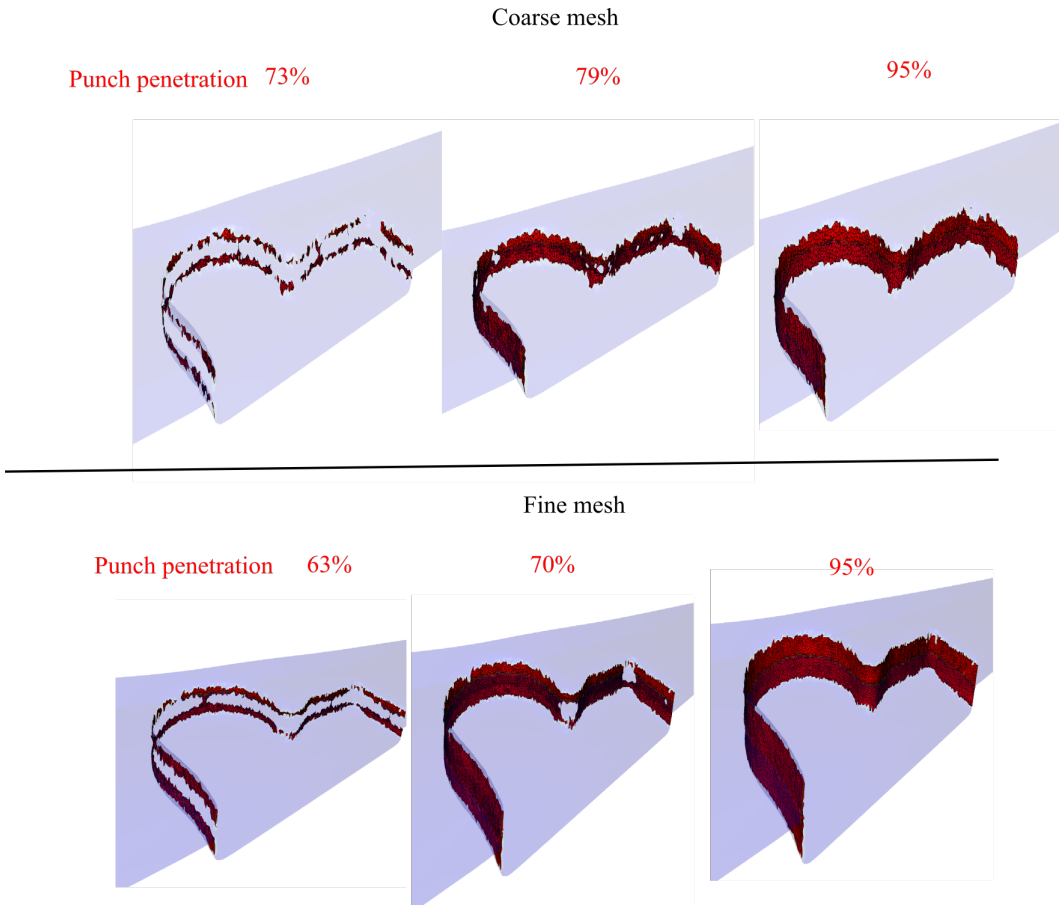


**Fig. 5.43** Initiation and propagation of crack surfaces during the blanking stage for a coarse mesh with $h_{min} = 0.6$ mm and a fine mesh with $h_{min} = 0.3$ mm.

Fig. 5.45 shows a comparison between the CIPFAR and element deletion algorithms on

the final sheared workpiece. In this comparison, a critical damage value of 0.8 is used in the element deletion simulation. A better smoothness of the fracture surface can be observed with the CIPFAR algorithm. In addition, the formation of burrs can be accurately captured with the CIPFAR algorithm since the surface details are not eliminated during the simulation which is the case with the element deletion algorithm. On the other hand, all burrs are removed from the mesh when the element deletion technique is adopted.

Fig. 5.46 shows the phase field evolution on the plane CD for different punch penetrations in the stage 2 of a piercing process where a fine mesh is used. The results are shown for three different values of the damage threshold $D_{thresh}$. It should be noted here that the purpose of this parametric study is to see the effect of $D_{thresh}$ on the shearing process from a modeling point of view since the experimental calibration is not carried out yet. As expected, the increase in the damage threshold leads to a delay in the crack initiation moment.

A comparison of the final crack surfaces between the CIPFAR algorithm with a value of $D_{thresh}$ =0.2 and element deletion algorithm with a critical value of 0.4 is shown in Fig. 5.47. The two thresholds in this case are chosen so that the crack initiation moments are as close as possible. Two main observations can be made: (i). The discrete crack predicted by the CIPFAR algorithm leads to a better quality of the sheared surfaces as compared to the element deletion algorithm; (ii). the CIPFAR algorithm leads to an accurate prediction of the crack path which can be clearly seen in the exact contact between the punch and sheared edge. On the other hand, the deletion of elements results in a gap without any contact between the punch and the sheared edge in which the size of this gap is dependent on the mesh size.

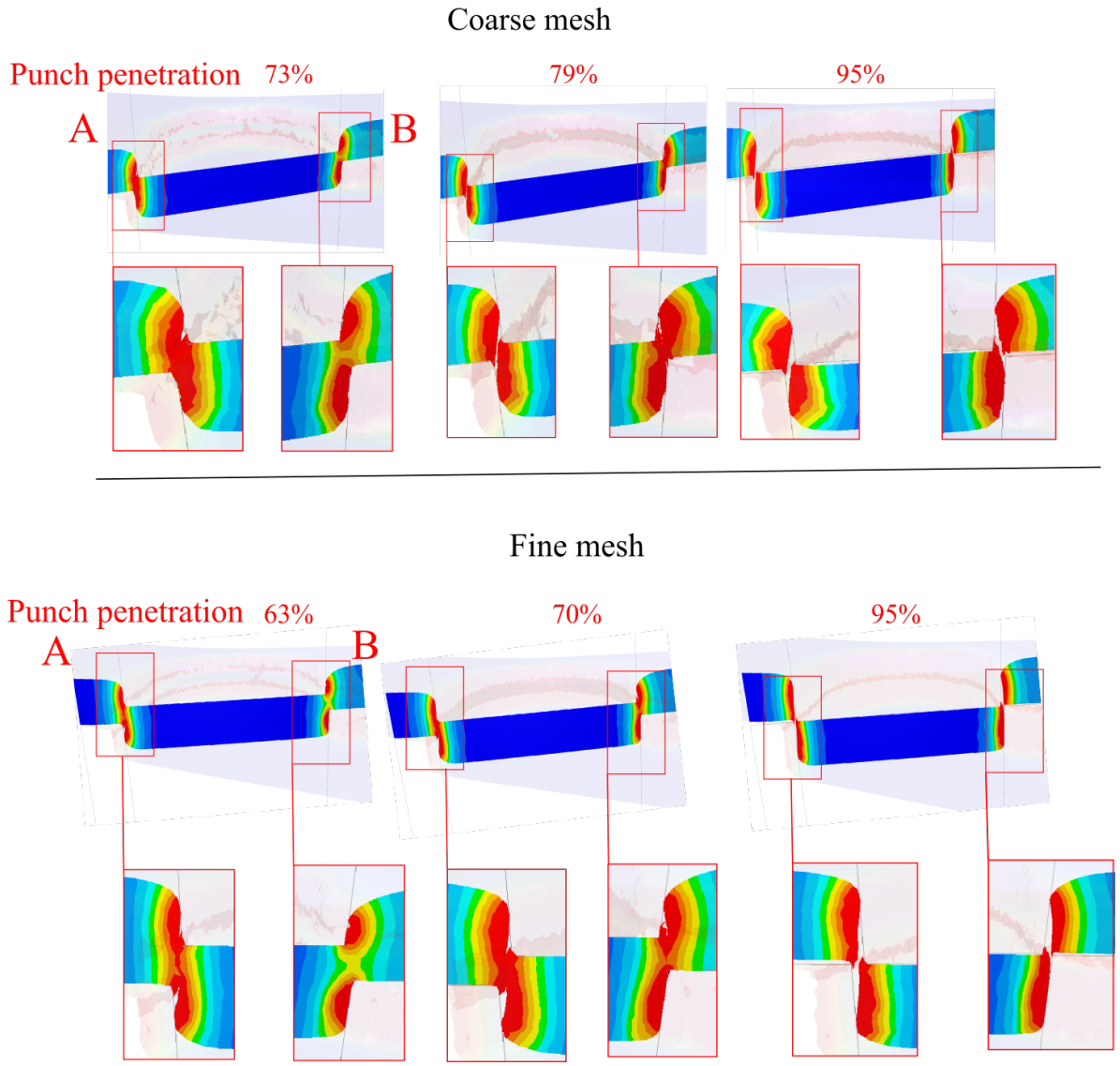


**Fig. 5.44** Discrete crack propagation accompanied with the phase field evolution for coarse and fine meshes. The results are shown on the plane AB shown in Fig. 5.42.

In order to get an idea about the computation time needed for the two industrial stages, Fig. 5.48 shows the evolution of CPU computation time and number of elements during the simulation for each modeling technique where a fine mesh is used. It is clear that the computation time for both models are very similar with a slight decrease in the case of CIPFAR algorithm especially for stage 1. This can be further explained by Fig. 5.49 that shows the number of Newton-Raphson iterations versus the process time for the first and second stages. It can be observed that the convergence behaviour of the CIPFAR is in general faster than the element deletion method. This observation can be clearly seen in stage 1 after the second 0.003 and in stage 2 after the second 0.025. This difference in the convergence behaviour can be related to the contact treatment during and after the formation of final crack surfaces. The CIPFAR algorithm gives a very smooth definition for the crack surface topology which leads to a faster detection of contact points.

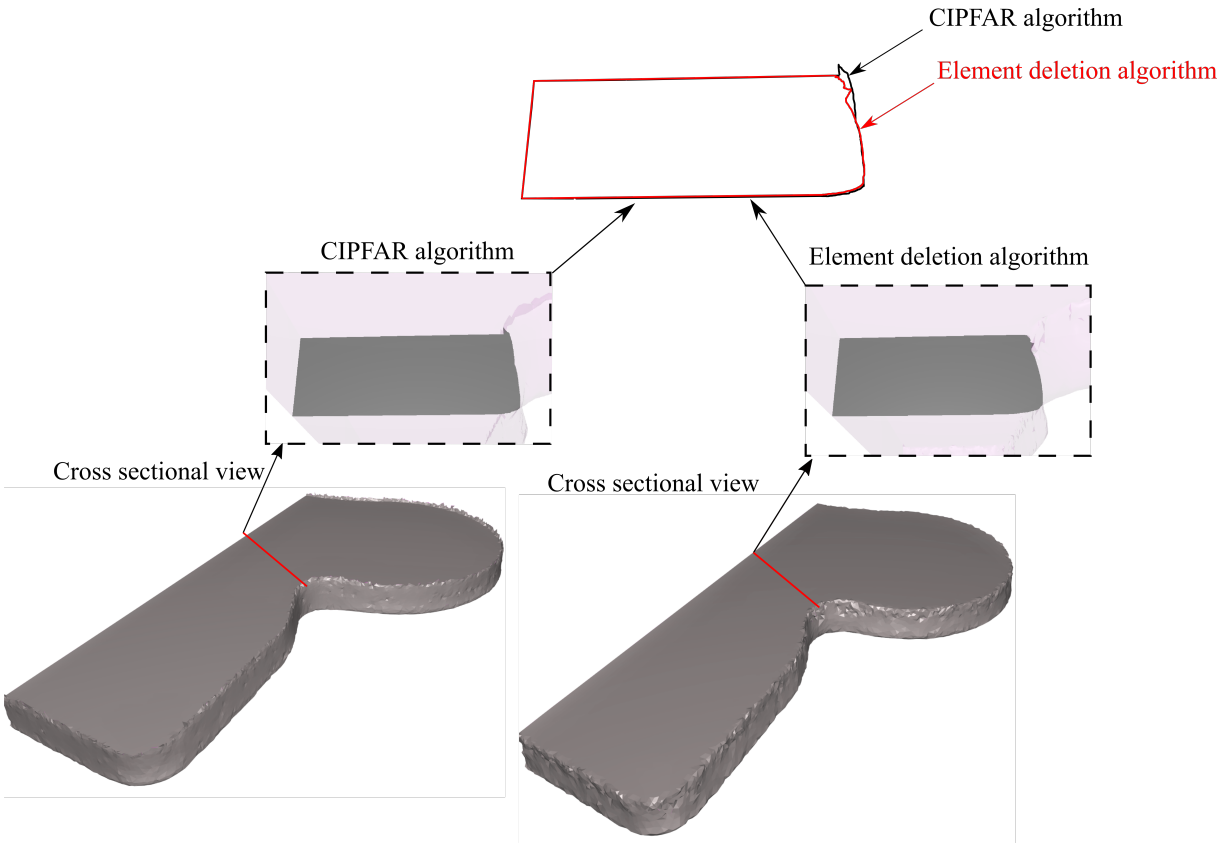


**Fig. 5.45** A comparison between CIPFAR and element deletion algorithms on the final workpiece after the blanking stage.

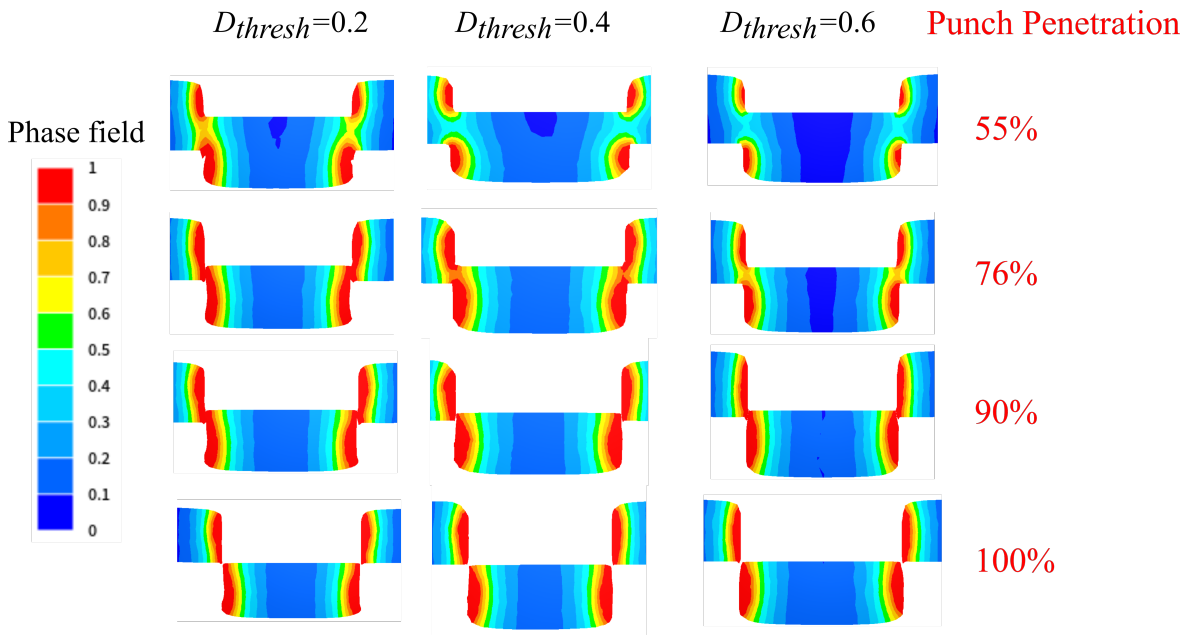


**Fig. 5.46** Simulation of the initiation and propagation of crack surfaces during the piercing stage for different values of $D_{thresh}$.

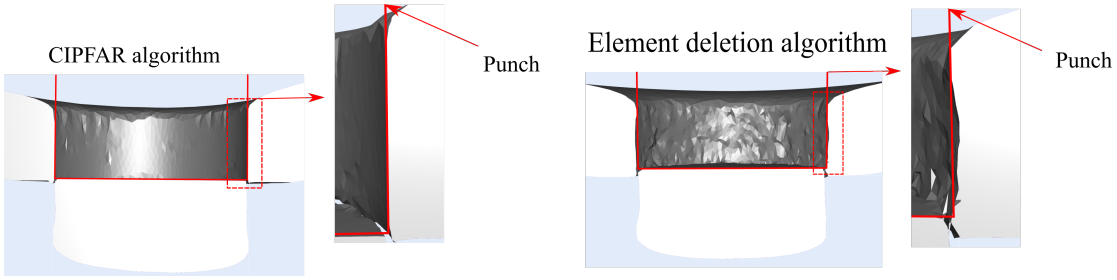


**Fig. 5.47** Simulation of the initiation and propagation of crack surfaces during the piercing stage. Comparison between CIPFAR and element deletion algorithms.

In addition, the satisfaction of the non-penetration condition becomes easier when the contact boundary is accurately defined. On the other hand, the element deletion method leads to a very poor definition of external boundaries. In consequence, the contact detection becomes difficult and the stress singularities are very likely to appear. This result confirms the significant advantage of the CIPFAR algorithm which leads to a noticeable improvement in the results with a similar level of algorithmic efficiency when compared to the element deletion algorithm.

Fig. 5.50 demonstrates the phase field evolution in addition to crack surfaces propagation at three displacement states during the bending stage. In this case, the loading is applied on the upper surface (shown in Fig. 5.41) where burrs appear during the first blanking stage. The objective is to investigate the possibility of crack initiation during the bending process.

The results of two damage threshold values are compared where a fine mesh is used. When $D_{thresh} = 0.6$ is used, two cracks are initiated at the left and right boundaries of the bending line. As bending continues, the two cracks propagate toward the center of the bending line and finally merge. When $D_{thresh}$ increases to a value of $0.7$, it can be observed that two tiny cracks initiate at the left and right boundaries and propagate for a small distance toward the center. This result can be qualitatively compared with the experimental observation shown in Fig. 5.51. It can be seen that the same tiny cracks have been observed experimentally with a very good correlation in both location and size with the numerical simulation.

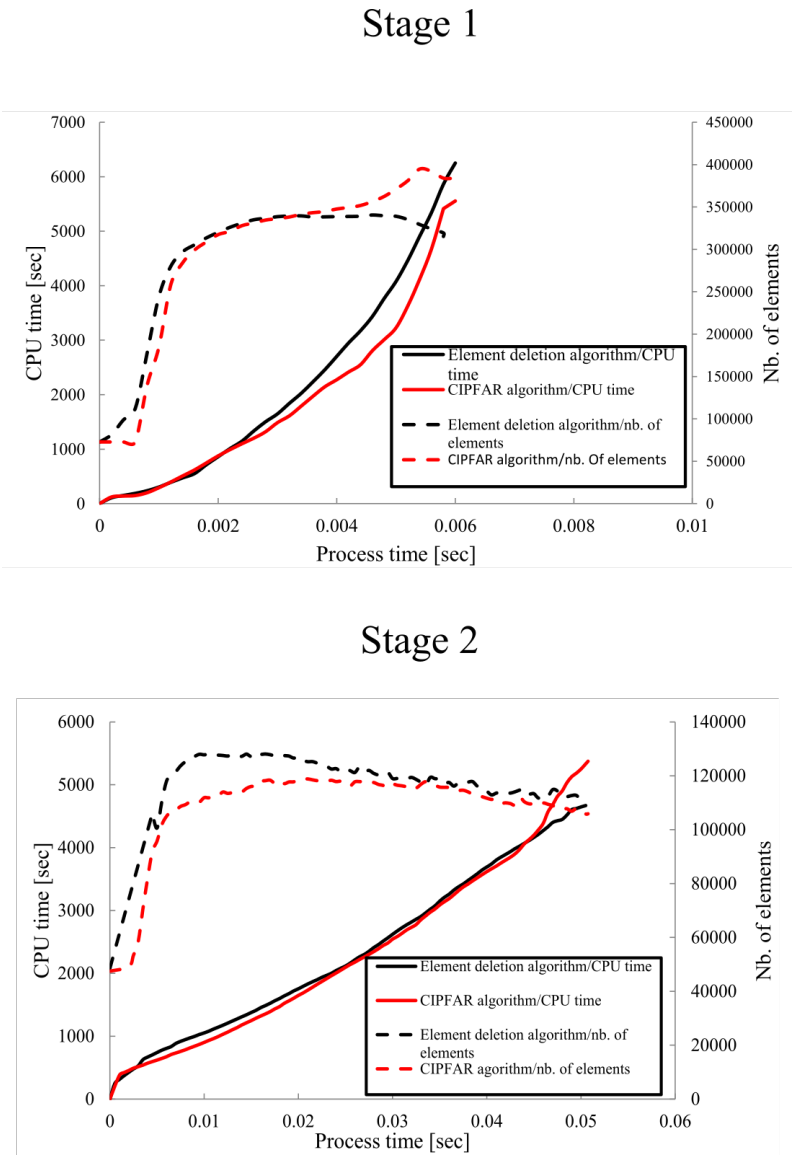


**Fig. 5.48** A comparison between the CIPFAR and element deletion algorithms in terms of the CPU time and the evolution of number of elements.

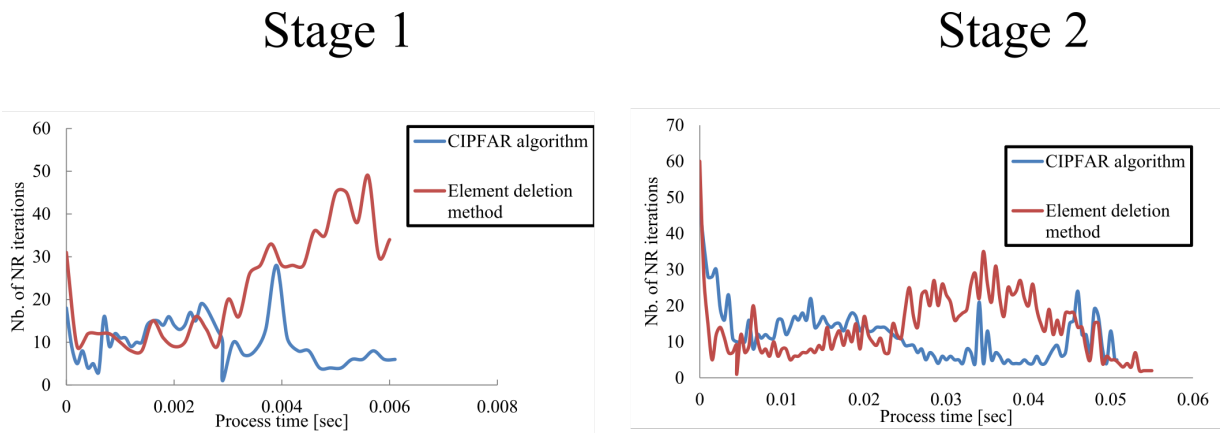


**Fig. 5.49** The number of Newton-Raphson iterations vs. process time for the first and second production stages. A comparison is shown between CIPFAR and element deletion algorithms.

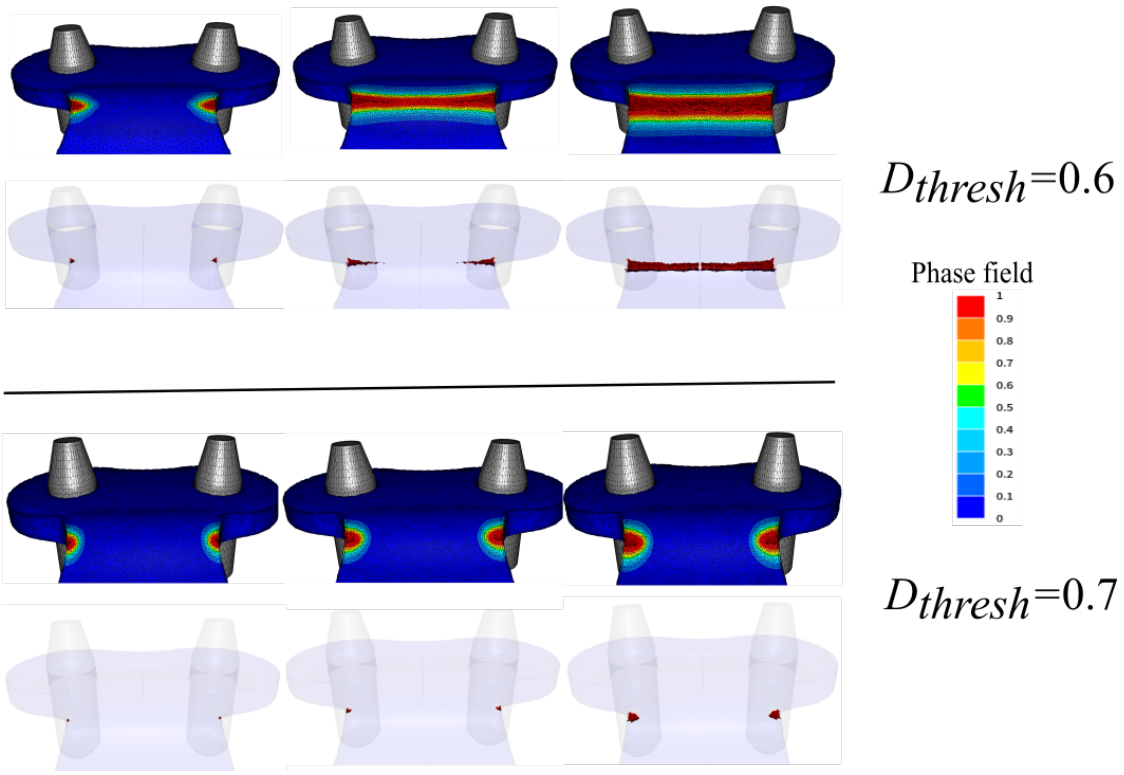


**Fig. 5.50** The effect of $D_{thresh}$ on crack initiation in the third bending stage.

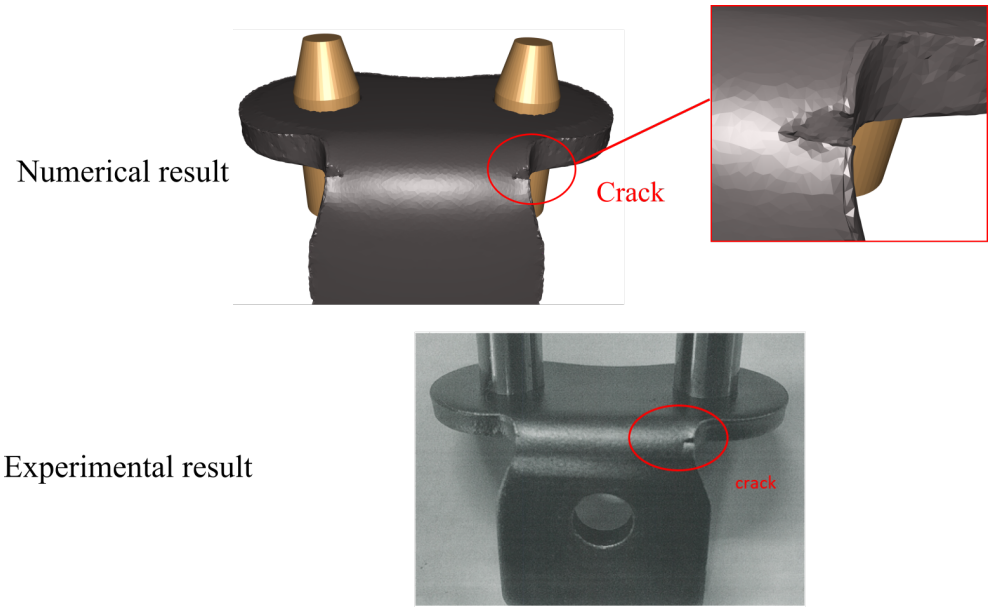


**Fig. 5.51** A qualitative comparison between the CIPFAR algorithm and experimental results. The objective is to predict the formation of tiny cracks during the bending process.

To conclude, preliminary results are obtained toward the modeling of multi-stages industrial processes in which the ductile fracture plays an important role. The main advantage of the algorithm is the ability to capture the different features of the output product at each stage using the numerical simulation. In consequence, the mechanical behaviour of the final product can be

predicted using the numerical simulation before going to the experimental validations that the number of mechanical tests is reduces. Despite the advantages of the new proposed strategy, two main challenges need to be addressed: (i). an experimental analysis of the main mechanical factors that affect the damage evolution in the three stages so that the same experimental crack propagation scenario can obtained in the simulation; (ii). understanding the limitations of neglecting the effect of damage of the sheared surfaces in the next production stages.

## 5.8 Summary of chapter 6

In the first part of this chapter, a coupled phase field-damage model is proposed to predict the crack initiation and propagation under complex loading conditions. The main advantage is the ability to use the rich library of damage models (fracture criteria, continuum damage mechanics (CDM) models or micro-mechanics models for the modeling of ductile fracture processes.

The model contains two parameters, a damage threshold $D_{thresh}$ introduced to delay the onset of fracture and a fracture parameter $\eta_c$ that controls the rate of phase field evolution due to damage evolution in the material. A comprehensive analysis of the physical basis that motivated the proposal of the model is presented. It has been shown that the model can be adapted with all models that represent the damage state in the material.

Numerical examples of a bar shearing process are first presented in order to show the effect of damage model on the phase field evolution. Four damage models based on different driving factors are tested and results are reported both qualitatively and quantitatively. It has been shown that the proposed model is able to capture the effect of different stress states on the initiation and propagation of discrete cracks.

A second example is then presented of a symmetrically notched specimen subjected to a quasi-static tensile loading. It has been shown that the model is able to predict three crack initiations: two cracks are initiated at the boundaries of the notches while a third crack is initiated in the center of the specimen. The algorithm is able to obtain results with a good matching with the experimental Force vs. Displacement curve and the crack propagation scenario. In addition, it is possible to handle multiple initiations of cracks and also to deal with the merging of different crack branches without an ad-hoc criteria. The results are very promising toward the simulation of different industrial processes that are subjected to complex loading conditions.

The second part is dedicated to the modeling of the transition between damage to fracture in metal forming applications. This objective is realized by replacing the element deletion algorithm widely used in numerical codes by a more accurate technique that resolves the following issues: (i). the dependency of the final crack path on the mesh size; (ii). the inability to capture specific characteristic features of crack surfaces such as the burr height in the case of shearing; (iii). the non-physical volume loss.

Three numerical examples are presented in the second part. First, a bar extrusion process is studied where the initiation of chevron-shaped cracks in the core of the material is expected.

The crack insertion algorithm is able to accurately predict the number and shape of chevron cracks where the results are independent from the mesh size. In consequence, the accuracy of the results is only related to the resolution of the mechanical and phase field equations so that a convergence behaviour is expected when the mesh size is reduced. In addition, a qualitative comparison with experimental results confirms the improvements in the prediction of final cracks when compared to the element deletion algorithm. In the second example, a blanking process is presented to show the ability of the algorithm to predict the characteristic surface features of the workpiece as a result of the shearing process such as the smoothness of the fracture surfaces and the appearance of sharp burrs. Last, the numerical simulation of a multi-stages industrial process is presented in which the quality of the product at each stage affects the other production stages. The proposed numerical framework can properly predict the main features of the output product of each manufacturing stage such as the apparition of burrs and the smoothness of the sheared surfaces. It has been shown that a good qualitative agreement with the experimental observation of tiny cracks formation at two boundaries during a bending process is possible by tailoring the phase field model parameters. These results are very promising toward the accurate modeling of multi-stages industrial processes. However, more investigations are necessary regarding the experimental calibration of the models parameters. In addition, the uniqueness of the model parameters should be validated through the use of full field measurements.

## 5.9 Résumé en français

Dans la première partie de ce chapitre, un modèle couplant endommagement et champ de phase est proposé pour prédire l'amorçage et la propagation des fissures dans des conditions de chargement complexes. Le principal avantage est la possibilité d'utiliser la riche bibliothèque de modèles d'endommagement (critères de rupture, modèles de mécanique de l'endommagement continu (CDM) ou modèles micromécaniques pour la modélisation des procédés de rupture ductile.

Le modèle contient deux paramètres, un seuil d'endommagement $D_{thresh}$ utilisé pour retarder le début de la rupture et un paramètre de rupture $\eta_c$ qui contrôle le taux d'évolution du champ de phase dû à l'évolution de l'endommagement dans le matériau. Une analyse complète de la base physique qui a motivé la proposition du modèle est présentée. Il est montré que le modèle peut être adapté avec tous les modèles qui représentent un état d'endommagement dans le matériau.

Des exemples numériques d'un essaie de cisaillement de barre sont présentés afin de montrer l'effet du modèle d'endommagement sur l'évolution du champ de phase. Quatre modèles d'endommagement basés sur différents facteurs d'activation sont testés et les résultats sont rapportés à la fois qualitativement et quantitativement. Il est montré que le modèle proposé est capable de capturer l'effet de différents états de contrainte sur l'amorçage et la propagation

de fissures discrètes. Les résultats sont très prometteurs pour la simulation de différents essaie industriels soumis à des conditions de chargement complexes.

La deuxième partie est consacrée à la modélisation de la transition entre l'endommagement et la rupture dans les applications de mise en forme. Cet objectif est atteint en remplaçant l'algorithme de suppression d'éléments largement utilisé dans les codes numériques par une technique plus précise qui résout les problèmes suivants : (i). la dépendance du chemin de fissure final à la taille de maille ; (ii). l'incapacité à modéliser certaines caractéristiques des surfaces de rupture telles que la hauteur des bavures en cas de cisaillement ; (iii). la perte de volume non physique.

Un deuxième exemple est ensuite présenté d'une éprouvette entaillée symétriquement soumise à un chargement de traction quasi-statique. Il a été montré que le modèle est capable de prédire trois initiations de fissures: deux fissures s'amorçent aux bords des encoches tandis qu'une troisième fissure s'amorce au centre de l'éprouvette. L'algorithme est capable d'obtenir des résultats avec une bonne concordance avec les observations expérimentales en termes à la fois du scénario de propagation de fissure et de la courbe Force vs. Déplacement. Les résultats sont très prometteurs pour la simulation de différents procédés industriels soumis à des conditions de chargement complexes.

Trois exemples numériques sont présentés dans ce chapitre. Tout d'abord, un procédé d'extrusion de barre a été étudié où l'amorçage de fissures en forme de chevron dans le cœur du matériau est attendue. L'algorithme d'insertion de fissures a pu prédire avec précision le nombre et la forme des fissures en chevron où les résultats sont indépendants de la taille de maille. En conséquence, la précision des résultats n'est liée qu'à la résolution des équations de champ mécanique et de champ de phase de sorte qu'une convergence est attendue lorsque la taille de maille est réduite. De plus, une comparaison avec les résultats expérimentaux confirme les améliorations dans la prédiction des fissures finales par rapport à l'algorithme de suppression d'éléments. Dans le deuxième exemple, un essaie de découpage est présenté pour montrer la capacité de l'algorithme à prédire les caractéristiques de surface de la pièce résultant du essaie de cisaillement, telles que la précision des surfaces de rupture et l'apparition de bavures acérées. Enfin, la simulation numérique d'un procédé industriel multi-étapes a été présentée dans laquelle la qualité du produit de chaque étape affecte les autres étapes de production. Il est montré que le cadre numérique proposé permet de prédire correctement les principales caractéristiques du produit issu de chaque étape de fabrication telles que l'apparition de bavures et la régularité des surfaces cisaillées. Enfin, il est montré qu'un bon accord qualitatif avec l'observation expérimentale de la formation de minuscules fissures à deux surfaces libres au cours d'un essaie de flexion est possible en adaptant les paramètres du modèle de champ de phase. Ces résultats sont très prometteurs pour la modélisation précise de procédés industriels multi-étapes. Cependant, plus d'investigations sont nécessaires concernant la calibration expérimentale des paramètres des modèles.

# Discussions and perspectives

## 6.1 Summary and discussions

This thesis was dedicated to the simulation of damage to fracture transition under complex loading conditions. Following this objective, the work provides a detailed numerical framework for the modeling of real crack initiation and propagation in ductile materials. Different modeling strategies have been implemented in order to accomplish the final objective as follows: (i). implementation of a phase field model dedicated to ductile fracture simulation using an adaptive remeshing scheme; (ii). development of a real 3D crack insertion algorithm based on local remeshing operations; (iii). introduction of a coupled phase field-local damage model in order to simulate the failure processes in the metal forming field. A summary of each topic is presented in the following subsections.

### 6.1.1 Phase field model validation and comparison with non-local gradient damage models

First, a validation of the current implementation of the phase field model with the literature within a framework of large plastic strain was carried out. Then, a detailed comparison between the phase field and classical non-local gradient damage models was illustrated by presenting the analytical solution of a simple 1D bar followed by the numerical solution a double notched asymmetric specimen. The aim of the comparison was to show the different features of both formulations in addition to their ability and limitations to accurately model the damage to fracture transition. It was concluded that although the mathematical structure of both models is very similar, the phase field model is more suitable for the regularization of crack topology as it does not lead to damage diffusion once the crack is formed. In consequence, a real crack increment can be inserted once the full crack is formed without affecting the accuracy of the obtained results. This leads to a major decrease in the computational cost needed to simulation. However, non-local gradient damage models can be also used with a condition of inserting the crack increment at an earlier stage before reaching a value of one. In consequence, a frequent insertion of real crack increments is required in this case which leads to an increase in the computational cost with each remeshing operation.

### 6.1.2 Adaptive remeshing strategy

An adaptive remeshing strategy was developed in order to achieve two objectives: (i). refining the mesh in the zones where the crack is expected to initiate and propagate. This improvement is very important for metal forming applications where the crack path is not known a priori; (ii). reducing the computation time by keeping a coarse mesh in the weakly damaged zones and only refine the mesh in the highly damaged zones.

In order to achieve these objectives, a numerical strategy of mesh refinement based on two metrics was presented. The first metric represented a simple criterion used to indicate the regions that need to be refined. This criterion defines a field of interest such as the phase field variable, the equivalent plastic deformation or the normalized yielding function. In this context, it is assumed that a more closer solution to the exact one is obtained with the mesh refinement.

Once the mesh is refined, a field transport step is carried out in order to interpolate the old fields on the new mesh. However, the interpolation process is known to diffuse the numerical data due to the non-exact transport. In order to minimize the numerical diffusion, a second volume quality metric is defined with the aim of terminating the remeshing operations once the mesh is refined in the zone where the crack is expected to propagate. Remeshing is terminated once the relative volume quality between old and new meshes becomes less than a given threshold. This assumption is equivalent to saying that the error between the exact and computed solutions is less than a given threshold. The proposed strategy is found to be simple to use when coupled with the phase field model and leads to efficient numerical results.

### 6.1.3 CIPFAR: a crack insertion and propagation algorithm

A real crack insertion strategy was then developed in order to simulate the material decohesion and the opening of crack faces due to the crack propagation. In this context, a three-step algorithm was developed as follows: (i). the crack surface is identified as the intersection of the real crack with the mesh edges in the highly damaged zone; (ii). new nodes are inserted at the identified crack locations followed by local mesh partitioning strategy; (iii). a nodal duplication step is performed to split the elements crossed by the crack followed by a volume remeshing operation to keep a good mesh quality during the next computations.

In the first step, a crack intersection is identified for all mesh edges using two conditions: (i). finding the locations along the mesh edges at which the directional derivative of the phase field solution vanishes; (ii). the identified position of a vanishing gradient projection has a phase field value close to 1 (usually chosen as 0.99 for the purpose of numerical robustness). Once these positions are identified at each time step, the crack surface topology is fitted within the mesh by locally defining a new mesh connectivity. Finally, a local coloring algorithm is used to split the crossed elements by duplicating all the nodes that lie on the crack surface except for the crack front nodes. All algorithmic steps were implemented within a parallel numerical framework that is essential for the large scale industrial applications. Different numerical examples have

been presented in order to show the performance of the algorithm with the mixed fracture modes that include both tensile and shear loading. Finally, a flat specimen subjected to tensile loading was also tested in order to show the internal crack initiation and propagation. All the reported results confirm the robustness and efficiency of the developed numerical framework.

### 6.1.4 Toward the modeling of complex industrial processes

Another important component in the modeling framework was the ability to model the damage to fracture transition in the field of metal forming. In this context, complex stress states are produced due to the multi-axial and non-proportional loading scenarios. In order to achieve this objective, a coupled phase field-damage model with two parameters was proposed. The model is motivated by the phase field model generality that enables the inclusion of proper damage driving factors through the crack driving force. First, the coupling of the phase field with an uncoupled damage model can only describe the post-critical regime without affecting the material behaviour before reaching the critical damage value. The model can properly control the post-critical regime in which a crack at the macro-scale should be inserted as a result of the void coalescence at the micro-scale. It was shown that the model can be linked to the void coalescence phase in the GTN model where an accelerated degradation of Young's modulus and yield surface can be expected. In addition, a conceptual link to continuum damage mechanics models such as the Lemaitre model has been demonstrated in which the damage evolution can only affects the material behaviour once the damage variable exceeds a given threshold.

It was concluded at the end that a further investigation is needed to calibrate the model parameters in order to obtain physically-relevant results. The model was able to handle different cases of ductile fracture such as the initiation of internal cracks during bar extrusion and shearing processes. The main advantage of such formulation is the ability to integrate it with the rich library of damage models that exists in **FORGE ®**. Finally, the proposed modeling strategy has also succeeded to give very promising initial results toward the modeling of multi-stages processes. It has been shown that an accurate prediction of the quality and behaviour of the final product was possible even with coarse meshes.

## 6.2 Future work

The presented developments and numerical results confirm the robustness and efficiency of the numerical framework. However, many challenging points need to be studied in the future work and can be summarized as follows:

1. Introducing physically inspired fracture criteria to drive the phase field evolution through the crack driving force. The proposed model should be able to give a good compromise between accuracy and a low number of parameters to be identified. The model should contain the effect of different physical factors that lead to the damage evolution in ductile materials such as the plastic deformation state, stress triaxiality ratio and Lode parameter.
2. Experimental calibration of the phase field model parameters is essential for an accurate prediction of the physical behavior. The use of inverse analysis techniques seems to be suitable in this case since the mechanical behaviour is coupled with the phase field evolution. A simultaneous calibration of the damage and phase field model parameters would give an optimal set of parameters. Most importantly, the uniqueness of the solution should be ensured by enriching the measured data with local field measurements such as the displacement or strain fields. Finally, a cross validation of the predicted model parameters is also important to ensure the validity of the model with the actual loading conditions.
3. Using higher order finite element discretization is expected to improve the results of crack surface identification. With linear finite elements, very fine meshes are needed in the cracked zone in order to accurately capture the local maxima of the phase field profile in the sense of getting an accurate resolution of the gradient. However, a significant increase in computational time is associated with the mesh refinement. With higher order elements, a better resolution of the phase field gradient is expected. In consequence, a more accurate identification of the crack intersection with the mesh is expected.
4. Applying more conservative phase field gradient smoothing operators. As described in chapter 4, a gradient smoothness operator is essential for the transformation from a P0 field to a P1 field. In this study, simple models are proposed for the sake of demonstration. However, more accurate techniques can be used for the accurate determination of the crack intersection location along the edges.
5. Adapting the proposed modeling framework for other physical problems such as: (i). cyclic loading that induces fatigue; (ii). dynamic loading such as crash simulations and failure under impact loading.

# Bibliography


[1] A. E. Tekkaya et al. “Damage in metal forming”. *CIRP Annals* 69 (2020), pp. 600–623.

[2] P.-O. Bouchard. “Damage and discrete crack propagation modelling: Some results and challenges for 2d and 3d configurations”. *International Conference on Fracture*. 2005, 6 pages.

[3] P. Di Pietro and Y. L. Yao. “An investigation into characterizing and optimizing laser cutting quality—A review”. *International Journal of Machine Tools and Manufacture* 34 (1994), pp. 225–243.

[4] S. F. Golovashchenko. “A study on trimming of aluminum autobody sheet and development of a new robust process eliminating burrs and slivers”. *International Journal of Mechanical Sciences* 48 (2006), pp. 1384–1400.

[5] R. Hambli. “Prediction of burr height formation in blanking processes using neural network”. *International Journal of Mechanical Sciences* 44 (2002), pp. 2089–2102.

[6] R. Hambli and A. Potiron. “Finite element modeling of sheet-metal blanking operations with experimental verification”. *Journal of Materials Processing Technology* 102 (2000), pp. 257–265.

[7] H.-S. Choi et al. “Application of mechanical trimming to hot stamped 22MnB5 parts for energy saving”. *International Journal of Precision Engineering and Manufacturing* 15 (2014), pp. 1087–1093.

[8] H. So et al. “An investigation of the blanking process of the quenchable boron alloyed steel 22MnB5 before and after hot stamping process”. *Journal of Materials Processing Technology* 212 (2012), pp. 437–449.

[9] J.-S. Choi, H.-C. Lee, and Y.-T. Im. “A study on chevron crack formation and evolution in a cold extrusion”. *Journal of Mechanical Science and Technology* 24 (2010), pp. 1885–1890.

[10] Y. Bai and T. Wierzbicki. “A new model of metal plasticity and fracture with pressure and Lode dependence”. *International Journal of Plasticity* 24 (2008), pp. 1071–1096.

[11] L. Xue. “Damage accumulation and fracture initiation in uncracked ductile solids subject to triaxial loading”. *International Journal of Solids and Structures* 44 (2007), pp. 5163–5181.

[12] P.-O. Bouchard et al. “An enhanced Lemaitre model formulation for materials processing damage computation”. *International Journal of Material Forming* 4 (2011), pp. 299–315.

[13] T.-S. Cao. “Numerical simulation of 3D ductile cracks formation using recent improved Lode-dependent plasticity and damage models combined with remeshing”. *International Journal of Solids and Structures* 51 (2014), pp. 2370–2381.

[14] S. Fayolle. “Etude de la modélisation de la pose et de la tenue mécanique des assemblages par déformation plastique”. PhD thesis. Ecole Nationale Supérieure des Mines de Paris, 2009.

[15] J. K. Sahu et al. “Effect of 475 C embrittlement on the mechanical properties of duplex stainless steel”. *Materials Science and Engineering: A* 508 (2009), pp. 1–14.

[16] S. Li et al. “The interaction of dislocations and hydrogen-vacancy complexes and its importance for deformation-induced proto nano-voids formation in $\alpha$-Fe”. *International Journal of Plasticity* 74 (2015), pp. 175–191.

[17] K. Puttick. “Ductile fracture in metals”. *Philosophical Magazine* 4 (1959), pp. 964–969.

[18] N. R. Abdel Al. “An experimental study of deformation and fracture of a nanostructured metallic material”. PhD thesis. Texas A and M University, 2011.

[19] A. A. Benzerga and J.-B. Leblond. “Ductile fracture by void growth to coalescence”. *Advances in Applied Mechanics* 44 (2010), pp. 169–305.

[20] L. Babout et al. “On the competition between particle fracture and particle decohesion in metal matrix composites”. *Acta materialia* 52 (2004), pp. 4517–4525.

[21] J. Lian et al. “A method to quantitatively upscale the damage initiation of dual-phase steels under various stress states from microscale to macroscale”. *Computational materials science* 94 (2014), pp. 245–257.

[22] T.-S. Cao. “Modeling ductile damage for complex loading paths”. PhD thesis. PSL Research University, 2013.

[23] Y. Bao and T. Wierzbicki. “On fracture locus in the equivalent strain and stress triaxiality space”. *International Journal of Mechanical Sciences* 46 (2004), pp. 81–98.

[24] R. Ebeling and M. Ashby. “Dispersion hardening of copper single crystals”. *Philosophical Magazine* 13 (1966), pp. 805–834.

[25] M. D. John Wiley sons, 1962.

[26] W. Liu et al. “Simulation of void growth and coalescence behavior with 3D crystal plasticity theory”. *Computational Materials Science* 40 (2007), pp. 130–139.

[27] M. Achouri et al. “Experimental characterization and numerical modeling of micromechanical damage under different stress states”. *Materials and Design* 50 (2013), pp. 207–222.

[28] A. J. Gross and K. Ravi-Chandar. “On the deformation and failure of Al 6061-T6 in plane strain tension evaluated through in situ microscopy”. *International Journal of Fracture* 208 (2017), pp. 27–52.

[29] F. Mcclintock. “A criterion for ductile fracture by the growth of holes”. *Journal of Applied Mechanics* 35 (1968), pp. 363–371.

[30] A. Weck et al. “Visualization by X-ray tomography of void growth and coalescence leading to fracture in model materials”. *Acta Materialia* 56 (2008), pp. 2919–2928.

[31] J. R. Rice and D. M. Tracey. “On the ductile enlargement of voids in triaxial stress fields”. *Journal of the Mechanics and Physics of Solids* 17 (1969), pp. 201–217.

[32] P. Thomason. “A three-dimensional model for ductile fracture by the growth and coalescence of microvoids”. *Acta Metallurgica* 33 (1985), pp. 1087–1095.

[33] I. Barsoum and J. Faleskog. “Rupture mechanisms in combined tension and shear—Micromechanics”. *International Journal of Solids and Structures* 44 (2007), pp. 5481–5498.

[34] T. Cox and J. R. Low. “An investigation of the plastic fracture of AISI 4340 and 18 Nickel-200 grade maraging steels”. *Metallurgical Transactions* 5 (1974), pp. 1457–1470.

[35] A. Weck and D. S. Wilkinson. “Experimental investigation of void coalescence in metallic sheets containing laser drilled holes”. *Acta Materialia* 56 (2008), pp. 1774–1784.

[36] J. Mediavilla. “Continuous and discontinuous modelling of ductile fracture.” PhD thesis. Eindhoven School of Technology, 2005.

[37] I. Barsoum and J. Faleskog. “Micromechanical analysis on the influence of the Lode parameter on void growth and coalescence”. *International Journal of Solids and Structures* 48 (2011), pp. 925–938.

[38] O. Cazacu and F. Barlat. “A criterion for description of anisotropy and yield differential effects in pressure-insensitive metals”. *International Journal of Plasticity* 20 (2004), pp. 2027–2045.

[39] T.-S. Cao et al. “A Lode-dependent enhanced Lemaitre model for ductile fracture prediction at low stress triaxiality”. *Engineering Fracture Mechanics* 124 (2014), pp. 80–96.

[40] M. G. Cockcroft. “Ductility and workability of metals”. *Journal of Metals.* 96 (1968), p. 2444.

[41] G. R. Johnson and W. H. Cook. “Fracture characteristics of three metals subjected to various strains, strain rates, temperatures and pressures”. *Engineering Fracture Mechanics* 21 (1985), pp. 31–48.

[42] T.-S. Cao. “Models for ductile damage and fracture prediction in cold bulk metal forming processes: a review”. *International Journal of Material Forming* 10 (2017), pp. 139–171.

[43] Y. Lou et al. “New ductile fracture criterion for prediction of fracture forming limit diagrams of sheet metals”. *International Journal of Solids and Structures* 49 (2012), pp. 3605–3615.

[44] C. Defaisse et al. “Ductile fracture of an ultra-high strength steel under low to moderate stress triaxiality”. *Engineering Fracture Mechanics* 194 (2018), pp. 301–318.

[45] P. F. Bariani et al. “Ductile fracture prediction in cold forging process chains”. *CIRP annals* 60 (2011), pp. 287–290.

[46] M. Jirásek. “Mathematical analysis of strain localization”. *Revue européenne de génie civil* 11 (2007), pp. 977–991.

[47] R. H. J. Peerlings et al. “Gradient enhanced damage for quasi-brittle materials”. *International Journal for Numerical Methods in Engineering* 39 (1996), pp. 3391–3403.

[48] R. H. J. Peerlings et al. “Some observations on localization in non-local and gradient damage models”. *European Journal of Mechanics. A, Solids* 15 (1996), pp. 937–953.

[49] J. Besson, D. Moinereau, and D. Steglich. *Local approach to fracture*. Presses des MINES, 2006.

[50] G. A. Francfort and J.-J. Marigo. “Revisiting brittle fracture as an energy minimization problem”. *Journal of the Mechanics and Physics of Solids* 46 (1998), pp. 1319–1342.

[51] L. Ambrosio and V. M. Tortorelli. “Approximation of functional depending on jumps by elliptic functional via t-convergence”. *Communications on Pure and Applied Mathematics* 43 (1990), pp. 999–1036.

[52] A. Braides. *Approximation of free-discontinuity problems*. Springer Science and Business Media, 1998.

[53] C. Miehe, F. Welschinger, and M. Hofacker. “Thermodynamically consistent phase-field models of fracture: Variational principles and multi-field FE implementations”. *International Journal for Numerical Methods in Engineering* 83 (2010), pp. 1273–1311.

[54] M. Ambati, T. Gerasimov, and L. De Lorenzis. “Phase-field modeling of ductile fracture”. *Computational Mechanics* 55 (2015), pp. 1017–1040.

[55] M. Ambati, R. Kruse, and L. De Lorenzis. “A phase-field model for ductile fracture at finite strains and its experimental verification”. *Computational Mechanics* 57 (2016), pp. 149–167.

[56] M. J. Borden et al. “A phase-field formulation for fracture in ductile materials: Finite deformation balance law derivation, plastic degradation, and stress triaxiality effects”. *Computer Methods in Applied Mechanics and Engineering* 312 (2016), pp. 130–166.

[57] H. Eldahshan et al. “Phase field modeling of ductile fracture at large plastic strains using adaptive isotropic remeshing”. *Computational Mechanics* (2021), pp. 1–21.

[58] C. C. Tasan, J. P. M. Hoefnagels, and M. G. D. Geers. “Identification of the continuum damage parameter: An experimental challenge in modeling damage evolution”. *Acta Materialia* 60 (2012), pp. 3581–3589.

[59] L. M. Kachanov. “Rupture time under creep conditions”. *International Journal of Fracture* 97 (1999), pp. 11–18.

[60] S. Murakami and N. Ohno. “A continuum theory of creep and creep damage”. *Creep in Structures*. Springer, 1981, pp. 422–444.

[61] J. L. Chaboche. “Anisotropic creep damage in the framework of continuum damage mechanics”. *Nuclear engineering and design* 79 (1984), pp. 309–319.

[62] J. Lemaitre. “A continuous damage mechanics model for ductile fracture”. *Journal of Engineering Materials and Technology* 107 (1985), pp. 83–89.

[63] P.-O. Bouchard et al. “On the influence of particle distribution and reverse loading on damage mechanisms of ductile steels”. *Materials Science and Engineering: A* 496 (2008), pp. 223–233.

[64] T. Pardoen and J. W. Hutchinson. “Micromechanics-based model for trends in toughness of ductile metals”. *Acta Materialia* 51 (2003), pp. 133–148.

[65] A. L. Gurson. “Continuum Theory of Ductile Rupture by Void Nucleation and Growth: Part 1-Yield Criteria and Flow Rules for Porous Ductilr Media”. *Journal of Engineering Materials and Technology* 99 (1977), pp. 2–15.

[66] V. Tvergaard and A. Needleman. “Analysis of the cup-cone fracture in a round tensile bar”. *Acta Metallurgica* 32 (1984), pp. 157–169.

[67] C. C. Chu and A. Needleman. “Void Nucleation Effects in Biaxially Stretched Sheets”. *Journal of Engineering Materials and Technology* 102 (1980), pp. 249–256.

[68] F. Aldakheel, P. Wriggers, and C. Miehe. “A modified Gurson-type plasticity model at finite strains: formulation, numerical analysis and phase-field coupling”. *Computational Mechanics* 62 (2018), pp. 815–833.

[69] R. Hambli. “Comparison between Lemaitre and Gurson damage models in crack growth simulation during blanking process”. *International Journal of Mechanical Sciences* 43 (2001), pp. 2769–2790.

[70] K. Nahshon and J. W. Hutchinson. “Modification of the Gurson model for shear failure”. *European Journal of Mechanics-A/Solids* 27 (2008), pp. 1–17.

[71] J. Besson. “Continuum models of ductile fracture: a review”. *International Journal of Damage Mechanics* 19 (2010), pp. 3–52.

[72] H. P. Gavin. “The Levenberg-Marquardt algorithm for nonlinear least squares curve-fitting problems”. *Department of Civil and Environmental Engineering, Duke University* (2019), pp. 1–19.

[73] D. R. Jones, M. Schonlau, and W. J. Welch. “Efficient global optimization of expensive black-box functions”. *Journal of Global Optimization* 13 (1998), pp. 455–492.

[74] E. Roux. “Assemblage mécanique: stratégies d’optimisation des procédés et d’identification des comportements mécaniques des matériaux”. PhD thesis. PSL Research University, 2011.

[75] P.-O. Bouchard, J.-M. Gachet, and E. Roux. “Ductile damage parameters identification for cold metal forming applications”. *AIP Conference Proceedings*. Vol. 1353. American Institute of Physics. 2011, pp. 47–52.

[76] T.-S. Cao et al. “Identification methodology and comparison of phenomenological ductile damage models via hybrid numerical–experimental analysis of fracture experiments conducted on a zirconium alloy”. *International Journal of Solids and Structures* 50 (2013), pp. 3984–3999.

[77] H. Min, L. Fuguo, and W. Zhigang. “Forming limit stress diagram prediction of aluminum alloy 5052 based on GTN model parameters determined by in situ tensile test”. *Chinese Journal of Aeronautics* 24 (2011), pp. 378–386.

[78] M. G. D. Geers et al. “Strain-based transient-gradient damage model for failure analyses”. *Computer Methods in Applied Mechanics and Engineering* 160 (1998), pp. 133–153.

[79] Y. Zhang, E. Lorentz, and J. Besson. “Ductile damage modelling with locking-free regularised GTN model”. *International Journal for Numerical Methods in Engineering* 113 (2018), pp. 1871–1903.

[80] D. Mumford and J. Shah. “Optimal approximations by piecewise smooth functions and associated variational problems”. *Communications on Pure and Applied Mathematics* 42 (1989), pp. 577–685.

[81] C. Miehe, M. Hofacker, and F. Welschinger. “A phase field model for rate-independent crack propagation: Robust algorithmic implementation based on operator splits”. *Computer Methods in Applied Mechanics and Engineering* 199 (2010), pp. 2765–2778.

[82] B. Bourdin, G. A. Francfort, and J.-J. Marigo. “Numerical experiments in revisited brittle fracture”. *Journal of the Mechanics and Physics of Solids* 48 (2000), pp. 797–826.

[83] M. J. Borden et al. “A higher-order phase-field model for brittle fracture: Formulation and analysis within the isogeometric analysis framework”. *Computer Methods in Applied Mechanics and Engineering* 273 (2014), pp. 100–118.

[84] C. Miehe et al. “Phase field modeling of fracture in multi-physics problems. Part II. Coupled brittle-to-ductile failure criteria and crack propagation in thermo-elastic–plastic solids”. *Computer Methods in Applied Mechanics and Engineering* 294 (2015), pp. 486–522.

[85] M. Dittmann et al. “Variational phase-field formulation of non-linear ductile fracture”. *Computer Methods in Applied Mechanics and Engineering* 342 (2018), pp. 71–94.

[86] M. Ambati, T. Gerasimov, and L. De Lorenzis. “A review on phase-field models of brittle fracture and a new fast hybrid formulation”. *Computational Mechanics* 55 (2015), pp. 383–405.

[87] R. de Borst and C. V. Verhoosel. “Gradient damage vs phase-field approaches for fracture: Similarities and differences”. *Computer Methods in Applied Mechanics and Engineering* 312 (2016), pp. 78–94.

[88] J. Mediavilla, R. H. J. Peerlings, and M. G. D. Geers. “Discrete crack modelling of ductile fracture driven by non-local softening plasticity”. *International Journal for Numerical Methods in Engineering* 66 (2006), pp. 661–688.

[89] M. R. Seabra et al. “Damage driven crack initiation and propagation in ductile metals using XFEM”. *Computational Mechanics* 52 (2013), pp. 161–179.

[90] A. Hussein, B. Hudobivnik, and P. Wriggers. “A combined adaptive phase field and discrete cutting method for the prediction of crack paths”. *Computer Methods in Applied Mechanics and Engineering* 372 (2020), p. 113329.

[91] S. Feld-Payet et al. “A new marching ridges algorithm for crack path tracking in regularized media”. *International Journal of Solids and Structures* 71 (2015), pp. 57–69.

[92] J.-H. Song, H. Wang, and T. Belytschko. “A comparative study on finite element methods for dynamic fracture”. *Computational Mechanics* 42 (2008), pp. 239–250.

[93] R. El Khaoulani and P.-O. Bouchard. “An anisotropic mesh adaptation strategy for damage and failure in ductile materials”. *Finite Elements in Analysis and Design* 59 (2012), pp. 1–10.

[94] T. Belytschko and T. Black. “Elastic crack growth in finite elements with minimal remeshing”. *International Journal for Numerical Methods in Engineering* 45 (1999), pp. 601–620.

[95] M. R. Seabra et al. “Some numerical issues on the use of XFEM for ductile fracture”. *Computational Mechanics* 50 (2012), pp. 611–629.

[96] C. Karolak. “CarboFrac: Analysis and modelling of the failure behavior of carbonitrided parts”. PhD thesis. PSL Research University, 2016.

[97] F. Aldakheel et al. “Phase-field modeling of brittle fracture using an efficient virtual element scheme”. *Computer Methods in Applied Mechanics and Engineering* 341 (2018), pp. 443–466.

[98] F. Aldakheel, B. Hudobivnik, and P. Wriggers. “Virtual element formulation for phase-field modeling of ductile fracture”. *International Journal for Multiscale Computational Engineering* 17 (2019), pp. 181–200.

[99] V. Chiaruttini, V. Riolo, and F. Feyel. “Advanced remeshing techniques for complex 3D crack propagation”. *International Conference on Fracture* (2013), pp. 547–555.

[100] S. Feld-Payet. “Amorçage et propagation de fissures dans les milieux ductiles non locaux”. PhD thesis. École Nationale Supérieure des Mines de Paris, 2010.

[101] D. Uribe-Suárez et al. “Numerical modeling of crack propagation with dynamic insertion of cohesive elements”. *Engineering Fracture Mechanics* 227 (2020), p. 106918.

[102] C. Truesdell. *The Elements of Continuum Mechanics: Lectures given in August-September 1965 for the Department of Mechanical and Aerospace Engineering Syracuse University Syracuse, New York*. Springer Science and Business Media, 2012.

[103] S. Nemat-Nasser. “On finite deformation elasto-plasticity”. *International Journal of Solids and Structures* 18 (1982), pp. 857–872.

[104] E. H. Lee. “Elastic-plastic deformation at finite strain”. *Journal of Applied Mechanics* 36 (1969), pp. 1–6.

[105] T. J. R. Hughes, W. K. Liu, and A. Brooks. “Finite element analysis of incompressible viscous flows by the penalty function formulation”. *Journal of Computational Physics* 30 (1979), pp. 1–60.

[106] J. C. Simo and T. J. R. Hughes. “On the Variational Foundations of Assumed Strain Methods”. *Journal of Applied Mechanics* 53 (1986), p. 51.

[107] I. Babuška. “The finite element method with Lagrangian multipliers”. *Numerische Mathematik* 20 (1973), pp. 179–192.

[108] J. C. Simo, R. L. Taylor, and K. S. Pister. “Variational and projection methods for the volume constraint in finite deformation elasto-plasticity”. *Computer Methods in Applied Mechanics and Engineering* 51 (1985), pp. 177–208.

[109] T. J. R. Hughes. “Generalization of selective integration procedures to anisotropic and nonlinear media”. *International Journal for Numerical Methods in Engineering* 15 (1980), pp. 1413–1418.

[110] L. R. Herrmann. “Elasticity equations for incompressible and nearly incompressible materials by a variational theorem.” *AIAA journal* 3 (1965), pp. 1896–1900.

[111] T. J. R. Hughes. “Equivalence of finite elements for nearly incompressible elasticity”. *Journal of Applied Mechanics* 44 (1977), pp. 181–183.

[112] E. Pichelin and T. Coupez. “Finite element solution of the 3D mold filling problem for viscous incompressible fluid”. *Computer Methods in Applied Mchanics and Engineering* 163 (1998), pp. 359–371.

[113] F. Brezzi and A. Russo. “Choosing bubbles for advection-diffusion problems”. *Mathematical Models and Methods in Applied Sciences* 4 (1994), pp. 571–587.

[114] F. Auricchio et al. “Mixed finite element methods”. *Encyclopedia of Computational Mechanics Second Edition* (2017), pp. 1–53.

[115] K.-J. Bathe, E. Ramm, and E. L. Wilson. “Finite element formulations for large deformation dynamic analysis”. *International Journal for Numerical Methods in Engineering* 9 (1975), pp. 353–386.

[116] C Karakostas, D Talaslidis, and G Wempner. “Triangular C0 bending elements based on the Hu-Washizu principle and orthogonality conditions”. *International Journal for Numerical Methods in Engineering* 36 (1993), pp. 181–200.

[117] D. Talaslidis and G. Wempner. “A simple finite element for elastic-plastic deformations of shells”. *Computer Methods in Applied Mechanics and Engineering* 34 (1982), pp. 1051–1064.

[118] T. Belytschko and L. P. Bindeman. “Assumed strain stabilization of the eight node hexahedral element”. *Computer Methods in Applied Mechanics and Engineering* 105 (1993), pp. 225–260.

[119] P. Wriggers and G. Zavarise. “A formulation for frictionless contact problems using a weak form introduced by Nitsche”. *Computational Mechanics* 41 (2008), pp. 407–420.

[120] P. Wriggers and T. A. Laursen. *Computational contact mechanics*. Vol. 2. Springer, 2006.

[121] M. Hachani and L. Fourment. “A smoothing procedure based on quasi-C1 interpolation for 3D contact mechanics with applications to metal forming”. *Computers and Structures* 128 (2013), pp. 1–13.

[122] I. Temizer, P. Wriggers, and T. J. R. Hughes. “Contact treatment in isogeometric analysis with NURBS”. *Computer Methods in Applied Mechanics and Engineering* 200 (2011), pp. 1100–1112.

[123] K. Fischer and P. Wriggers. “Frictionless 2D contact formulations for finite deformations based on the mortar method”. *Computational Mechanics* 36 (2005), pp. 226–244.

[124] L. De Lorenzis, P. Wriggers, and C. Weißenfels. “Computational contact mechanics with the finite element method”. *Encyclopedia of Computational Mechanics Second Edition* (2017), pp. 1–45.

[125] M. J. Borden et al. “A phase-field description of dynamic brittle fracture”. *Computer Methods in Applied Mechanics and Engineering* 217 (2012), pp. 77–95.

[126] T. J. R. Hughes, J. A. Cottrell, and Y. Bazilevs. “Isogeometric analysis: CAD, finite elements, NURBS, exact geometry and mesh refinement”. *Computer methods in applied mechanics and engineering* 194 (2005), pp. 4135–4195.

[127] M. G. D. Geers. “Experimental analysis and computational modelling of damage and fracture.” PhD thesis. Eindhoven Technical university, 1998.

[128] T. Grätsch and K.-J. Bathe. “A posteriori error estimation techniques in practical finite element analysis”. *Computers and Structures* 83 (2005), pp. 235–265.

[129] O. C. Zienkiewicz and J. Z. Zhu. “A simple error estimator and adaptive procedure for practical engineerng analysis”. *International Journal for Numerical Methods in Engineering* 24 (1987), pp. 337–357.

[130] N.-S. Lee and K.-J. Bathe. “Error indicators and adaptive remeshing in large deformation finite element analysis”. *Finite Elements in Analysis and Design* 16 (1994), pp. 99–139.

[131] D. Perić et al. “Transfer operators for evolving meshes in small strain elasto-placticity”. *Computer Methods in Applied Mechanics and Engineering* 137 (1996), pp. 331–344.

[132] S. Kumar, L. Fourment, and S. Guerdoux. “Parallel, second-order and consistent remeshing transfer operators for evolving meshes with superconvergence property on surface and volume”. *Finite Elements in Analysis and Design* 93 (2015), pp. 70–84.

[133] O. C. Zienkiewicz and J. Z. Zhu. “The superconvergent patch recovery and a posteriori error estimates. Part 1: The recovery technique”. *International Journal for Numerical Methods in Engineering* 33 (1992), pp. 1331–1364.

[134] B. Boroomand and O. C. Zienkiewicz. “Recovery procedures in error estimation and adaptivity. Part II: Adaptivity in nonlinear problems of elasto-plasticity behaviour”. *Computer Methods in Applied Mechanics and Engineering* (1999), pp. 127–146.

[135] D. Brancherie and P. Villon. “Diffuse approximation for field transfer in non linear mechanics”. *European Journal of Computational Mechanics/Revue Européenne de Mécanique Numérique* 15 (2006), pp. 571–587.

[136] A. A. Griffith. “The phenomena of rupture and flow in solids”. *Philosophical Transactions of the Royal Society of London.* 221 (1921), pp. 163–198.

[137] D. Eberly et al. “Ridges for image analysis”. *Journal of Mathematical Imaging and Vision* 4 (1994), pp. 353–373.

[138] D. W. Matula, G. Marble, and J. D. Isaacson. “Graph coloring algorithms”. *Graph Theory and Computing*. Elsevier, 1972, pp. 109–122.

[139] T. Coupez, S. Marie, and R. Ducloux. “Parallel 3D simulation of forming processes including parallel remeshing and reloading”. *Numerical Methods in Engineering’96 (Proceedings of 2nd ECCOMAS Conference, J.-A. Désidéri et. al. Editors)*. 1996, pp. 738–743.

[140] E. Perchat. “Mini-élément et factorisations incomplètes pour la parallélisation d’un solveur de Stokes 2D. Application au forgeage”. PhD thesis. PSL Research University, 2000.

[141] A. Ghahremaninezhad and K. Ravi-Chandar. “Ductile failure behavior of polycrystalline Al 6061-T6”. *International Journal of Fracture* 174 (2012), pp. 177–202.

[142] C. Miehe, S. Teichtmeister, and F. Aldakheel. “Phase-field modelling of ductile fracture: a variational gradient-extended plasticity-damage theory and its micromorphic regularization”. *Philosophical Transactions of the Royal Society A: Mathematical, Physical and Engineering Sciences* 374 (2016), p. 20150170.

[143] V. Davaze et al. “Plastic and fracture behavior of a dual phase steel sheet under quasi-static and dynamic loadings”. *Engineering Fracture Mechanics* 235 (2020), p. 107165.

[144] V. Davaze. “Numerical modelling of crack initiation and propagation in ductile metallic sheets for crash simulations”. PhD thesis. Université Paris Sciences et Lettres, 2019.

[145] K. Saanouni et al. “Numerical prediction of discontinuous central bursting in axisymmetric forward extrusion by continuum damage mechanics”. *Computers and Structures* 82 (2004), pp. 2309–2332.

[146] C. Husson et al. “Finite elements simulations of thin copper sheets blanking: Study of blanking parameters on sheared edge quality”. *Journal of Materials Processing Technology* 199 (2008), pp. 74–83.

[147] J. C. de Sá, P. Areias, and C. Zheng. “Damage modelling in metal forming problems using an implicit non-local gradient model”. *Computer Methods in Applied Mechanics and Engineering* 195 (2006), pp. 6646–6660.

[148] F. Faura, A. Garcıa, and M Estrems. “Finite element analysis of optimum clearance in the blanking process”. *Journal of Materials Processing Technology* 80 (1998), pp. 121–125.

[149] N. Moës et al. “A level set based model for damage growth: the thick level set approach”. *International Journal for Numerical Methods in Engineering* 86 (2011), pp. 358–380.

[150] H. Amor, J.-J. Marigo, and C. Maurini. “Regularized formulation of the variational brittle fracture with unilateral contact: Numerical experiments”. *Journal of the Mechanics and Physics of Solids* 57 (2009), pp. 1209–1229.

[151] J. Goldsmith and J. Salmon. “Automatic creation of object hierarchies for ray tracing”. *IEEE Computer Graphics and Applications* 7 (1987), pp. 14–20.

[152] D. J. Benson and J. O. Hallquist. “A single surface contact algorithm for the post-buckling analysis of shell structures”. *Computer Methods in Applied Mechanics and Engineering* 78 (1990), pp. 141–163.

[153] L. De Lorenzis and T. Gerasimov. “Numerical implementation of phase-field models of brittle fracture”. *Modeling in Engineering Using Innovative Numerical Methods for Solids and Fluids*. Springer, 2020, pp. 75–101.

# Appendices

# APPENDIX A

## A.1 Mathematical formulation of the phase field model

Starting with the regularized energy functional of a cracked body

$$\mathcal{E}_l = \int_\Omega g_e(d)\, W_e(\boldsymbol{\varepsilon}^e)\, d\Omega + \int_\Omega \frac{G_c}{2l_c}(d^2 + l_c^2|\nabla d|^2)\, d\Omega \tag{A.1}$$

the variation of the functional with respect to the phase field variable $d$ reads as

$$\delta_d \mathcal{E}_l = \frac{\partial \mathcal{E}_l}{\partial d} - \nabla \cdot \frac{\partial \mathcal{E}_l}{\partial \nabla d} \tag{A.2}$$

where the condition of optimality is expressed as follows

$$\delta_d \mathcal{E}_l = 0. \tag{A.3}$$

Expanding the r.h.s in equation A.2 leads to

$$\frac{\partial \mathcal{E}_l}{\partial d} = \int_\Omega -2(1-d)\, W_e + \frac{G_c}{l_c} d\, d\Omega \tag{A.4}$$

$$\frac{\partial \mathcal{E}_l}{\partial \nabla d} = \int_\Omega G_c\, l_c \nabla d\, d\Omega. \tag{A.5}$$

Combining the different terms leads to leads to the same evolution equation as 1.47

$$d - l_c^2 \nabla^2 d = \frac{-2l_c}{G_c}(1-d) W_e. \tag{A.6}$$

## A.2 crack propagation in compression-dominant zones

The elastic strain energy can be decomposed as follows

$$W_e(\boldsymbol{\varepsilon}^e) = W_e^+(\boldsymbol{\varepsilon}^e) + W_e^-(\boldsymbol{\varepsilon}^e) \tag{A.7}$$

where $W_e^+$ and $W_e^-$ are the positive and negative parts, respectively.

The Euler-Lagrange equations of this "anistropic" formulation are given as:

$$\boldsymbol{\sigma}_{ij} = g_e(d)\frac{\partial W_e^+}{\partial \boldsymbol{\varepsilon}_{ij}^e} + \frac{\partial W_e^-}{\partial \boldsymbol{\varepsilon}_{ij}^e} \tag{A.8}$$

$$\frac{G_c}{l_c}(d - l_c^2\nabla^2 d) = -g_e'(d)W_e^+(\boldsymbol{\varepsilon}^e). \tag{A.9}$$

As can be observed in equation A.8, the degradation function affects only the positive part of the energy. Likewise, the right hand side of equation A.9 contains the positive part of the energy. The next step is to define a criterion at which the energy is decomposed, three different approaches have been proposed in the literature:

## A.2.1 First approach

Miehe et al. in [53, 81] suggested a decomposition of the elastic strain energy into positive and negative parts based on spectral decomposition of the elastic strain tensor as follows:

$$W_e^+(\boldsymbol{\varepsilon}^e) = \frac{E\nu}{2(1+\nu)(1-2\nu)}\langle tr(\boldsymbol{\varepsilon}^e)\rangle_+^2 + \frac{E}{2(1+\nu)}tr(\boldsymbol{\varepsilon}^{e2}_+) \tag{A.10a}$$

$$W_e^-(\boldsymbol{\varepsilon}^e) = \frac{E\nu}{2(1+\nu)(1-2\nu)}\langle tr(\boldsymbol{\varepsilon}^e)\rangle_-^2 + \frac{E}{2(1+\nu)}tr(\boldsymbol{\varepsilon}^{e2}_-) \tag{A.10b}$$

where $\langle x\rangle_- = \max(-x, 0)$ and $\langle x\rangle_+ = \max(x, 0)$, $\boldsymbol{\varepsilon}^e{}_\pm = \sum_{i=1}^3 \boldsymbol{\epsilon}_\pm b_i \otimes b_i$ given that $\boldsymbol{\epsilon}_\pm$ and $b_i$ are the eigenvalues and eigenvectors of the elastic strain tensor, respectively. The stress tensor can be obtained as follows [149]:

$$\boldsymbol{\sigma}_{ij} = \big(g_e(d)\frac{\partial W_e^+}{\partial \boldsymbol{\varepsilon}_k} + \frac{\partial W_e^-}{\partial \boldsymbol{\varepsilon}_k}\big)\frac{\partial \boldsymbol{\varepsilon}_k}{\partial \boldsymbol{\varepsilon}_{ij}} = \bar{\boldsymbol{\sigma}}_k\frac{\partial \boldsymbol{\varepsilon}_k}{\partial \boldsymbol{\varepsilon}_{ij}} \tag{A.11}$$

$$\begin{pmatrix} \bar{\boldsymbol{\sigma}}_1 \\ \bar{\boldsymbol{\sigma}}_2 \\ \bar{\boldsymbol{\sigma}}_3 \end{pmatrix} = \begin{pmatrix} (1-\alpha_1 d)^2 + (1-\alpha d)^2 & \gamma(1-\alpha d)^2 & \gamma(1-\alpha d)^2 \\ \gamma(1-\alpha d)^2 & (1-\alpha_2 d)^2 + (1-\alpha d)^2 & \gamma(1-\alpha d)^2 \\ \gamma(1-\alpha d)^2 & \gamma(1-\alpha d)^2 & 1-\alpha_3 d)^2 + (1-\alpha d)^2 \end{pmatrix} \begin{pmatrix} \boldsymbol{\epsilon}_1 \\ \boldsymbol{\epsilon}_2 \\ \boldsymbol{\epsilon}_3 \end{pmatrix}$$

with the two conditions:

**if** $\boldsymbol{\epsilon}_i < 0$ **then**
  $\alpha_i = 0$
**else**
  $\alpha_i = 1$
**if** $\boldsymbol{\epsilon}_1 + \boldsymbol{\epsilon}_2 + \boldsymbol{\epsilon}_3 < 0$ **then**
  $\alpha = 0$
**else**
  $\alpha = 1$

where $\gamma = \frac{\nu}{1-2\nu}$. The Taylor series is used in order to numerically compute the derivatives

of the strain tensor as follows

$$\frac{\partial \boldsymbol{\varepsilon}_k}{\partial \boldsymbol{\varepsilon}^e_{ij}} = \frac{\boldsymbol{\varepsilon}_k(\boldsymbol{\varepsilon}^e_{ij} + \delta\boldsymbol{\varepsilon}^e_{ij}) - \boldsymbol{\varepsilon}_k(\boldsymbol{\varepsilon}^e_{ij})}{\delta\boldsymbol{\varepsilon}^e_{ij}} + \cancel{O(\boldsymbol{\delta\varepsilon}^{e2}_{ij})}. \tag{A.12}$$

## A.2.2 Second approach

The second approach introduced by Amor et al. [150] reads as follows:

$$\begin{aligned} W^+_e(\boldsymbol{\varepsilon}^e, d) &= \frac{\kappa}{2}\langle tr(\boldsymbol{\varepsilon}^e)\rangle^2_+ + \mu\, \boldsymbol{\varepsilon}^e_{dev} : \boldsymbol{\varepsilon}^e_{dev} \\ W^-_e(\boldsymbol{\varepsilon}^e, d) &= \frac{\kappa}{2}\langle tr(\boldsymbol{\varepsilon}^e)\rangle^2_-, \end{aligned} \tag{A.13}$$

equation A.14 represents the form of the phase field evolution equation:

$$\frac{G_c}{l_c}(d - l_c^2\nabla^2 d) = g'_e(d)\big(\kappa\frac{\langle tr(\boldsymbol{\varepsilon}^e)\rangle_+}{2} + \mu\, \boldsymbol{\varepsilon}^e_{dev} : \boldsymbol{\varepsilon}^e_{dev}\big). \tag{A.14}$$

It can be seen from equation A.14 that the positive part of the volumetric strain energy reflects the effect of dilatation. On the other hand, the deviatoric part that reflects the effect of shear deformation which is assumed to compete with the fracture energy resulting in the evolution of the phase field. The negative part of the volumetric energy that is related to reduction in volume does not contribute to the evolution of the phase field. the resulting constitutive relation is shown as

$$\boldsymbol{\sigma} = \kappa(1-\alpha d)^2\,\mathrm{tr}(\boldsymbol{\varepsilon}^e) + 2(1-d)^2\,\boldsymbol{\varepsilon}^e_{dev}\, I^{dev} \tag{A.15}$$

where $I^{Dev}_{ijkl} = I_{ijkl} - \frac{1}{3}\delta_{ij}\delta_{kl}$, $I_{ijkl} = \frac{1}{2}(\delta_{ij}\delta_{kl} - \delta_{ik}\delta_{jl})$ with $\delta$ is the Kronecker's delta. With the condition:

---

**if** $\varepsilon_1 + \varepsilon_2 + \varepsilon_3 < 0$ **then**
  $\alpha = 0$
**else**
  $\alpha = 1$

---

## A.2.3 Third approach

Ambati et al. in [86] suggested a new hybrid formulation that uses the advantages of both isotropic and anistropic energy degradation models as follows:

$$\boldsymbol{\sigma}_{ij} = g_e(d)\frac{\partial W_e}{\partial \boldsymbol{\varepsilon}^e_{ij}} \tag{A.16}$$

$$\frac{G_c}{l_c}(d - l_c^2\nabla^2 d) = g'_e(d)W^+_e(\boldsymbol{\varepsilon}^e) \tag{A.17}$$

with an additional constraint: If $W^+_e < W^-_e$ then $d = 0$.

The presented formulation combines the advantages of both isotropic and anistopic formu-

lations. the first equation in A.16 mimics the isotropic formulations in the sense of degrading the whole energy derivative with no distinction between tension and compression. On the contrary, the second equation uses the positive part of the energy in the crack driving force. The addition of the constraint prevents the damage evolution in compression-dominated zones interpenetration of crack faces as proposed by the isotropic energy decomposition. The main advantage of the hybrid formulations is the linear constitutive relation as compared to the nonlinear case with anistropic formulation proposed in the first approach. Authors in [86] have shown that by adopting the hybrid formulation, the computational time is reduced by almost one order of magnitude as compared to the anistropic case.

### A.2.4 Which approach is the optimum?

Neither of the proposed decomposition strategies can work with all problems without drawbacks. In consequence, the choice is limited to the type of problem being solved. For example, when the three eigenvalues of the strain tensor become negative in the first equation in A.10, the right hand side of equation A.9 vanishes. In consequence, the driving force is vanished with no further evolution of the phase field. On the contrary, the evolution of the phase field continues according to the second formulation. This can be clearly observed in the shear terms in equation A.13. Finally, it should be noted that the hybrid formulation is considered the most efficient since a linear momentum equation is obtained as opposed to the anisotroic degradation cases where a nonlinear constitutive relation is obtained.

# APPENDIX B

## B.1 Contact treatment

The contact problem can be divided in two main parts: (i). detection of the surfaces that are in contact; (ii). computation of the transmitted forces across the contact surfaces. Contact detection is basically a search process that aims to define the active contact surfaces between multiple bodies. First, a global search is used in order to determine the bodies/surfaces that will be potentially in contact without doing costly computations. Next, a local search operation is used to determine the projection of each slave node on the master surface so that the penetration and slip distances are calculated by determining the closest point projection on the master surface within the predefined region of the global search. Different global search algorithms can be found in the literature (see [151] for the dynamic ray-tracing algorithm that is considered, an efficient bucket search algorithm applied on post-buckling analysis [152], and [124] for a review about the existing models in the literature). Once the active contact faces are determined, mathematical constraints must be imposed to the problem in order to prohibit the violation of the non-penetration condition in the normal direction of different bodies. In addition, more constraints should be added to describe the effect of friction between the surfaces in the tangential direction during the sticking/sliding condition.

In the general setting, the contact conditions are imposed in two ways: $(i)$. contact between external dies and the deformable body; $(ii)$. a self contact between the crack faces that is considered as a contact between two deformable bodies. Without the loss of generality, the following analysis describe the self contact between the crack faces shown in Fig. 2.1, however the same formulation applies for the other type of contact. The contact surfaces in the reference configuration are defined as follows:

1. $\Gamma_d$: the contact surface with the external die;
2. $\Gamma_c^m$: the master contact surface of the crack;
3. $\Gamma_c^s$: the slave contact surface of the crack.

The deformation map $\Phi$ that maps the reference configuration $\Omega$ to the current configuration $\omega = \Phi_t(\Omega)$ where the $\gamma_v$ = $\Phi_t(\Gamma_v)$ and $\gamma_t = \Phi_t(\Gamma_t)$ are the the surfaces in the current configuration where Dirichlet and Newmann boundary, respectively. In addition, $\gamma_d = \Phi_t(\Gamma_d)$

is the contact surface with the external die in the current configuration. The active crack faces for the master and slave surfaces are $\gamma_c^m$ and $\gamma_c^s$. For any point $\mathrm{x}_2$ on the slave surface $\gamma_c^s$, its closest point projection on the master surface $\gamma_c^m$ leads to an orthogonal projection at the point $\bar{\mathrm{x}}_1$. A gap function $g_n$ that defines the orthogonal distance is defined in the rate form as follows

$$\dot{g}_n = (v_2 - \bar{v}_1) \cdot \bar{\boldsymbol{n}} \tag{B.1}$$

where $\bar{\boldsymbol{n}}$ is the normal unit vector to the master surface at the point $\bar{\mathrm{x}}_1$. $v_2$ and $\bar{v}_1$ are the velocities of the slave and master points that are in contact, respectively. The bar here is used to indicate that the master point velocity is evaluated at the closet projection point.

The following conditions need to be satisfied during the contact between the crack faces

1. The gap function $\dot{g}_n$ should be equal to 0 in the case of contact and positive in the case of non-contact;
2. The contact normal stress should be negative;
3. Frictionless contact condition in the tangential direction should be satisfied.

The resulting conditions can be expressed mathematically as follows

$$\dot{g}_n \geq 0, \sigma_n \leq 0, \dot{g}_n \, \sigma_n = 0 \text{ (Kuhn–Tucker conditions)} \tag{B.2a}$$

$$\sigma_t = 0 \text{ (Frictionless contact condition)} \tag{B.2b}$$

where $\sigma_n$ and $\sigma_t$ are the magnitudes of the normal and tangential traction vectors, respectively. The normal and tangential stresses can be computed as follows

$$\sigma_n = \sigma \cdot \bar{\boldsymbol{n}} \cdot \bar{\boldsymbol{n}} \tag{B.3a}$$

$$\sigma_t = \|\sigma \cdot \bar{\boldsymbol{n}} - \sigma_n \bar{\boldsymbol{n}}\|. \tag{B.3b}$$

For the contact surface with the external die $\Gamma_d$, a Coulomb limited by Tresca law is used. The friction law can be explained as follows: a sticking contact condition is imposed between the master and slave bodies if $\sigma_t \leq \sigma_c$. Once $\sigma_t$ becomes greater than $\sigma_c$, a relative motion between the two bodies occurs. $\sigma_c$ is defined as follows

$$\sigma_c = \varepsilon_f \, \sigma_n \tag{B.4}$$

where $\varepsilon_f$ is Coulomb friction coefficient. Tresca shear stress defined as follows

$$\sigma_c = \bar{m} \frac{\bar{\boldsymbol{\sigma}}}{\sqrt{3}} \tag{B.5}$$

where $\bar{m}$ is Tresca's friction coefficient that takes a value between 0 and 1. Tresca friction

stress limits Coulomb's stress according to the following condition

$$\sigma_c = \min(\varepsilon_f \, \sigma_n, \bar{m} \frac{\bar{\boldsymbol{\sigma}}}{\sqrt{3}}). \tag{B.6}$$

## B.2 Solution strategy

The final form of the residual equations can be found after substituting equations 2.47, 2.48 and 2.50 in 2.49a-2.49d. It can be written on the following form:

$$\boldsymbol{R}^{ll} + \boldsymbol{R}^{lp} = \boldsymbol{0} \tag{B.7a}$$

$$\boldsymbol{R}^{bb} + \boldsymbol{R}^{bp} = \boldsymbol{0} \tag{B.7b}$$

$$\boldsymbol{R}^{pl} + \boldsymbol{R}^{pb} + \boldsymbol{R}^{pp} = \boldsymbol{0} \tag{B.7c}$$

$$\boldsymbol{R}^{dd} + \boldsymbol{R}^{dl} = \boldsymbol{0} \tag{B.7d}$$

where $\boldsymbol{R}^{xy}$ is the residual force vector of coupled set of unknowns $x$ and $y$. The resulting coupled system of equations is non-linear and an adequate solution strategy should be used.

A staggered algorithm is used to decouple the solution of mechanical equations from the phase field or non-local damage equations [81]. First, the velocity and pressure are obtained by applying the Newton-Raphson solver on equations (B.7a, B.7b, B.7c) while freezing the phase field or the non-local damage variables. Then, equation B.7d is solved while freezing the velocity and pressure solutions obtained in the previous step. For more details about the solution strategies, see [153]. A summary of all algorithmic operations is found in algorithm 1.

**Algorithm 1:** Staggered algorithm

**Result:** $v_{t=0:T}, p_{t=0:T}, [d_{t=0:T}, \bar{D}_{t=0:T}]$

1. Initialize $v_t, p_t$ and [$d_t$,$\bar{D}_t$];

**for** $t = 0 : T$ **do**

$i \leftarrow 0$, $v_i \leftarrow v_t$, $p_i \leftarrow p_t$ ;

2. **while** *(*$Res_1 > Tol_{NR}$ *and* $i < i_{max}$*)* **do**

Solve the system of equations B.7a, B.7b and B.7c using a Newton Raphson solver to obtain $v_{i+1}$, $p_{i+1}$;

Compute the new plastic strain increment using equation 2.35 or 2.36;

$i \leftarrow i + 1$

**end**

$v_t \leftarrow v_{i+1}$;

$p_t \leftarrow p_{i+1}$;

3. Solve equation B.7d to obtain $d_{t+\Delta t}$ or $\bar{D}_{t+\Delta t}$;

5. Go to step 2;

**end**

## RÉSUMÉ

Cette thèse contribue à la modélisation de la transition endommagement - rupture dans un cadre numérique parallèle 3D basé sur la méthode des éléments finis. Les nouvelles contributions comprennent: (i). une formulation champ de phase - endommagement couplée qui est adaptée pour les applications de mise en forme; (ii). un remaillage adaptatif suivi par l'identification de l'intersection de la surface de la fissure avec des topologies de maillage arbitraires basées sur l'évolution du champ de phase; (iii). l'insertion de la surface de la fissure dans le maillage à l'aide d'opérations locales de partitionnement du maillage; (iv). une stratégie de dédoublage nodale basée sur l'algorithme de coloration locale afin d'ouvrir les faces des fissures suivi par une étape de remaillage volumique.

Le cadre proposé offre un outil numérique robuste pour la modélisation de la transition endommagement - rupture dans des procédés industriels complexes tels que: (i). la formation de fissures internes en chevrons lors du procédé d'extrusion; (ii). des simulations de découpe telle que le procédé de cisaillement de barres, de découpage et de perçage. Les comparaisons avec la méthode de suppression d'éléments (kill element) montrent une amélioration significative de la qualité des surfaces cisaillées prédites avec la capacité de détecter avec précision les caractéristiques de surfaces rompues telles que les bavures. De plus, le volume et l'énergie sont conservés pendant la simulation, ce qui résout l'un des principaux problèmes qui apparaît avec la méthode de suppression d'éléments.

## MOTS CLÉS

Rupture ductile, Transition endommagement – rupture, Modèle de champ de phase, Remaillage adaptatif, Propagation de fissures discrètes, Application à la mise en forme

## ABSTRACT

This PhD contributes to the modeling of damage to fracture transition within a 3D parallel numerical framework based on the finite element method. The new contributions include: (i). a coupled phase field-damage formulation that is adapted to metal forming applications; (ii). adaptive remeshing followed by the identification of the crack surface intersection with arbitrary mesh topologies based on the phase field evolution; (iii). fitting the crack surface within the mesh using local mesh partitioning operations; (iv). a nodal duplication strategy based on the local coloring algorithm in order to open the crack faces followed by a volume remeshing step.

The proposed framework offers a robust numerical tool for the modeling of damage to fracture transition in complex industrial processes such as: (i). the formation of internal chevron cracks during bar extrusion process; (ii). metal cutting simulations including bar shearing, blanking and piercing processes. Comparisons with the element deletion method show significant improvement in the quality of predicted sheared surfaces with the ability to accurately detect surface features such as burrs. In addition, both volume and energy are conserved during the simulation which resolves one of the main issues that appears with the element deletion method.

## KEYWORDS

Ductile fracture, Damage to fracture transition, Phase field model, Adaptive remeshing, Discrete crack propagation, Metal forming applications